LIQUEFACTION EVALUATION IN STRATIFIED SOILS

By

Aimee Rhodes

Supervised by:

Misko Cubrinovski

Co-supervised by:

Jennifer Haskell and Mark Stringer

A thesis submitted in partial fulfilment of the requirements for the Degree of Master of Engineering in Earthquake Engineering at the University of Canterbury

Department of Civil and Natural Resources Engineering

University of Canterbury

Christchurch, New Zealand

February 2017

Abstract

The Canterbury Earthquake Sequence (CES) of 2010-2011 caused widespread liquefaction in many parts of Christchurch. Observations from the CES highlight some sites were liquefaction was predicted by the simplified method but did not manifest. There are a number of reasons why the simplified method may over-predict liquefaction, one of these is the dynamic interaction between soil layers within a stratified deposit. Soil layer interaction occurs through two key mechanisms; modification of the ground motion due to seismic waves passing through deep liquefied layers, and the effect of pore water seepage from an area of high excess pore water pressure to the surrounding soil. In this way, soil layer interaction can significantly alter the liquefaction behaviour and surface manifestation of soils subject to seismic loading. This research aimed to develop an understanding of how soil layer interaction, in particular ground motion modification, affects the development of excess pore water pressures and liquefaction manifestation in a soil deposit subject to seismic loading.

A 1-D soil column time history Effective Stress Analysis (ESA) was conducted to give an in depth assessment of the development of pore pressures in a number of soil deposits. For this analysis, ground motions, soil profiles and model parameters were required for the ESA. Deconvolution of ground motions recorded at the surface during the CES was used to develop some acceleration time histories to input at the base of the soil-column model. An analysis of 55 sites around Christchurch, where detailed site investigations have been carried out, was then conducted to identify some simplified soil profiles and soil characteristics. From this analysis, four soil profiles representative of different levels of liquefaction manifestation were developed. These were; two thick uniform and vertically continuous sandy deposits that were representative of sites were liquefaction manifested in both the M_w 7.1 September 2010 and the M_w 6.3 February 2011 earthquakes, and two vertically discontinuous profiles with interlayered liquefiable and non-liquefiable layers representative of sites that did not manifest liquefaction in either the September 2010 or the February 2011 events. Model parameters were then developed for these four representative soil profiles through calibration of the constitutive model in element test simulations.

Simulations were run for each of the four profiles subject to three levels of loading intensity. The results were analysed for the effect of soil layer interaction. These were then compared to a simplified triggering analysis for the same four profiles to determine where the simplified method was accurate in predicting soil liquefaction (for the continuous sandy deposits) and were it was less accurate (the vertically discontinuous deposits where soil layer interaction was a factor).

Acknowledgements

First and foremost I want to thank my supervisor Prof. Misko Cubrinovski. Your expertise and readiness to give guidance have been invaluable, as has been the time, patience and energy you have put in to make this project possible.

I would like to acknowledge the financial support and scholarship provided by the New Zealand Earthquake Commission (EQC) and partial support of the research efforts by QuakeCoRE.

This study is part of a large research effort at the University of Canterbury. The 55 well- documented sites were investigated in a comprehensive effort involving Tonkin & Taylor, the University of Canterbury, University of California, Berkeley, University of Texas, Austin, and University of Auckland. The contributions of many researchers to these large collaborative efforts are gratefully acknowledged.

I would also like to thank my fellow postgraduate Nikos Ntritsos. Your contribution to the classification and development of the simplified soil profiles has been instrumental to this research, without your help I would still be developing those profiles today.

Lastly, my thanks go to my family, to Noreen and Mike – thank-you for your understanding and support, we often take for granted those things we need the most. To Rebecca, thanks for always been a ready ear, and to Nic – thank-you for your unending tolerance and encouragement. You have all made sacrifices for this research, and without you I wouldn't have made it here today.

Table of Contents

Abstract ii
Acknowledgements iii
Table of Contents iv
List of Figures vii
List of Tables xii
1 Introduction 1
1.1 Motivation 1
1.2 Objectives 2
1.3 Thesis organisation 2
2 Background 3
2.1 Liquefaction 3
2.1.1 Factors affecting liquefaction resistance 4
2.1.2 Time dependency 6
2.2 Soil layer interaction 6
2.2.1 Centrifuge studies 7
2.2.2 Canterbury earthquake sequence 9
2.3 Evaluation of liquefaction triggering 11
2.3.1 Simplified method 11
2.3.2 Effective stress analysis 16
3 Deconvolution 21
3.1 Sites used in the deconvolution of recorded motions 21
3.2 Methodology 24
3.3 Degradation curves 27
3.3.1 Modulus reduction curves 27
3.3.2 Damping ratio reduction curves 29
3.4 Validation of deconvolution 30
3.4.1 Deconvoluted motion at the same site 30
3.4.2 Deconvoluted motion at other sites 30
3.5 Variations on the method of deconvolution 32
4 Soil Profile Characterisation 34
4.1 Factors contributing to over-prediction by the simplified method 36
4.2 Simplified soil profiles 37
4.2.1 Data and characterisation method 38
4.2.2 Critical layer analysis 42
4.3 Characteristic soil profiles 48

4.3.1 Yes/Yes group 1 (YY1) soil profile characterisation 50
4.3.2 Yes/Yes group 2 (YY2) soil profile characterisation 52
4.3.3 No/No group 1 (NN1) soil profile characterisation 53
4.3.4 No/No group 2 (NN2) soil profile characterisation 54
4.3.5 Summary 56
5 Element Test Simulations 57
5.1 Methodology 57
5.2 Modelling liquefiable layers 60
5.2.1 Determination of target liquefaction resistance curves 60
5.2.2 Model simulation of target liquefaction resistance curves 63
5.3 Non-liquefiable layers 64
5.3.1 Determination of target degradation curves 64
5.3.2 Model simulation of target degradation curves 66
5.4 Permeability 67
6 Results 69
6.1 Input motions 69
6.2 YY1 Analyses 70
6.2.1 High shaking intensity (a_{max}=0.4g) 70
6.2.2 YY1 Analyses: All shaking intensities 76
6.3 YY2 Analyses 79
6.4 Comparison of the YY1 and YY2 analyses 83
6.5 NN1 Analyses 84
6.6 NN2 Analyses 87
6.7 Comparison of the NN1 and NN2 analyses 90
6.8 Comparison of the YY and NN analyses 91
6.9 Comparison of results from ESA and simplified method of analysis 94
6.10 Sensitivity of the ground response at shallow depths 97
7 Summary and Conclusions 101
7.1 Key findings and conclusions 103
7.2 Recommendations for further research 104
References 106
Appendix A: Analysis of centrifuge tests 109
Appendix B: CACS modulus and damping degradation curves 113
Appendix C: RHSC modulus and damping degradation curves 114
Appendix D: CHHC modulus and damping degradation curves 115
Appendix E: Scale factors used in validation of deconvoluted motions 117
Appendix F: Validation of motions deconvoluted for the 13 June 2011 earthquake 118

Appendix G: Results of critical layer analysis showing for q_{c1Ncs} for a single critical layer per site 119

Appendix H: Target LRCs for YY2, NN1 and NN2 liquefiable layers 120

Appendix I: S-D Modelling of target LRCs for YY2, NN1 and NN2 liquefiable layers..... 121

Appendix J: Modelling target degradation curves for the non-liquefiable layers..... 124

Appendix K: Permeability values adopted for each layer in the YY1, YY2, NN1 and NN2 profiles 127

Appendix L: Suitability of the CACS 22 Feb 2011 ground motion with scaling factor I_3=1.12 as representative of the 4 Sep 2010 earthquake 128

Appendix M: Stress-strain curves for all layers in YY1 profile with I_1=2.23 (a_{max}=0.4g) input motion.... 131

Appendix N: Comparison of response of YY1 and YY2 profiles for I_2=1.67 (a_{max}=0.3g) and I_3=1.12 (a_{max}=0.2g) 133

Appendix O: Comparison of the response of the NN1 and NN2 profiles for I_2=1.67 (a_{max}=0.3g) and I_3=1.12 (a_{max}=0.2g)..... 134

Appendix P: Comparison of results from simplified method and ESA for all soil profiles and all ground motion intensities..... 135

List of Figures

Figure 2.1: Illustration of uniform cyclic loading causing liquefaction (Cubrinovski, 2011) 4
Figure 2.2: Shear stress-shear strain relationship for liquefied soil (Cubrinovski, 2011) 4
Figure 2.3: Example of a critical state line 5
Figure 2.4: CRR with normalised SPT blow count showing variation with fines content of soil (Cubrinovski, 2015) 5
Figure 2.5: Liquefaction resistance of soil samples with different fabric (Cubrinovski, 2015) 6
Figure 2.6: Modification of ground motion due to soil liquefaction in a centrifuge model (Zeghal et al., 1999) 7
Figure 2.7: Model 3 layout from Byrne et al. (2003) 8
Figure 2.8: Excess pore water pressure (EPP) with time at different depths measured in model 3 (Byrne et al, 2003) 9
Figure 2.9: Factor of safety (FS) with depth for model 3 using the simplified method (Boulanger and Idriss, 2014) and the data of Byrne et al. (2003) 9
Figure 2.10: Preliminarily liquefaction map for the M_w 6.3 February 2011 earthquake. Red indicates moderate-severe liquefaction and yellow low-moderate liquefaction based on drive through observations (Cubrinovski et al., 2011) 10
Figure 2.11: Factor of safety against liquefaction triggering (Green et al., 2014): (a) for the Kaiapoi site; (b) for the CBD site 11
Figure 2.12: *CRR*-q_{c1Ncs} relationship using the updated CPT database from Boulanger and Idriss (2014) 13
Figure 2.13: MSF for various earthquake magnitudes and CPT tip resistances (Boulanger and Idriss, 2014) 14
Figure 2.14: Overburden correction factor (Boulanger and Idriss, 2014) 14
Figure 2.15: Post-liquefaction volumetric strain from Zhang et al. (2002) 15
Figure 2.16: Comparison of experimental and simulated LRCs (Cubrinovski, 2011) 18
Figure 2.17: Schematic of the iterative process for determining the stress increment from strain increment 18
Figure 2.18: Determination of stress-strain parameters using the state-index framework (Cubrinovski and Ishihara, 1998: (a) $G_{N,max}$ and $G_{N,min}$; (b) $(q/p)_{max}$ 19
Figure 2.19: Definition of the state index I_s (Cubrinovski and Ishihara, 1998) 19
Figure 3.1: Map of SMSs used in the deconvolution process (Google Maps, 2017) 22
Figure 3.2: Soil and V_s profile at CACS (Wotherspoon et al., 2013) 23
Figure 3.3: Soil and V_s profile at RHSC (Wotherspoon et al., 2013) 23
Figure 3.4: Soil and V_s profile at CHHC (Wotherspoon et al., 2013) 24
Figure 3.5: Illustration of the deconvolution process 26

Figure 3.6: Modified modulus reduction curve for RHSC at z = 10 m 28
Figure 3.7: Comparison of failure stress for original Darendeli curve and the strength based modification for RHSC at z = 10 m 28
Figure 3.8: Damping reduction curve for RHSC z=10 m 30
Figure 3.9: Comparison of response spectra between the recorded surface motion and the surface motion computed using a deconvoluted motion for 22 February 2011 earthquake: (a) CACS deconvoluted motion at RHSC site; (b) CACS deconvoluted motion at CHHC site; (c) RHSC deconvoluted motion at CACS site; (d) RHSC deconvoluted motion at CHHC site 32
Figure 4.1: Land damage during the 4 September 2010 M_w 7.1 earthquake (Tonkin & Taylor, 2015) 35
Figure 4.2: Land damage during the 22 February 2011 M_w 6.2 earthquake (Tonkin & Taylor, 2015)..... 35
Figure 4.3: Map of 55 sites used for simplified analysis (Tonkin & Taylor, 2015) 39
Figure 4.4: Simplified soil profile for site at 1128 Avonside Drive, Avondale 40
Figure 4.5: Comparison of triggering analysis on simplified soil profile and full CPT trace at 1128 Avonside Drive, Avondale 41
Figure 4.6: Critical layers identified from triggering analysis on simplified soil profile at 1128 Avonside Drive, Avondale 45
Figure 4.7: Illustration of different critical zones identified in critical layer analysis at 1128 Avonside Drive, Avondale 46
Figure 4.8: Results of critical layer analysis showing comparison of properties for the YY and NN cases of liquefaction manifestation (values at the end of the whiskers represent the minimum and maximum values for each dataset) (a) q_{c1Ncs} using Boulanger and Idriss (2014) (b) depth to the top of the critical zone (CZ) (c) depth to the top of FS < 1 (d) thickness of the CZ (e) cumulative thickness of FS < 1 (f) cumulative thickness of liquefiable material 47
Figure 4.9: Outline of two characteristic soil profiles in Christchurch 49
Figure 4.10: $CRR_{7.5,100kPa}$ ratios for four soil profiles in YY1 51
Figure 4.11: q_{c1Ncs} values for sites used to characterise YY1 51
Figure 4.12: Simplified representative soil profile for YY1 52
Figure 4.13: Variation in $CRR_{7.5,100kPa}$ due to uncertainty in q_{c1Ncs} values for a given layer 52
Figure 4.14: q_{c1Ncs} values for sites used to characterise YY2 53
Figure 4.15: Simplified representative soil profile for YY2 53
Figure 4.16: Simplified representative soil profile for NN1 55
Figure 4.17: Simplified representative soil profile for NN2 55
Figure 5.1: Schematic of the methodology used to calibrate soil parameters for the 1-D soil column model 59
Figure 5.2: Schematic illustration of the concept of element test simulations 59

Figure 5.3: Relationship between MSF_{max} and b value used in calculation of N_c for LRCs (Boulanger and Idriss, 2014) 61
Figure 5.4: Liquefaction resistance curves for YY1 liquefiable soils at 100 kPa 62
Figure 5.5: S-D Model (SDM) LRCs (symbols and dashed lines) and target LRCs (solid lines) for YY1 soils of different densities 64
Figure 5.6: Target shear modulus degradation curves for two types of non-liquefiable layers: (a) non-liquefiable sand at z=15 m; (b) silt at z=5.5 m in NN1 profile 65
Figure 5.7: Stress density modelling of degradation curves for (a) non-liquefiable sand at z=15 m and (b) silt at z=5.5 m in the NN1 profile 67
Figure 6.1: Pore water pressure ratio time histories for YY1, a_{max}=0.4g: (a) z = 0-6 m; (b) z = 6-10 m 71
Figure 6.2: Pore water pressure build up with time (YY1, a_{max}=0.4g) 71
Figure 6.3: Horizontal acceleration time histories throughout depth (YY1, a_{max}=0.4g) 73
Figure 6.4: Pore water pressure ratio throughout depth (YY1, a_{max}=0.4g) 73
Figure 6.5: Acceleration response spectra for YY1, a_{max}=0.4g: (a) at the ground surface; (b) at the top of the critical layer; (c) at the bottom of the critical zone; (d) at 10 m depth 74
Figure 6.6: Distribution of maximum horizontal acceleration with depth (YY1, a_{max}=0.4g) 74
Figure 6.7: Distribution of maximum shear strain with depth (YY1, a_{max}=0.4g) 74
Figure 6.8: Stress-strain curves for YY1, a_{max}=0.4g: (a) in crust layer (z=0.45m); (b) in the critical zone (z=3.3m); (c) below critical zone (z=7.5m); (d) below 10m (z=15.5m) 75
Figure 6.9: Horizontal displacement with depth (YY1, a_{max}=0.4g) 75
Figure 6.10: Maximum horizontal displacement with depth (YY1, a_{max}=0.4g) 76
Figure 6.11: Pore water pressures at t=20s for YY1 profile and all ground motion intensities 78
Figure 6.12: Spatial and temporal distribution of excess pore water pressure for YY1 profile: (a) high intensity motion (a_{max}=0.4g); (b) intermediate intensity motion (a_{max}=0.3g); (c) low intensity motion (a_{max}=0.2g) 78
Figure 6.13: Distribution of ground response parameters throughout the depth of YY1 profile for three levels of shaking intensity: (a) maximum shear strains; (b) maximum horizontal displacements; (c) maximum horizontal accelerations 79
Figure 6.14: Pore water pressures at t=20s for YY2 profile and all ground motion intensities 81
Figure 6.15: Spatial and temporal distribution of excess pore water pressure for YY2 profile: (a) high intensity motion (a_{max}=0.4g); (b) intermediate intensity motion (a_{max}=0.3g); (c) low intensity motion (a_{max}=0.2g) 82
Figure 6.16: Distribution of ground response parameters throughout the depth of YY2 profile for three levels of shaking intensity: (a) maximum shear strains; (b) maximum horizontal displacements; (c) maximum horizontal accelerations 82

Figure 6.17: Distribution of ground response parameters throughout the depth of both YY profiles for highest shaking intensity, a_{max}=0.4g: (a) maximum shear strain; (b maximum horizontal displacement; (c) maximum pore water pressure ratio at t = 20s 84
Figure 6.18: Pore water pressures at t=20s for NN1 profile and all ground motion intensities 86
Figure 6.19: Spatial and temporal distribution of excess pore water pressure for NN1 profile: (a) high intensity motion (a_{max}=0.4g); (b) intermediate intensity motion (a_{max}=0.3g); (c) low intensity motion (a_{max}=0.2g) 86
Figure 6.20: Distribution of ground response parameters throughout the depth of NN1 profile for three levels of shaking intensity: (a) maximum shear strains; (b) maximum horizontal displacements; (c) maximum horizontal accelerations 87
Figure 6.21: Pore water pressures at t=20s for NN2 profile and all ground motion intensities 89
Figure 6.22: Spatial and temporal distribution of excess pore water pressure for NN2 profile: (a) high intensity motion (a_{max}=0.4g); (b) intermediate intensity motion (a_{max}=0.3g); (c) low intensity motion (a_{max}=0.2g) 89
Figure 6.23: Distribution of ground response parameters throughout the depth of NN2 profile for three levels of shaking intensity: (a) maximum shear strains; (b) maximum horizontal displacements; (c) maximum horizontal accelerations 90
Figure 6.24: Distribution of ground response parameters throughout the depth of both NN profiles for highest shaking intensity, a_{max}=0.4g: (a) maximum shear strain; (b) maximum horizontal displacement; (c) maximum horizontal acceleration 91
Figure 6.25: Pore water pressure ratio with depth for all YY and NN sites for ground motion with a_{max}=0.4g 93
Figure 6.26: Comparison plots for soil response predicted by the simplified method and the 1-D soil column model for YY1, a_{max}=0.4g: (a) maximum pore water pressure ratios; (b) maximum shear strains; (c) vertical settlement 95
Figure 6.27: Relationship between FS and pore water pressure ratio (R_U) from Marcuson et al. (1990) 96
Figure 6.28: Comparison plots for soil response predicted by the simplified method and the 1-D soil column model for NN2, a_{max}=0.2g: (a) maximum pore water pressure ratios; (b) maximum shear strains; (c) vertical settlement 96
Figure 6.29: Plot of increase in *CRR* required to prevent liquefaction in shallow soil layers of NN1 profile: (a) using pore water pressure ratio; (b) using single amplitude shear strain 99
Figure 6.30: Pore water pressure ratios for liquefiable layers in the NN1 profile with a 1.35 increase in liquefaction resistance in the layer 2.5-4.0 m and a_{max}=0.4g 99
Figure 6.31: Response spectra of acceleration time history at the base of the shallow liquefiable layer for NN1, a_{max}=0.4g 100
Figure 6.32: Relationship between V_p and increase in *CRR* of sandy soil (Tsukamoto et al., 2002) 100

Figure 6.33: Pore water pressure ratio calculated using the simplified method and ESA for NN1, a_{max}=0.4g with a 1.35 increase in CRR in the layer 2.5-4.0 m 100
Figure 6.34: V_p data for site 38178 at Paeroa Reserve in Riccarton 100

List of Tables

Table 3.1: Properties of the three sites used in deconvolution (Wotherspoon et al., 2013 and Markham, 2015)..... 22
Table 4.1: Classification of main soil behavioural types present in Christchurch soil profiles..... 38
Table 4.2: Summary of properties identified for scrutiny of liquefaction-manifestation characteristics of each site..... 44
Table 4.3: q_{c1Ncs} and $CRR_{7.5,100kPa}$ values adopted for use in the ESA for each layer within the YY1 profile 51
Table 4.4: q_{c1Ncs} and $CRR_{7.5,100kPa}$ values adopted for use in the ESA for each layer within the YY2 profile 53
Table 4.5: q_{c1Ncs} and V_s values adopted for use in the ESA for each layer within the NN1 profile 54
Table 4.6: q_{c1Ncs} and V_s values for use in the ESA for each layer within the NN2 profile 55
Table 5.2: Permeability values adopted for the different soil behaviour types in the YY profiles..... 68

1 Introduction

1.1 Motivation

The Canterbury Earthquake Sequence (CES) of 2010-2011 highlighted the importance of design for and consideration of liquefaction problems in engineered structures. In the M_w 7.1 Darfield earthquake of September 2010, and more significantly in the M_w 6.3 Christchurch earthquake of February 2011, severe and widespread liquefaction was observed throughout Christchurch city. This caused damage to many built structures and critical infrastructure. Six years on, the rebuild of the city is well underway, however ongoing seismic events in New Zealand, like the Seddon earthquakes of 2013 and the most recent Kaikoura earthquake in November 2016, serve as reminders that construction in seismic areas must be designed appropriately. To achieve this, in terms of liquefaction prone areas, engineers need to have a solid understanding of the liquefaction phenomenon. This research set out to further that understanding by investigating one aspect of liquefaction, namely how it develops in highly stratified soils.

The CES has provided researchers with a wealth of data and analysis of this data indicates where liquefaction did and did not occur during the Canterbury earthquakes. Comparison of observed instances of liquefaction and liquefaction prediction using the simplified method of assessing liquefaction triggering (Boulanger and Idriss, 2014; Idriss and Boulanger, 2008; Robertson and Wride, 1998, referred to generically as the simplified method) show that, while fairly accurate on the whole, there were many cases of over-prediction of liquefaction, particularly for the September 2010 earthquake. This conservatism in the simplified method is well understood by engineers, however it is important to understand the sources of this conservatism to enable well-informed design. An overly conservative design is inefficient and can incur unnecessary expenses. This is particularly relevant for areas such as Christchurch that face large-scale rebuild of the city's infrastructure.

There are number of factors that cause an over-prediction of liquefaction. Over-prediction could be due to partial saturation of the upper few metres of soil below the water table, the poorly understood behaviour of silty soils during cyclic shaking, or the effects that interlayering of soils has on the dynamic properties of the soil deposit. It is this last point that the research aims to investigate in some depth.

1.2 Objectives

The objectives of this research are two-fold, the first focus is on furthering engineering understanding of liquefaction, and the second is on how this impacts design practices. The two objectives are:

1. To determine if the interaction between soil layers during cyclic loading has a significant effect on the development of liquefaction and its manifestation
2. To evaluate the inherent conservatism in the simplified method as a result of neglecting this soil layer interaction effect.

These objectives were achieved using an Effective Stress Analysis (ESA) to provide a thorough assessment of the dynamic properties of a soil deposit during cyclic loading. Two types of global soil profiles were investigated; one that represents sites that liquefied in both the September 2010 and February 2011 earthquakes, these are generally thick, continuous, uniform sandy deposits, and the other representing sites that did not liquefy in either event, soil deposits that are characterised by highly stratified layers of liquefiable and non-liquefiable material.

The ESA was used to assess how soil layering affects the development of excess pore water pressures during seismic shaking. The results were then compared to predictions, for the same soil profiles, by the simplified method and to observations from the CES to thoroughly assess the effect that these soil properties have on liquefaction prediction and manifestation. Through this process, an understanding of the system response of deposits with different characteristics was developed along with an understanding of the applicability of the simplified method in circumstances where highly stratified deposits are present. The outcome of the study will lead the way for further advancements to the industry's understanding of liquefaction evaluation.

1.3 Thesis organisation

The thesis is set out as follows: Chapter 2 first addresses some background research into liquefaction, the dynamic properties of layered soils under cyclic loading, and observations and predictions by the simplified method using data and observations from the CES, as well as outlining the two methods of liquefaction evaluation used in this research; the simplified method and ESA. Chapter 3 addresses the deconvolution process used to derive ground motions (from motions recorded at the ground surface during the CES) that were input into the ESA. Chapter 4 outlines the process used to characterise the Christchurch sites, and the development of four representative soil profiles used in the analysis. Then Chapter 5 outlines the process used to calibrate the constitutive model to the specific soils to be modelled in these representative profiles. Finally, Chapter 6 provides a discussion of the results and findings along with key observations of soil layer interaction effects, and Chapter 7 contains some concluding remarks.

2 Background

2.1 Liquefaction

Liquefaction is the state a soil reaches when the effective stress of a soil reduces to zero, usually due to cyclic loading. When a loose soil is liquefied, the soil particles are in suspension and the soil acts as a viscous fluid resulting in significant deformations to the soil and severe damage to infrastructure.

Soil has the tendency to contract under shear load as the soil particles are rearranged and pore water flows from the soil. However, when a soil is subject to an earthquake load, the loading cycle is of such short duration that pore water cannot flow from the soil and the soil is restricted to the undrained loading condition. When the loading is undrained, the soils tendency to contract causes an increase in the pore water pressure. This in turn causes a decrease in the effective stress of the soil as

$$\sigma = \sigma' + u$$

Where σ is the total stress, σ' is the effective stress, and u is the pore water pressure.

When the cyclic loading causes stress reversal in the soil (i.e. positive and negative amplitudes of shear stresses), the effective strength of the soil can reduce to zero, at which point liquefaction is initiated. Prior to liquefaction, the soil undergoes significant softening through reductions in both shear strength and stiffness. This is illustrated in Figure 2.1 where liquefaction is characterised by the 'butterfly loop' in the effective stress path, and by the flat portion of the shear stress-shear strain plot in Figure 2.2

In its liquefied state, soil has extremely low strength and stiffness and as a result the soil can undergo large permanent deformations. This can occur through three main mechanisms; reconsolidation settlements as pore water seeps upwards; loss of soil volume through sand ejecta, as upwards flowing water takes fine soil particles in suspension; and lateral spreading if the site is on sloping ground or located near a free face. Liquefaction induced settlements are often not uniform and can significantly affect surrounding structures.

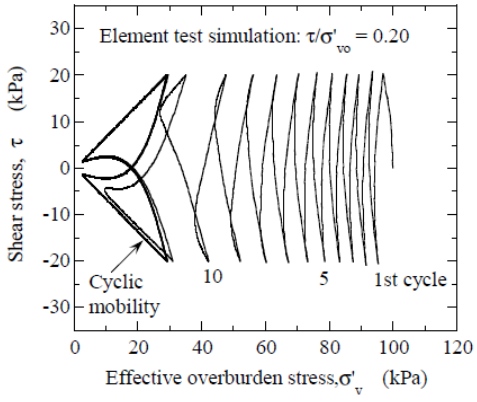

Figure 2.1: Illustration of uniform cyclic loading causing liquefaction (Cubrinovski, 2011)

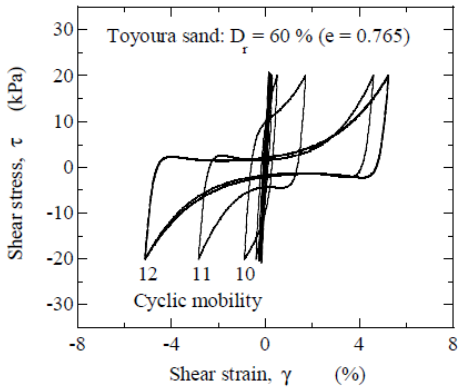

Figure 2.2: Shear stress-shear strain relationship for liquefied soil (Cubrinovski, 2011)

2.1.1 Factors affecting liquefaction resistance

Liquefaction can occur in a wide range of soils, however not all soils are susceptible to liquefaction. For a soil to be liquefiable, it must be frictional and fully saturated. Liquefiable soils are also generally medium-low density. High density soils can liquefy, however this type of liquefaction does not incur the same instability as it does in low density soils. When a dense soil liquefies some contact remains between soil particles so while the soil may undergo significant softening and cyclic mobility, the deformations will not be on the same scale as a loose soil that loses all particle contact on liquefaction. Soils with plasticity, such as clays, are also not susceptible to liquefaction, the soil may undergo large deformations, but cohesion between the soil particles prevents full liquefaction from developing.

A number of other factors also affect the liquefaction susceptibility of a soil. These fall into three general categories; state parameters, grain characteristics and ground conditions. State conditions include the density of the soil, its confining stress, fines content, soil fabric and age. The density of the soil and its confining stress give the initial state of a soil. This can be interpreted using critical state soil mechanics. A soil that is very contractive (i.e. plots to the upper right of the critical state line shown in Figure 2.3) will have a higher liquefaction susceptibility. On the other hand, a soil that is very dilative (i.e. plots to the lower left of the critical state line in Figure 2.3) will have a very low liquefaction susceptibility as highly dilative soils exhibit only minor contraction on initial loading.

In addition to the state of the soil, the liquefaction susceptibility is also affected by the fines content and fabric of the soil. The liquefaction susceptibility of the soil increases as the fines content increases as a sand with fines is more contractive than clean sand as long as the soil matrix dominates the soil structure (i.e. FC<30%). This trend is clearly shown in Figure 2.4 where, for a given density, clean sand has a much higher liquefaction resistance than the sand with 30% fines. Ageing effects such as cementation and micro-particle movement also increase the liquefaction resistance of a soil, hence young soils tend to be more susceptible to liquefaction. Also important is the soil fabric as illustrated in

Figure 2.5 where cyclic laboratory tests on different reconstituted samples showed markedly different liquefaction susceptibility depending on the sample preparation method.

Grain characteristics such as the grain size and angularity of the soil particles also influence liquefaction susceptibility, as do the ground conditions. This includes the depth to the water table, the saturation of the soil (it must be fully saturated to be liquefiable), the drainage conditions of the soil (i.e. whether pore water flow is impeded by impermeable soil layers), and the soil stratification. Furthermore, the depth to the liquefiable layers, also known as the crust thickness, relative to the thickness of the liquefiable layer will influence whether liquefaction is manifested on the surface and to what extent. Overall, the most susceptible soils are loose, non-plastic, young, thick, fully saturated sandy deposits.

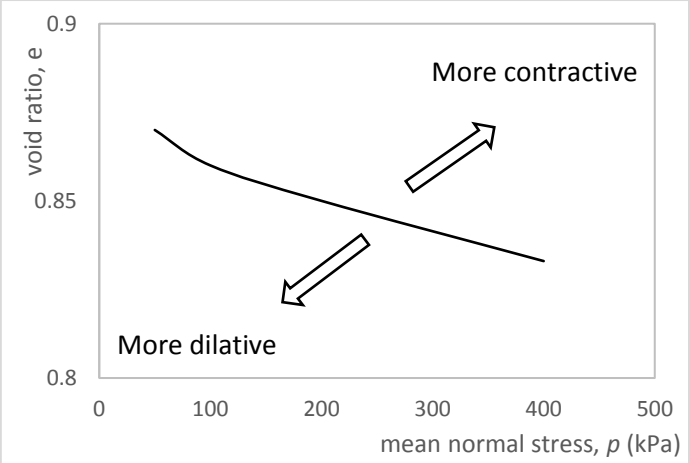

Figure 2.3: Example of a critical state line

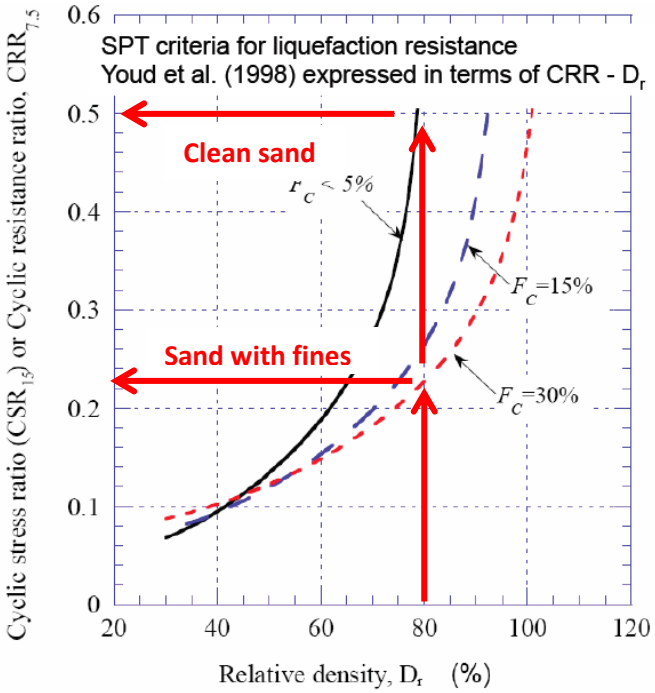

Figure 2.4: CRR with normalised SPT blow count showing variation with fines content of soil (Cubrinovski, 2015)

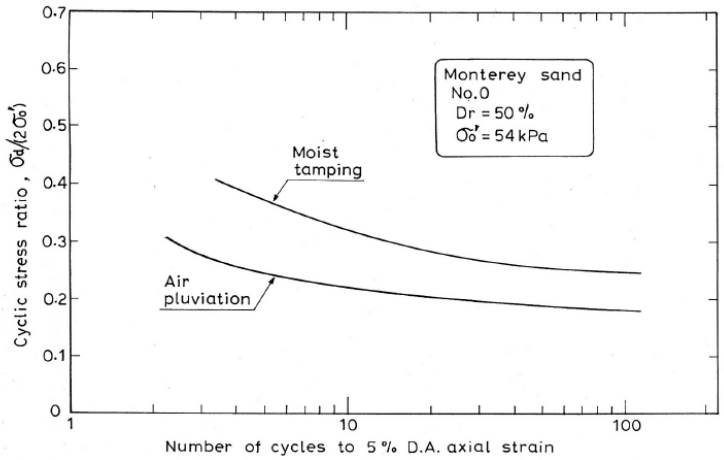

Figure 2.5: Liquefaction resistance of soil samples with different fabric (Cubrinovski, 2015)

2.1.2 Time dependency

Liquefaction triggering depends not only on the soil but also on the magnitude and duration of loading. Highly liquefiable soils will liquefy in a small number of loading cycles, whereas other soils may require a higher magnitude acceleration and greater number of loading cycles to fully develop excess pore water pressures. Any given soil deposit will contain a mixture of both non-liquefiable and liquefiable soils which will be triggered under different degrees of loading. Hence, for a given load, some portions of a soil deposit may liquefy first, others a little later in the loading sequence and other layers not at all. Therefore, the temporal and spatial evolution of liquefaction within a given soil deposit is both non-uniform and highly dependent on the specific soil characteristics.

2.2 Soil layer interaction

Interaction between soil layers in stratified profiles can influence the development of excess pore water pressures and hence the liquefaction characteristics of the deposit as a whole. There are two mechanisms of soil layer interaction; the effects of the dynamic response and deformation of any given layer on the remaining layers within the soil deposit, and the redistribution of excess pore water pressure through pore water flow. When one layer of the soil liquefies, the ground motion will be substantially modified as the seismic waves pass through this area. Softening of the soil due to a loss in stiffness and strength causes accelerations to be damped and the period of the motion to be elongated. This can affect the shear stresses in the soils and either reduce or modify the earthquake load, changing the development of excess pore water pressure in soil layers above and below the liquefied layer. In addition, when pore water pressures build up in excess of the equilibrium pressures, water will start to flow towards the surface. If this flow is hindered by a relatively impermeable layer of soil, pore water pressures will be redistributed to the surrounding soil layers altering the density of the soil and causing an increase in liquefaction susceptibility.

Figure 2.6 illustrates soil layer interaction through ground motion modification. From Figure 2.6 it can be seen that the uniform input acceleration at the base of the model has been significantly damped by the second cycle at the surface. This is a result of the deeper soil layer liquefying almost immediately upon the application of the cyclic load. Once this layer has liquefied, the strength and stiffness of the soil is significantly reduced. This causes the seismic waves passing through this layer to be damped, resulting in the behaviour illustrated in Figure 2.6. The slight increase in acceleration amplitudes near the end of the cyclic loading was most likely due to densification of the soil causing the soil to regain some strength and stiffness.

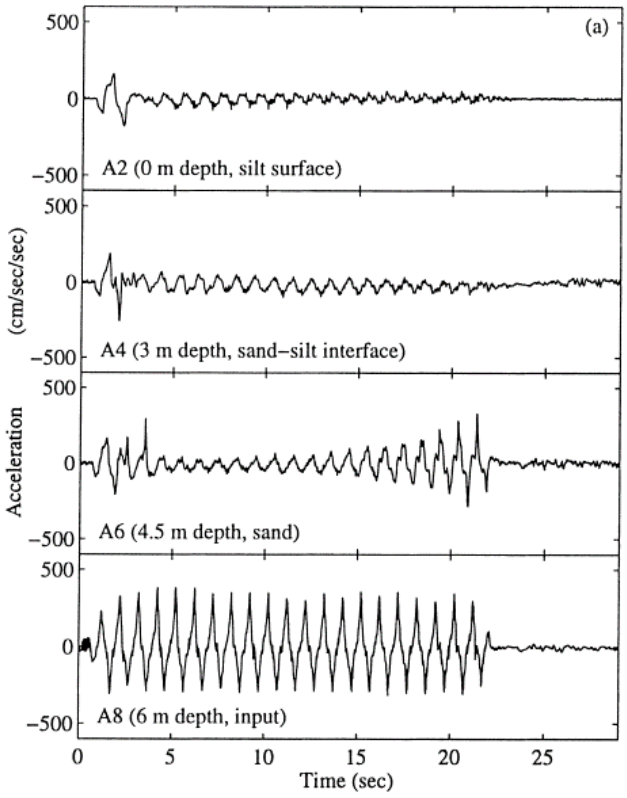

Figure 2.6: Modification of ground motion due to soil liquefaction in a centrifuge model (Zeghal et al., 1999)

2.2.1 Centrifuge studies

In a centrifuge test, a small scale soil deposit is tested under an increased gravity field by rotating the model in a horizontal circle. This ensures that the stresses induced in the model are equivalent to those in the prototype (full scale) model. A well implemented model includes a systematic layout of transducers which produce detailed recordings of accelerations, pore water pressures, and deformations. Therefore, this type of modelling enables a full time history analysis of the development of excess pore water pressures and shear strains allowing the time and location of initial liquefaction to be determined.

An analysis of soil layer interaction was conducted for the centrifuge tests presented in Byrne et al. (2003). In this research, centrifuge studies were modelled numerically to assess the liquefaction potential of soils at depth. The layout of centrifuge model 3 from Byrne et al. (2003) is presented in Figure 2.7. Figure 2.8 and Figure 2.9 show the excess pore water pressures from the test and the factor of safety calculated using the simplified method respectively (full calculations are in Appendix A). Figure 2.9 clearly shows the simplified method predicting liquefaction in the lower medium sand layer but not in the dense sand above 16 m depth. On the other hand, the recorded excess pore water pressures in Figure 2.8 show the deposit has also liquefied at a depth of 13.4 m. This is due to the upward flow of water from the lower liquefied layer. This upward flow causes void redistribution in the lower part of the dense sand layer resulting in a decrease in density and making this portion of the deposit more susceptible to liquefaction. The delay between the liquefaction of the medium sand layer and the liquefaction of the layer at a depth of 13.4 m (shown in Figure 2.8) reinforces this theory. This example indicates that the simplified method is unconservative in predicting liquefaction, however this is only one possible result of soil layer interaction.

The example from Byrne et al. (2003) clearly illustrates that interaction between soil layers does occur, and that the simplified method fails to accurately represent this soil behaviour. Processes such as seepage of pore water due to excess pore water pressures cannot be modelled by the simplified method. Neither does this method account for the modification of the ground motion that is caused by the liquefaction of layers deeper within the deposit. These two processes act in different ways. As seen above, seepage from lower liquefied soil layers can cause void redistribution resulting in a soil more susceptible to liquefaction, on the other hand modification of ground motion acts to reduce liquefaction triggering in upper layers. It is this latter component of soil layer interaction that was investigated in this thesis research.

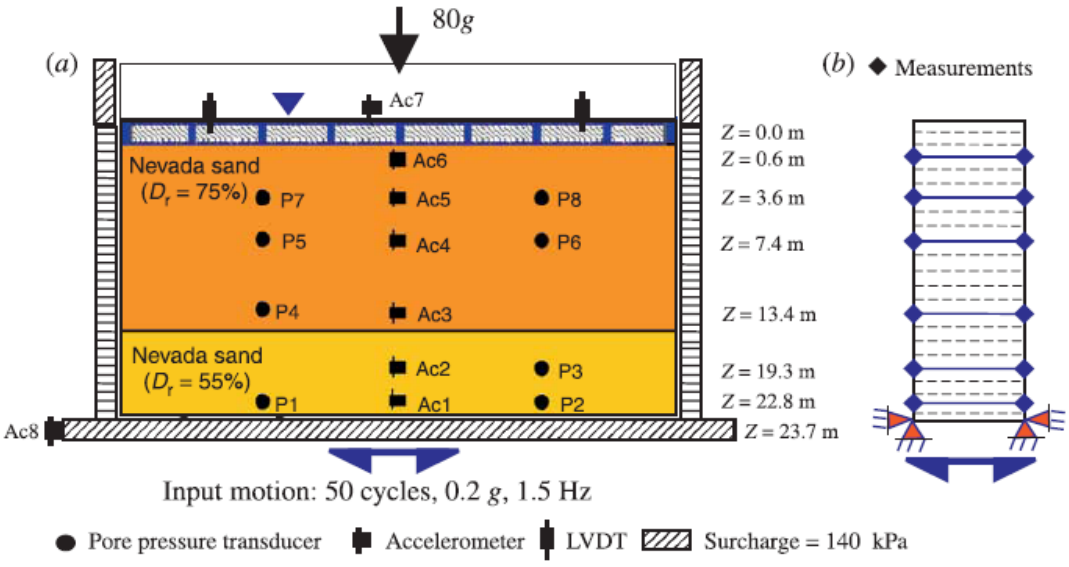

Figure 2.7: Model 3 layout from Byrne et al. (2003)

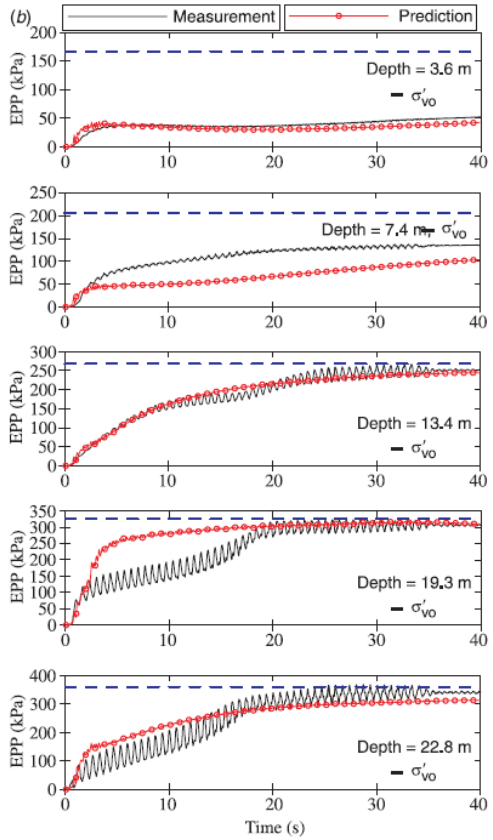

Figure 2.8: Excess pore water pressure (EPP) with time at different depths measured in model 3 (Byrne et al, 2003)

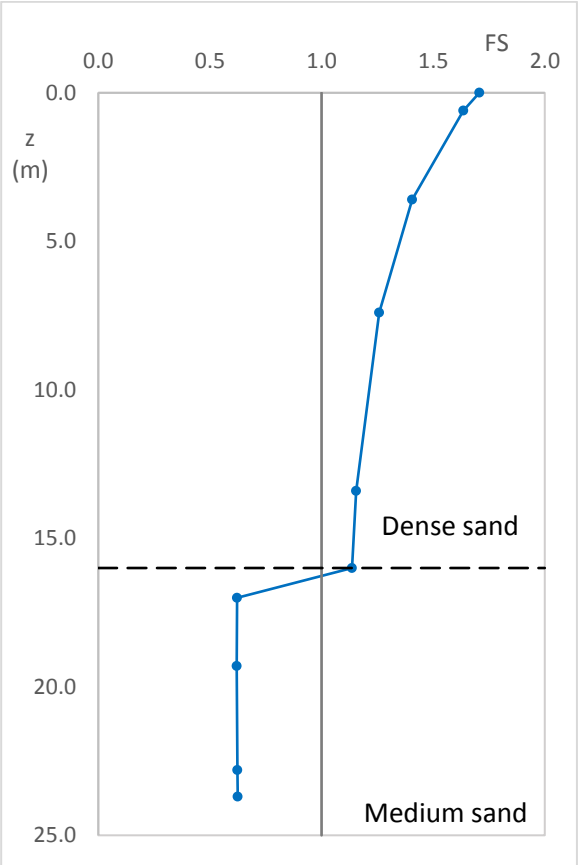

Figure 2.9: Factor of safety (FS) with depth for model 3 using the simplified method (Boulanger and Idriss, 2014) and the data of Byrne et al. (2003)

2.2.2 Canterbury earthquake sequence

The 2010-2011 Canterbury Earthquake Sequence (CES) caused widespread liquefaction, most notably during the 4 September 2010 M_w 7.1 Darfield and the 22 February 2011 M_w 6.3 Christchurch earthquakes. In general, the eastern part of the city experienced severe liquefaction, whereas western areas experienced minor to no liquefaction (see Figure 2.10). These areas are characterised by relatively loose sandy deposits with the groundwater table close to the surface (approximately 1-2 m depth). The Riccarton gravel is approximately 40 m below the ground surface in the east, and is overlain by soils predominantly from the Christchurch formation (swamp, beach and estuarine derived sands and silts). The western part of the city has a deeper water table, the Riccarton gravel is approximately 10-15 m deep, and the surface soils are predominantly alluvial sands, silts and gravels from the Springston formation (Cubrinovski et al., 2011).

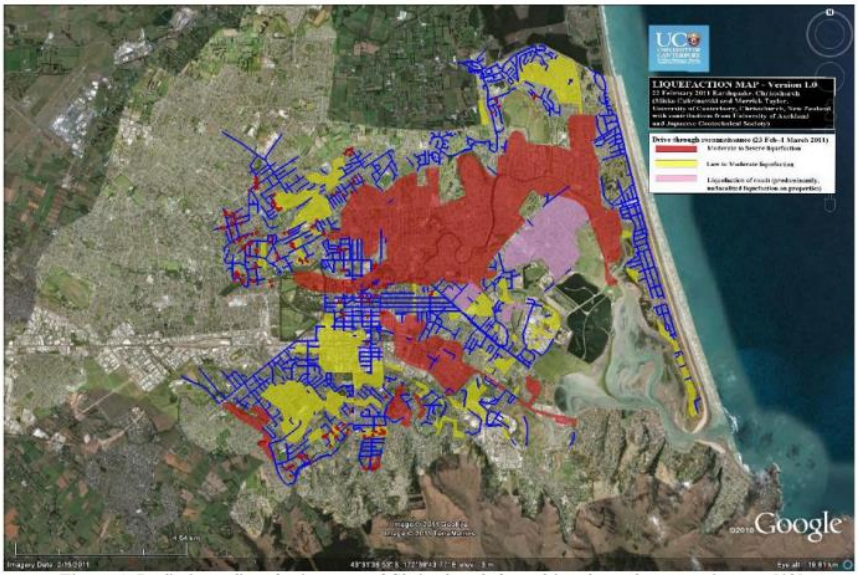

Figure 2.10: Preliminarily liquefaction map for the M_w 6.3 February 2011 earthquake. Red indicates moderate-severe liquefaction and yellow low-moderate liquefaction based on drive through observations (Cubrinovski et al., 2011)

Following the CES, a number of sites throughout the region were selected to add to the liquefaction case history database (Green et al., 2014). The simplified method was used to analyse these sites based on CPT data, and the results were compared to observations from the September 2010 and February 2011 events. In general, the simplified method gave an accurate prediction of liquefaction manifestation, however there were a few sites where the simplified method falsely predicted liquefaction manifestation. One of these sites was located in North Kaiapoi, where liquefaction was predicted in a critical layer at 1.3 m-2.5 m depth (Figure 2.11(a)) for the February 2011 earthquake but none was observed. Another example was a site in the central business district (CBD) where liquefaction was predicted in a critical layer between 2 m-3.3 m depth (Figure 2.11(b)) for the September 2010 earthquake however none was observed.

The simplified method includes a number of uncertainties, any of which may have contributed to the false liquefaction predictions. The false predictions could be due to the correction for the fines content of the soil, partial saturation of the soil layers immediately below the water table, or due to the conservative approach adopted in the empirical triggering relationships. Alternatively, the false predictions may also have come about from the effects of soil layer interaction. It is evident from Figure 2.11 that liquefaction was also predicted in layers located deeper in the deposit (i.e. below the critical layer) for both cases. As a result of these layers liquefying, modification of the ground motion may have altered the dynamic response of soil layers closer to the surface, an effect which is not accounted for in the simplified method. This research aimed to investigate these effects of soil layer interaction, and the results of such analysis may help in the re-interpretation of some of the liquefaction patterns observed during the CES.

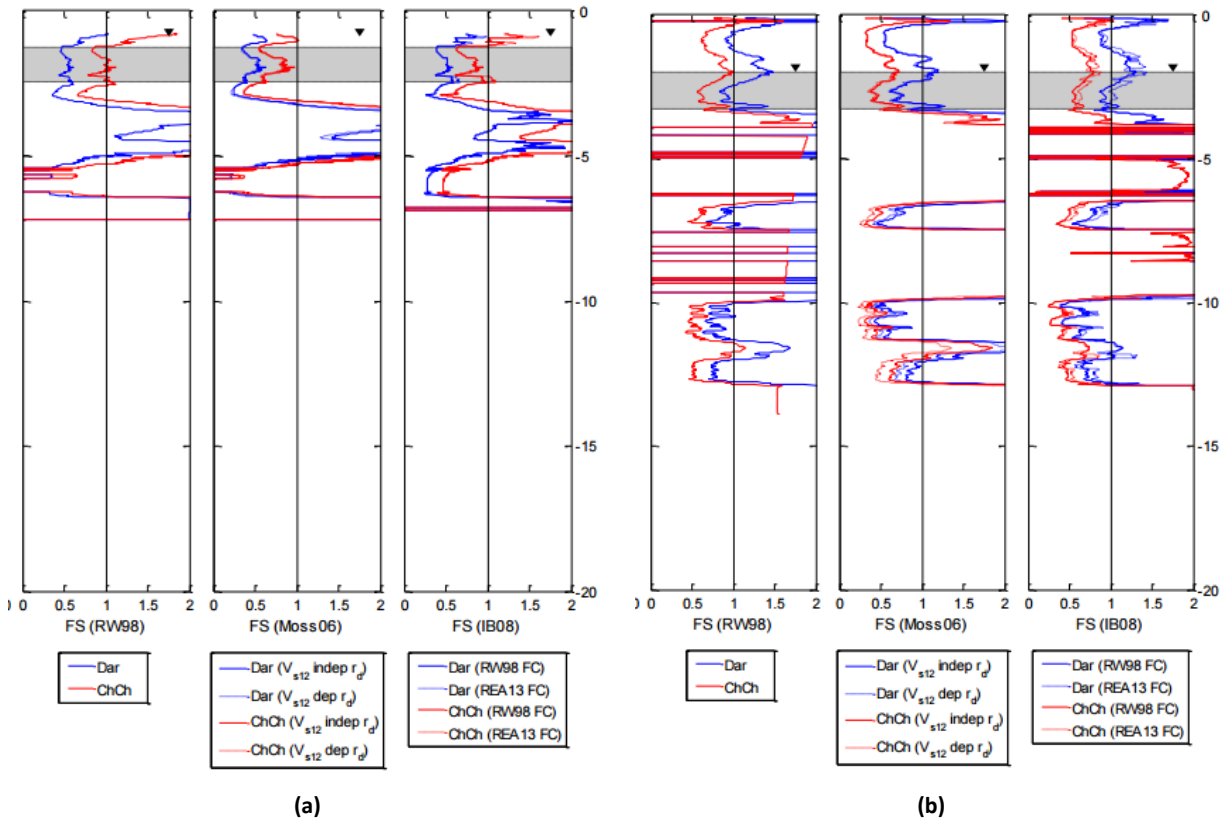

Figure 2.11: Factor of safety against liquefaction triggering (Green et al., 2014): (a) for the Kaiapoi site; (b) for the CBD site

2.3 Evaluation of liquefaction triggering

There are a number of analysis methods that can be used to assess the response of a soil deposit to seismic loading. Field observations show the response of the soil under in situ conditions, however these give little indication of when and where liquefaction was initiated within the soil deposit. More detail can be obtained using the simplified method which enables identification of the soil layer that liquefied, and an approximate assessment of the load cycle at which liquefaction occurred, through the factor of safety. More detailed time histories can be obtained using an Effective Stress Analysis (ESA), which shows the temporal and spatial development of liquefaction and is discussed in Section 2.3.2. But it is full-scale physical models that best represent field conditions. These are expensive, so scaled-down models, such as centrifuge tests, are more often used. For this research, an ESA was chosen to investigate soil layer interaction, and the results compared to predictions made using the simplified method.

2.3.1 Simplified method

The simplified method is a semi-empirical approach that enables liquefaction triggering and deformations to be estimated. The simplified method uses correlations between field tests and the liquefaction resistance of soils, back-calculated from case studies, to assess liquefaction triggering from a factor of safety as shown in Equation 2.1.

$$FS = \frac{CRR}{CSR} \cdot MSF \cdot K_\sigma \quad \textbf{2.1}$$

Where *CRR* is the cyclic resistance ratio of a M_w 7.5 earthquake for a soil with 100 kPa overburden pressure, this represents the soil liquefaction resistance; *CSR* is the cyclic stress ratio and represents the stress induced by the earthquake load; *MSF* is a magnitude scaling factor (accounting for earthquakes other than magnitude 7.5); and K_σ is a correction for overburden stress (accounting for stresses other than 100 kPa). This method of analysis assigns each soil layer a factor of safety based on these parameters. First developed by Seed and Idriss (1971) and more recently adapted, the Boulanger and Idriss (2014) method was used for this analysis (and is presented herein) as it is derived from the most up-to-date case history database.

The *CSR* is defined as the ratio between the applied cyclic shear stress and the initial overburden pressure. During earthquake loading the shear stress is highly irregular, so for ease of calculation, an equivalent uniform shear stress is assumed in the simplified analysis. This is taken as 65% of the maximum shear stress. The *CSR* is then derived from the equilibrium of forces acting on a rigid body (Equation 2.2).

$$CSR = \frac{\tau_{cyc}}{\sigma'_{v0}} = 0.65 \cdot \frac{a_{max}}{g} \cdot \frac{\sigma_{vo}}{\sigma'_{v0}} \cdot r_d \quad \textbf{2.2}$$

Where a_{max} is the peak ground acceleration, σ'_{v0} is the initial effective overburden stress, σ_{vo} is the initial total overburden stress, and r_d is an empirical reduction factor, as a function of depth and magnitude, that accounts for the deformability of soil as per Equations 2.3-2.5.

$$r_d = \exp[\alpha(z) + \beta(z) \cdot M] \quad \textbf{2.3}$$

$$\alpha(z) = -1.012 - 1.126 \sin\left(\frac{z}{11.73} + 5.133\right) \quad \textbf{2.4}$$

$$\beta(z) = 0.106 + 0.118 \sin\left(\frac{z}{11.28} + 5.142\right) \quad \textbf{2.5}$$

The *CRR* is the ratio between the cyclic shear resistance of the soil and the initial overburden pressure and it is developed from a case history database based on field test data. This is illustrated in Figure 2.12 where the normalised clean sand equivalent CPT tip resistance (q_{c1Ncs}) is used to determine the *CRR*. This is the most commonly used formulation, however relationships have also been developed for *CRR* using SPT blow count and shear wave velocity (V_s) measurements. Using the method of Boulanger and Idriss (2014), the *CRR* curve can be expressed as per Equation 2.6 where q_{c1Ncs} is determined as per Equation 2.7.

$$CRR_{7.5,100kPa} = \exp\left(\frac{q_{c1Ncs}}{113} + \left(\frac{q_{c1Ncs}}{1000}\right)^2 - \left(\frac{q_{c1Ncs}}{140}\right)^3 + \left(\frac{q_{c1Ncs}}{137}\right)^4 - 2.80\right) \quad \textbf{2.6}$$

$$q_{c1Ncs} = q_{c1N} + \Delta q_{c1N} \quad \textbf{2.7}$$

The normalised CPT tip resistance is calculated following Equations 2.8-2.10 and the correction for fines content (Δq_{c1N}) as per Equation 2.11.

$$q_{c1N} = C_N \frac{q_c}{P_a} \quad \textbf{2.8}$$

$$C_N = \left(\frac{P_a}{\sigma'_v}\right)^m \leq 1.7 \quad \textbf{2.9}$$

$$m = 1.338 - 0.249(q_{c1Ncs})^{0.264} \quad \textbf{2.10}$$

$$\Delta q_{c1N} = \left(11.9 + \frac{q_{c1N}}{14.6}\right) \exp\left(1.63 - \frac{9.7}{FC+2} - \left(\frac{15.7}{FC+2}\right)^2\right) \quad \textbf{2.11}$$

Where P_a is the atmospheric pressure; *FC* is the fines content determined either from laboratory tests or based on the Roberston and Wride (1998) soil behaviour type index, I_c, as shown in Equation 2.12.

$$FC = 80(I_c + C_{FC}) - 137 \quad \textbf{2.12}$$

Where C_{FC} is a fitting parameter with standard deviation ± 0.29. A mean value of $C_{FC} = 0$ was used in this study.

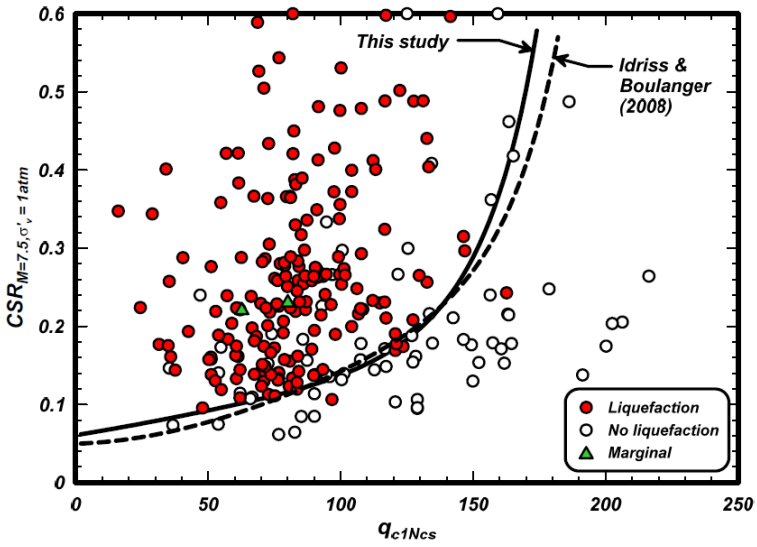

Figure 2.12: *CRR*-q_{c1Ncs} relationship using the updated CPT database from Boulanger and Idriss (2014)

As the *CRR* is determined for a magnitude 7.5 earthquake and a soil overburden pressure of 100 kPa, correction factors need to be applied to account for conditions outside of these parameters, these corrections are the Magnitude Scaling Factor (*MSF*) and correction for overburden pressure (K_σ). The *MSF* is determined as per Equations 2.13 and 2.14 and is illustrated in Figure 2.13. K_σ is determined as per Equations 2.15 and 2.16, and illustrated in Figure 2.14.

$$MSF = 1 + (MSF_{max} - 1)\left(8.64\exp\left(-\frac{M}{4}\right) - 1.325\right) \quad \textbf{2.13}$$

$$MSF_{max} = 1.09 + \left(\frac{q_{c1csN}}{180}\right)^3 \leq 2.2 \quad \textbf{2.14}$$

$$K_\sigma = 1 - C_\sigma \ln\left(\frac{\sigma'_v}{P_a}\right) \leq 1.1 \quad \textbf{2.15}$$

$$C_\sigma = \frac{1}{37.3 - 8.27(q_{c1csN})^{0.264}} \leq 0.3 \quad \textbf{2.16}$$

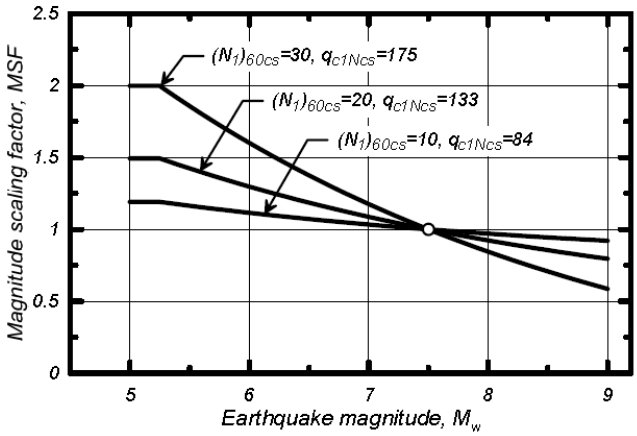

Figure 2.13: MSF for various earthquake magnitudes and CPT tip resistances (Boulanger and Idriss, 2014)

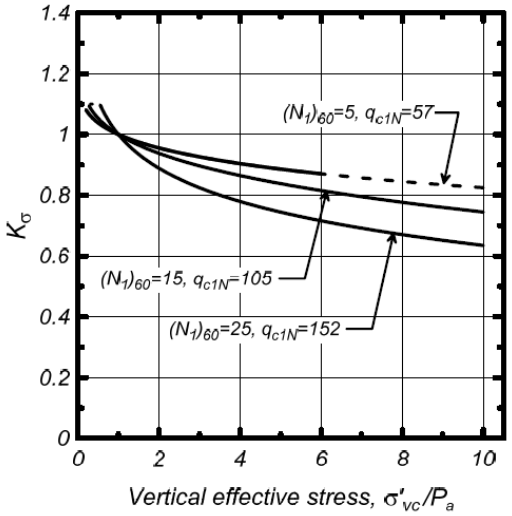

Figure 2.14: Overburden correction factor (Boulanger and Idriss, 2014)

The simplified method also enables strains and deformations to be estimated. There are two commonly used methods for estimating shear deformations within soil layers; those developed by Idriss and Boulanger (2008) and Zhang et al. (2002). Both of these methods are derived from the Ishihara and Yoshimine (1992) method and database. The Idriss and Boulanger (2008) method determines volumetric strains as per Equations 2.17-2.22.

$$\varepsilon_v = 1.5\exp(2.551 - 1.147(q_{c1Ncs})^{0.264}) \cdot \min(0.08, \gamma_{max}) \quad \textbf{2.17}$$

Where

$$\gamma_{max} = 0 \qquad \boldsymbol{if\ FS \geq 2} \quad \textbf{2.18}$$

$$\gamma_{max} = \min\left(\gamma_{lim}, 0.035(2 - FS)\left(\frac{1 - F_\alpha}{FS - F_\alpha}\right)\right) \qquad \boldsymbol{if\ 2 > FS > F_\alpha} \quad \textbf{2.19}$$

$$\gamma_{max} = \gamma_{lim} \qquad \boldsymbol{if\ FS \leq F_\alpha} \quad \textbf{2.20}$$

And

$$\gamma_{lim} = 1.859(2.163 - 0.478(q_{c1Ncs})^{0.264})^3 \geq 0 \quad \textbf{2.21}$$

$$F_{\alpha} = -11.74 + 8.34(q_{c1Ncs})^{0.264} - 1.371(q_{c1Ncs})^{0.0.528} \quad \textbf{2.22}$$

On the other hand, the Zhang et al. (2002) method determines volumetric strain from the following graph (Figure 2.15) where the factor of safety is calculated via Robertson and Wride (1998) or Youd et al. (2001).

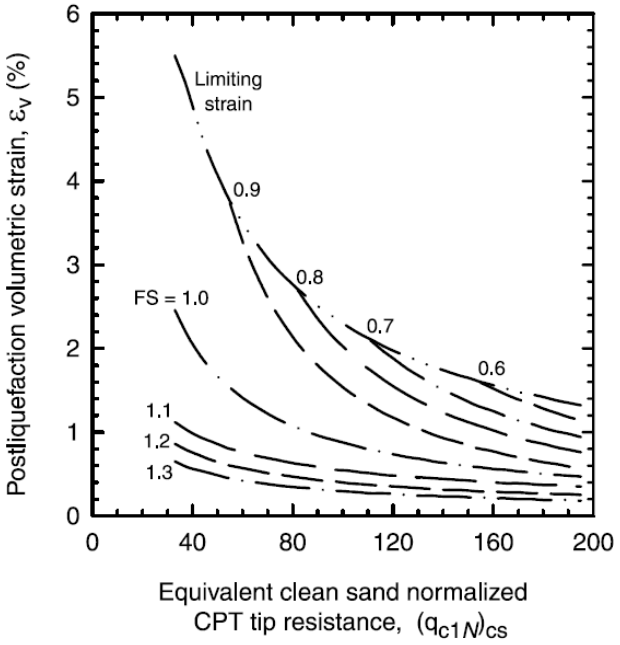

Figure 2.15: Post-liquefaction volumetric strain from Zhang et al. (2002)

The simplified method is easy to implement and has been adopted by a number of design guidelines (e.g. NZGS, 2010 and NZTA, 2014), however it is generally conservative in the estimation of liquefaction triggering. As is show in Figure 2.12, there is significant scatter in the case history data used to characterise the liquefaction resistance, hence there is room for interpretation in defining the *CRR*-q_{c1Ncs} curve. The exact shape of the *CRR*-q_{c1Ncs} curve varies slightly between different methods, however all curves are generally conservative and positioned relatively close to each other. In the case of Boulanger and Idriss (2014), the *CRR* curve represents the value at which there is a 15% chance that liquefaction will occur. There is also uncertainty in the *MSF* and K_{σ} relationships, and most notably in the fines correction, especially for silty soils. Therefore, although this method has proven to be relatively accurate for evaluating liquefaction in uniform sandy deposits, it is important to acknowledge that it is based on empirical data and therefore contains uncertainties and inherent conservatism.

In addition to this inherent conservatism, the simplified method does not account for the interaction between soil layers. Therefore, the factor of safety against liquefaction triggering for any given layer is estimated in isolation from the response of other layers in the soil deposit. The effect of this on the prediction of liquefaction triggering is one focus of this thesis research.

2.3.2 Effective stress analysis

ESA is a numerical tool that enables complex geotechnical engineering problems, such as seismic loading of soil, to be accurately modelled. This analysis method can represent the interaction between soil layers, model water flow and pore water pressure dissipation, and produces detailed time history analyses of the soil response, which makes it the appropriate tool to use for this research. For this analysis, the elasto-plastic Stress-Density Model (S-D Model) (Cubrinovski, 1993, Cubrinovski and Ishihara 1998a and 1998b) which was specifically developed for liquefaction problems will be used in a drained ESA with a 1-D soil-column model where the input is the ground displacement at each node. ESA using the S-D Model have accurately modelled a number of case histories, such as the Kobe Port Island liquefaction in Japan (Cubrinovski et al., 1996) and the Fitzgerald Bridge in Christchurch, New Zealand (Bowen and Cubrinovski, 2008). Hence, there is good evidence that this is an effective and accurate tool for modelling soil liquefaction under seismic loading.

The ability of the constitutive model is a key parameter in the ESA. When modelling liquefaction problems, the model needs to accurately represent the highly non-linear stress-strain behaviour of soils and development of pore water pressures under irregular loading. The S-D Model is based on the assumptions of a modified hyperbolic stress-strain relationship and energy based stress-dilatancy relationship which enables accurate modelling of non-linear stress-strain behaviour. The modified hyperbolic relationship is presented in Equation 2.23.

$$\left(\frac{q}{p}\right) = \frac{G_N \varepsilon_q^p \left(\frac{q}{p}\right)_{max}}{\left(\frac{q}{p}\right)_{max} + G_N \varepsilon_q^p} \quad \textbf{2.23}$$

Where ε_q^p is the plastic strain, $\left(\frac{q}{p}\right)$ is the stress ratio and G_N is the initial shear modulus calculated from Equation 2.24.

$$G_N = \left(G_{N,max} - G_{N,min}\right) \exp\left(-f \frac{\varepsilon_q^p}{\varepsilon_q^0}\right) + G_{N,min} \quad \textbf{2.24}$$

Where $G_{N,max}$ is the best fit initial shear modulus at small strains, $G_{N,min}$ is the best fit initial shear modulus at large strains, ε_q^0 is the shear strain at which G_N approaches $G_{N,min}$ (usually assumed as 1%) and f is a constant. The stress-dilatancy relationship is also essential for determining the plastic strain increment. In this model, the energy based stress-dilatancy relation has the form shown in Equation 2.25.

$$\frac{d\varepsilon_v^p}{d\varepsilon_q^p} = \mu - \frac{q}{p} \quad \textbf{2.25}$$

Where $d\varepsilon_v^p$ is the plastic volumetric strain defined as $d\varepsilon_v^p = d\varepsilon_x^p + d\varepsilon_y^p$, c is the non-coaxially term and relates to the degree by which the strain increment differs from the stress increment (this term is 1 when the loading is fully elastic), and μ is the rate at which energy is dissipated during shear strain and is defined as per Equation 2.26.

$$\mu = \mu_0 + \frac{2}{\pi}(M - \mu_0)\tan^{-1}\left(\frac{\varepsilon_q^p}{S_c}\right) \quad \textbf{2.26}$$

Where μ_0 is the slope of the shear work – plastic shear strain relationship at small strains, M is slope of this relationship at large strains, and S_c is the shear strain at which $(\mu_0 + M)/2$. S_c is usually determined through element tests simulations by fitting the model simulation to a target liquefaction resistance curve (LRC), obtained in laboratory tests, this process is illustrated in Figure 2.16 and enables the accurate modelling of pore water pressure development. With the modified hyperbolic relationship to model the stress-strain behaviour of the soil and the stress-dilatancy relationship, the plastic strain increment can be established given the total strain increment.

The additional assumptions of continuous yielding, combined isotropic and kinematic hardening plasticity, and the dependence of the strain increment direction on the stress increment direction enable highly irregular loading to be modelled. This final assumption requires an iterative procedure to be used in the calculation of the stress increment for each increment of loading as illustrated in Figure 2.17. The total strain increment is input to the model, and the plastic strain increment is determined using Equations 2.23-2.26. The elastic strain is $d\varepsilon^e = d\varepsilon - d\varepsilon^p$, which enables the stress increment to be determined using the Young's modulus of the soil as $d\sigma_{ij} = E_{ijkl}d\varepsilon_{kl}^p$ where

$$E_{ijkl} = \frac{2G_e\nu}{1-2\nu}\delta_{ij}\delta_{kl} + G_e\left(\delta_{ik}\delta_{jl} + \delta_{il}\delta_{jk}\right) \quad \textbf{2.27}$$

Where ν is the Poisson's ratio of the soil, δ is the Kronecker delta, and G_e is the elastic shear modulus defined as per Equation 2.28.

$$G_e = A \cdot p_a \frac{(2.17 - e)^2}{1 + e}\left(\frac{p}{p_a}\right)^n \quad \textbf{2.28}$$

Where p_a is the atmospheric pressure, and A and n are constants. The stress increment must be assumed to determine the plastic strain increment, which results in the iterative procedure outlined in Figure 2.17.

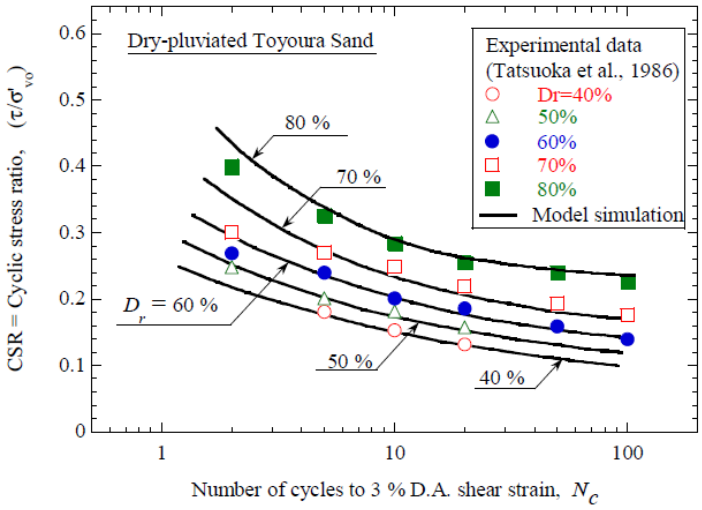

Figure 2.16: Comparison of experimental and simulated LRCs (Cubrinovski, 2011)

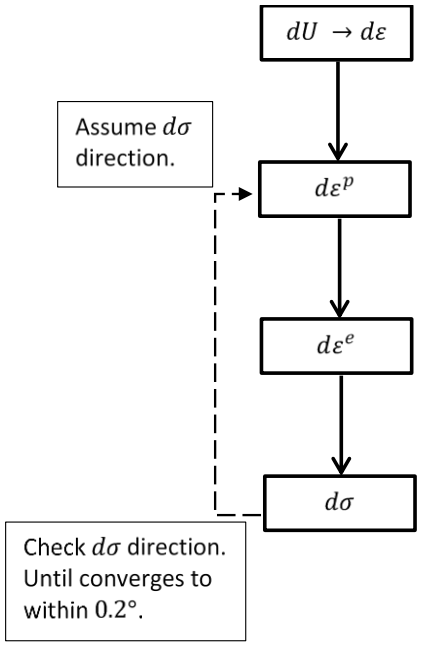

Figure 2.17: Schematic of the iterative process for determining the stress increment from strain increment

The S-D Model uses the state concept to model the combined effects of soil density and confining stress on stress-strain behaviour of the soil. The state index (I_s), which is used as a measure for the state of the soil in terms of its initial density and confining stress, is a key parameter in the S-D Model. A linear relationship between the state index and the key stress-strain parameters (the initial shear modulus, $G_{N,max}$ and $G_{N,min}$, and the peak shear strength, $\left(\frac{q}{p}\right)_{max}$) has been established by Cubrinovski and Ishihara (1998a). These are expressed in the following relationships (Equations 2.29-2.31).

$$\left(\frac{q}{p}\right)_{max} = a_1 + b_1 I_s \quad \textbf{2.29}$$

$$G_{N,max} = a_2 + b_2 I_s \quad \textbf{2.30}$$

$$G_{N,min} = a_3 + b_3 I_s \quad \textbf{2.31}$$

Where a_1, b_1, a_2, b_2, a_3, b_3 are constants as illustrated in Figure 2.18, and the state index is defined in Equation 2.32.

$$I_s = \frac{e_U - e}{e_U - e_Q} \quad \textbf{2.32}$$

Where e is the void ratio, e_U is the void ratio at the upper reference line, and e_Q is the void ratio at the quasi-steady state line as illustrated in Figure 2.19.

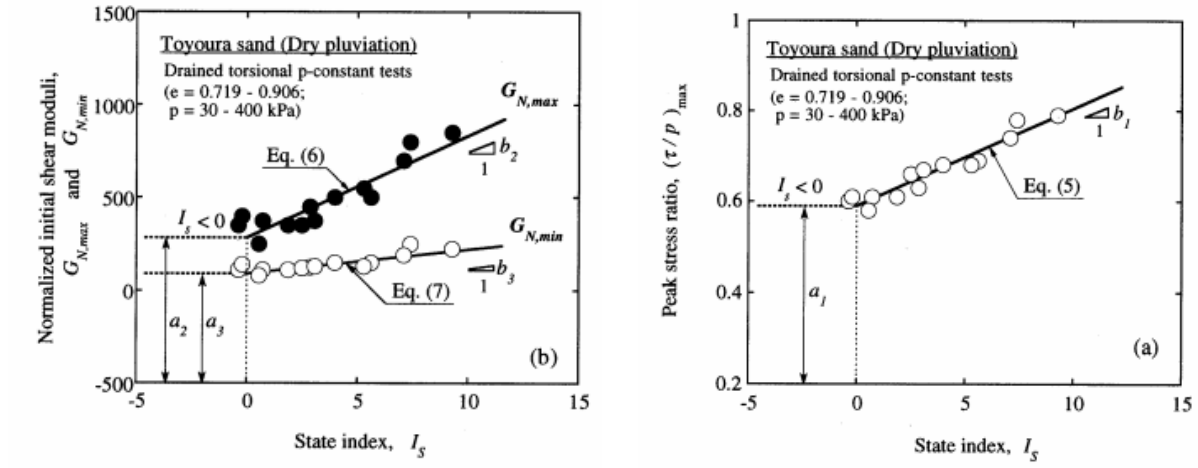

(a) **(b)**

Figure 2.18: Determination of stress-strain parameters using the state-index framework (Cubrinovski and Ishihara, 1998: (a) $G_{N,max}$ and $G_{N,min}$; (b) $\left(\frac{q}{p}\right)_{max}$

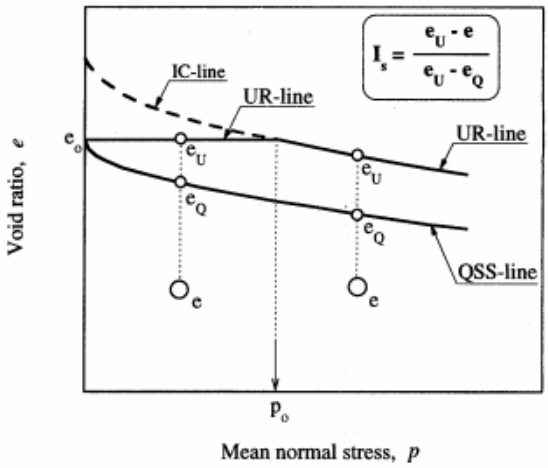

Figure 2.19: Definition of the state index I_s (Cubrinovski and Ishihara, 1998)

Using this relationship to update the stress-strain parameters of the model with each load increment not only enables accurate modelling of the change in stress-strain relationship with the state of the soil, but also enables a soil to be modelled with a single set of material parameters.

The S-D Model can provide accurate simulation of excess pore water pressure build-up and its effect on the dynamic response of soil deposits during earthquakes, including the dissipation of pore water pressure due to pore water flow. These are essential aspects of soil layer interaction and are therefore vital for this analysis.

3 Deconvolution

A key factor in the response of a soil deposit to seismic loading is the ground motion it is subject to, hence the motion that is input at the base of the soil profile is an important parameter in the Effective Stress Analysis (ESA). Ideally, this motion would be in the form of an acceleration time history recorded at the bedrock, however due to the large depth to bedrock and the basin structure of Christchurch, an appropriate bedrock ground motion was not readily available. Instead, two surface ground motions recorded during the Canterbury Earthquake Sequence (CES) were deconvoluted to the Riccarton Gravel and the resulting motions were used as input ground motions, representative of the seismic shaking during the CES, in the ESA. The Riccarton Gravel was chosen to represent the bedrock (i.e. the point where the seismic waves can propagate with no modification from soils) as it is a firm strata and the depth to the bedrock in Christchurch is significant. This approach for producing input ground motions was considered appropriate for the purposes of the research as the aim was to assess the response of different soil deposits to different levels of shaking intensity, as opposed to accurately simulating events of the CES.

3.1 Sites used in the deconvolution of recorded motions

The motions recorded at two strong ground motion sites (SMS) during the CES were chosen for deconvolution. These were the motions recorded at the Canterbury Aero Club (CACS) and at Riccarton High School (RHSC). These sites were chosen for deconvolution as they did not liquefy during the Canterbury earthquakes, had relatively low accelerations (so the level of non-linearity was low) and relatively shallow depth to the Riccarton Gravel. These were important considerations in the deconvolution process as the equivalent linear site response analysis used to deconvolute the ground motions cannot capture high levels of non-linearity (this method produces the best results when maximum strains are less than 0.5%), and the shallow depth to the Riccarton Gravel prevents cumulative error from significantly influencing the deconvolution process, hence reducing the possibility of producing unrealistic ground motions.

As the ground motions were deconvoluted to an equivalent bedrock stratum (i.e. the Riccarton Gravel was taken as representative of the bedrock), it was necessary to define this bedrock stratum in some manner. The shear wave velocity (V_s) was used for this purpose, and the equivalent bedrock was deemed to be the stratum with $V_s \geq 350$ m/s. This was chosen as the data presented in Wotherspoon et al. (2013) (and used herein to establish soil parameters for the SMS) showed agreement between this value and the presence of the Riccarton Gravel for the particular SMS considered in this study.

The location of the two SMS used in the deconvolution (CACS and RHSC) are shown in Figure 3.1, and the properties of these two sites are presented in Table 3.1 and illustrated in Figure 3.2 and Figure 3.3

for CACS and RHSC respectively. The profiles for the Christchurch Hospital (CHHC) are also presented in Figure 3.4 and the details included in Table 3.1. This site was located in the Christchurch CBD and liquefied in the M_w 6.3 February 2011 earthquake (but not in the M_w 7.1 September 2010 or M_w 6.0 13 June 2011 earthquakes). This site was used in the deconvolution process to verify the computed ground motions.

Table 3.1: Properties of the three sites used in deconvolution (Wotherspoon et al., 2013 and Markham, 2015)

Site	Latitude	Longitude	Depth to Riccarton gravel	Water table	SEP 2010		FEB 2011	
					R (km)	PGA (g)	R (km)	PGA (g)
CACS	-43.4832	172.5300	6 m	> 10 m	11.7	0.20	12.8	0.21
RHSC	-43.5362	172.5644	15.9 m	6.4 m	10.0	0.21	6.5	0.28
CHHC	-43.5359	172.6275	22 m	3 m	14.7	0.17	3.8	0.37

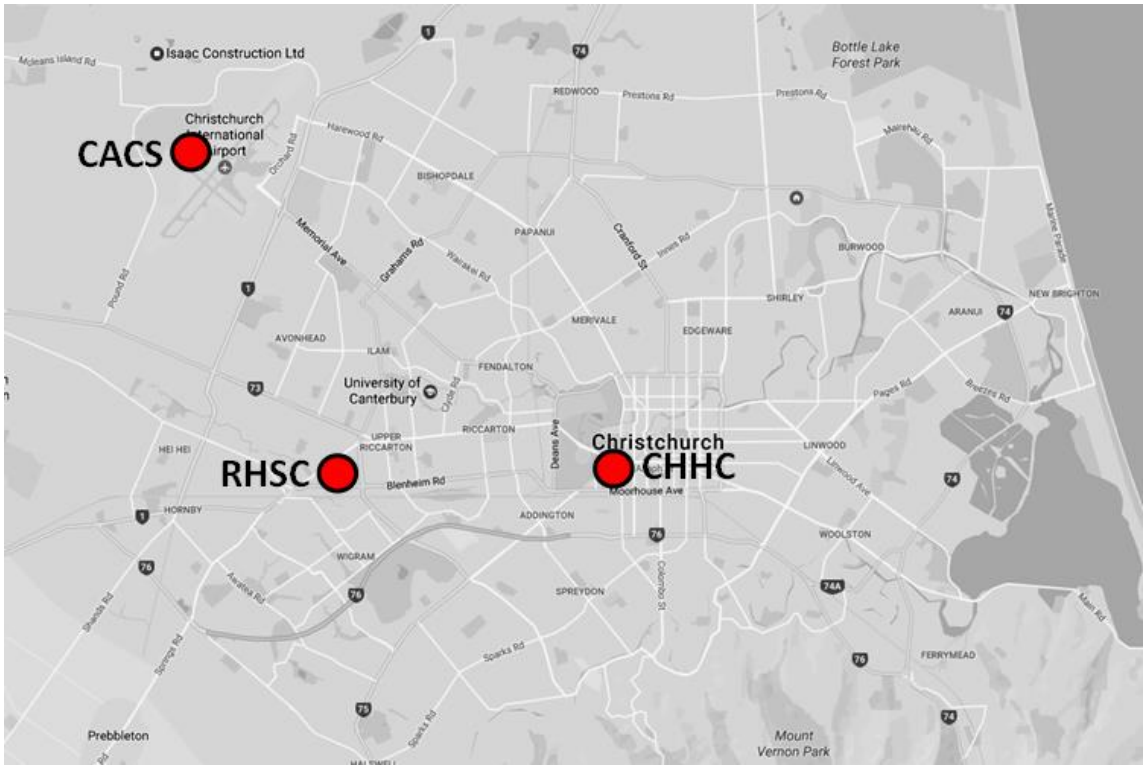

Figure 3.1: Map of SMSs used in the deconvolution process (Google Maps, 2017)

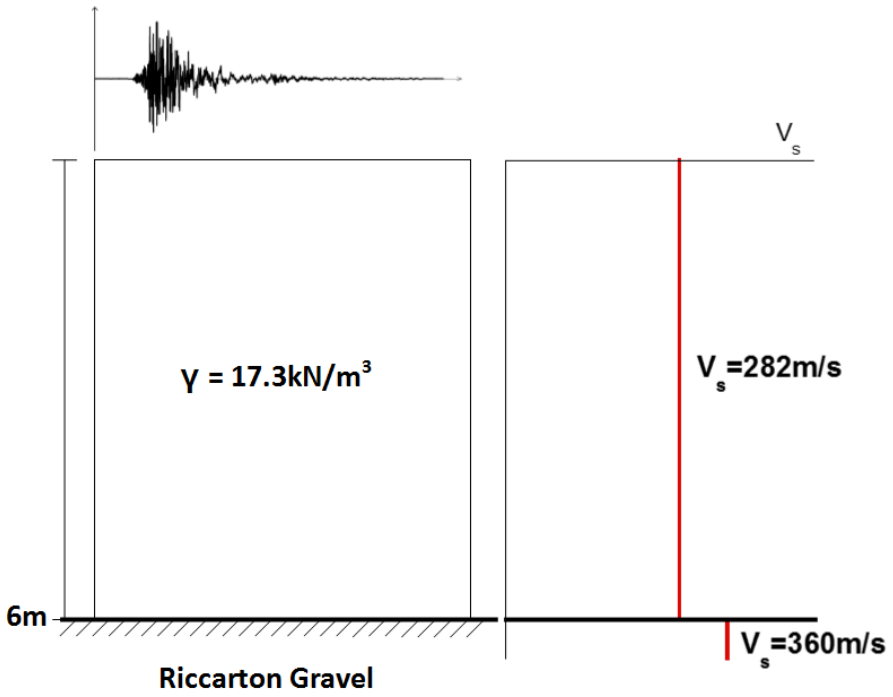

Figure 3.2: Soil and V_s profile at CACS (Wotherspoon et al., 2013)

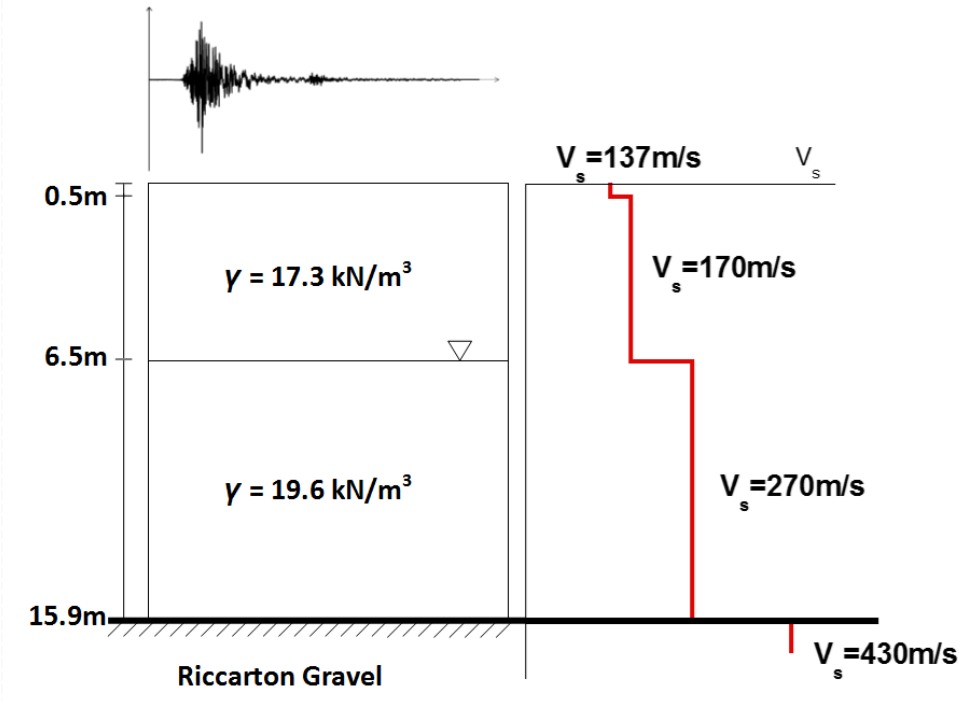

Figure 3.3: Soil and V_s profile at RHSC (Wotherspoon et al., 2013)

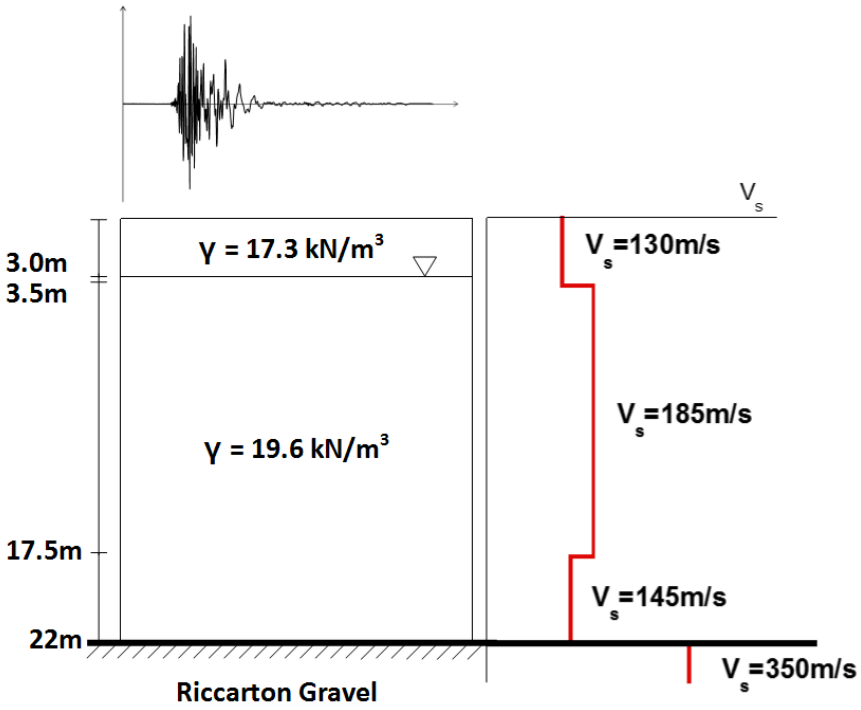

Figure 3.4: Soil and V_s profile at CHHC (Wotherspoon et al., 2013)

3.2 Methodology

The deconvolution process utilises an equivalent linear site response analysis to back-calculate ground motion at the bedrock based on recorded accelerations at the ground surface. The ground motion is converted from the time domain into the frequency domain using the Fast Fourier Transform (FFT), divided by the transfer function between the ground surface and (outcropping) bedrock, then converted back into the time domain (using Inverse FFT) to give the output time history. The transfer function describes how different frequencies are amplified by the soil deposit from the bedrock to the ground surface (or any depth of interest). The variables required are the density (ρ), thickness (h), shear modulus (G) and damping ratio (ξ) for each soil layer. To perform an equivalent linear analysis, degraded values of shear modulus and representative damping ratios are used. For this research, Strata (Rathje and Kottke, 2010) was used to perform the deconvolution.

The process used to deconvolute a surface ground motion into an equivalent bedrock motion is illustrated in Figure 3.5 and described in the following. This process follows the recommendations of Kramer (1996) and Markham (2015).

1. Identify an equivalent depth to deconvolute the ground motion at
2. Establish a soil profile and shear wave velocity profile for the site
3. Filter the surface ground motion with a 4th order lowpass Butterworth filter with cutoff frequency of 15 Hz

4. Perform an equivalent linear (EQL) site response analysis using the filtered ground motion recorded at the surface scaled by 0.87
5. Extract iterated equivalent shear modulus values (and respective values of shear wave velocity) and damping ratios for each soil layer (at around 1 m intervals) obtained from the equivalent linear analysis performed in Step 4
6. Perform a deconvolution using an elastic linear (EL) site response analysis with the filtered surface ground motion at full scale and the previously identified values of V_s and damping ratio (from Step 5)

Once the deconvoluted motion has been obtained it is validated through the following two steps:

1. Conduct equivalent linear site response analysis using the deconvoluted motion as bedrock input and compare with original recorded motion – these should be nearly identical
2. Use the deconvoluted motion at another site, applying an appropriate scaling factor to account for the different source to site distance, to assess if the deconvoluted motion can be used as a reasonable predictor of ground response at other sites.

The above processes were conducted for the two sites and will be outlined in this chapter.

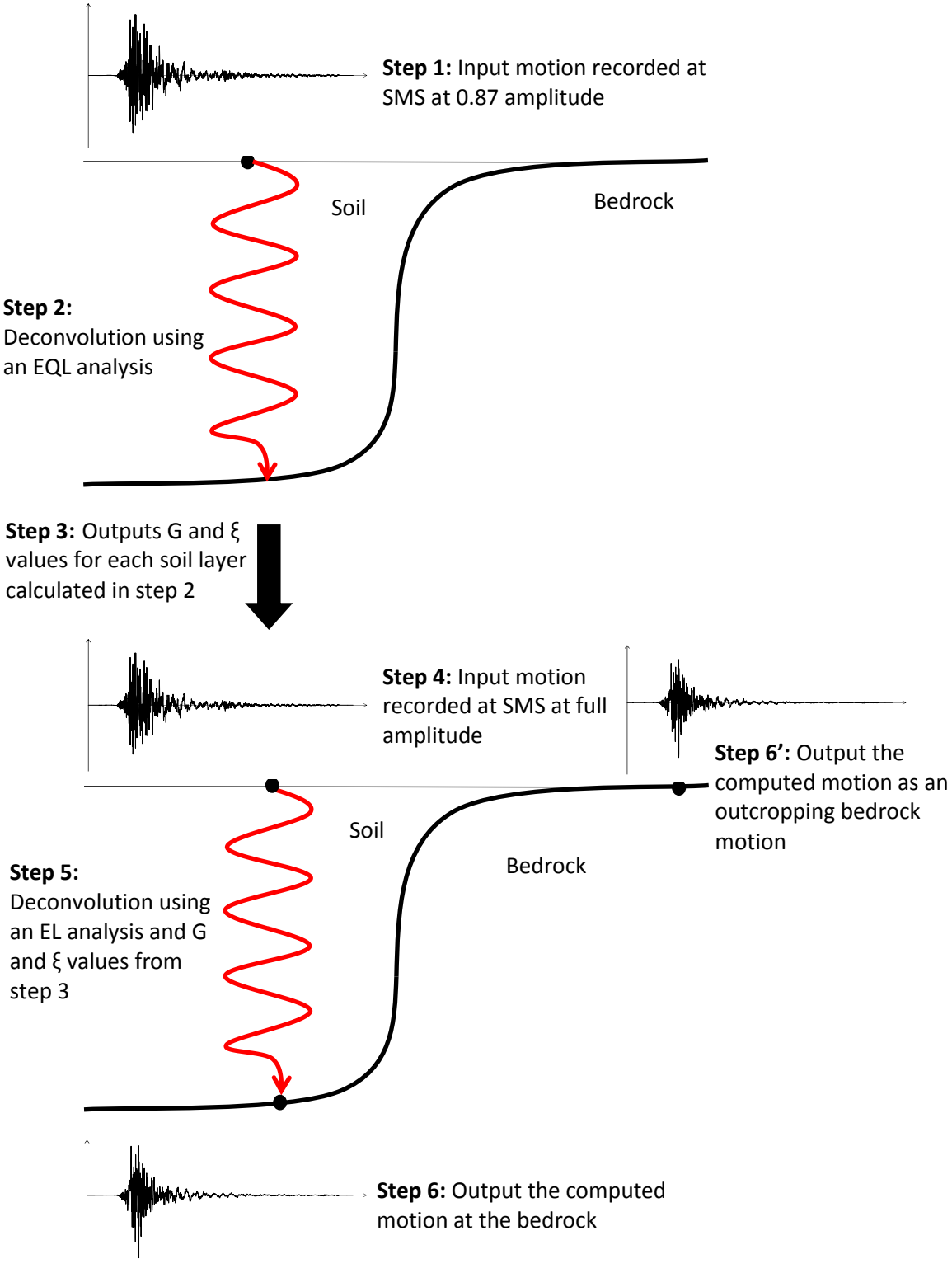

Figure 3.5: Illustration of the deconvolution process

3.3 Degradation curves

When soils are subject to seismic shaking they tend to undergo a loss of shear strength. This is observed in a flattening of the stress-strain curve and an increase in hysteresis damping, hence an important aspect of an equivalent linear site response analysis are the degradation curves adopted to model this soil softening. The base curves used in this analysis were those proposed by Darendeli (2001) which are based on Masing behaviour. However, these degradation curves (and many others) overestimate soil softening at large strains. To overcome this issue, a strength based modification was applied to the original Darendeli curves as outlined in the following.

3.3.1 Modulus reduction curves

The hyperbolic stress-strain relationship (backbone curve) was used as the base modulus reduction curve as shown in Equation 3.1 (Darendeli, 2001).

$$\frac{G}{G_{max}} = \frac{1}{1 + \beta\left(\frac{\gamma}{\gamma_r}\right)^{\alpha}} \quad \textbf{3.1}$$

Where α and β are constants taken as 0.92 and 1.0 respectively, and γ_r is a pseudo-reference strain defined as per Equation 3.2.

$$\gamma_r = \gamma_{r,1}\left(\frac{\sigma'_m}{p_a}\right)^n \quad \textbf{3.2}$$

Where $\gamma_{r,1}$ was taken as 0.0352%, *n* as 0.3488 and p_a is the atmospheric pressure (100 kPa).

This curve accurately models shear modulus degradation up to shear strains of around 0.3-0.5%, however past this strain level it underestimates the strength of the soil. This can have significant implications for deconvolution as underestimation of the shear strength of the soil can result in damping of high frequency motion when significant soil softening occurs (i.e. the soil liquefies). To overcome these issues, a modification was made to the degradation curves.

The modified Yee et al. (2013) degradation curve was adopted for this study. This modification transitioned the degradation curve from the original backbone curve (Equation 3.1) to a strength based curve at the chosen threshold strain. The modified degradation curve was based on a pseudo-reference strain derived from the actual failure strength of the soil. This was determined as per Equation 3.3.

$$\gamma_r = \frac{\tau_f}{G_{max}} \quad \textbf{3.3}$$

Where τ_f was established from the Mohr-Coulomb failure criterion, $\tau_f = \sigma' \tan\phi'$ and G_{max} is a function of soil density and shear wave velocity, $G_{max} = {V_s}^2\rho$

The final form of the modified modulus reduction curve is

$$\frac{G}{G_{max}} = \frac{\frac{\gamma_1}{1+\left(\frac{\gamma_1}{\gamma_r}\right)^{\alpha}} + \frac{\left(\frac{G_{\gamma 1}}{G_{max}}\right)\gamma'}{1+\left(\frac{\gamma'}{\gamma'_{ref}}\right)}}{\gamma} \quad \textbf{3.4}$$

Where γ_1 is the threshold strain where the curve transitions from the original Darendeli curve to the modified strength based curve, this was taken as the strain at approximately $\frac{G}{G_{max}} = 0.5$; γ' is the difference between the actual strain and threshold strain $\gamma' = \gamma - \gamma_1$; γ'_{ref} is the new pseudo-reference strain defined as $\gamma'_{ref} = \frac{\tau_f - \tau_1}{G_{\gamma 1}}$ where τ_1 is the shear stress at the threshold strain and is defined as per Equation 3.5; and $G_{\gamma 1}$ is the gradient of the original curve at the threshold strain (Equation 3.6) and was used to ensure continuity between the original and modified curves. See Yee et al. (2013) for a more in depth description of the strength based modification.

$$\tau_1 = \frac{G_{max}\gamma_1}{1+\left(\frac{\gamma_1}{\gamma_r}\right)^{\alpha}} \quad \textbf{3.5}$$

$$\frac{G_{\gamma 1}}{G_{max}} = \frac{1+(1-\alpha)\left(\frac{\gamma_1}{\gamma_r}\right)^{\alpha}}{\left[1+\left(\frac{\gamma_1}{\gamma_r}\right)^{\alpha}\right]^2} \quad \textbf{3.6}$$

Figure 3.6 and Figure 3.7 illustrate the modified curve for RHSC at z = 10 m. The modified degradation curves for CACS, RHSC and CHHC at all depths in the deposits are in Appendices B, C and D respectively.

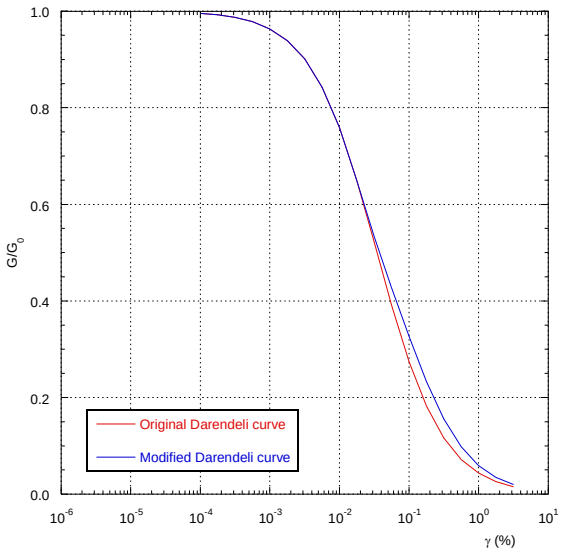

Figure 3.6: Modified modulus reduction curve for RHSC at z = 10 m

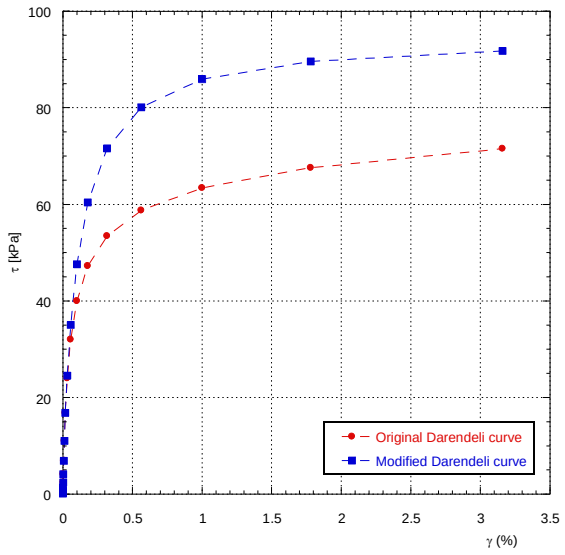

Figure 3.7: Comparison of failure stress for original Darendeli curve and the strength based modification for RHSC at z = 10 m

3.3.2 Damping ratio reduction curves

The original damping reduction curve was based on Masing behaviour and is defined in Equation 3.7.

$$D_{\alpha=1}(\%) = \frac{100}{\pi}\left[4\frac{\gamma - \gamma_r \ln\left(\frac{\gamma+\gamma_r}{\gamma_r}\right)}{\left(\frac{\gamma^2}{\gamma+\gamma_r}\right)} - 2\right] \quad \textbf{3.7}$$

With the following modifiers for $\alpha \neq 1$

$$D_{masing}(\%) = c_1 D_{\alpha=1} + c_2 {D_{\alpha=1}}^2 + c_3 {D_{\alpha=1}}^3 \quad \textbf{3.8}$$

$$c_1 = -1.1143\alpha^2 + 1.8618\alpha + 0.2523$$

$$c_2 = 0.0805\alpha^2 - 0.0710\alpha - 0.0095$$

$$c_3 = -0.0005\alpha^2 + 0.0002\alpha + 0.0003$$

And to correct for the shape and height of curve

$$D(\%) = b\left(\frac{G}{G_{max}}\right)^{0.1} D_{masing} + D_{min} \quad \textbf{3.9}$$

For this case, *b* was taken as 0.62 and D_{min} as 0.6.

There is less literature on the modification for damping reduction curves so for this case a linear modification was used. First, the strength based damping reduction curve was developed using Equations 3.7-3.9 and the threshold strain $\gamma_r = \frac{\tau_f}{G_{max}}$ (as for the strength based modulus degradation curve). Then a linear relationship was established between the threshold strain and an arbitrary point on the strength based curve (a point chosen at high levels of strain). The resulting relationship was used as the modified damping curve and is illustrated in Figure 3.8 for a depth of 10 m at RHSC. The damping degradation curves for CACS, RHSC and CHHC at all depths in the deposit are in Appendices B, C and D respectively.

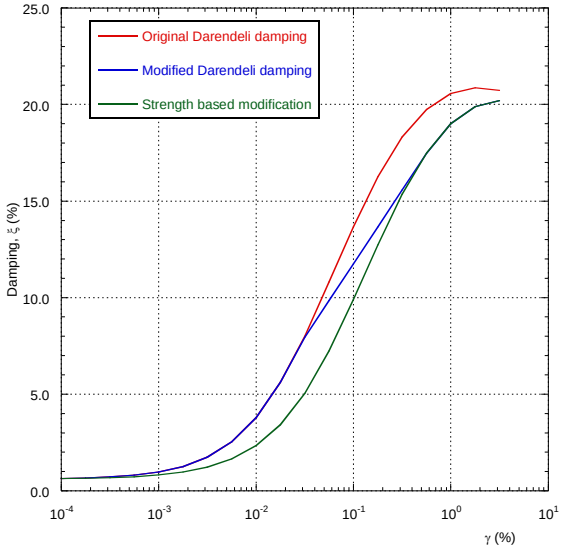

Figure 3.8: Damping reduction curve for RHSC z=10 m

3.4 Validation of deconvolution

The ground motions recorded at CACS and RHSC during three events (4 September 2010 M_w 7.1, 22 February 2011 M_w 6.3, and 13 June 2011 M_w 6.0 earthquakes) were deconvoluted following the process outlined in Section 3.2 and using the curves derived on Section 3.3 with the fault normal component of the ground motion. To verify that these deconvoluted ground motions were accurate representations of the bedrock ground motion, they were used as inputs to an EQL site response analysis first at the site of deconvolution then at one other site using the appropriate scale factors. The deconvoluted ground motions for each site and event can be found in the electronic supplement.

3.4.1 Deconvoluted motion at the same site

To ensure that the deconvolution was correctly conducted, the deconvoluted motion was first used in a site response analysis at the site of deconvolution. The deconvoluted motion was input at the base of the soil profile in the equivalent linear site response analysis and the computed motions at the ground surface were compared to the original recorded surface motions. The two motions were almost identical for all deconvoluted time histories indicating that no undue error had occurred in the deconvolution process.

3.4.2 Deconvoluted motion at other sites

The next step was to use the deconvoluted motion at another site to verify that the motions obtained could reasonably be used as general inputs to any site response analysis. Two adjustment factors were required for this; a scale factor to account for the path effects that result from a different source-to-site

distance, and an adjustment for any time lag between the time at which recording started at the two sites.

The scale factor was determined using the New Zealand specific Ground Motion Prediction Equations (GMPE) outlined in Bradley (2013). The key parameters in the GMPE, when using a deconvoluted ground motion as input at another site for any given event, are the source-to-site distance parameters and the shear wave velocity at the two sites ($V_{s(30)}$). These equations produce ground motion parameters (in this case spectral acceleration) for shaking periods of 0.01-10 s. This provides some difficulty when applying a single scale factor to a single site, hence the scale factor adopted was the mean ratio of convolution site to deconvolution site across the period range 0.1 – 5 s. This range was chosen as it encompassed the fundamental period of the sites considered, and was deemed to include any motion of significance. It should be noted that due to the use of the 15 Hz lowpass filter, any motion at periods less than 0.07 s cannot be considered. The scale factors for all sites and events are presented in Appendix E. See Bradley (2013) for full description and formulation of the GMPE.

The time lag correction was determined by adjusting the deconvoluted motion to have the strong ground shaking start at the same value on the time scale as the recorded motion. The start of the ground motion was considered to be when the acceleration exceeded a certain threshold, generally set at 0.005 g.

Using the above adjustment factors, the deconvoluted motion was used in an EQL site response analysis at two other sites, these were; RHSC and CHHC to verify the CACS deconvolutions, and CACS and CHHC to verify RHSC. Figure 3.9 shows the comparison between the recorded motions and the computed motions at the ground surface using both the CACS and RHSC February 2011 deconvoluted motions as input to the site response analysis. The surface ground motion computed using the deconvoluted motion in this manner corresponded reasonably well with the recorded ground motions, indicating that the deconvolution gave a reasonable result. It should be noted that the CHHC site is on soft soil and did experience liquefaction during the February 2011 earthquake, therefore some error, associated with modelling highly non-linear soil behaviour with a linear model, was present in the results. Corresponding validation figures for the June 2011 earthquake are shown in Appendix F, the validation for September 2010 was not performed as there was satisfactory evidence that the deconvolution process produced reasonable results.

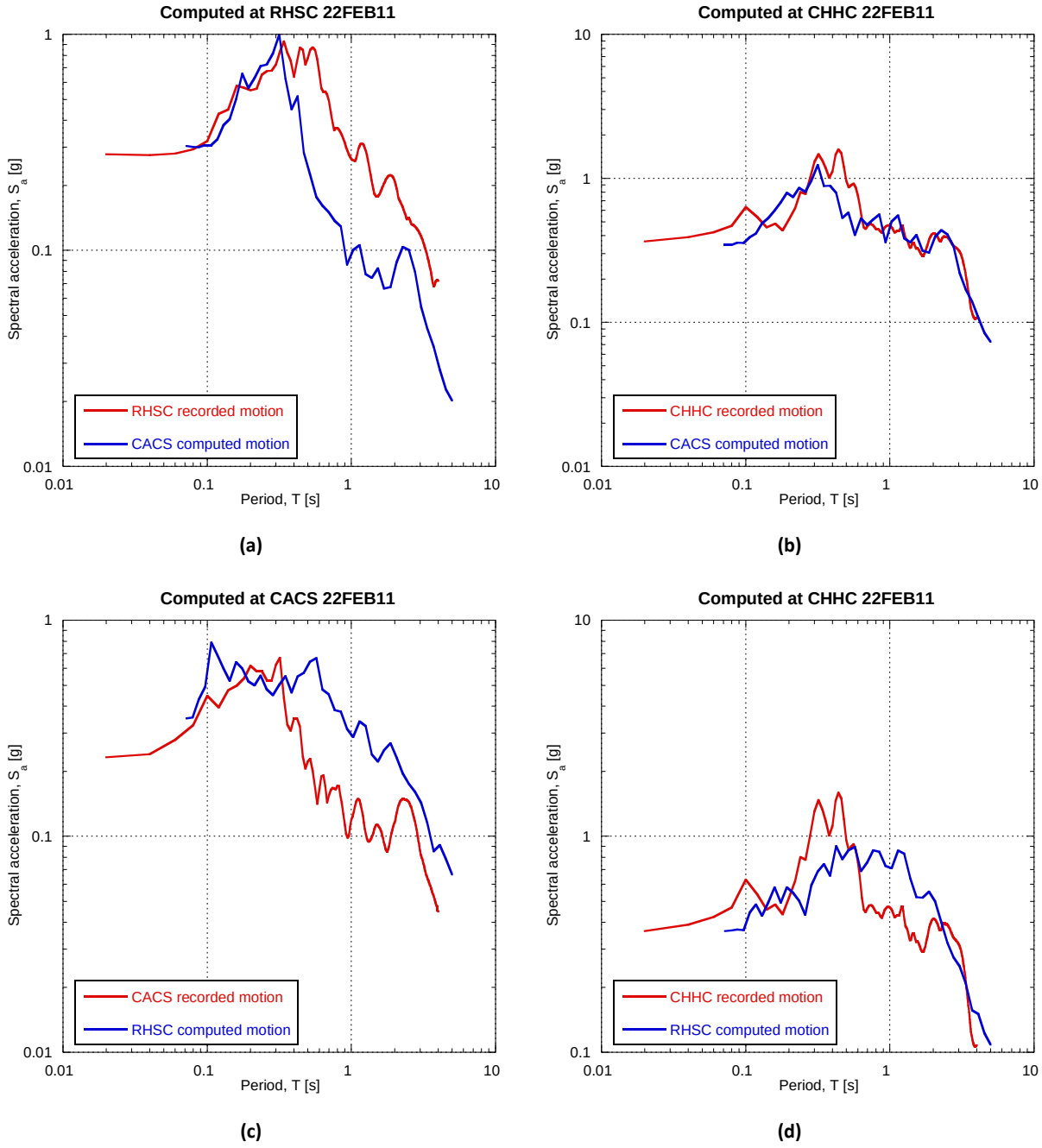

Figure 3.9: Comparison of response spectra between the recorded surface motion and the surface motion computed using a deconvoluted motion for 22 February 2011 earthquake: (a) CACS deconvoluted motion at RHSC site; (b) CACS deconvoluted motion at CHHC site; (c) RHSC deconvoluted motion at CACS site; (d) RHSC deconvoluted motion at CHHC site

3.5 Variations on the method of deconvolution

The method outlined above was the one adopted for this analysis, however it is important to note that there are a number of variations in the deconvolution process that could yield slightly different results. The first of these is the definition of what constitutes an appropriate stratum to deconvolute to. For this study, the Riccarton Gravel was chosen as representative of the bedrock and was identified based on the shear wave velocity, however there are other parameters by which this boundary could be set. Secondly, modified Darendeli (2001; Yee et al., 2013) modulus and damping reduction curves were

adopted to model soil softening. There are other degradation curves available that could also be adopted, and other modifications that could be used to address the issue of underestimation of soil strength at large strains. Lastly, there is variation within the estimation of scale factors when using a deconvoluted motion at a different site. Within the NZ specific GMPE (Bradley, 2014) there are a number of different parameters which can form the basis of the scale factor and different ways of averaging across the periods, as well as other options outside of the Bradley (2014) formulation. All in all, there is more than one appropriate way of conducting the deconvolution analysis and the chosen method will be dependent on the user and the purpose to be served.

4 Soil Profile Characterisation

In the 2010-2011 Canterbury Earthquake Sequence (CES) widespread liquefaction occurred over nearly half of the urban area of Christchurch. The liquefaction manifestation ranged from low or moderate to severe across various suburbs, and often was non-uniform even within a given suburb. Following the earthquakes, comprehensive damage inspections and field investigations were carried out to document a large number of case histories. Further research studies were then performed for in-depth scrutiny of particular aspects of soil liquefaction and its effects on buildings and infrastructure.

Within these efforts, 55 sites were selected for in-depth field investigations to scrutinise various contributing factors to the development of liquefaction and consequent damage, as well as to rigorously examine the accuracy of (state-of-the-practice) simplified liquefaction evaluation procedures. The 55 sites were strategically selected to include cases where the site manifested liquefaction both during the 4 September 2010 (M_w 7.1) and 22 February 2011 (M_w 6.3) earthquakes (Yes/Yes cases), sites where there was no liquefaction manifestation in either event (No/No cases), and sites where liquefaction did not manifest in the September 2010 earthquake but manifested in the February 2011 earthquake (No/Yes cases). The simplified method was generally over-predicting the occurrence of liquefaction for the No/No sites, for which practically no evidence of liquefaction was observed during the earthquakes. The distribution of the 55 sites in relation to liquefaction manifestation in the two events is shown in Figure 4.1 and Figure 4.2.

At each site detailed field investigations were performed including CPT, boreholes, cross-hole testing for V_s and V_p profiling, recovery of undisturbed samples and laboratory index testing of soils. In this research, CPT, borehole and shear wave velocity data at the 55 sites were used to develop simplified soil profiles for each site. The goal was to identify representative soil profiles for various sites in Christchurch, associate soil characteristics and properties to representative soil layers and then scrutinise differences or similarities between profiles associated with Yes/Yes and No/No sites. This approach was intended to help identify the key factors that influence liquefaction manifestation and associate those with key soil types and characteristics of the soil profiles. The soil profiles and soil characteristics identified as representative of Christchurch soils were then used to develop numerical models for Effective Stress Analysis (ESA).

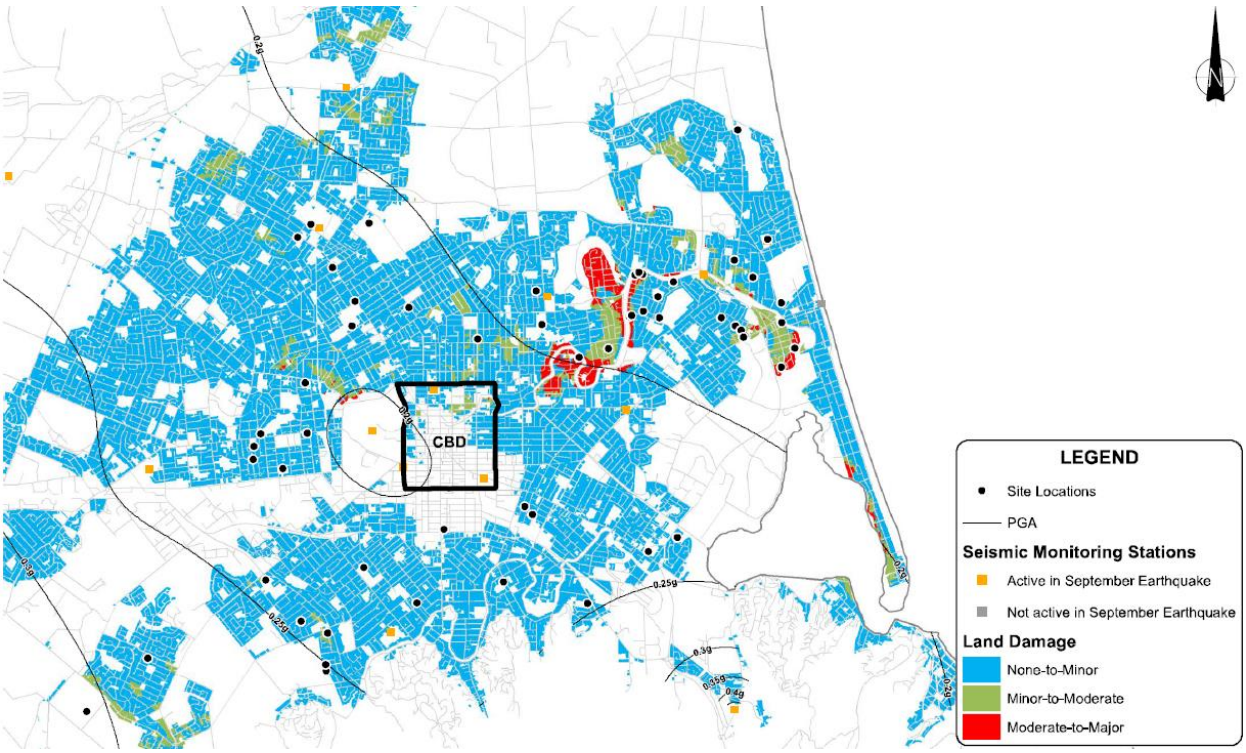

Figure 4.1: Land damage during the 4 September 2010 M_w 7.1 earthquake (Tonkin & Taylor, 2015)

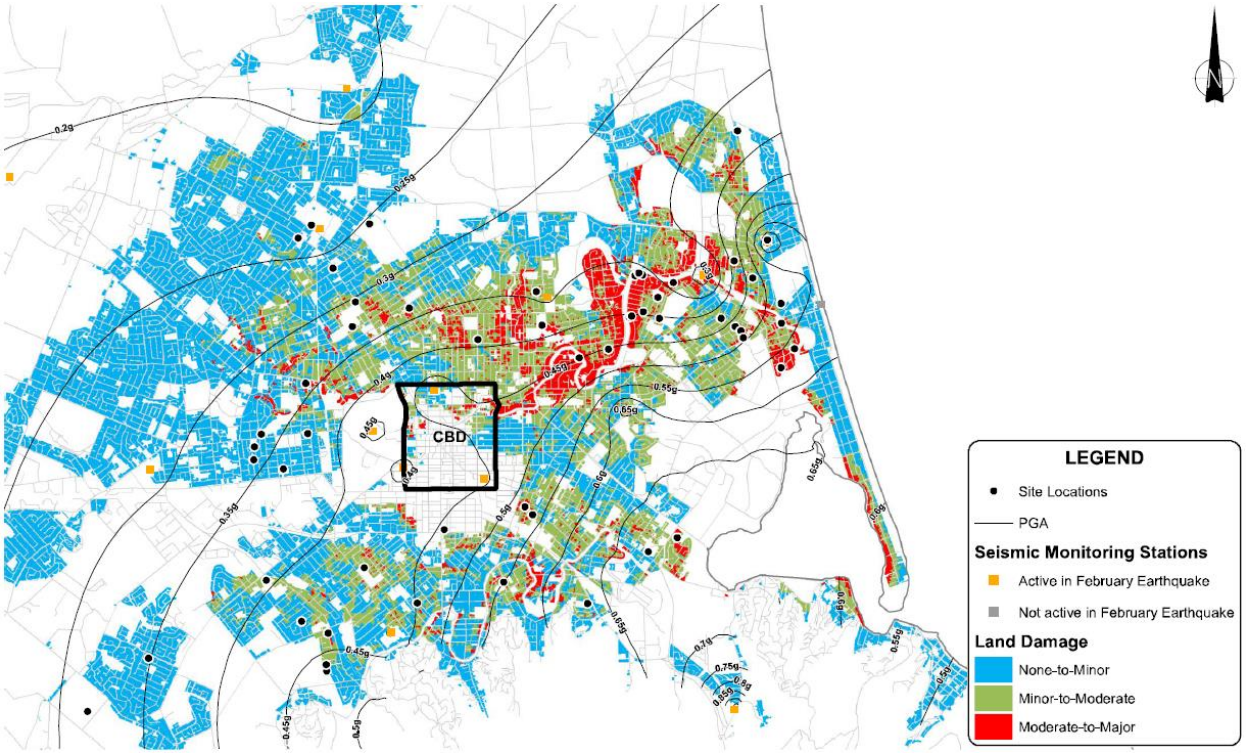

Figure 4.2: Land damage during the 22 February 2011 M_w 6.2 earthquake (Tonkin & Taylor, 2015)

4.1 Factors contributing to over-prediction by the simplified method

The simplified method of liquefaction evaluation has a few characteristic properties that affect how parameters such as the soil type, soil in situ state and soil profile are incorporated in a triggering analysis. Clean uniform sand is taken as a reference material and corrections are made for the effects of grain size, fines content and the plasticity of fines using soil behaviour type (I_c), (e.g. Robertson and Wride, 1998), or fines content (FC), (e.g. Idriss and Boulanger, 2008; Boulanger and Idriss, 2014) in the adjustment for the clean sand equivalent normalised CPT tip resistance q_{c1Ncs}. For clean sand, and liquefiable soils in general, it is well established that the principal factors affecting liquefaction potential are soil density, which is accounted for through the use of CPT tip resistance (q_c), and confining stress, which is accounted for through the K_σ correction, use of the normalised tip resistance (q_{c1N}), and use of shear stress ratios in the evaluation.

These factors are incorporated in the simplified method along with the assumptions that soils are fully saturated below the water table and that the factor of safety for a given layer is estimated in isolation, without reference to the response from other layers or of the deposit as a whole. In this context, there are a number of factors that affect the cyclic response of soil deposits that are not directly accounted for by the simplified method. These include:

- The presence of a thick crust and its effects on liquefaction manifestation
- Partial saturation of the shallow layers immediately below the water table
- The characteristics of silty soils and the effects of plasticity
- Stratification of the deposit including thin interlayering of liquefiable and non-liquefiable layers
- System response of the deposit where interactions in the dynamic response, or water flow, significantly affects the evolution of liquefaction and its consequences.

The first three factors will be briefly discussed here. The last two, the effect of soil stratification and the dynamic response of the soil deposit, are the focus of this study and will be examined in more depth.

Crust thickness has a significant impact on whether liquefaction is manifested at the ground surface when liquefaction occurs in deeper layers. The crust is generally taken as the upper layer of soil above the water table and is therefore considered non-liquefiable. A thin crust will crack under the upward pressure from deeper liquefied soil resulting in sand ejecta on the surface. However, if the crust is thick enough it will stay intact preventing the upward migration of liquefied material and the surface manifestation (and the associated damage) of liquefaction.

Partial saturation of upper soil layers can also influence liquefaction susceptibility. The simplified method assumes that all soil below the water table is fully saturated. This means that these soils (if sandy) are liquefiable and, being close to the surface, would cause the greatest damage if they liquefy.

However, partial saturation of the upper few metres of soil immediately below the water table can restrict the build-up of pore water pressure and prevent liquefaction from occurring in the shallow part of the deposit. This can result in no manifestation of liquefaction and cause substantially different consequences.

Other factors that can also lead to over-prediction of liquefaction based on simplified assessment, are the behaviour of silty soils under cyclic loading and the effect that the presence of fines and the plasticity of those fines have on the liquefaction resistance of a soil. Silty soils are widespread in Christchurch and so were an important factor in soil response during the CES. When using the simplified method, all soils are assessed based on a framework developed for clean uniform sands and therefore may have limited applicability for silts. Characteristics of both the micro and macro stratification of silts and the plasticity of fines will affect the liquefaction susceptibility of a silty soil (Beyzaei et al., 2015; Stringer et al., 2015).

The focus of this study is how stratification of soil deposits affects liquefaction triggering. Thin interlayering of non-liquefiable and liquefiable soils can affect the generation and dissipation of pore water pressures and hence change the dynamic properties and response of a soil deposit to seismic loading. For example, if a thin layer liquefies at depth (and the liquefaction may not manifest on the surface), this can modify the seismic waves passing through this layer by damping high intensity accelerations and elongating the period of motion. This results in the layers above and below the liquefied layer being subjected to ground motions considerably different to what otherwise would be the case in the absence of liquefaction.

In addition, once excess pore water pressures develop (and particularly when one layer liquefies generating higher pore water pressures) water starts to flow to the surrounding soil as the pore water migrates from an area of high pressure to an area of lower pressure. This can change the density of the surrounding soil, altering its liquefaction characteristics and disturbing its skeleton structure. Through these two mechanisms, ground motion modification and the dissipation of pore water pressures, highly interlayered soil deposits can significantly alter the dynamic properties of soils and change how they respond to seismic shaking (i.e. change both their liquefaction potential and the manifestation of liquefaction).

4.2 Simplified soil profiles

All the factors discussed above can impact liquefaction development, but are either ignored or not explicitly accounted for by the simplified method. As the effects of soil stratification are targeted in this study, simplified soil profiles were developed to help define soil layers based on a generalised description (see subsequent sections), and to help identify which deposits are expected to behave differently due to different soil stratification. This type of analysis had two benefits; firstly, it enabled

representative parameters determining the soil composition (for example, grain size, fines and plasticity) to be identified for each layer; secondly, it enabled the identification of representative soil profiles and their similarities and differences in relation to observations from the CES. As a result, representative profiles and associated soil properties provided a basis, and the necessary data, for developing computational models for ESA.

4.2.1 Data and characterisation method

The locations of the 55 sites used to develop the simplified profiles are shown in Figure 4.3. The aim of the process described below was to systematically characterise the 55 profiles in regards to all parameters of importance to liquefaction evaluation. For each site there was available; CPT data, borehole data, and V_s and V_p data, as well as detailed observations from the CES with regard to liquefaction manifestation. Using the CPT data, simplified profiles were developed based predominantly on the CPT tip resistance, q_c and soil behaviour type index, I_c (Robertson and Wride, 1998). Layers were defined over a certain depth in the profile in which nearly constant q_c and I_c values were observed. In order to group the soils based on their overall composition, a generalised classification based on I_c was adopted as shown in Table 4.1. The CPT tip resistance was then used to discriminate between different densities within a given soil-type. Figure 4.4 gives an illustration of the simplified (idealised) soil profile for the site at 1128 Avonside Drive in Avondale. It shows the original q_c and I_c traces, their constant-value approximations over certain depth, and schematic stratification of the deposit together with borehole data, V_s and V_p profiles. The simplified profiles developed in this fashion for all 55 sites can be found in the electronic supplement.

Table 4.1: Classification of main soil behavioural types present in Christchurch soil profiles

Soil Type	**I_c**
GRAVEL	$I_c \leq 1.3$
Clean SAND	$1.3 < I_c \leq 1.8$
SAND with small amount of fines	$1.9 \leq I_c \leq 2.1$
Sandy SILT/ non-plastic SILT	$2.2 \leq I_c < 2.6$
Non-liquefiable silt/clayey soil	$I_c \geq 2.6$

As this process modified the key parameters q_c and I_c, there was the potential that it also modified the factor of safety calculated using the simplified method. To confirm that the simplified profiles derived as above did not alter the outcome of the simplified analysis at a given site, a liquefaction triggering analysis was conducted for the simplified profiles (using the methods of Robertson and Wride, 1998 and Zhang et al., 2002) and compared to a simplified triggering analysis conducted on the original CPT traces (using CLiq software; GeoLogismiki, 2006). The results of these analyses for 1128 Avonside Drive are shown in Figure 4.5.

It can be seen from Figure 4.5 that the results of the analysis of the simplified profile were very similar to those obtained from the analysis with the original CPT trace. The discrepancies between the analysis of the simplified profile and the original CPT trace are most notable around depths of 5 m and 7 m in the factor of safety plots. On the whole, this is of little concern for the purpose of this study. The simplified profile sometimes over-estimated and sometimes under-estimated the actual profile response but generally these balanced each other, and the differences never significantly changed the outcome of the simplified analysis in regard to liquefaction. A typical result is shown in Figure 4.5 where there is a good agreement between the analyses including between the calculated settlements for both profiles.

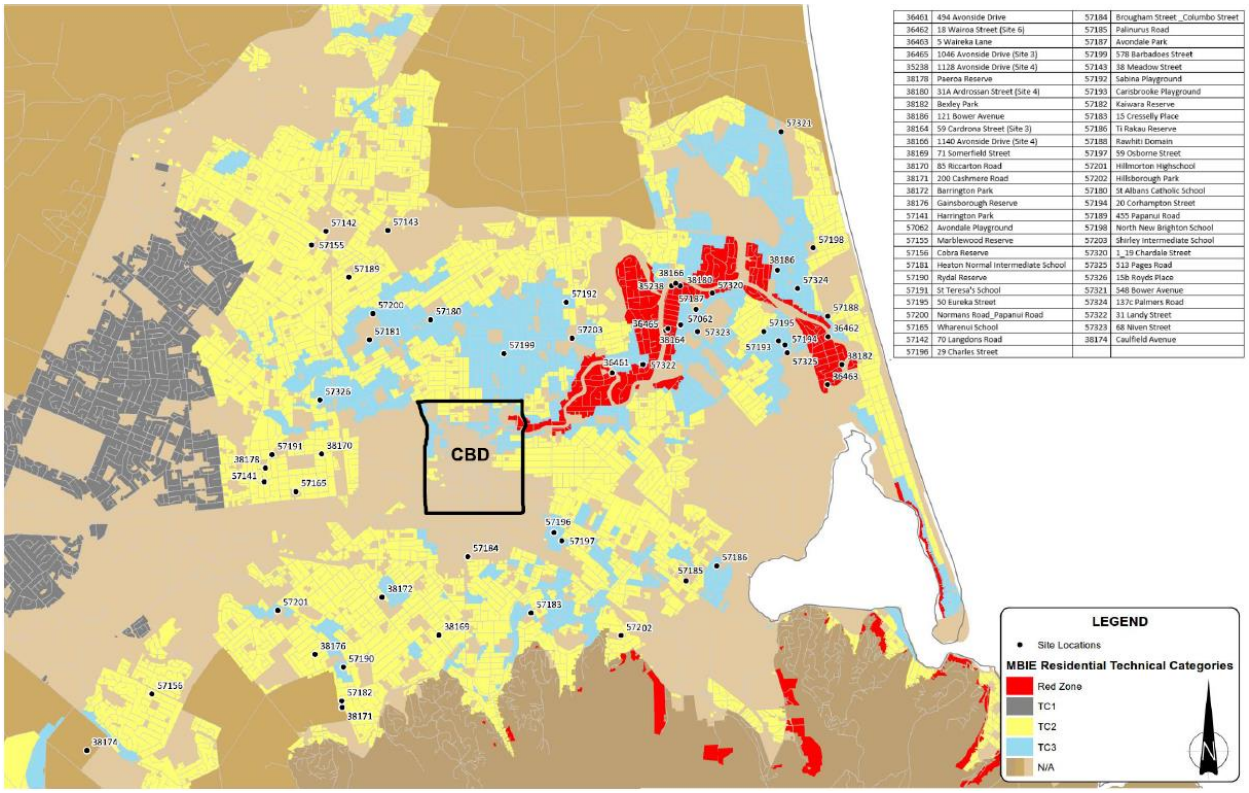

36461	494 Avonside Drive	57184	Brougham Street_Columbo Street
36462	18 Wainoa Street (Site 6)	57185	Palmyrus Road
36463	5 Waireka Lane	57187	Avondale Park
36465	1046 Avonside Drive (Site 3)	57199	578 Barbadoes Street
35238	1128 Avonside Drive (Site 4)	57143	38 Meadow Street
38178	Paeroa Reserve	57192	Sabina Playground
38180	31A Ardrossan Street (Site 4)	57193	Carisbrooke Playground
38182	Bexley Park	57182	Kaiwara Reserve
38186	121 Bower Avenue	57183	15 Cressella Place
38164	59 Cardrona Street (Site 3)	57186	Ti Rakau Reserve
38166	1140 Avonside Drive (Site 4)	57188	Rawhiti Domain
38169	71 Somerfield Street	57197	59 Osborne Street
38170	85 Riccarton Road	57201	Hillmorton Highschool
38171	200 Cashmere Road	57202	Hillsborough Park
38172	Barrington Park	57180	St Albans Catholic School
38176	Gainsborough Reserve	57194	20 Corhampton Street
57141	Harrington Park	57189	455 Papanui Road
57062	Avondale Playground	57198	North New Brighton School
57155	Marblewood Reserve	57203	Shirley Intermediate School
57156	Cebra Reserve	57320	1_19 Chardale Street
57181	Heaton Normal Intermediate School	57325	513 Pages Road
57190	Rydal Reserve	57326	15b Royds Place
57191	St Teresa's School	57321	548 Bower Avenue
57195	50 Eureka Street	57324	137c Palmers Road
57200	Normans Road_Papanui Road	57322	31 Landy Street
57165	Wharenui School	57323	68 Niven Street
57142	70 Langdons Road	38174	Caulfield Avenue
57196	29 Charles Street		

Figure 4.3: Map of 55 sites used for simplified analysis (Tonkin & Taylor, 2015)

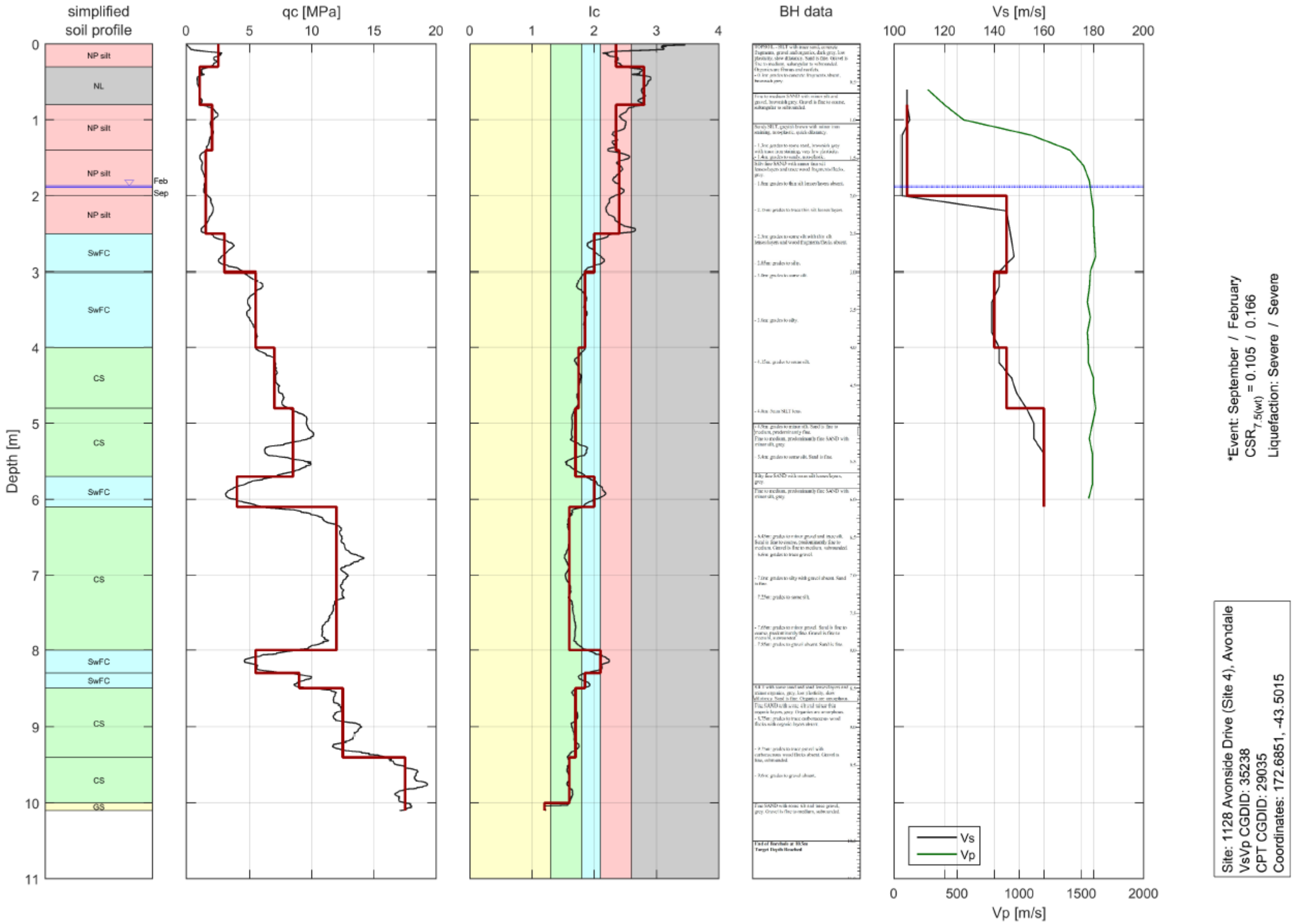

*Event: September / February
$CSR_{7.5(wt)}$ = 0.105 / 0.166
Liquefaction: Severe / Severe

Figure 4.4: Simplified soil profile for site at 1128 Avonside Drive, Avondale

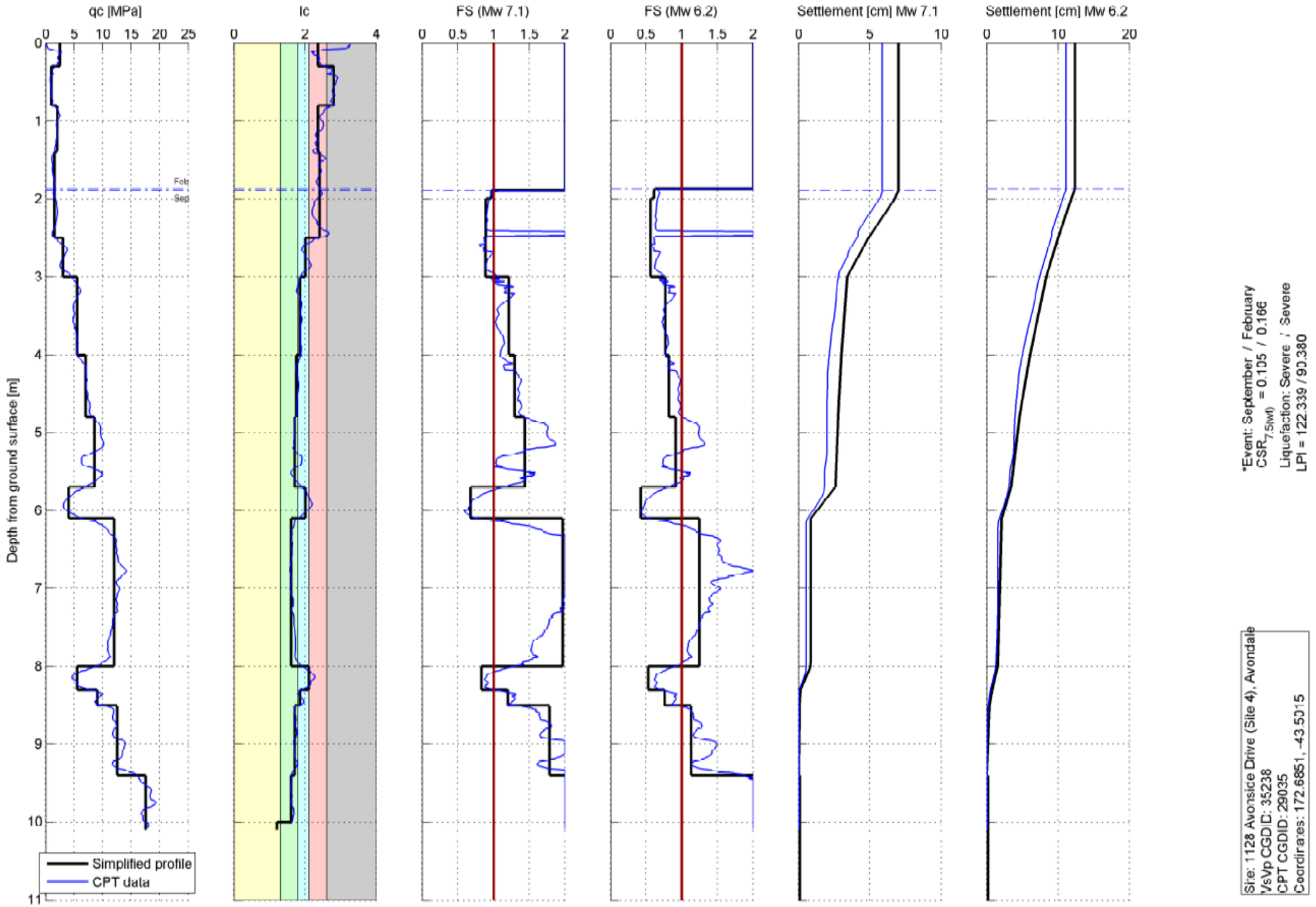

Figure 4.5: Comparison of triggering analysis on simplified soil profile and full CPT trace at 1128 Avonside Drive, Avondale

4.2.2 Critical layer analysis

The simplified soil profiles were grouped into three categories based on cases in which liquefaction was observed in both the September 2010 and February 2011 events (Yes/Yes; YY), no liquefaction was observed in September but was present in February (No/Yes; NY), or no liquefaction was observed in either event (No/No; NN). These two events were chosen as they were the two greatest magnitude earthquakes from the CES but had very different characteristics. The 4 September 2010 earthquake had M_w 7.1 and source-to-site distance of about 20-40 km for the sites of interest (Geonet, 2017). The 22 February 2011 earthquake was M_w 6.3 with a source-to-site distance of 4-5 km (Geonet, 2016). In Christchurch, liquefaction was experienced in both events but, unlike the September earthquake, there was loss of life and more significant damage to infrastructure during the February quake. Whilst greater in magnitude, the September earthquake was less damaging than the February event because the source of the February quake was located closer to the city resulting in extremely high ground accelerations, especially in the area from the CBD to the coast line.

Critical layers with regard to liquefaction occurrence, manifestation and damage were identified for each site using results of the simplified analyses. The properties of the critical layers were then summarised for each site and for each category of liquefaction manifestation. Critical layers were identified by considering the most critical combination of the factor of safety, depth from the ground surface and thickness of the liquefied layer resulting from a triggering analysis (Robertson and Wride, 1998) of the simplified soil profiles. On the whole, layers with the lowest factor of safety were identified as the critical layers except in cases when such layers were located too deep within the deposit (e.g. at depths greater than 10 m) or the layers were too thin (e.g. less than 0.1 m). Shallow layers with slightly higher factors of safety were also considered as potentially critical layers due to the higher likelihood of damage from liquefaction close to the surface. As a result, multiple potentially critical layers were identified at many of the sites. I_c values were also taken into account in the identification of a critical layer. If a layer had a low factor of safety but I_c close to 2.6, such layers were not considered critical as they exhibit threshold properties between liquefiable and non-liquefiable soils.

Critical layers were chosen to have constant characteristics to enable some simple analysis and identification of their representative properties. Hence, a continuous layer of the same factor of safety may consist of three sublayers with different I_c values. In the critical layer analysis, these were identified as three separate critical layers for the site. Figure 4.6 illustrates, as an example, the critical layers identified for 1128 Avonside Drive. It can be seen in Figure 4.6 that the layer at 6 m

depth was considered a critical layer as it had the lowest factor of safety and was overlain by liquefiable material (i.e. it was unconfined from above by thick non-liquefiable layers). Furthermore, the layer immediately below the water table, despite having a slightly higher factor of safety than the deeper layer at 6 m, was also chosen as a critical layer due to the thickness of the layer and its proximity to the ground surface. Conversely, the layer at 8 m was not considered a critical layer as it was located too deep within the deposit and had higher factor of safety than the layer at 6 m depth.

In the next step of the assessment, after identifying the critical layer(s) for each site, a number of key properties for the critical layer were scrutinised and plotted for each category of liquefaction manifestation. These properties were: q_{c1Ncs} (as a proxy for the soil density), depth to the top of the critical zone (as a proxy for the location of the layer) and thickness of the critical zone. A number of different definitions of the critical zone were considered to perform a more robust analysis of soil properties. These are summarised in Table 4.2 and schematically illustrated in Figure 4.7. In this research only the YY and NN cases were considered. This was done for simplicity as it was expected that these two instances of liquefaction manifestation would represent the two extremes of soil characteristics and the NY cases would fall somewhere in between. Figure 4.8 comparatively shows the summarised data for the YY and NN categories.

Soil layers generally do not act in isolation from each other so a number of additional parameters, outlined in Table 4.2, were considered in the critical layer analysis to give a more comprehensive assessment of the damaging effects of liquefaction. These were the critical zone, extent of FS < 1 and extent of liquefiable material, and were introduced to account for the effect of excess pore water pressures on the soil deposit as a whole. When excess pore water pressures are generated in one area of a soil deposit, water can flow between layers and influence the liquefaction behaviour of the surrounding soil, hence continuity of liquefiable material is an important factor in a liquefaction analysis. The critical zone (CZ) was defined to account for water flow and pore water pressure communication between the critical layer and any liquefiable layers in contact with it, the zone of FS < 1 gave an indication of the extent of the deposit likely to liquefy under the given shaking intensity, and the zone of liquefiable material gave an indication of the extent of the deposit that was potentially liquefiable and hence contributing to the hydraulic conductivity of the soils.

Table 4.2: Summary of properties identified for scrutiny of liquefaction-manifestation characteristics of each site

q_{c1Ncs}	Calculated using both Robertson and Wride (1998) and Boulanger and Idriss (2014) methods. Plotted for all identified critical layers at the site (Figure 4.8(a)), and also plotted for only one critical layer per site (Figure G.1 and G.2, Appendix G). In the latter case, the layer considered was that deemed to have the most critical combination of FS, depth from ground surface and thickness.
Critical layer (CL) (depth to and thickness of)	The critical layer was identified as a continuous layer of critical combination of FS and depth from ground surface. This included sublayers of different I_c values.
Critical zone (CZ) (depth to and thickness of)	The critical zone was any continuous layer of FS < 1 that was in contact with the critical layer. The layer was also considered continuous if there was a layer of FS > 1 separating a layer of FS < 1 conditional on the non-liquefied layer not having a thickness greater than that of the liquefied layer. In this scenario, only the thickness of FS < 1 was considered as the thickness of the critical zone.
FS < 1 (depth to and thickness of)	The zone of FS < 1 was the cumulative thickness of all layers with FS < 1 for the site for the M_w 6.3 22 February 2011 earthquake up to 10 m depth. The depth to this zone was the shallowest instance of FS < 1.
Liquefiable material (LM) (depth to and thickness of)	The zone of liquefiable material was the cumulative thickness of soils with I_c < 2.6. This included soil above the water table as these layers could also develop excess pore water pressures through water flow (i.e. migration of the water table). The depth to this zone was also the shallowest instance of I_c < 2.6.

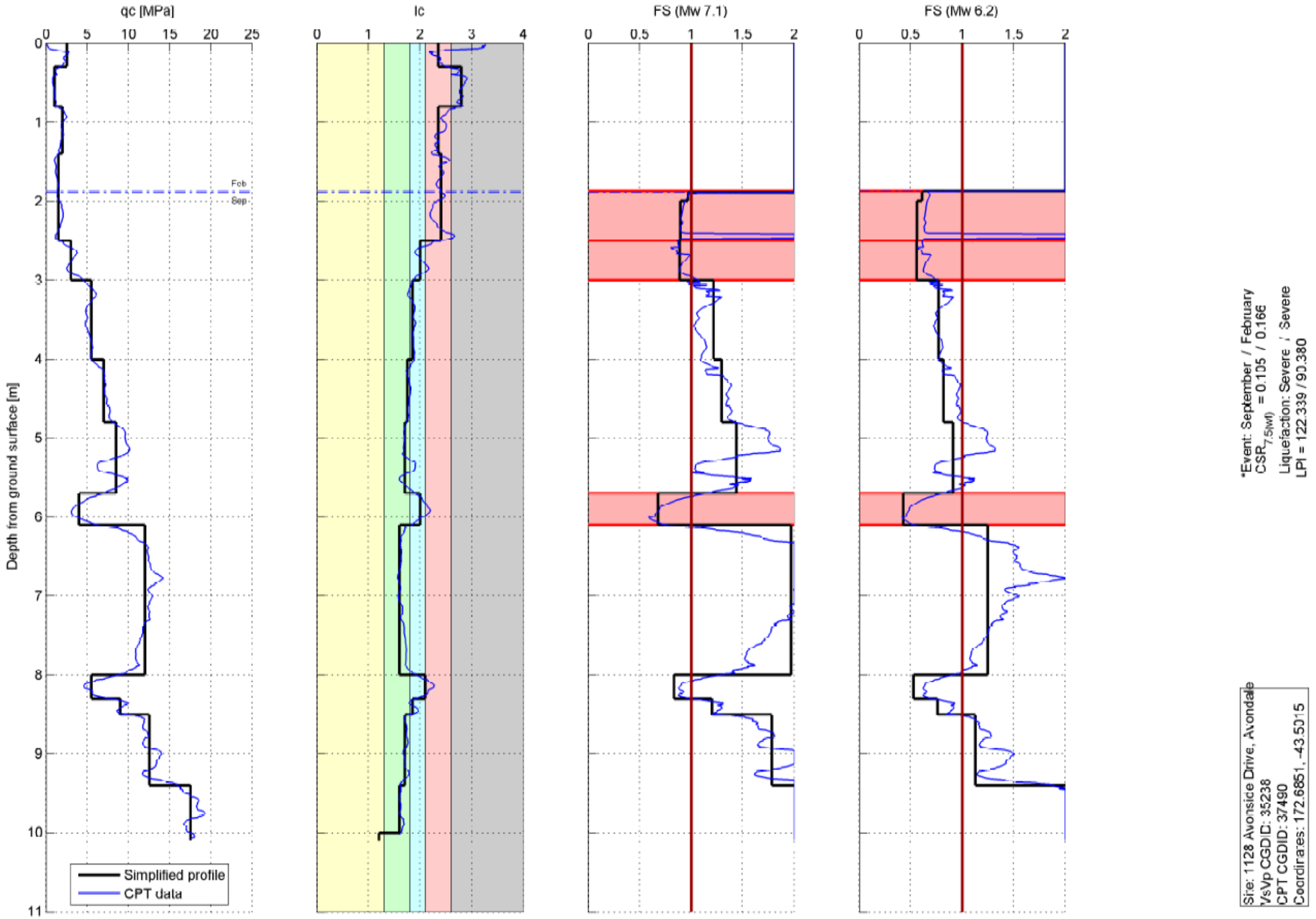

Figure 4.6: Critical layers identified from triggering analysis on simplified soil profile at 1128 Avonside Drive, Avondale

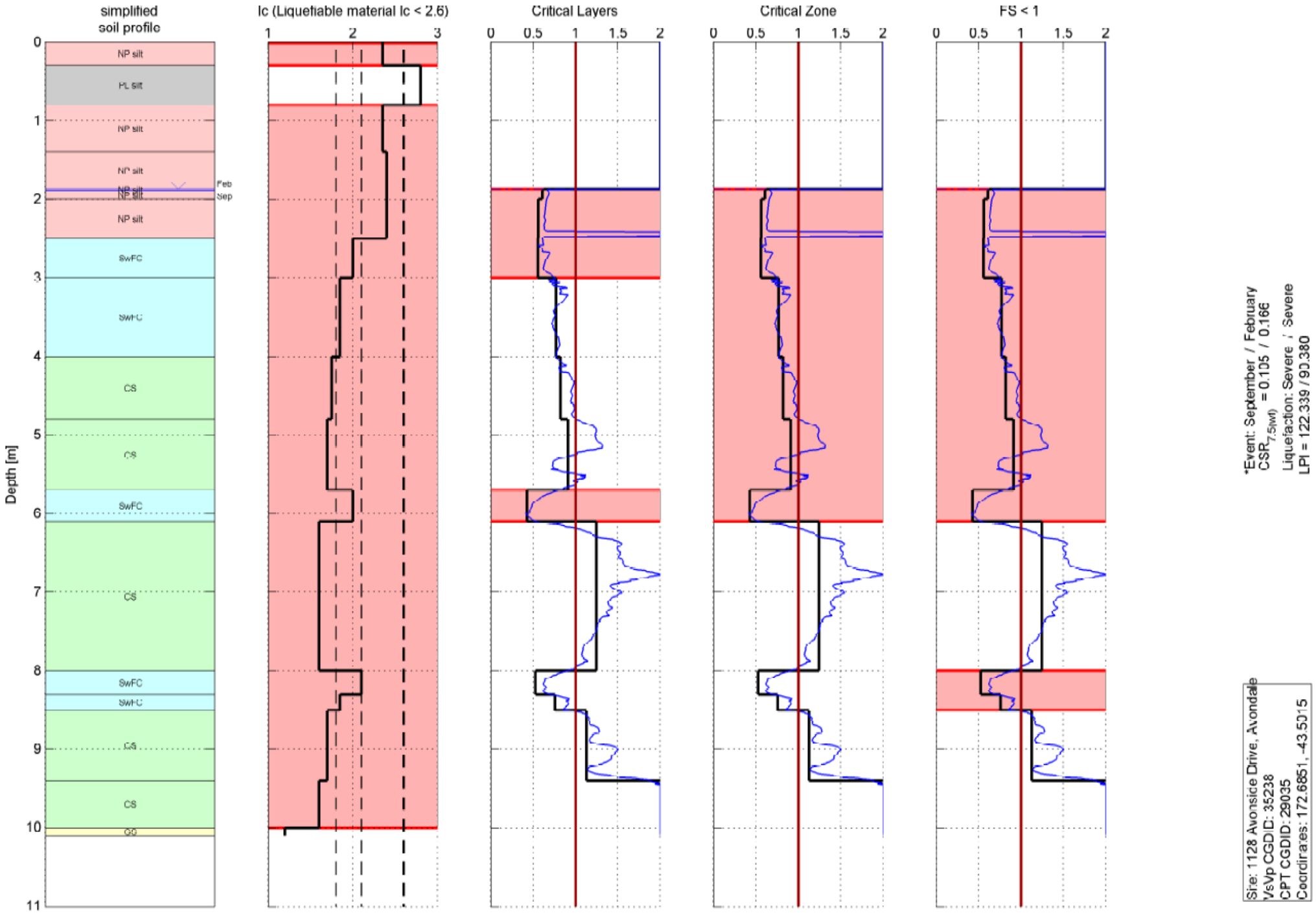

Figure 4.7: Illustration of different critical zones identified in critical layer analysis at 1128 Avonside Drive, Avondale

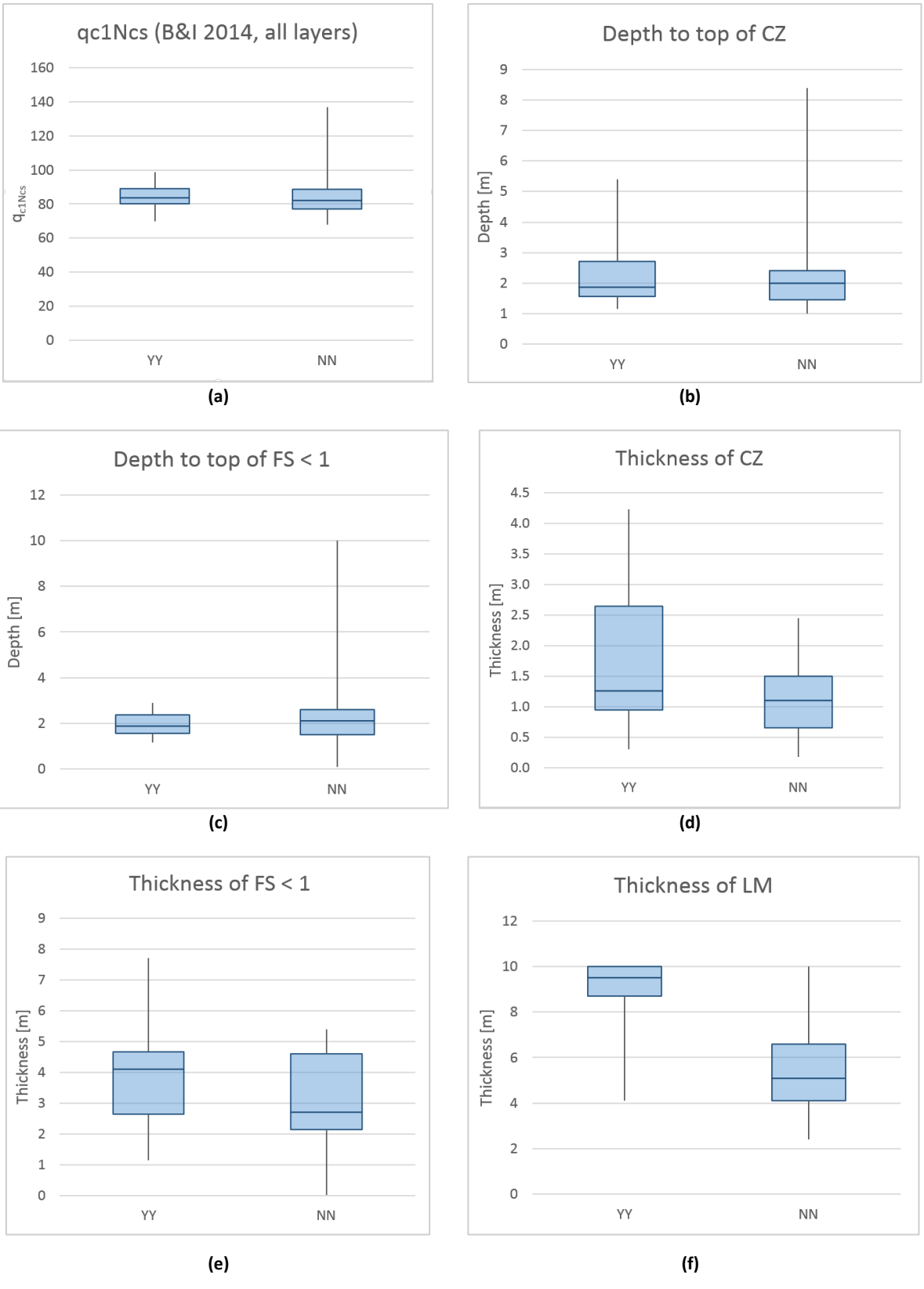

Figure 4.8: Results of critical layer analysis showing comparison of properties for the YY and NN cases of liquefaction manifestation (values at the end of the whiskers represent the minimum and maximum values for each dataset) (a) q_{c1Ncs} using Boulanger and Idriss (2014) (b) depth to the top of the critical zone (CZ) (c) depth to the top of FS < 1 (d) thickness of the CZ (e) cumulative thickness of FS < 1 (f) cumulative thickness of liquefiable material

From the box and whisker plot shown in Figure 4.8(a) it can be seen that the critical layers in both YY and NN profiles had relatively similar q_{c1Ncs} values, with the median value around 83. The only significant difference is in the fourth quartile of the data where q_{c1Ncs} ranges from 86 to 100 for YY, while the respective range for NN is 90-140. There was a similar depth to the critical zone in both profiles, with the critical layer most commonly located immediately below the ground water table (see Figure 4.8(b) and (c)). Again, the fourth quartile for the NN profiles shows much larger depths than the YY profiles. It is in the thickness of the critical zone that the two profiles differ most significantly. Figure 4.8(d) shows that the YY profiles had a greater critical zone thickness, indicating greater continuity of low liquefaction resistance layers in the YY profiles. Similarly, Figure 4.8(f) indicates that the YY profiles have a greater extent of liquefiable material, and that for 75% of these profiles 7.5 m or more are liquefiable materials in the top 10 m, and for 50% of the profiles 9.5 m are liquefiable materials in the top 10 m of the deposit. This suggests that the YY profiles were predominately sandy, liquefiable deposits whereas many of the NN profiles had non-liquefiable layers of significant cumulative thickness. These observations, in particular the differences between the two profiles, were taken into account when developing representative soil profiles for modelling and use in the ESA.

4.3 Characteristic soil profiles

The simplified profiles for the 55 sites were further analysed to identify some key characteristic profiles that were representative of the Christchurch sites. On first inspection, two simplified profiles were identified that represented global stratification characteristics over the top 10 m. The first was a thick, uniform sandy deposit which liquefied in both the September 2010 and February 2011 earthquakes (YY). The second, a highly stratified soil deposit with interlayering of liquefiable and non-liquefiable soils which did not manifest liquefaction in the September 2010 event, and either did or did not manifest in February 2011 (NY and NN sites respectively). Both profiles are summarised in general terms in Figure 4.9. Only the top 10 m of the soil deposits were considered in the characterisation process as the soil below 10 m is unlikely to have an impact on liquefaction manifestation at the surface, and therefore was modelled as non-liquefiable. This also allowed the focus to be the top 10 m by having the bottom section of all profiles, from 10 m to 20 m depth, identical.

These global soil profiles were then developed in more detail for use in the ESA. Two soil profiles were identified for the YY and NN cases each, giving four representative soil profiles in total. The YY category consisted predominately of uniform continuous sandy deposits in the top 10 m. This category was divided into two sub-groups based on the density of the sand layers. On the other

hand, the NN sites were highly non-uniform and consisted of a number of interlayered liquefiable and non-liquefiable layers in the top 10 m. This category was divided into two subgroups based on the number, thickness of non-liquefiable layers and their location in the deposit. In this process, a few of the soil profiles in each category were disregarded if they did not fit the general trend, or introduced additional complexities. For example, three sites out of the 15 in the YY category exhibited interlayered (rather than continuous sandy) deposits as would be more characteristic of the NY and NN categories. The above described approach was acceptable as the target was to identify a couple of generally representative soil profiles to be used in the ESA, as opposed to a comprehensive categorisation and analysis of all 55 sites. The adopted characterisation approach covers about 80% of the sites which are well represented by the chosen representative profiles, the remaining 20% of sites constitute more complex cases.

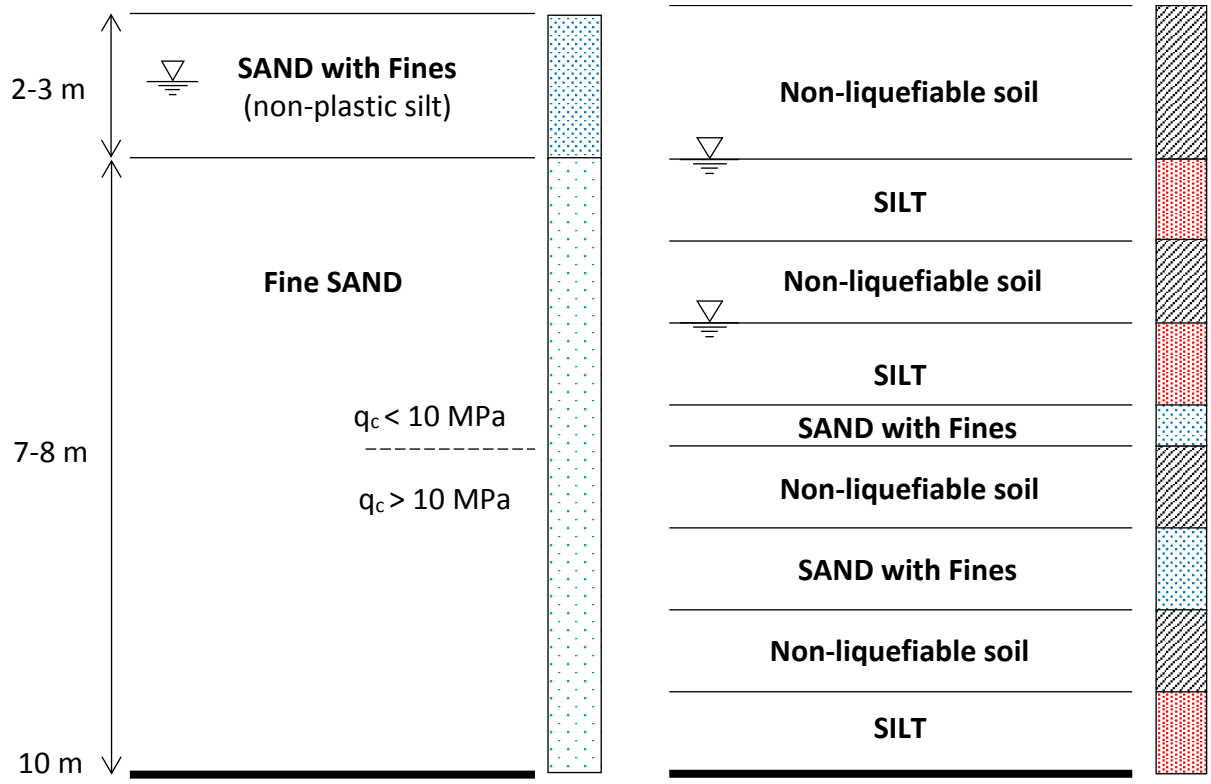

Uniform sandy deposit:
- All layers liquefiable
- Uniform and continuous sand layers
- Predominantly fine sand
- Liquefied in both September 2010 and February 2011 earthquakes

Thinly interlayered deposit:
- Highly stratified
- Vertically discontinuous profile
- Sequence of silt, silty sand and non-liquefiable layers; absence of clean sand
- Did not manifest liquefaction in September 2010 earthquake; liquefaction either manifested or not in February 2011 earthquake

Figure 4.9: Outline of two characteristic soil profiles in Christchurch

4.3.1 Yes/Yes group 1 (YY1) soil profile characterisation

The YY1 representative profile was characterised by four YY sites that were identified as having similar profiles. YY1 was established based on the density and soil type present throughout the deposit using these four sites and the simplified profiles established in Section 4.2. Initially, this was done as a continuation of the critical layer analysis by analysing plots of the ratio of $CRR_{7.5}$ (for 100 kPa confining stress) in each layer to $CRR_{7.5\,(CL)}$ in the critical layer, where $CRR_{7.5}$ was calculated using Boulanger and Idriss (2014). The $CRR_{7.5}$ ratio plots for the four sites in YY1 are illustrated in Figure 4.10. From this analysis, layers of constant $CRR_{7.5}$ ratio could be identified. This process was initially adopted as it gave a good indication of relative liquefaction resistance throughout the deposit, and because it enabled the soil profile to be defined in terms of the critical layer. In this process, some of the extreme data points (such as at 3.5 m and 5.4 m in Figure 4.10) were ignored to give more uniform and representative values.

Once a general soil profile was established from the $CRR_{7.5}$ ratios, it became imperative to define the soil layers that were not critical in a rigorous manner that could be used in the ESA. As it is a good indicator of soil density, q_{c1Ncs} was used for this purpose. In a similar manner to the $CRR_{7.5}$ ratios, q_{c1Ncs} was determined for each soil layer and plotted throughout the depth of the deposit for each of the four identified sites. From these plots, a range of q_{c1Ncs} values was identified as shown in Figure 4.11. Upper and lower bound lines were used to constrain the data to a general trend that could be used to easily identify a characteristic range of values for each layer.

As a result of this analysis, the YY1 profile shown in Figure 4.12 was established. This profile is characterised as a relatively thick continuous sandy deposit with the critical layer located immediately below the water table at 1.8-3.8 m depth followed by layers of low liquefaction resistance that continued until 6 m depth. Hence, the critical zone for this profile was substantial and extended from 1.8 m to 6 m depth. This top 6 m of liquefiable material generally had higher I_c values and lower q_c values than deeper layers indicating the presence of fine sand or some silty material in the shallow part of the deposit. The soil from 6 m to 10 m depth was coarser grained sand and generally denser than the critical zone. For the purpose of the finite-element ESA, discrete layers of uniform q_{c1Ncs} were identified for layers between 1.8-3.8 m, 3.8-6 m, 6-9 m and 9-10 m depth, as shown in Figure 4.12.

As a range of q_{c1Ncs} values had been identified for each layer, a sensitivity study was conducted to assess the effect of uncertainty in q_{c1Ncs} on liquefaction resistance. The upper and lower bound values identified in Figure 4.11 were input to the Boulanger and Idriss (2014) $CRR_{7.5}$ vs q_{c1Ncs} relationship to determine an upper and lower bound on $CRR_{7.5}$ as illustrated for the layer 3.8-6 m in

Figure 4.13. The range of q_{c1Ncs} for the layer was 80-105 (Figure 4.11) which gave a range of $CRR_{7.5}$ of 0.12-0.14 (Figure 4.13). As a result, a $CRR_{7.5}$ and associated q_{c1Ncs} value of 0.13 and 90 respectively was chosen to represent this soil layer. This process was repeated for the remaining soil layers and the results of the interpretation are summarised in Figure 4.12 and Table 4.3. The q_{c1Ncs} value adopted was not always the median or average value of the layer, instead these values were chosen based on judgement of what were the most appropriate values to best model the representative YY1 soil profile. The soils above the water table were considered non-liquefiable in the sense that they do not generate excess pore pressures due to cyclic shearing, but they do allow for the generation of excess pore water pressures due to ground water flow. These layers were modelled with the same parameters as the layer of highest liquefaction resistance (q_{c1Ncs}=140). Under the low confining stress and high q_{c1Ncs} liquefaction would not develop due to cyclic shearing in these layers.

Table 4.3: q_{c1Ncs} and $CRR_{7.5,100kPa}$ values adopted for use in the ESA for each layer within the YY1 profile

Layer	q_{c1Ncs} range	$CRR_{7.5,100kPa}$ range	adopted q_{c1Ncs}	adopted $CRR_{7.5,100kPa}$
0-1.8 m	80-155	0.12-0.33	140	0.24
1.8-3.8 m	75-95	0.11-0.13	80	0.12
3.8-6 m	80-105	0.12-0.14	90	0.13
6-9 m	95-130	0.13-0.20	115	0.16
9-10 m	90-170	0.13-0.50	140	0.24

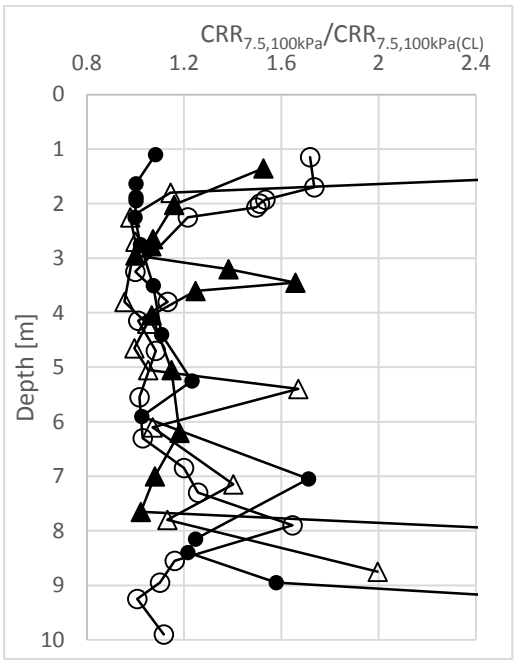

Figure 4.10: $CRR_{7.5,100kPa}$ ratios for four soil profiles in YY1

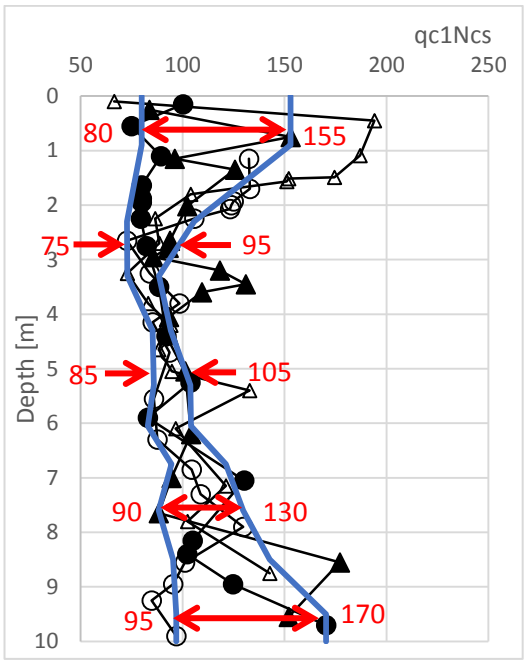

Figure 4.11: q_{c1Ncs} values for sites used to characterise YY1

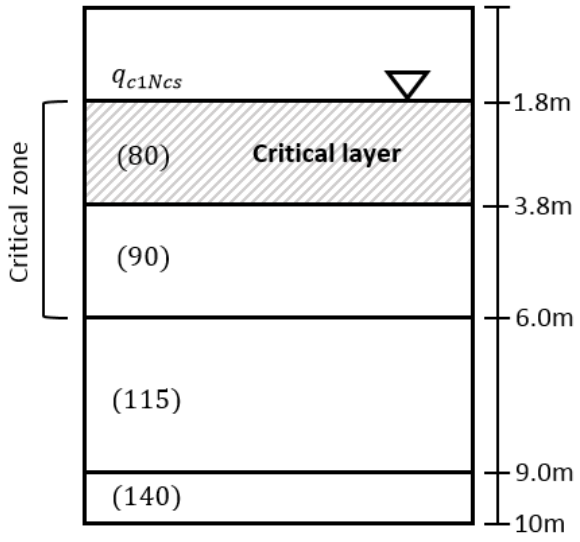

Figure 4.12: Simplified representative soil profile for YY1

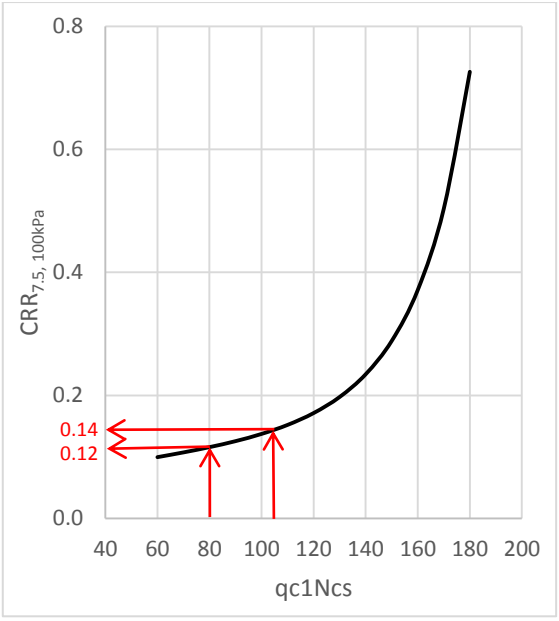

Figure 4.13: Variation in $CRR_{7.5,100kPa}$ due to uncertainty in q_{c1Ncs} values for a given layer

4.3.2 Yes/Yes group 2 (YY2) soil profile characterisation

The YY2 profile was characterised in the same manner as YY1. Six sites from the YY category were chosen as representative of the YY2 profile and used in the characterisation process. $CRR_{7.5}$ ratios were calculated to establish the general profile, and then an analysis of the q_{c1Ncs} values in the deposit was conducted to characterise each soil layer. The q_{c1Ncs} analysis is shown in Figure 4.14 and the resulting soil profile in Figure 4.15. As more sites were considered in the characterisation of YY2 (compared to YY1), there was larger scatter in the q_{c1Ncs} of the YY2 profiles, see Figure 4.14. The soil parameters used to characterise each layer are summarised in Table 4.4

The YY2 profile differed from YY1 in that the density of the deposit increased much more rapidly below the critical layer. YY2 consisted of a critical layer immediately below the water table from 1.8-2.5 m, however the critical zone of low liquefaction resistance was much thinner than for YY1, from 1.8-4.0 m. From 4-10 m the YY2 profile consisted of sandy soil of relatively high density, showing more rapid increase in density with depth than YY1. The adopted q_{c1Ncs} values for ESA modelling are summarised in Table 4.4.

Table 4.4: q_{c1Ncs} and $CRR_{7.5,100kPa}$ values adopted for use in the ESA for each layer within the YY2 profile

Layer	q_{c1Ncs} range	$CRR_{7.5,100kPa}$ range	adopted q_{c1Ncs}	adopted $CRR_{7.5,100kPa}$
0-1.8 m	90-125	0.13-0.18	140	0.23
1.8-2.5 m	75-95	0.11-0.13	85	0.12
2.5-3.2 m	85-110	0.12-0.15	95	0.13
3.2-4 m	95-130	0.13-0.20	115	0.16
4-6.8 m	115-140	0.16-0.23	125	0.18
6.8-8.5 m	120-155	0.17-0.33	135	0.21
8.5-10 m	130-160	0.20-0.37	140	0.23

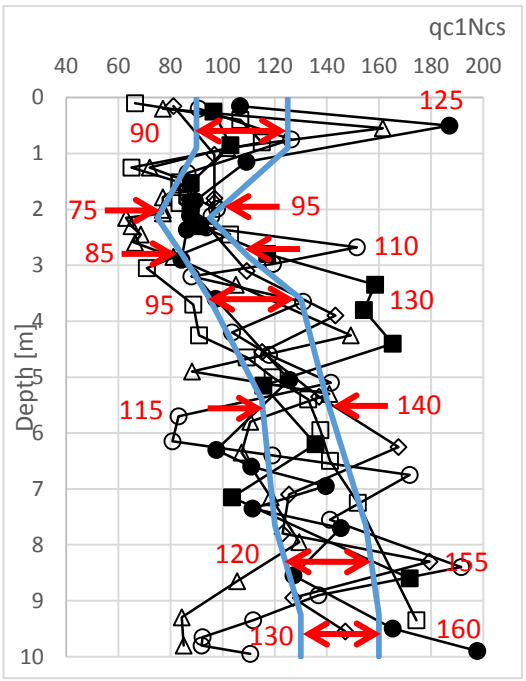

Figure 4.14: q_{c1Ncs} values for sites used to characterise YY2

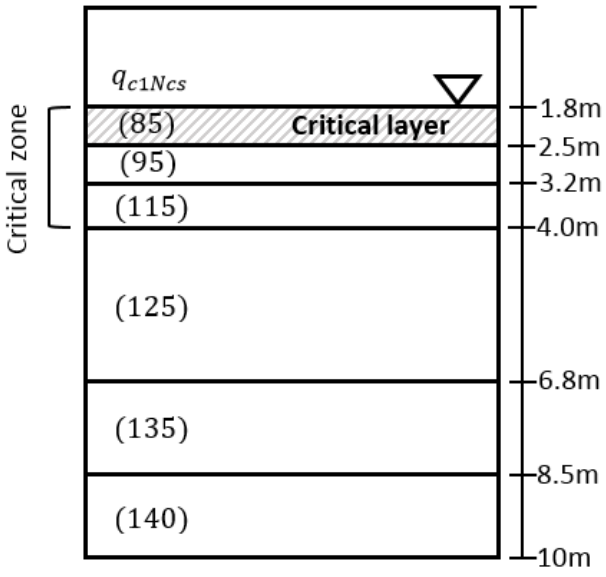

Figure 4.15: Simplified representative soil profile for YY2

4.3.3 No/No group 1 (NN1) soil profile characterisation

The NN sites were characterised in a slightly different manner to the YY sites. These were more variable in geometry so it was more difficult to develop generalised soil profiles based on multiple q_{c1Ncs} traces. Instead, the sites were first grouped into two groups based on their general characteristics, and then representative site(s) from each group were considered in the development of the two representative NN profiles.

The NN1 sites were developed to be representative of soil profiles observed in Papanui. Two sites were chosen as representative of this area and were used in characterising the NN1 profile. These were located at 455 Papanui Road and 70 Langdons Road, their simplified profiles can be found in the electronic supplement. From these two sites, a simplified profile was determined based on the

number, thickness and location of the non-liquefiable layers. In this manner, NN1 was determined to consist of two non-liquefiable layers; one directly below the ground water table at 1.6-2.5 m and the other a very thick layer at 4-8.5 m. The thicker non-liquefiable layer and a single critical layer were the key features of the NN1 profile. The non-liquefiable layers were interlaid by liquefiable layers of very low liquefaction resistance. This generalised NN1 profile is illustrated in Figure 4.16.

The liquefiable layers were characterised by q_{c1Ncs} as for the YY profiles. To do this, representative I_c and q_c values were identified for the relevant layers from the two sites, then q_{c1Ncs} was calculated using Boulanger and Idriss (2014). The soils above the ground water table were given the same soil parameters as in the YY cases as they were not expected to liquefy. The non-liquefiable layers were characterised by V_s values which were also determined from the field tests at the two sites. The properties of all soil layers in the NN1 profile are summarised in Table 4.5.

Table 4.5: q_{c1Ncs} and V_s values adopted for use in the ESA for each layer within the NN1 profile

Layer	I_c	q_c (MPa)	V_s (m/s)	adopted q_{c1Ncs}
0-1.6 m	2.2-2.6	1.5-3.5	(1)	140
1.6-2.5 m	> 2.6	(1)	150	(1)
2.5-4.0 m	1.8-2.2	2.0-5.0	(1)	80
4.0-8.5 m	> 2.6	(1)	110	(1)
8.5-9.2 m	1.9-2.0	4.0-7.0	(1)	90
9.2-10 m	2.4	2.5	(1)	80

(1) Not required for the purposes of ESA modelling

4.3.4 No/No group 2 (NN2) soil profile characterisation

The NN2 profile was developed in the same manner as the NN1 profile, and was to be representative of soil profiles in the Riccarton suburb. NN2 consisted of finer interlayering of liquefiable and non-liquefiable layers than NN1, and was the most difficult to characterise due to the highly stratified nature. Therefore, only a single site (at Paeroa Reserve, Riccarton, see electronic supplement for simplified profile) was chosen to represent similar profiles and it was this site that was modelled as NN2. The NN2 profile is characterised by highly interbeded and relatively thin non-liquefiable and liquefiable layers, including multiple critical layers. The soil parameters were determined in the same manner as for the NN1 site. First, the number and distribution of non-liquefiable layers were determined, then the properties of liquefiable layers assigned based on q_c and I_c values, and properties of non-liquefiable layers assigned based on the V_s at the representative site in Riccarton.

The NN2 profile consisted of five non-liquefiable layers with no soil layers thicker than 1.5 m. The critical layers (of lowest liquefaction resistance) were located at 2.3-2.8 m, 3.6-4.5 m and 7-7.7 m.

The density of the liquefiable layers generally tended to increase with depth. On the other hand, the V_s of the non-liquefiable layers decreased with depth with a maximum value near the surface (this was a characteristic of the specific site chosen to model NN2). As for all previous profiles, soils above the ground water table were assigned properties consistent with high q_{c1Ncs}. The NN2 profile is summarised in Figure 4.17 and all key soil properties are outlined in Table 4.6.

Table 4.6: q_{c1Ncs} and V_s values for use in the ESA for each layer within the NN2 profile

Layer	I_c	q_c (MPa)	V_s (m/s)	adopted q_{c1Ncs}
0-1.1 m	1.8-2.4	4.5-10	(1)	140
1.1-2.3 m	> 2.6	(1)	200	(1)
2.3-2.8 m	2.3	1.5	(1)	80
2.8-3.6 m	> 2.6	(1)	190	(1)
3.6-4.5 m	2.1-2.4	1.5-3.0	(1)	80
4.5-5.1 m	> 2.6	(1)	120	(1)
5.1-5.8 m	2.0	4.5	(1)	95
5.8-7.0 m	> 2.6	(1)	150	(1)
7.0-7.7 m	2.2-2.5	1.8-3.0	(1)	80
7.7-8.5 m	> 2.6	(1)	150	(1)
8.5-10 m	1.7-2.0	5.5-11	(1)	115

(1) Not required for the purposes of ESA modelling

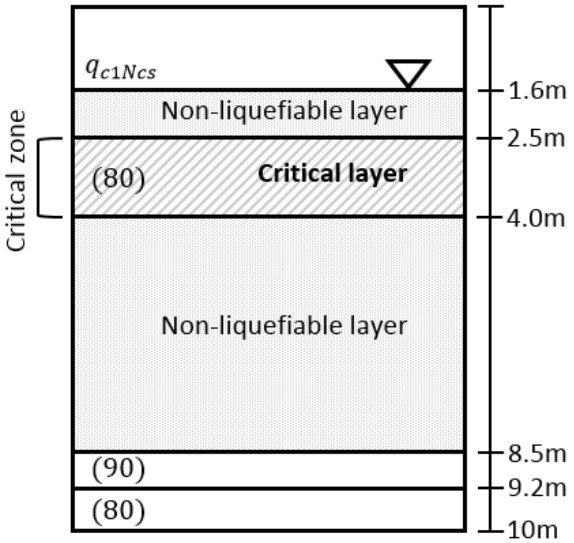

Figure 4.16: Simplified representative soil profile for NN1

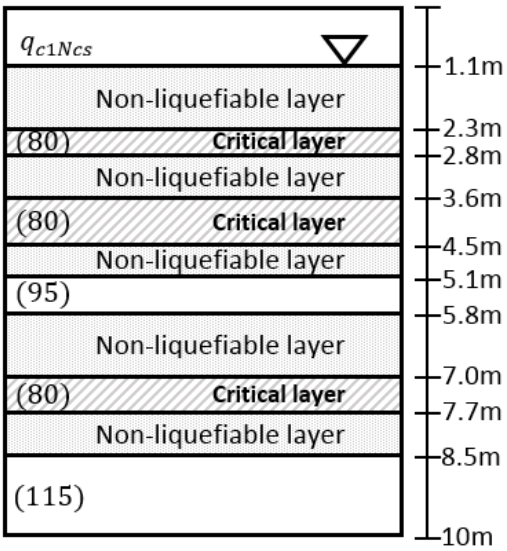

Figure 4.17: Simplified representative soil profile for NN2

4.3.5 Summary

Four representative profiles were defined; YY1 and YY2 to represent the sites that manifested liquefaction in both the September 2010 and February 2011 earthquakes, and NN1 and NN2 to represent the sites that did not manifest liquefaction in either event. The YY profiles were characterised by thick uniform and continuous sandy deposits with critical layers located directly below the water table. The difference between YY1 and YY2 was the thickness of the critical zone and the rate at which soil density increased below the critical zone. YY1 had a thicker critical zone (4.2 m) than YY2 (2.2 m) and lower densities (and therefore lower liquefaction resistance) in the layers below the critical zone.

The NN profiles were highly non-uniform and were characterised by interlayered liquefiable and non-liquefiable layers. NN1 consisted of two non-liquefiable layers, one directly below the water table (1.6-2.5 m) and the other – the key feature of the NN1 profile – located at 4-8.5 m. The NN2 profile was more highly stratified with five non-liquefiable layers (of thickness ≤ 1.5 m) throughout the top 10 m of the deposit. The liquefiable layers in both NN1 and NN2 were characterised by low liquefaction resistances, similar to those of the critical layers in the YY profiles. In the following chapter, numerical models of these four profiles are developed for the ESA.

5 Element Test Simulations

For the Effective Stress Analysis (ESA) of the soil deposits, a time-history 1-D soil-column analysis is performed. In the analysis, an input ground motion is defined at the base of the model and the soil profile is modelled with a series of soil elements representing the layers and sub-layers in the profile. For each soil element, properties of the soil are defined for the constitutive model. The input ground motion was established through deconvolution, as described in in Chapter 3, and soil characteristics were defined for four representative profiles (YY1, YY2, NN1, NN2) in Chapter 4. In this chapter, the soil properties for each sub-layer will be established through element test simulations and details of the numerical model will be defined.

The particular constitutive model used in this study is the Stress-Density Model (S-D Model) developed in Cubrinovski and Ishihara (1998a; 1998b). The S-D Model is an elastic-plastic constitutive model specifically tailored for liquefaction problems. It is a state-concept based model that accounts for the combined effects of density and confining stresses through the state-concept framework.

Soil properties required for the constitutive model fall into four categories: state index parameters (used to define the state of the soil relative to the reference state, the critical state line), plastic stress-strain parameters (defining the shear stress-shear strain relationship), elastic stress-strain parameters (determining the stress-strain relationship over the elastic range of deformation) and stress-dilatancy parameters (providing the link between the plastic shear strains and plastic volumetric strains). The S-D Model parameters are usually determined through a series of laboratory tests, or based on a combined use of empirical relationships and generic data for the liquefaction resistance of sandy soils. For this research, the second approach has been adopted. Christchurch soils were modelled using model parameters established from laboratory tests on Toyoura sand, and these parameters were then modified so that the model was able to simulate the target liquefaction resistance as defined by the semi-empirical triggering procedure of Boulanger and Idriss (2014), referred to as BI2014 in the following. This calibration process, through element-test simulations, is presented in this chapter for the characteristic soil properties identified in Chapter 4.

5.1 Methodology

The ESA was conducted on a 1-D soil column model as illustrated in Figure 5.1. The ground motion as established through deconvolution of surface recorded motions in Chapter 3 was defined as an input at the base of the soil column. The soil profiles, established in Chapter 4, are represented in

the model as a series of elements with each element defined by a set of soil parameters. These soil parameters, together with the relationships established in the constitutive model, define the dynamic behaviour of the soil when subjected to the input ground motion. In the analyses, simple shear conditions were enforced by tying the nodes of the left-boundary to share identical horizontal and vertical displacements with the corresponding nodes of the right-boundary of the soil column model. This boundary condition enforced zero lateral strain, or simple shear mode of deformation, for all elements of the soil-column.

Element test simulations are conducted to calibrate the constitutive model and identify specific soil properties in each element of the model depending on the soil composition, density of the soil and vertical overburden stress. In the element test simulations, a single soil element is subject to a series of uniform-amplitude cyclic loadings of varying magnitude. From each simulation, the number of load cycles required to initiate liquefaction (defined as 5% double amplitude shear strain) is determined. Running a number of element test simulations using different magnitudes of shear stress (i.e. changing the cyclic-stress-ratio, *CSR*) enables a Liquefaction Resistance Curve (LRC) to be established. This process is schematically illustrated in Figure 5.2.

For the element test simulations, a target LRC is required to represent the liquefaction resistance of a given layer (i.e. *CSR*-N_c combinations required to cause liquefaction). Target LRCs for each soil element were developed using BI2014. The constitutive model was then calibrated to reproduce this liquefaction resistance by modifying some of the stress-dilatancy parameters of the S-D Model. This is achieved primarily through changing the parameters controlling the density of the soils (*e*, the void ratio of the soil), and the dilatancy parameters μ_{cyc} (the minimum μ after the reversal in cyclic loading) and S_c (Cubrinovski and Ishihara, 1998b). Changing S_c and μ_{cyc} together controls the vertical position and slope of the LRC (whereas only changing S_c moves the LRC vertically). In this manner, the liquefaction resistance of a soil can be changed in the model without changing any other material parameters. This process allows calibration of the constitutive model for use in an ESA with specific target LRCs. An ESA was then performed using a finite element and two-phase formulation based on Biot's theory for a porous medium.

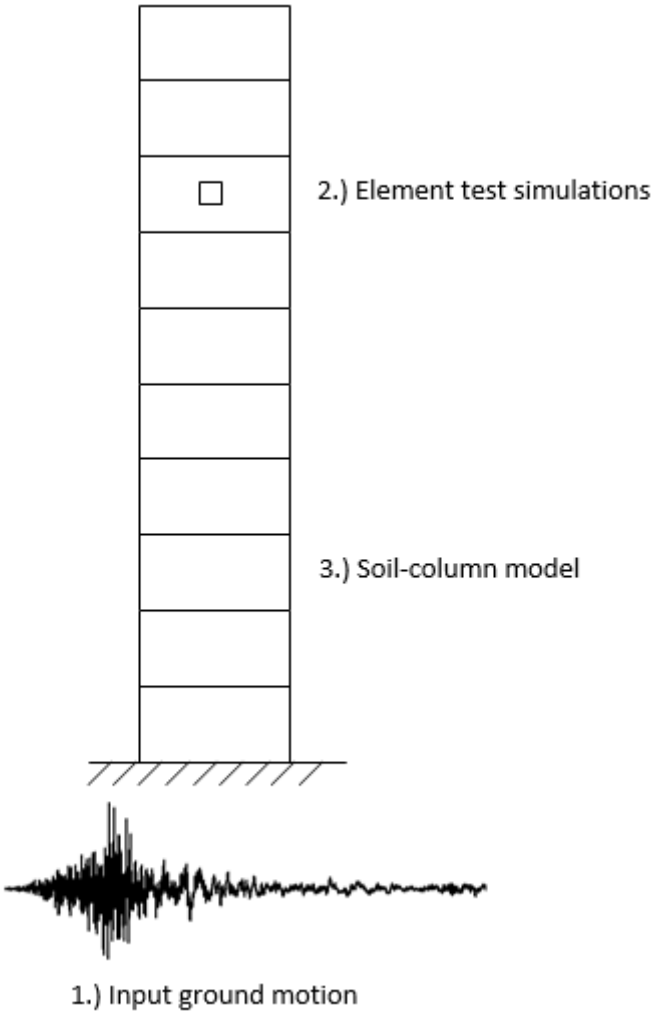

Figure 5.1: Schematic of the methodology used to calibrate soil parameters for the 1-D soil column model

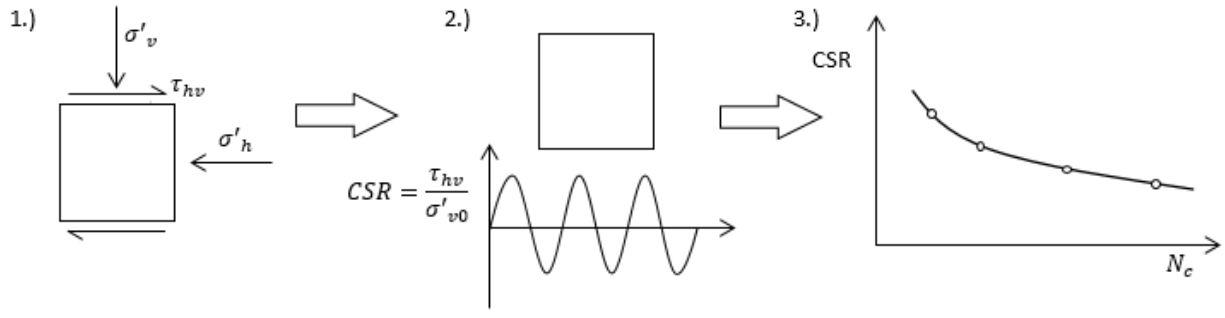

Figure 5.2: Schematic illustration of the concept of element test simulations

5.2 Modelling liquefiable layers

5.2.1 Determination of target liquefaction resistance curves

The target LRCs were developed using BI2014. There are two components of an LRC, the vertical position of the curve in the *CRR*-N_c plot, and the slope of the curve. To model the LRCs, two fundamental relationships in the simplified method need to be combined; the $CRR_{7.5,100\ kPa} - q_{c1Ncs}$ and *MSF*-M_w relationships. The former defines the vertical position of the LRC through the parameter $CRR_{7.5,100kPa}$, the liquefaction resistance for a magnitude 7.5 earthquake (or the *CSR* required to trigger liquefaction in 15 equivalent cycles) and an effective vertical stress of 100 kPa. The latter relationship defines the slope of the LRC through the Magnitude Scaling Factor (*MSF*).

The target curves were calculated using the following process and the BI2014 method:

1. Determine q_{c1Ncs} from the soil profile analysis (as detailed in Chapter 4)
2. For a given q_{c1Ncs}, calculate $CRR_{7.5,100kPa}$ using Equation 5.5

$$CRR_{7.5,100kPa} = f(q_{c1Ncs}) \quad \textbf{5.1}$$

3. For the adopted q_{c1Ncs} and earthquake magnitude associated with the input motion, calculate *MSF* using Equations 5.6 and 5.7

$$MSF = f(M_w, q_{c1Ncs}) \quad \textbf{5.2}$$

4. Calculate *CRR* using $CRR_{7.5,100kPa}$ and *MSF* from Steps 3 and 4

$$CRR = CRR_{7.5,100\text{kPa}} \cdot MSF \quad \textbf{5.3}$$

5. Calculate N_c corresponding to *MSF* using Equation 5.8 and the relationship between *MSF* and *b* (slope of LRC in *CRR*-N_c plot) shown in Figure 5.3

$$N_c = f(MSF, b) \quad \text{and} \quad b = f(MSF_{max}) \quad \textbf{5.4}$$

6. Extrapolate the *CRR* curves in log-log space so as not to be constrained by the MSF_{max} cut-off values imposed in BI2014
7. Plot resulting LRCs

First, $CRR_{7.5,100kPa}$ was established for the specific values of q_{c1Ncs} to be modelled. This sets the value of the LRC at 15 equivalent cycles, and therefore sets the height of the curve as per Equation 5.5.

$$CRR_{7.5,100kPa} = \exp\left(\frac{q_{c1Ncs}}{113} + \left(\frac{q_{c1Ncs}}{1000}\right)^2 - \left(\frac{q_{c1Ncs}}{140}\right)^3 + \left(\frac{q_{c1Ncs}}{137}\right)^4 - 2.8\right) \quad \textbf{5.5}$$

Next, *MSF* was determined as a function of q_{c1Ncs} and earthquake magnitude (Equations 5.6 and 5.7). A range of earthquake magnitudes of M_w 5.5-9.5 were used in establishing the LRC.

$$MSF = 1 + (MSF_{max} - 1)\left(8.64 \exp\left(\frac{-M_w}{4} - 1.325\right)\right) \quad \textbf{5.6}$$

$$MSF_{max} = 1.09 + \left(\frac{q_{c1Ncs}}{180}\right)^3 \leq 2.2 \quad \textbf{5.7}$$

As LRCs are generally presented in the *CSR*-N_c (number of equivalent cycles to liquefaction) plot, the final step was to determine the number of equivalent cycles (N_c) for the earthquake magnitudes chosen to be modelled. This was established using Equation 5.8, where $N_{M=7.5}$=15, and the parameter *b* as determined from Figure 5.3 as a function of MSF_{max} (Equation 5.7).

$$N_M = \frac{N_{M=7.5}}{MSF^{1/b}} \quad \textbf{5.8}$$

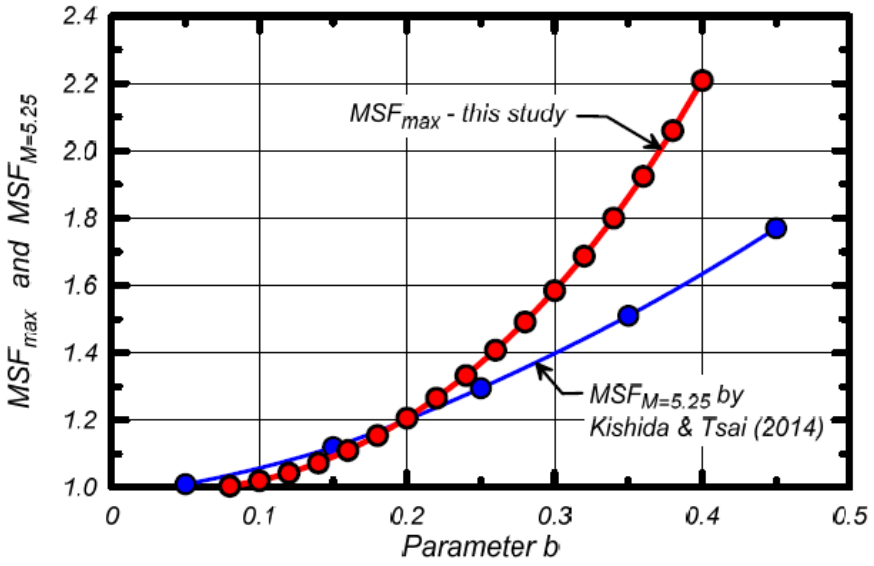

Figure 5.3: Relationship between MSF_{max} and *b* value used in calculation of N_c for LRCs (Boulanger and Idriss, 2014)

The use of MSF_{max} in the calculation of *MSF* puts a limit on N_c by restricting the range of magnitudes that are considered in the simplified method. This limitation was relaxed for the purpose of modelling the target LRCs since it is inconsistent with trends observed in laboratory tests. Instead, the calculated LRCs were computed over values of N_c=2-50 cycles. The LRC can be approximated by a linear plot in log-log space, and the gradient of this line is defined by the parameter *b*. The resulting LRCs for YY1, obtained following the above procedure, are shown in Figure 5.4 (similar target curves for the liquefiable layers in YY2, NN1 and NN2 can be found in Appendix H).

The curves in Figure 5.4 are for an overburden stress of 100 kPa. To account for the effect of confining stress, the effective stress for the given element and its respective depth in the soil column model was calculated, then the corresponding LRC at 100 kPa (the curves shown in Figure 5.4) was corrected for the effects of the effective overburden stress using the K_σ correction factor. K_σ was calculated following BI2014 as outlined in Equations 5.9 and 5.10. In this way, the LRCs for the elements in the soil-column model representing liquefiable soils were established. These LRCs were then used as target curves in the model calibration through element test simulations, as described in the following section.

$$K_\sigma = 1 - C_\sigma \ln\left(\frac{\sigma'_v}{p_a}\right) \leq 1.1 \quad \textbf{5.9}$$

$$C_\sigma = \frac{1}{37.3 - 8.27(q_{c1Ncs})^{0.264}} \leq 0.3 \quad \textbf{5.10}$$

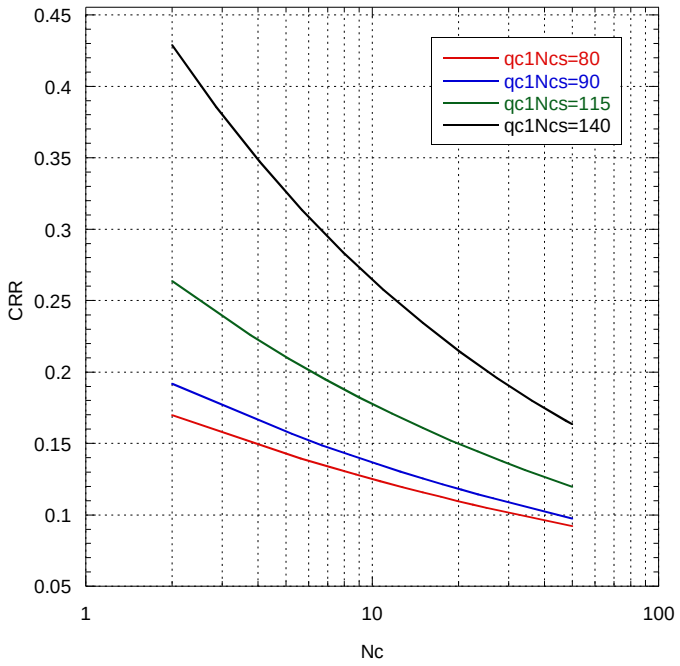

Figure 5.4: Liquefaction resistance curves for YY1 liquefiable soils at 100 kPa

5.2.2 Model simulation of target liquefaction resistance curves

The following approach was adopted in the element test simulations for determination of the constitutive model parameters:

(i) S-D Model parameters already established for Toyoura sand (Cubrinovski and Ishihara, 1998a; 1998b) were used as the initial set of model parameters

(ii) The void ratio was selected to provide an appropriate vertical position of the LRC in the simulated *CRR*-N_c plot (consistent with the target curves)

(iii) Two dilatancy parameters were modified to further adjust the vertical position and slope of the simulated LRC

In the above process, the void ratio was used to account for different densities of soil. This was the only modification needed to model the higher density soils (e.g. q_{c1Ncs}=140). Slight changes in the dilatancy parameter μ_{cyc} were then used to rotate the LRC to achieve the flatter slope of the target curves for the lower density soils (q_{c1Ncs}=80-115). Finally, the other dilatancy parameter, S_c was used to make fine adjustments to the height of the LRC if needed. In this way, the LRC produced by the model was adjusted to fit the target LRC defined in Section 5.2.1.

In the modelling process it was important that a void ratio greater than, or too close to, the upper reference line in the Critical State Line (CSL) was not modelled as this would locate the initial state of the soil above its CSL, which was deemed unrealistic for the in situ state of the soils considered. The void ratios used in the S-D Model simulations ranged between e=0.70 and e=0.86 for the normalised penetration resistances of q_{c1Ncs}=140 and q_{c1Ncs}=80 respectively. The results of the simulations are shown in Figure 5.5 for YY1 soils, where the solid lines indicate the target curves and the symbols (and dashed lines) indicate the S-D Model simulations. The simulations for the liquefiable layers in the YY2, NN1 and NN2 profiles are shown in Appendix I.

Once the target LRCs had been modelled to an appropriate level of accuracy, the model parameters developed through the element test simulations were used as input into the ESA in the form of material cards for the constitutive model. Each soil element was assigned a particular material card with the appropriate model parameters depending on the q_{c1Ncs} and σ'_{v0} values for the soil and the respective element in the analysis.

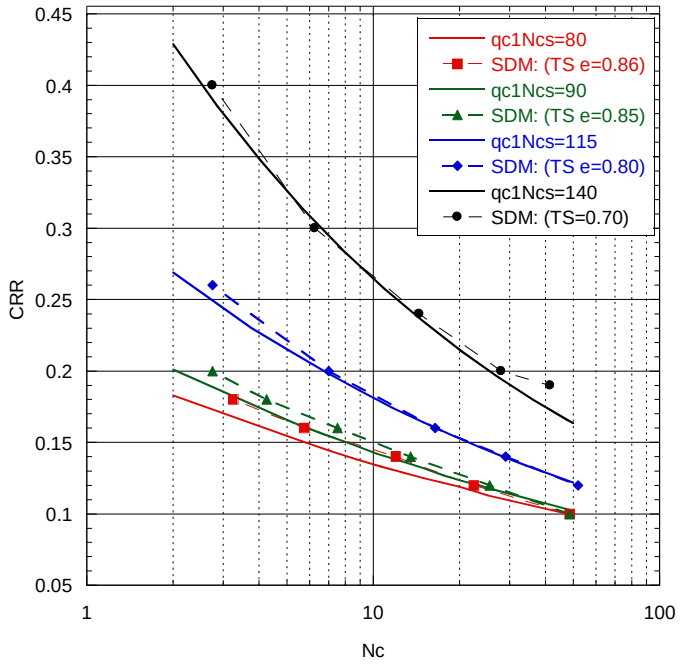

Figure 5.5: S-D Model (SDM) LRCs (symbols and dashed lines) and target LRCs (solid lines) for YY1 soils of different densities

5.3 Non-liquefiable layers

Non-liquefiable layers were also modelled using Toyoura sand properties as the basis but in a total stress model (i.e. without pore pressure generation). There were two types of non-liquefiable layers to model; soils that could not liquefy due to high plasticity (i.e. $I_c \geq 2.6$), and soils below 10 m depth. The latter were assumed non-liquefiable in order to simplify the analysis and its interpretation, as the soil below 10 m depth was considered of less importance in an analysis that focussed on the damaging effects of liquefaction and its manifestation at the ground surface. Deeper soil layers generally have higher density (due to the higher overburden stresses) and greater age which gives them a lower liquefaction susceptibility. This, coupled with the greater depth, means that even if liquefaction does occur in deeper layers it is unlikely to manifest on the surface.

5.3.1 Determination of target degradation curves

To model the non-liquefiable layers, two target modulus degradation ($G/G_0 - \gamma$) curves were established, one for the silty soils in the NN profiles and the other for sandy soils at a depth greater than 10 m. To model a specific soil layer, the appropriate curve was then adjusted for the relevant depths and confining stresses.

The target degradation curves were modelled using the modified formulation of Darendeli (2001; Yee et al., 2013; Markham, 2015) outlined in Chapter 3. The Darendeli degradation curves tend to

underestimate the strength of soil at large strains. The modified formulation used herein adjusted the curve for γ > 0.01%, this had the effect of lifting the tail of the degradation curve at these higher shear strain levels. Additional modifiers (as per Darenedeli 2001) were applied to the silty soil. These modified the reference strain (γ_r) as shown in Equations 5.11 and 5.12 using the specific parameters for silty soils listed in Equation 5.13.

$$\gamma_r = \left(\phi_1 + \phi_2 \cdot PI \cdot OCR^{\phi_3}\right) \cdot {\sigma'_{v0}}^{\phi_4} \quad \textbf{5.11}$$

$$\alpha = \phi_5 \quad \textbf{5.12}$$

$$\phi_1 = 0.0416 \quad \textbf{5.13}$$

$$\phi_2 = 0.000689$$

$$\phi_3 = 0.321$$

$$\phi_4 = 0.280$$

$$\phi_5 = 1.0$$

The key parameters to model the target curves were the soil mass density (ρ), and OCR and PI for the layers with $I_c \geq 2.6$. Soil unit weight was assumed to be 18 kN/m^3 above the water table and 19 kN/m^3 below. The OCR was taken as 1.0 (for normally consolidated soil), and the plasticity index (*PI*) was averaged from available data for the NN sites. This gave a value of 9 above 10 m depth. This was assumed for all layers with I_c > 2.6. Idriss and Boulanger (2008) recommend a *PI* of 7 as the threshold between liquefiable and non-liquefiable soils, so a value of 9 was deemed appropriate for characterisation of the non-liquefiable soils. With the effect of overburden pressure, this produced the target degradation curves for all non-liquefiable soils. Two examples of these curves, for sandy and silty soils respectively, are shown in Figure 5.6.

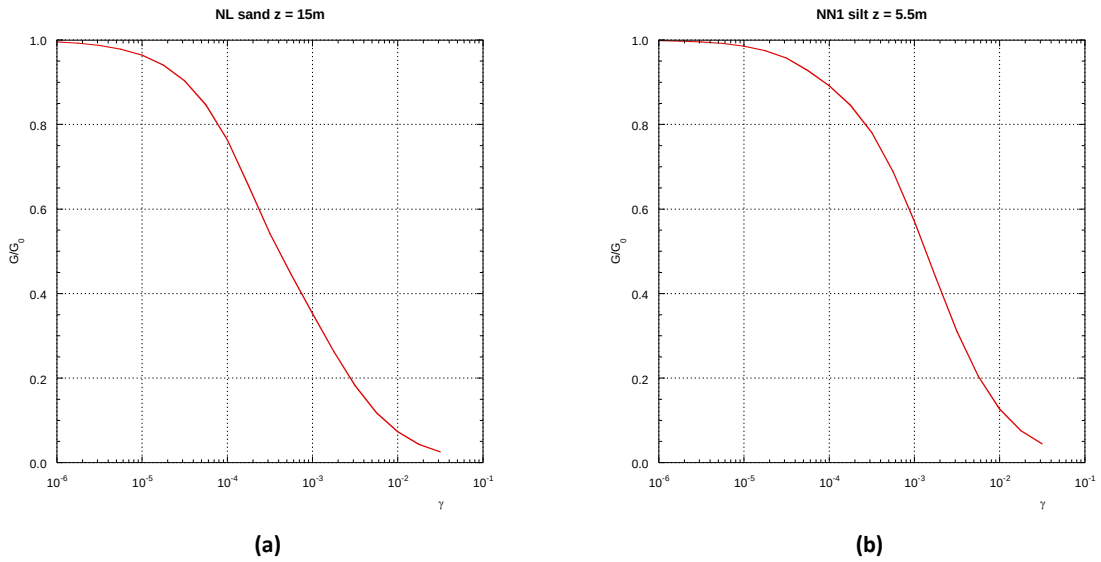

Figure 5.6: Target shear modulus degradation curves for two types of non-liquefiable layers: (a) non-liquefiable sand at *z*=15 m; (b) silt at *z*=5.5 m in NN1 profile

5.3.2 Model simulation of target degradation curves

To model the target degradation curves, the shear-wave velocity (V_s) was used to determine the initial shear modulus, then S-D Model parameters were changed in element test simulations to simulate the correct shape of the target G/G_o - γ relationship using a total stress model under monotonic loading in these element test simulations. V_s above 10 m depth was obtained from the data for the 55 sites, and shear-wave velocity below 10 m depth was determined using the empirical V_s-CPT relationship developed by McGann et al. (2015) (Equation 5.14) and averaging the V_s values for the appropriate sites at the appropriate depths to be modelled.

$$V_s = 18.4 \cdot {q_c}^{0.144} \cdot {f_s}^{0.0832} \cdot z^{0.278} \quad \textbf{5.14}$$

The V_s value was then used to determine G_0, and from this the elastic constant A and modelling parameter $G_{N,\,max}$ (β_3) as follows

$$G_0 = {V_s}^2 \rho \quad \textbf{5.15}$$

$$A = \frac{G_0}{p_a} \quad \textbf{5.16}$$

$$G_{N,max} = \beta_3 = \frac{G_0}{p'} \quad \textbf{5.17}$$

where p_a is the atmospheric pressure and p' is the mean effective stress.

The target curves were modelled by varying the stress ratio ($(\tau/p')_{max}$) (modelling parameter β_1) to achieve the desired shape of the curve. Two examples of the resulting curves are illustrated in Figure 5.7(a) for a non-liquefiable sandy layer and Figure 5.7(b) for a non-liquefiable silt layer (all target and simulated degradation curves are presented in Appendix J). Note that the modelled curves exceed the target curves at small strains, this was not of concern as it was anticipated that shear strains in the simulations would reach or exceed 10^{-3} where model simulations were in good agreement with the target curves.

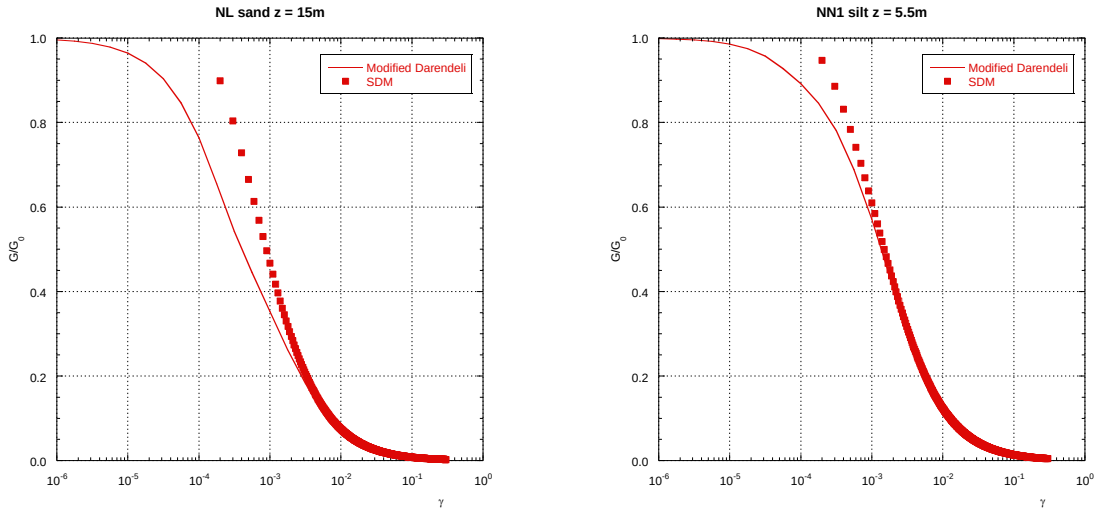

(a) (b)

Figure 5.7: Stress density modelling of degradation curves for (a) non-liquefiable sand at *z*=15 m and (b) silt at *z*=5.5 m in the NN1 profile

5.4 Permeability

The soil in the 1-D soil column ESA is modelled as a two-phase medium, composed of a solid phase and fluid phase. This allows excess pore pressures to be generated in the pore water, and the flow of ground water due to pressure gradients between soil layers. This means that parameters need to be defined for both the solid and fluid phases. For this study, a drained analysis was used for the YY profiles so water could flow between soil elements, hence soil permeability was an important parameter in the ESA. To enable S-D modelling of the non-liquefiable layers in the NN profiles an undrained condition was assumed, and as a result there was no pore water drainage in these analyses.

Permeability values were chosen as representative of each soil type based on the grain size distribution and D_{10} values in particular, as it is well known that fine fractions of grain size control the permeability of soils. The adopted permeability values for the ESA are summarised in Table 5.1 (and in Appendix K for specific soil layers in the YY and NN profiles). As the critical layers generally consisted of siltier soils, lower permeability values were used for these layers. The deeper sandy layers (those below the critical zone) were given higher permeability values increasing from $1x10^{-4}$ to $3x10^{-4}$ corresponding to grain size increase with depth below the water table. The non-liquefiable silt layers in the NN profiles were assigned a lower permeability to represent the more plastic nature of these soils (note that while permeability of the NN profiles was considered, the analysis was conducted using the undrained condition). All soils above the water table were assumed to be silty

and given the corresponding permeability. The values presented in Table 5.1 were used for all four soil profiles, the specific details for each profile are outlined in Appendix K.

Table 5.1: Permeability values adopted for the different soil behaviour types in the YY profiles

Soil Type	I_c	k (m/s)
Fine sand	1.8-2.2	$1x10^{-4}$
Silty sand	2.2-2.6	$4x10^{-6}$
Non-liquefiable	>2.6	$1x10^{-7}$
z > 10m	1.8	$1x10^{-4}$

6 Results

The ESA was conducted with the deconvoluted motions from Chapter 3, soil profiles from Chapter 4 and model parameters from Chapter 5. Simulations for the four representative soil profiles (Chapter 4) were run with three different intensities of ground motion (12 simulations in total). The results were extracted and analysed to identify whether soil layer interaction affected the development of liquefaction. A simplified analysis was also conducted for the same representative profiles and compared to the results from the ESA to see if the simplified method was consistent with the more rigorous ESA in predicting liquefaction in layered deposits. The results from the analyses are presented and discussed in this chapter.

6.1 Input motions

The deconvoluted ground motion at the Canterbury Aero Club strong motion station (CACS) fault normal component for the 22 February 2011 earthquake (Section 3.4), was used as input to the 1-D soil column model. Three scaling factors were applied to this motion to simulate different shaking intensities. These intensities, including adjustments for the source-to-site distance, were:

- a_{max} =0.4g (I_1 = 2.23)
- a_{max} =0.3g (I_2 = 1.67)
- a_{max} =0.2g (I_3 = 1.12)

where a_{max} is the resulting maximum acceleration of the scaled base input motion, and I_x is the applied scaling factor to the CACS deconvoluted motion.

The first ground motion intensity (a_{max} = 0.4g; I_1=2.23) approximately corresponds to the shaking level caused along the Avon River during the February 2011 earthquake, and the third (a_{max} = 0.2g; I_3 = 1.12) corresponds to the respective motions of the 4 September 2010 earthquake. The second shaking intensity (a_{max} = 0.3g; I_2=1.67) was chosen as an intermediate value to give a full illustration of the effects of different ground motion intensities on the dynamic response of the soil deposits considered. In the following, the three intensity levels are also referred to in relative terms as high, intermediate and low shaking intensities.

The February 2011 ground motion contains a specific composition of amplitudes and frequency content, which is of potential concern when using this motion to simulate earthquakes of different magnitudes. When scaling this time history, the motion is scaled on the peak acceleration, which may be significantly higher than the acceleration amplitudes of the main body of shaking. Hence, to

ensure that the scaled ground motions as above were representative of realistic seismic shaking, the computed response in the YY1 analysis to the input ground with I_3=1.12 was compared to the respective YY1 response to the ground motions deconvoluted from both CACS and RHSC using records for the 4 September 2010 earthquake. The results confirmed that the scaling of CACS 22 February 2011 motion was appropriate for the analysis (see Appendix L). Furthermore, the aim of this study was not to accurately simulate the events of the CES, but to investigate the response of different representative soil profiles to realistic seismic excitations which was sufficiently achieved with the CACS-based 22 February 2011 input motion.

6.2 YY1 Analyses

6.2.1 High shaking intensity (a_{max}=0.4g)

The outputs from the 1-D effective stress analyses included time histories of accelerations, displacements, strains, stresses and pore water pressures all computed throughout the deposit. The results from the 1-D analysis on the YY1 profile under a_{max}=0.4g are presented in detail below as an example of the analysis process and to illustrate typical outputs. For further analyses, only summary plots will be discussed.

The YY1 profile was a thick, continuous sandy deposit with a critical zone of low liquefaction resistance from 1.8-6.0 m (see Section 4.3.1). Under the most intense shaking, the whole critical zone liquefied. This is evident from Figure 6.1(a) where the whole critical zone from 1.8 m-6.0 m had an excess pore water pressure ratio of $r_u = u_E / \sigma'_{vo}$ = 1.0 indicating full liquefaction over this depth. Figure 6.1(b) shows the lower layers, which had a slightly higher liquefaction resistance, also developed significant pore water pressures in the range of 70-90% of the initial effective overburden stress. Both figures clearly indicate that liquefaction rapidly developed within 1 or 2 seconds of intensive shaking. Figure 6.2 illustrates the temporal evolution of excess pore water pressures throughout the depth of the deposit. Pore water pressure develops most rapidly in the layer from 2.8-3.8 m, but the whole critical zone has liquefied at 10 s on the time scale. This indicates a severe response to the ground motion and significant damage would be expected from this scenario.

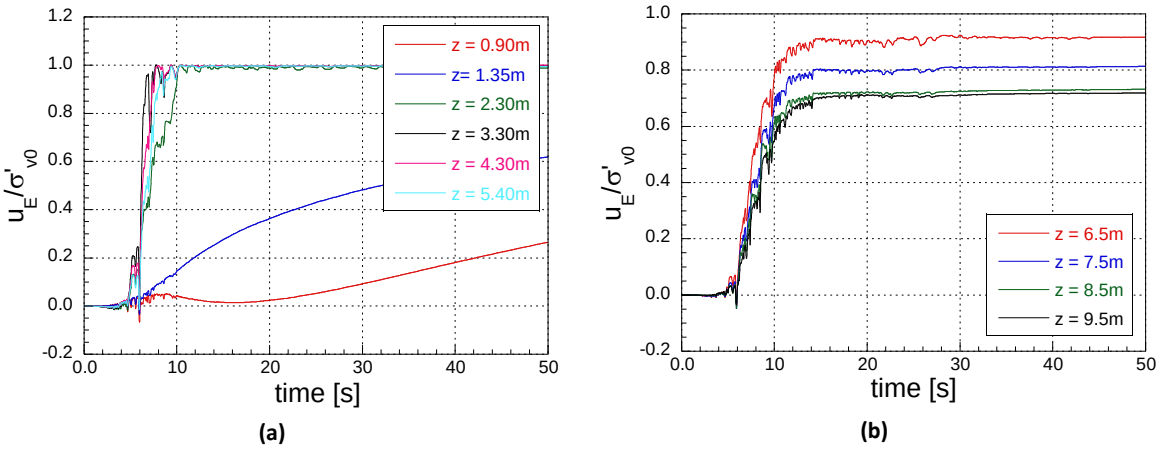

Figure 6.1: Pore water pressure ratio time histories for YY1, a_{max}=0.4g: (a) z = 0-6 m; (b) z = 6-10 m

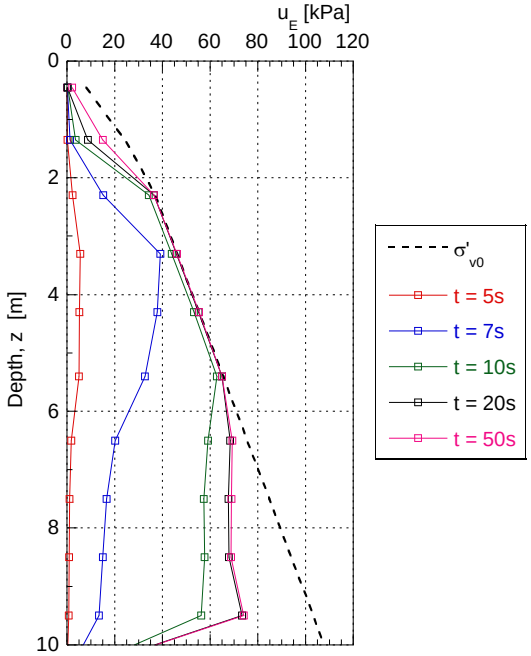

Figure 6.2: Pore water pressure build up with time (YY1, a_{max}=0.4g)

The computed acceleration time history at key locations within the deposit, along with the corresponding pore water pressure ratios at those locations, are illustrated in Figure 6.3 and Figure 6.4. These plots show a reduction of acceleration amplitudes and elongation of the oscillation period of the ground motion in the liquefied layer. This is a key characteristic of the dynamic response of liquefied deposits. The high frequency waves of the ground motion become damped as they pass through the liquefied layer. As peak accelerations often occur at high frequencies, this damping is observed as a decrease in the amplitude of the ground motion. This effect is also observed in the response spectra in Figure 6.5. In the upper layers (z = 0 m and z = 1.8 m) the spectral acceleration has decreased in amplitude at short period motion (T < 0.5s). This affects the

response of the whole soil deposit as shallower layers are being shaken by a lower-amplitude motion than was the input at the base.

This modification of ground motion is observed in the marked decrease in acceleration amplitude from the ground motion at the base of the critical layer (z = 6.0 m) to the top of the critical layer (z= 1.8 m). There is some slight recovery of ground motion amplitude from a depth of 1.8 m to the surface, this is the effect of soft soil response in the layers above the ground water table causing some frequency components to be amplified. This was also observed in the response spectra (Figure 6.5) as an increase in spectral acceleration at longer period motion (around T = 0.5-1.0 s). The distribution of maximum acceleration throughout the deposit is shown in Figure 6.6. Again, this shows a sharp decrease in the peak acceleration in the liquefied layer and some recovery of acceleration amplitudes in the shallow soil layers above the ground water table.

The stress-strain curves at four key points in the deposit (above the ground water table, in the critical zone of liquefaction, directly below the critical zone and in the lower 10 m of the deposit) are illustrated in Figure 6.8. These show the difference in stress-strain behaviour between the liquefied and non-liquefied layers. The non-liquefied layers have higher stiffness and, depending on the strength of the layer, show damping in the development of the hysteresis loop. The liquefied layer on the other hand, shows excessive development of strains and a very flat stress-strain curve once liquefaction has been initiated. The stress-strain curves for all layers in the deposit can be found in Appendix M.

This development of large strains in the critical layer and liquefied zone is also illustrated in the distribution of maximum shear strain with depth in Figure 6.7. The maximum shear strains in the liquefied layers reached approximately 2.6% to 3.8%. In the layers below the liquefied zone (in which substantial excess pore pressures developed) γ_{max} was about 0.5% to 0.9%, as opposed to the relatively low levels of shear strains of less than 0.2% in all layers without significant excess pore water pressures. Figure 6.9 shows time histories of displacements at four depths in the deposit and Figure 6.10 shows the distribution of maximum displacement with depth. The maximum horizontal displacement within the deposit reaches 0.13 m at the ground surface, and most of it is accumulated in the liquefied zone between 1.8 m and 6 m depth. Hence, the extent of liquefaction and the thickness of liquefied layers has a significant influence on the damage induced from an earthquake event. Experience from the Canterbury earthquakes suggests that the location of the liquefied layer relative to the ground surface, or building foundations, is also an important factor for damaging effects of liquefaction (see van Ballegooy et al., 2014; Bray et al., 2014; Cubrinovski et al., 2011).

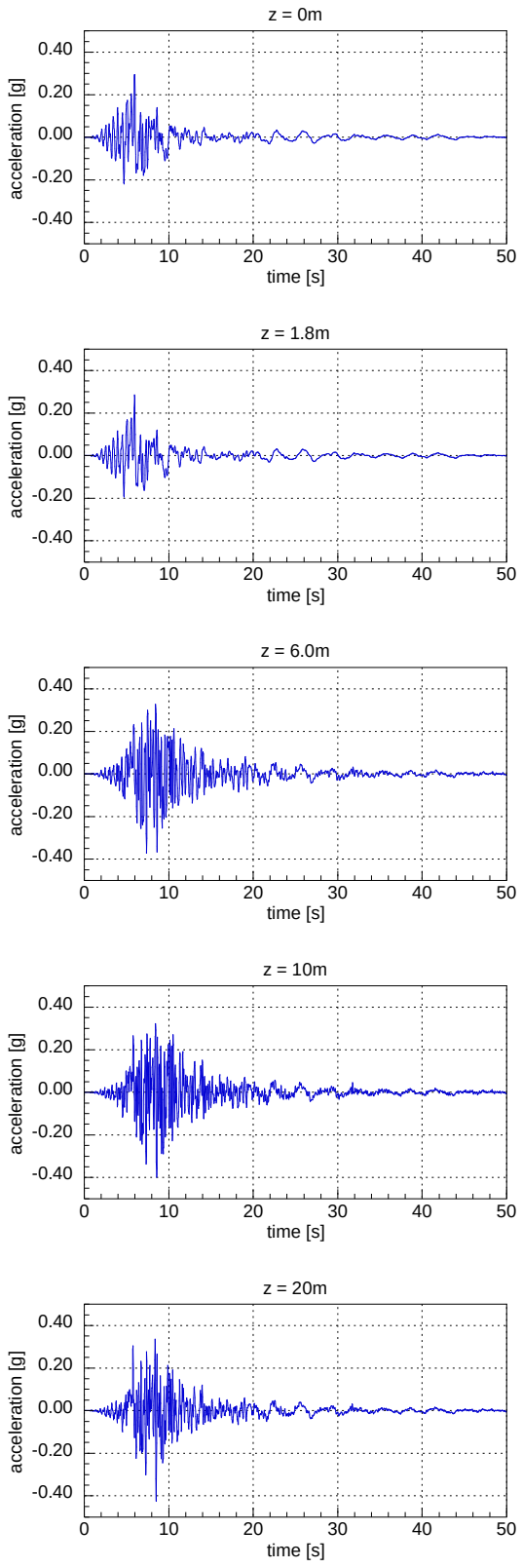

Figure 6.3: Horizontal acceleration time histories throughout depth (YY1, a_{max}=0.4g)

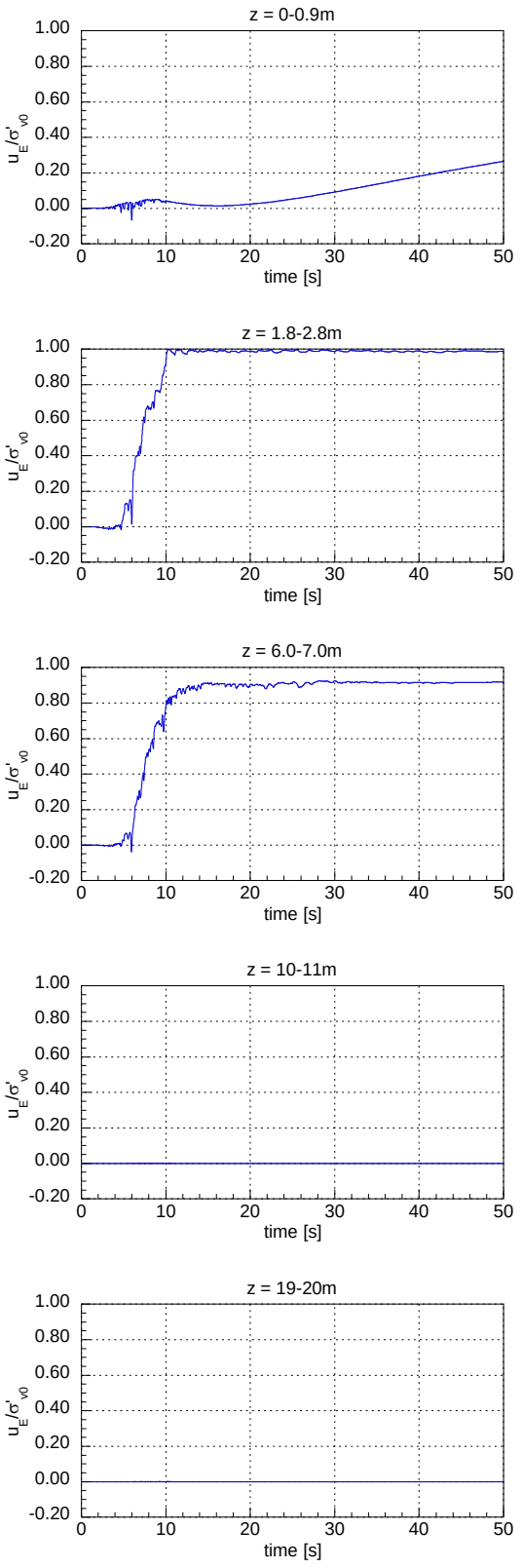

Figure 6.4: Pore water pressure ratio throughout depth (YY1, a_{max}=0.4g)

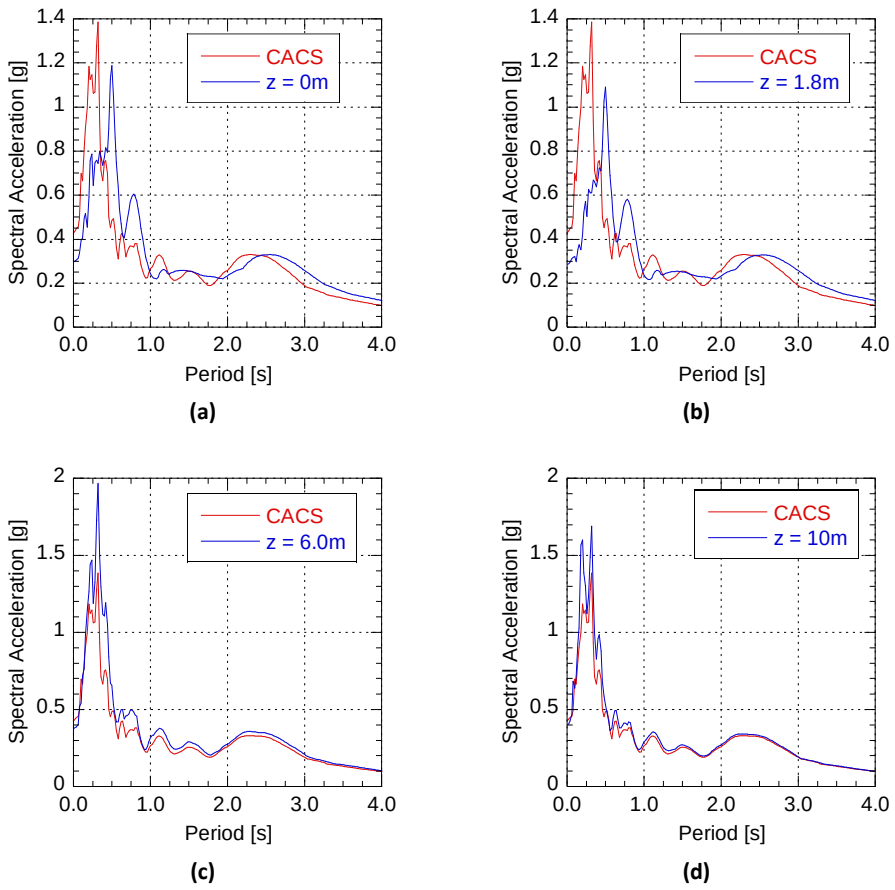

Figure 6.5: Acceleration response spectra for YY1, a_{max}=0.4g: (a) at the ground surface; (b) at the top of the critical layer; (c) at the bottom of the critical zone; (d) at 10 m depth

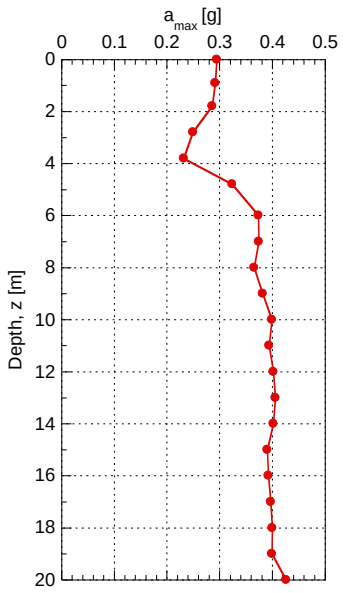

Figure 6.6: Distribution of maximum horizontal acceleration with depth (YY1, a_{max}=0.4g)

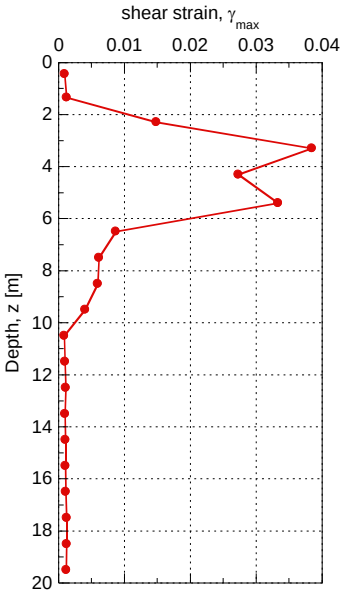

Figure 6.7: Distribution of maximum shear strain with depth (YY1, a_{max}=0.4g)

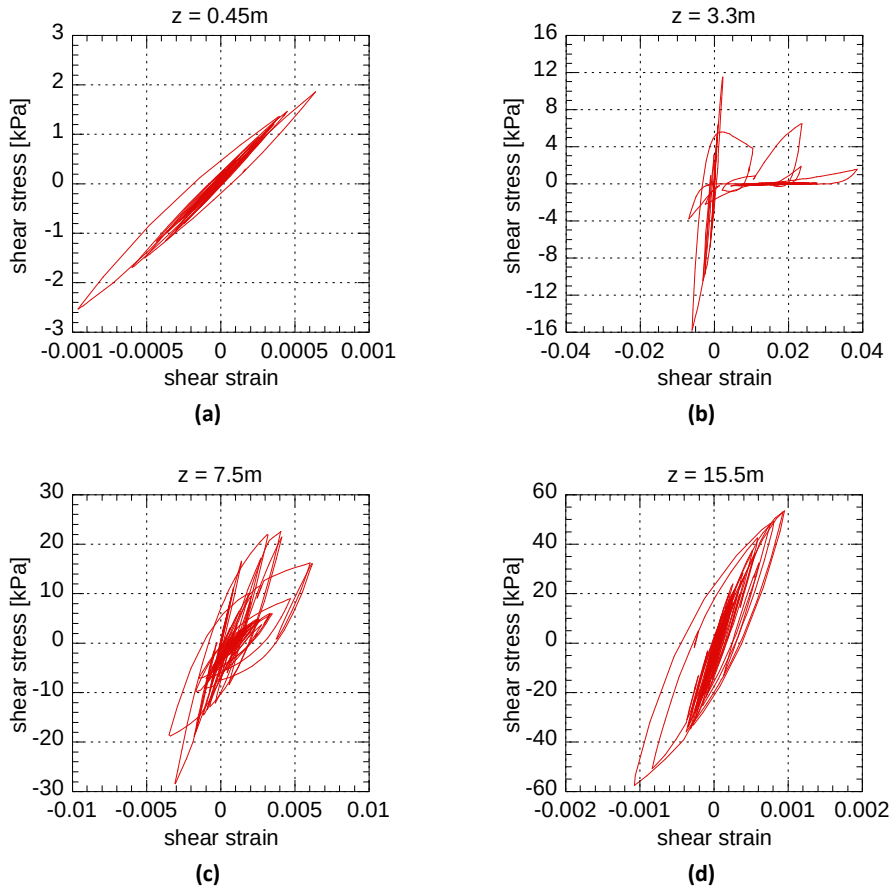

Figure 6.8: Stress-strain curves for YY1, a_{max}=0.4g: (a) in crust layer (z=0.45m); (b) in the critical zone (z=3.3m); (c) below critical zone (z=7.5m); (d) below 10m (z=15.5m)

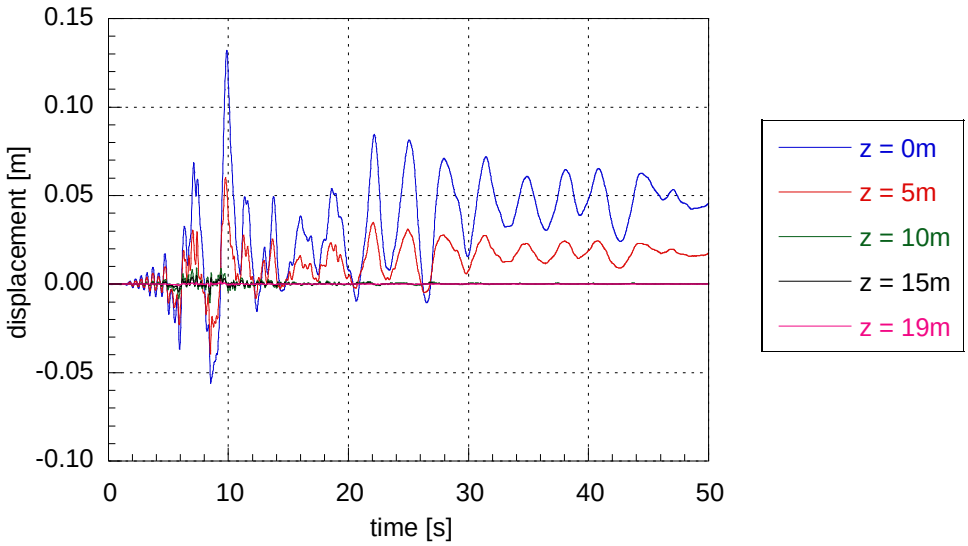

Figure 6.9: Horizontal displacement with depth (YY1, a_{max}=0.4g)

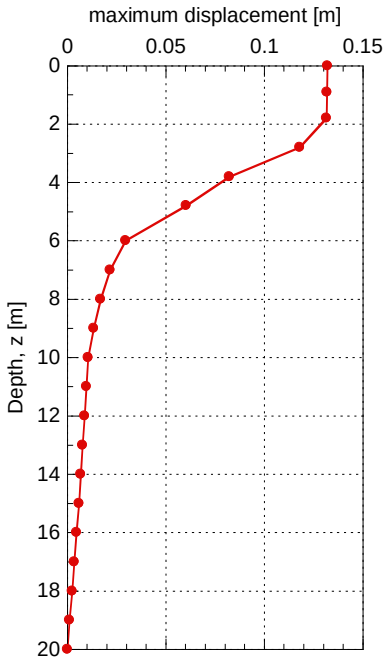

Figure 6.10: Maximum horizontal displacement with depth (YY1, a_{max}=0.4g)

6.2.2 YY1 Analyses: All shaking intensities

The response of the YY1 deposit was comparatively assessed for the three levels of ground motion intensities. As was expected, the most intense ground shaking induced the most severe liquefaction within the deposit. The key difference between the responses of the YY1 profile to the different levels of ground shaking was the extent and severity of the liquefaction induced in the critical layer and the associated damage parameters.

Figure 6.11 illustrates the pore water pressures at t=20s for the three ground shaking intensities. It shows that the whole critical zone liquefies under 0.4g input acceleration, 2.8-6.0 m of the critical zone liquefies under 0.3g acceleration and only an isolated single soil layer from 2.8-3.8 m liquefies under the lowest intensity shaking of 0.2g. Hence, the most intense ground shaking induces the largest extent of liquefaction within the deposit. Figure 6.12 shows the temporal development of excess pore water pressures and liquefaction for 0.4g, 0.3g and 0.2g acceleration levels. Figure 6.12 indicates that the pore water pressures developed slower and to a lesser extent under the lower intensity excitation levels. One notable difference with regard to liquefaction manifestation, and the damaging effects of liquefaction at the ground surface, is the significant reduction in the effective stresses in the shallowest part of the soil deposit from the ground surface to 2 m depth, this is only apparent for the highest intensity of shaking (0.4g), seen in Figure 6.12.

Figure 6.13(a) illustrates the maximum shear strain with depth for all three shaking intensities. It is evident from this plot that under both 0.4g and 0.3g excitations similar levels of shear strains occurred in the critical zone (3-4%). However, under the lower acceleration input of 0.2g, relatively large strains are only present in one thin layer, corresponding to the liquefied layer, and these strains were much smaller (γ_{max}=1.7%) as compared to the strains under higher intensity shaking. The plot of maximum displacement with depth (Figure 6.13(b)) also illustrates this effect where the displacements under I_1 (0.4g) and I_2 (0.3g) are significant (0.13 m and 0.075 m respectively) compared to the displacement from I_3 (0.2g) of 0.03 m. Figure 6.13(b) also shows that the majority of the displacement is accumulated in the liquefied layers.

The plot of maximum acceleration (Figure 6.13(c)) shows a similar trend with regard to the distribution of accelerations with depth. There is a damping of peak accelerations in the liquefied layers and a slight amplification of acceleration amplitude in the surface layers. The key difference between the different shaking intensities is the extent to which accelerations are damped in the liquefied layers, this is directly related to the extent and severity of liquefaction within the deposit.

From these analyses it is clear that the ESA captures the key features of the soil deposit response to seismic shaking. The soil response and development of liquefaction are illustrated in pore water pressure time histories, and the effects of liquefaction can be seen in plots of shear strain and displacement. The ESA also captures the interaction between soil layers showing the effects on accelerations, and the spatial and temporal evolution of liquefaction. The ESA also models water flow between layers. Hence, the ESA is a good basis for a rigorous assessment of the responses of different soil profiles to seismic shaking, the objective of this research.

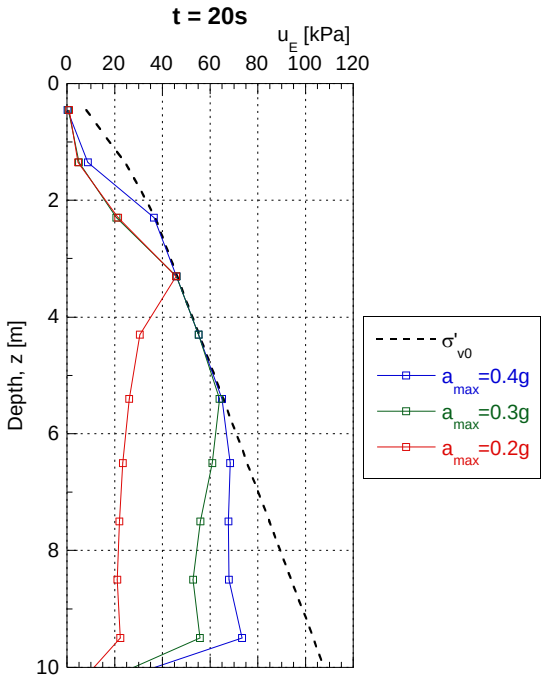

Figure 6.11: Pore water pressures at t=20s for YY1 profile and all ground motion intensities

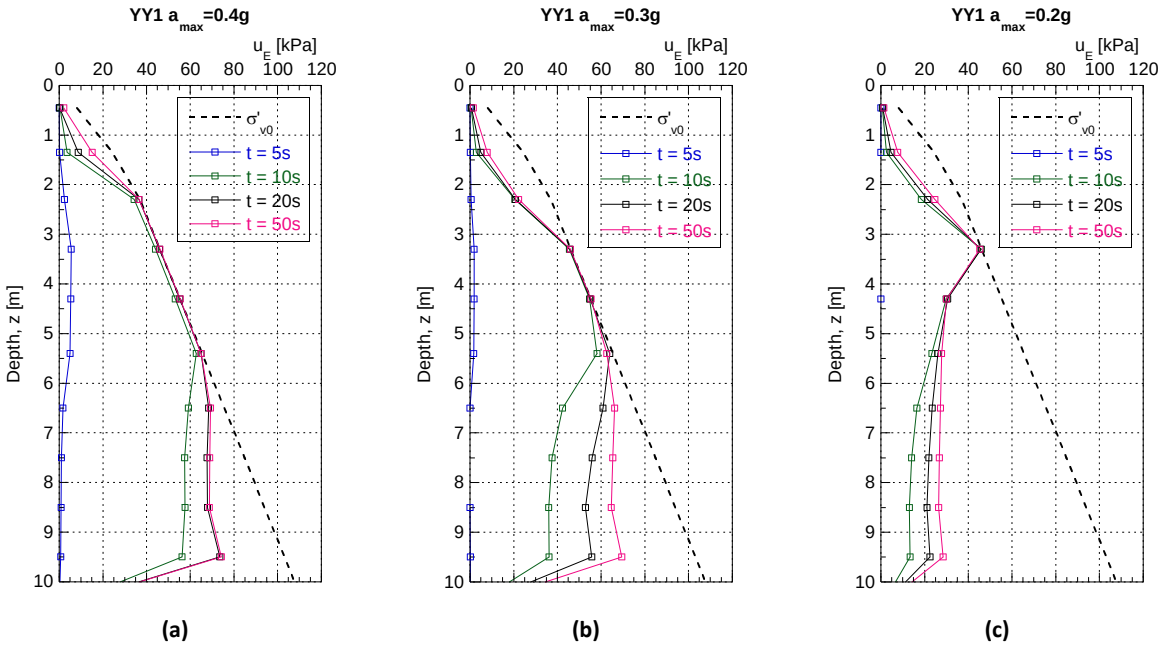

Figure 6.12: Spatial and temporal distribution of excess pore water pressure for YY1 profile: (a) high intensity motion (a_{max}=0.4g); (b) intermediate intensity motion (a_{max}=0.3g); (c) low intensity motion (a_{max}=0.2g)

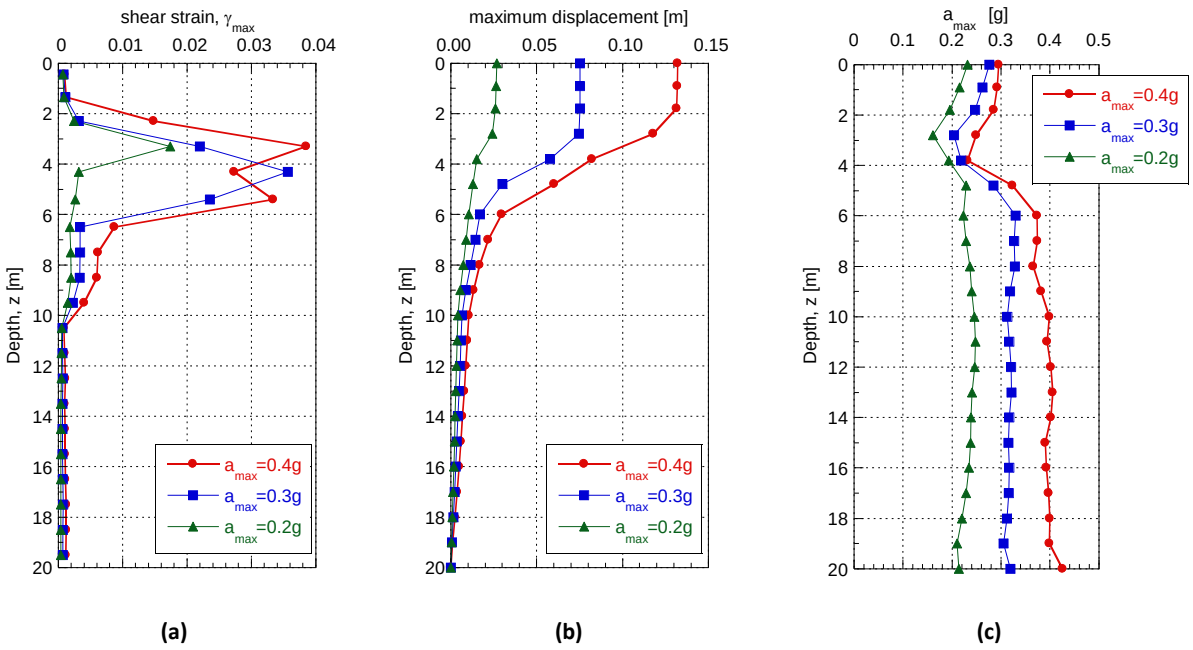

Figure 6.13: Distribution of ground response parameters throughout the depth of YY1 profile for three levels of shaking intensity: (a) maximum shear strains; (b) maximum horizontal displacements; (c) maximum horizontal accelerations

6.3 YY2 Analyses

The results from the analyses for the YY2 profile under the same three levels of shaking intensity are presented in this section. Like the YY1 profile, YY2 was a thick, continuous sandy deposit, however YY2 had a thinner critical layer (from 1.8-4.0 m) compared to YY1. This critical layer was underlain by sandy soil of higher density, and therefore greater liquefaction resistance, than that in YY1 (see Section 4.3.2). The YY2 profile had a relatively similar response to all three levels of shaking with the majority of the critical zone liquefying in all events. However, the levels of excess pore water pressures in the soils below the critical layer differed depending on the input accelerations.

Figure 6.14 illustrates pore water pressures at t=20s for the top 10 m of the soil deposit. This shows the same critical layer from 1.8-3.2 m liquefying under I_2 (a_{max}=0.3g) and I_3 (a_{max}=0.2g). The most intense ground shaking (I_1; a_{max}=0.4g) also induces liquefaction in a lower layer at 3.2-4.0 m. Figure 6.15 shows the temporal development of excess pore water pressures and liquefaction for the three shaking intensities. At t=10s, the top two layers of the critical zone (1.8-3.2 m) have liquefied under all shaking intensities and the full extent of liquefaction has developed by t=20s, approximately at the end of the high-amplitude motion in the input time history.

Comparing the pore water pressure profiles at t=20s and t=50s, the effects of pore water pressure dissipation through groundwater flow are observed. For the most intense ground shaking (a_{max}=0.4g), dissipation of pore water pressures is observed in the deeper layers of the deposit (4-

10 m) from t=20-50s. However, for the lowest intensity shaking (a_{max}=0.2g) there is continual increase in pore water pressures in these lower 6 m over the same period. This is partially attributed to the last 30s of the input ground motion which gives the time history a tail (see Figure 6.3), as a result there is still some demand after the strong shaking has reduced (see Figure 6.9). Under the most intense shaking, this tail has a negligible effect on pore water pressure development as the steep pore water pressure gradients between layers means dissipation effects govern the response. However, for the lowest level of ground shaking, these small acceleration amplitudes become significant and contribute to the continual, but small, increase in pore water pressures even after the strong ground motion has diminished. This effect can be observed in most of the simulations presented herein, but was beyond the scope of this study. Another important response feature contributing to these differences is the fact that in the analyses with the lowest accelerations (a_{max}=0.2g) the highest excess pore water pressures have been generated in the critical layer (Figure 6.15(c)). This results in pore water flow both upwards and downwards from the critical layer. Under the highest intensity shaking, the excess pore water pressures increase with depth (Figure 6.15(a)) resulting in bottom up dissipation of pressures.

Figure 6.16(a) shows the maximum strains developed in the profile for all ground motion intensities and illustrates the localisation and development of large strains in the liquefied layers. The strains developed under I_1 in the liquefied layer were significantly larger than those developed in the liquefied layers under I_2 and I_3 (4% compared to 2%). This plot also shows that the extent of the deposit that liquefied remained relatively constant under I_2 and I_3, and was only slightly increased for I_1. However, there are significant differences between the generation of excess pore water pressures, especially in the soils below the critical layer.

Figure 6.16(b) shows the maximum displacement throughout the deposit and reflects the trend shown in the shear strains. The profile developed larger strains under I_1 and resulted in significantly larger displacements in the critical zone for this level of ground shaking. Consequently, the displacement at the surface under I_1 was 0.10 m compared to 0.04 m and 0.02 m for I_2 and I_3 respectively. Figure 6.16(b) also shows the most rapid development of displacements occurring in the liquefied layers, where there is maximum strain for all three simulations.

Figure 6.16(c) shows the maximum accelerations throughout the deposit for the three levels of ground shaking. All three simulations follow the same trend; slight reduction of accelerations from 6-10 m of the deposit, large damping of amplitudes in the liquefied layers and some acceleration amplification in the surface layers. The differences between the analyses are the extent to which the accelerations are damped in the liquefied layer and how much amplification occurs in the non-

liquefied layers. The simulation with the most severe liquefaction (a_{max}=0.4g) caused a reduction in acceleration amplitude from 0.4g at the base to 0.3g at the surface, however the lowest shaking intensity (a_{max}=0.2g) underwent an overall increase in acceleration amplitude from 0.2g at the base to 0.26g at the surface. This was because the amplification of accelerations in the non-liquefied layers was more significant than the damping for the low intensity shaking. The slight decrease in peak accelerations observed in the deposit from 6-10 m is characteristic of soft soil response, high frequency motion is damped when seismic waves move from a relatively stiff medium to a softer medium.

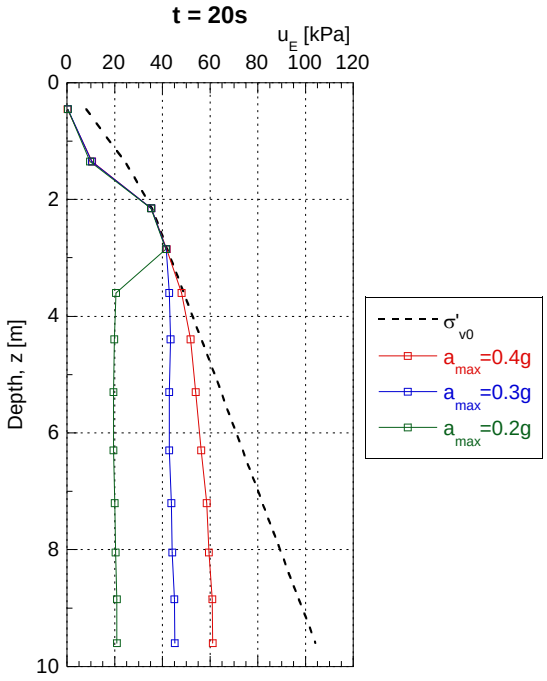

Figure 6.14: Pore water pressures at t=20s for YY2 profile and all ground motion intensities

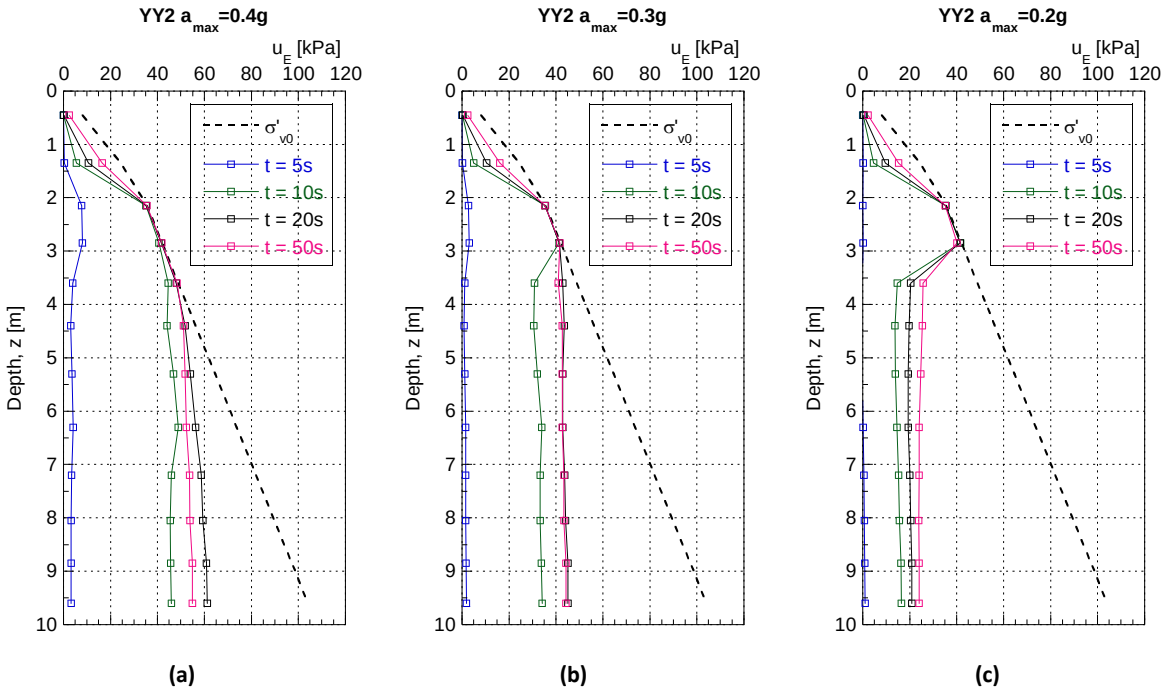

Figure 6.15: Spatial and temporal distribution of excess pore water pressure for YY2 profile: (a) high intensity motion (a_{max}=0.4g); (b) intermediate intensity motion (a_{max}=0.3g); (c) low intensity motion (a_{max}=0.2g)

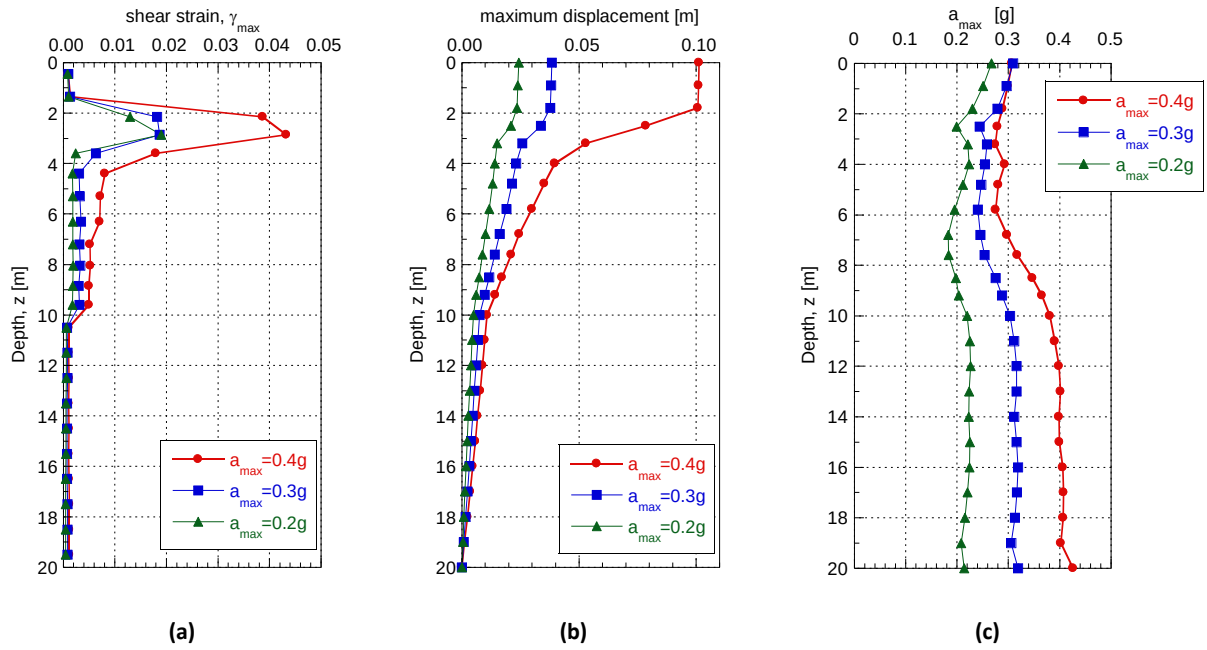

Figure 6.16: Distribution of ground response parameters throughout the depth of YY2 profile for three levels of shaking intensity: (a) maximum shear strains; (b) maximum horizontal displacements; (c) maximum horizontal accelerations

6.4 Comparison of the YY1 and YY2 analyses

The two YY profiles were both thick, uniform, continuous sandy deposits and had critical zones that liquefied under all ground motion intensities, they therefore responded in many similar ways to the input ground motion. Figure 6.17(a) shows the maximum strains developed throughout the top 10 m of the profiles for a_{max}=0.4g. It is evident from this plot that both profiles developed large strains (on the order of 4%) in the liquefied critical zones. These large strains caused accumulation of displacements in the critical layer and resulted in horizontal displacements greater than 0.1 m at the surface for highest shaking intensity as shown in Figure 6.17(b).

The differences between the two deposits are the thickness of the critical zone (4.2 m for YY1 as opposed to 2.2 m for YY2) and the liquefaction resistance of soils below the critical zone (the soils from 4-10 m had a much lower density in YY1 than YY2). These differences caused the two profiles to respond differently to the earthquake loading. Most notably, the YY1 profile developed liquefaction to a much larger extent (due to the thicker critical zone) than YY2. This is highlighted in Figure 6.17(c). The YY1 profile generated excess pore water pressures over a much larger depth than the YY2 profile for the highest intensity shaking. This is also illustrated in the displacements in Figure 6.17(b). As YY1 had a thicker liquefied layer, displacements were more severe at the surface.

The sensitivity of the soil profiles to the intensity of ground shaking differed between YY1 and YY2. YY1 responded differently to the different shaking intensities developing a greater extent of liquefaction under the highest shaking intensity compared to the lowest. The whole critical zone liquefied at I_1, but only a single 1.0 m layer liquefied at I_3 as can be seen in Figure 6.11. On the other hand, the YY2 profile was relatively insensitive to the input ground motion. Similar levels of liquefaction were induced in the critical zone across all three ground motion intensities, only the highest intensity motion induced an additional 0.8 m of the deposit to liquefy (Figure 6.14). This is because the presence of stronger soil layers below the critical zone caused energy dissipation to be focussed in the critical layer, whereas in YY1 more layers contributed to the energy dissipation. Instead, the main difference between the response of YY2 to the different intensities of shaking was in the level of excess pore water pressure beneath the critical zone (Figure 6.15), and the degree to which strains and displacements were accumulated (Figure 6.16(a) and (b)). The summary plots comparing YY1 and YY2 for the I_2 and I_3 excitations can be found in Appendix N.

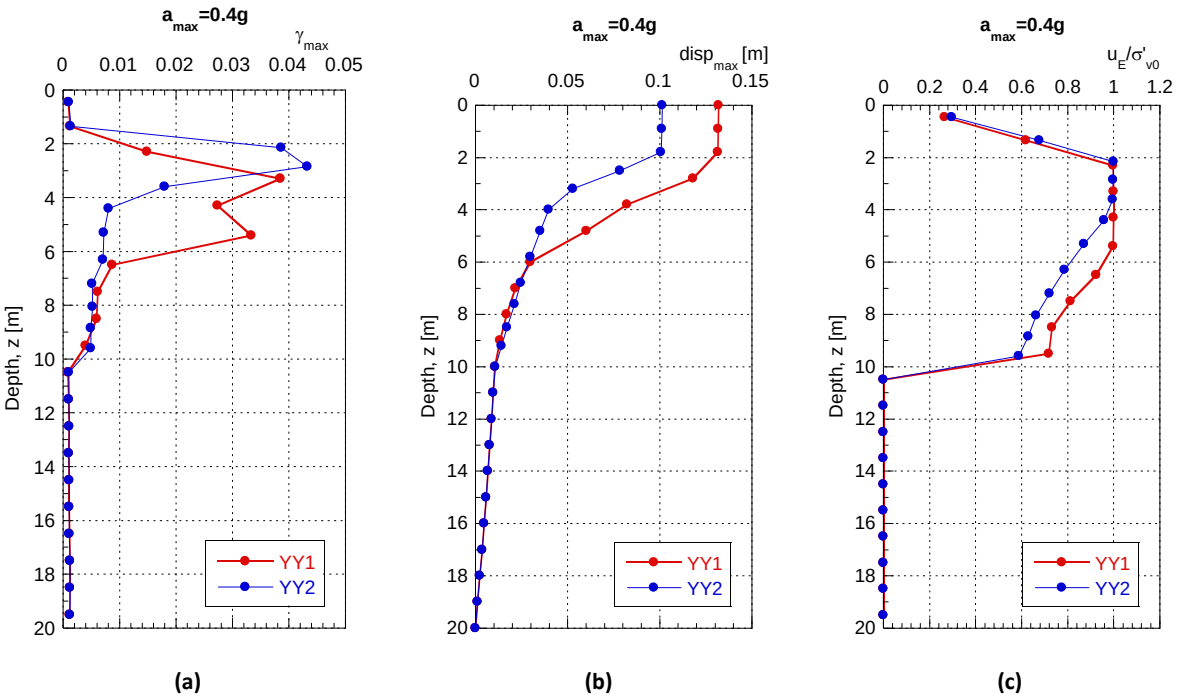

Figure 6.17: Distribution of ground response parameters throughout the depth of both YY profiles for highest shaking intensity, a_{max}=0.4g: (a) maximum shear strain; (b maximum horizontal displacement; (c) maximum pore water pressure ratio at t = 20s

6.5 NN1 Analyses

The results for NN1 profile under all three ground motion intensities are presented in this section. The NN1 profile consisted of a non-liquefiable layer directly below the water table at 1.6-2.5 m and another thick non-liquefiable layer from 4-8.5 m (see Section 4.3.3). The liquefiable soils in the NN1 profile were given a similar liquefaction resistance to those in the critical zones of the YY profiles. Due to this low resistance in the liquefiable layers, the deposit had an extreme response to the earthquake loading, with almost all liquefiable layers liquefying rapidly under all loading conditions. The effect of a slight increase in the liquefaction resistance of the shallow soil layers is investigated in Section 6.10.

Figure 6.18 illustrates the distribution of excess pore water pressures throughout the deposit at t=20s for the three ground motion levels. This shows the two liquefiable layers at 2.5-4.0 m and 8.5-10 m liquefying under almost all three ground motion intensities. Only for the lowest intensity motion (a_{max}=0.2g) the layer from 8.5-9.2 m (which had a slightly higher resistance) did not liquefy. Furthermore, as illustrated in Figure 6.19, the generation of excess pore water pressures in the critical zone (2.5-4.0 m) developed rapidly under all three intensities of shaking. This layer has fully liquefied after approximately 5 seconds of strong shaking (at t=10s on the time scale), for all three

ground motion intensities. Note that as a first approximation in the modelling of the non-liquefiable layers, an undrained condition was assumed in this study for these models, hence no effects of pore water pressure dissipation are seen in the NN1 and NN2 analyses.

Figure 6.20(a) shows key response features associated with the behaviour described above, illustrating consistently large strains in the liquefiable layers. The effect that the development of large strains has on the observed surface effects is highlighted in the plot of maximum horizontal displacement with depth in Figure 6.20(b). Large displacements are rapidly accumulated in the liquefied layers, with little contribution from the rest of the soil deposit.

Figure 6.20(c) shows significant reduction of accelerations due to damping in the deepest liquefied layer. This damping is more pronounced for the higher intensities of shaking. This illustrates important effects on the seismic demand and on the overall response of the deposit from the occurrence of liquefaction in deeper layers. Acceleration amplitudes are significantly reduced as the seismic waves pass first through the deepest liquefied layer at 9.2-10 m. This affects the rest of the deposit so that under all three ground motion intensities the peak accelerations are reduced to a similar value of 0.23g to 0.25g at the surface. This means that the shallow liquefiable layers (2.5-4 m) were shaken with a significantly modified ground motion to what was the base input. NN1 was modelled with low liquefaction resistance in these shallow layers (similar to the resistance of critical layers in the YY1 and YY2 profiles) so liquefaction was still induced under all shaking intensities. The effect of slightly increasing the liquefaction resistance in these layers, and how this affects the dynamic response of the entire soil deposit, are investigated in some depth later in this chapter.

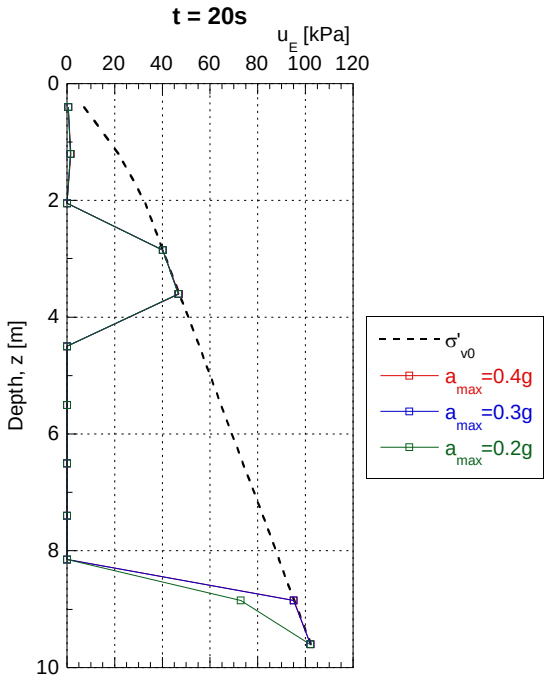

Figure 6.18: Pore water pressures at t=20s for NN1 profile and all ground motion intensities

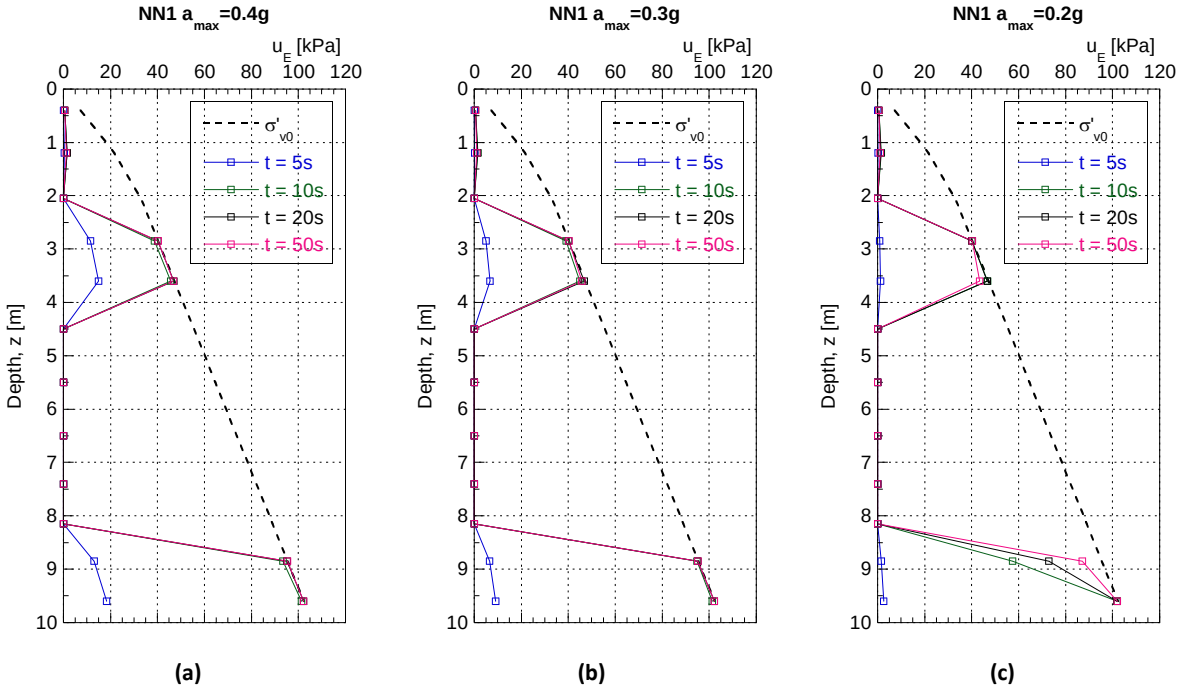

Figure 6.19: Spatial and temporal distribution of excess pore water pressure for NN1 profile: (a) high intensity motion (a_{max}=0.4g); (b) intermediate intensity motion (a_{max}=0.3g); (c) low intensity motion (a_{max}=0.2g)

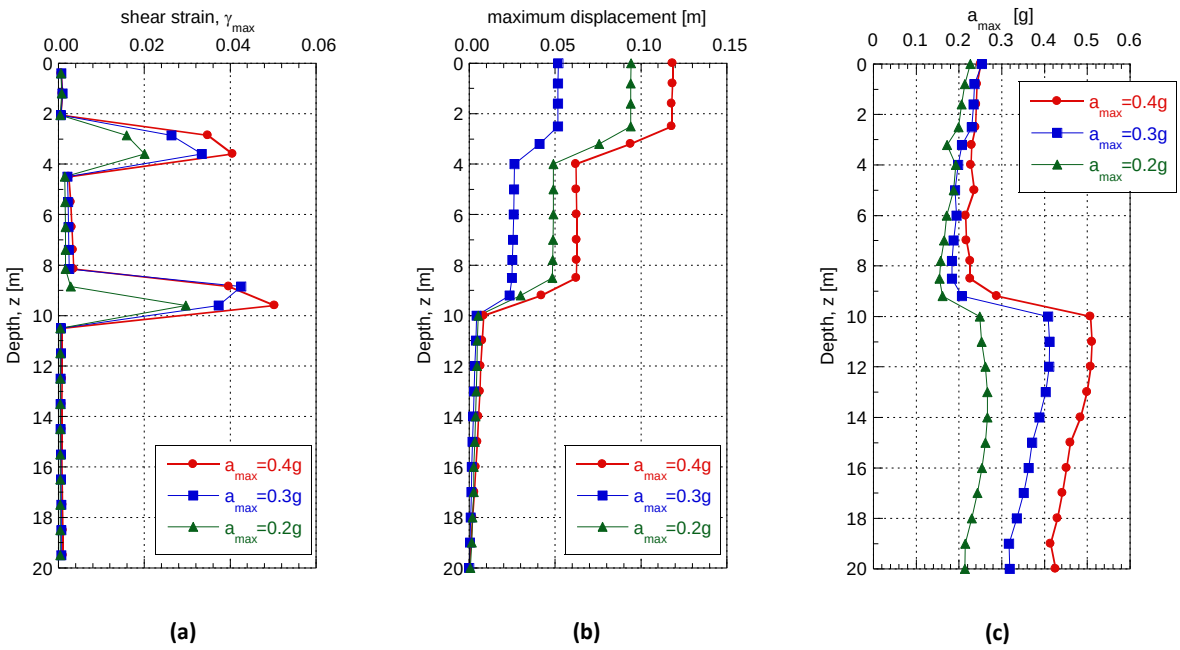

Figure 6.20: Distribution of ground response parameters throughout the depth of NN1 profile for three levels of shaking intensity: (a) maximum shear strains; (b) maximum horizontal displacements; (c) maximum horizontal accelerations

6.6 NN2 Analyses

The results of the simulations with the NN2 soil profile under all three loading conditions are presented and discussed in this section. The NN2 profile was more stratified than NN1. There were five non-liquefiable layers, of thickness no greater than 1.5 m, distributed throughout the top 10 m of the deposit (see Section 4.3.4). Like the NN1 profile, the liquefiable layers had low liquefaction resistance similar to those of the critical layers in the YY profiles, except for the deepest liquefiable layer from 8.5-10 m which had a slightly higher resistance. All loading scenarios induced some level of liquefaction, however there was a marked difference in the extent of liquefaction between the two higher intensity motions (I_1; a_{max}=0.4g and I_2; a_{max}=0.3g) and the lower intensity shaking (I_3; a_{max}=0.2g). This indicates that the NN2 profile was sensitive to the level of earthquake loading.

Figure 6.21 illustrates the pore water pressures in the NN2 profile at t=20s for all three loading intensities. This shows a relatively similar response under I_1 and I_2, with all but the deepest (8.5-10 m) liquefiable layers liquefying within the first 20 seconds. The main difference being a slightly slower development of pore water pressures in the first and third layers (2.3-2.8 m and 5.1-5.8 m respectively) under I_2 as is seen in Figure 6.22.

However, the response of the deposit under I_3 differs from that under the two higher intensity levels and shows some features of soil layer interaction. Under this loading intensity, only the second (3.6-4.5 m) and fourth (7-7.7 m) liquefiable layers liquefy. The third (5.1-5.8 m) and fifth (8.5-10 m)

liquefiable layers do not liquefy as they have slightly higher liquefaction resistance (q_{c1Ncs}=95 and q_{c1Ncs}=115 respectively). However, the shallowest liquefiable layer (2.3-2.8 m) has the same low liquefaction resistance as the layers that did liquefy (q_{c1Ncs}=80) but did not liquefy in this simulation. This was due to soil layer interaction and variation of demand throughout the depth of the deposit. Figure 6.23(c) shows that there was significant reduction of acceleration amplitudes in the liquefied layer at 7-7.7 m depth, similar to the reduction of accelerations that occurred for the strongest intensity of shaking (a_{max}=0.4g). This means that the upper soil layers were shaken with a motion that had lower accelerations and less high frequency content than the input motion at the base of the soil column. For the lowest intensity excitation (a_{max}=0.2g), this damping of the ground motion was enough to prevent liquefaction developing in the shallowest liquefiable layer. It is this type of dynamic cross-interaction of soil layers that was the focus of this study, and it is this effect that can cause false predictions by the simplified method.

Figure 6.23(a) shows the maximum shear strains throughout the profile for all three loading conditions. This clearly shows the generation of large strains in the liquefied layers, and also illustrates the marked difference in the response of the profile to the I_3 (i.e. the lowest) shaking intensity. Under this excitation, the strains in the first (2.3-2.8 m), third (5.1-5.8 m) and deepest fifth (8.5-10 m) potentially liquefiable layers remain relatively low due to these layers developing excess pore water pressures but not liquefying. As these layers did not produce the same levels of strain as under the I_1 and I_2 loadings, the displacements in the deposit at I_3 were also significantly less (0.03 m) compared to the other shaking intensities (0.13 m and 0.10 m for I_1 and I_2 respectively). This is illustrated in Figure 6.23(b). All three loading conditions caused significant damping of accelerations throughout the profile due to the presence of liquefied material, as seen in Figure 6.23(c) where all loading conditions result in a peak ground acceleration at the surface of around 0.22 g. This damping is less significant for I_3 as there is some amplification of accelerations near the surface due to the response of soft non-liquefied soils.

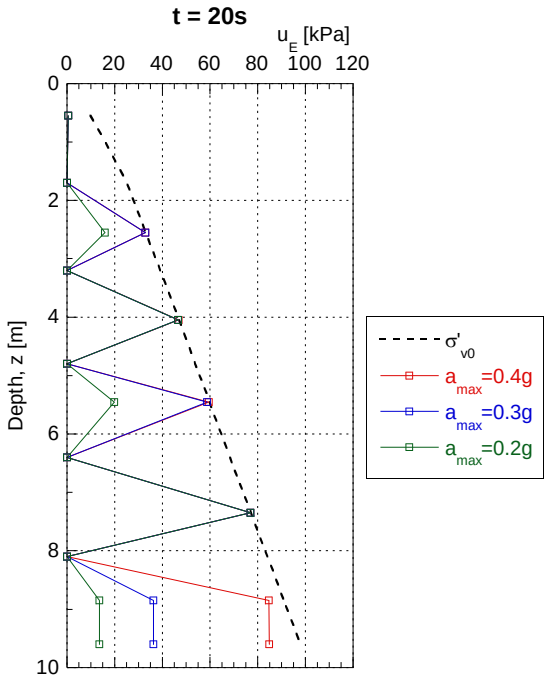

Figure 6.21: Pore water pressures at t=20s for NN2 profile and all ground motion intensities

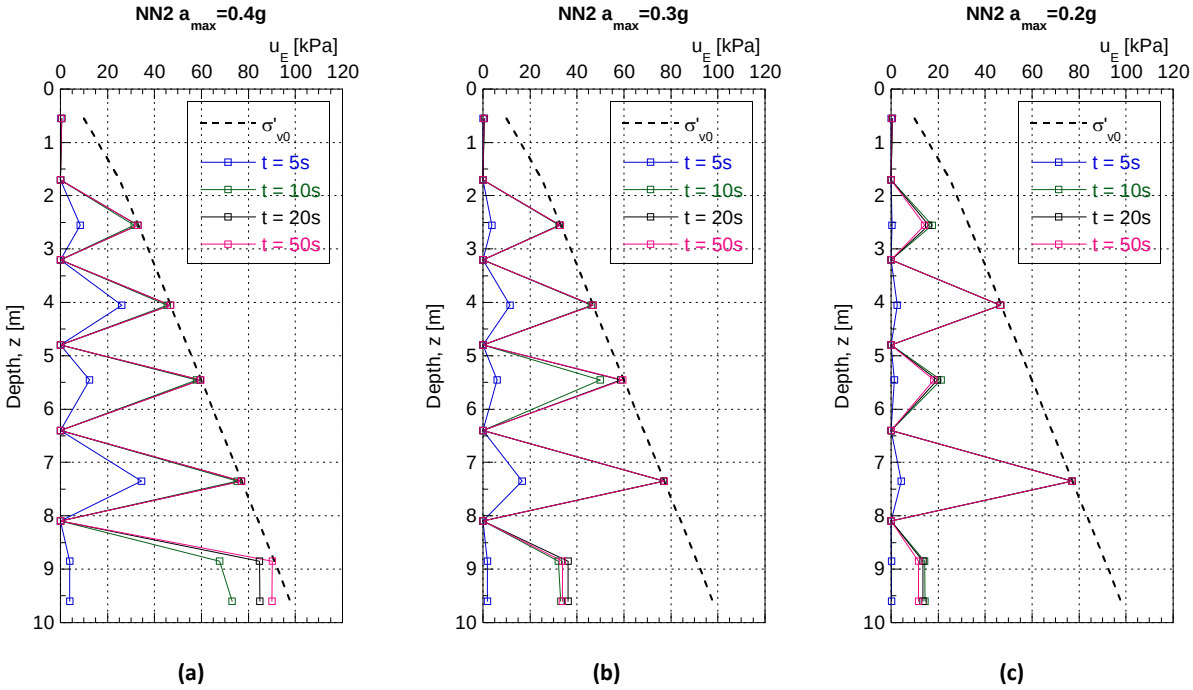

Figure 6.22: Spatial and temporal distribution of excess pore water pressure for NN2 profile: (a) high intensity motion (a_{max}=0.4g); (b) intermediate intensity motion (a_{max}=0.3g); (c) low intensity motion (a_{max}=0.2g)

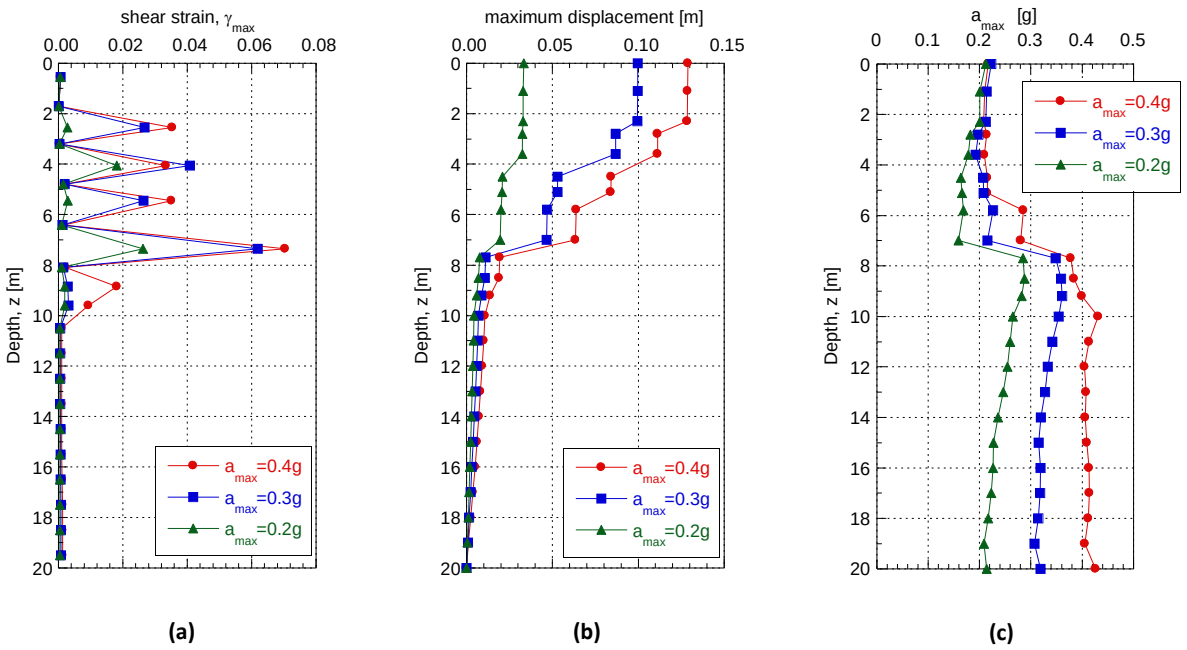

Figure 6.23: Distribution of ground response parameters throughout the depth of NN2 profile for three levels of shaking intensity: (a) maximum shear strains; (b) maximum horizontal displacements; (c) maximum horizontal accelerations

6.7 Comparison of the NN1 and NN2 analyses

The NN1 and NN2 profiles were similar in that they were highly non-uniform and vertically discontinuous deposits consisting of interlayered liquefiable and non-liquefiable layers. The liquefiable layers were characterised by relatively low liquefaction resistances and therefore tended to liquefy under most loading intensities. This led to the generation of large strains as illustrated in Figure 6.24(a) for I_1 (a_{max}=0.4g) and resulted in relatively large displacements at the surface as illustrated in Figure 6.24(b) (also for I_1). Despite the difference in location of liquefied layers between the two profiles, the extent of liquefaction was relatively similar leading to similar displacements at the surface (0.12 m and 0.13 m for NN1 and NN2 respectively).

Both profiles also underwent similar levels of acceleration damping in the upper 10 m of the profile as illustrated in Figure 6.24(c) for I_1, where a reduction in accelerations from 0.4 g at the base of the model to 0.25 g at the surface can be seen. However, for the NN1 profile this damping happened almost solely in the deep liquefied layer at 8.5 m-10 m as opposed to the NN2 profile where the damping of accelerations was distributed through several of the liquefied layers in the upper 10 m.

The key difference between these two profiles was the location and thickness of the non-liquefied layers. This is evident in Figure 6.24(a) which shows the NN1 profile develops excessive strains in two thick liquefied layers, whereas excess pore water pressures and liquefaction effects are distributed in five thinner layers across the whole upper 10 m of the NN2 profile.

The higher number of liquefiable layers in the NN2 profile made it more sensitive to the loading condition and more pronounced soil layer interaction was observed at I_3 (see Section 6.6). This dynamic response was not observed in the NN1 profile (where the extent of liquefaction was relatively similar across all loading intensities) however, a further investigation into the effect of increasing the liquefaction resistance in the shallowest liquefiable layer (see Section 6.10) shows that a slight increase in the liquefaction resistance of the shallow layers causes soil layer interaction to become significant for the NN1 profile also. The summary plots comparing NN1 and NN2 for I_2 and I_3 excitations can be found in Appendix O.

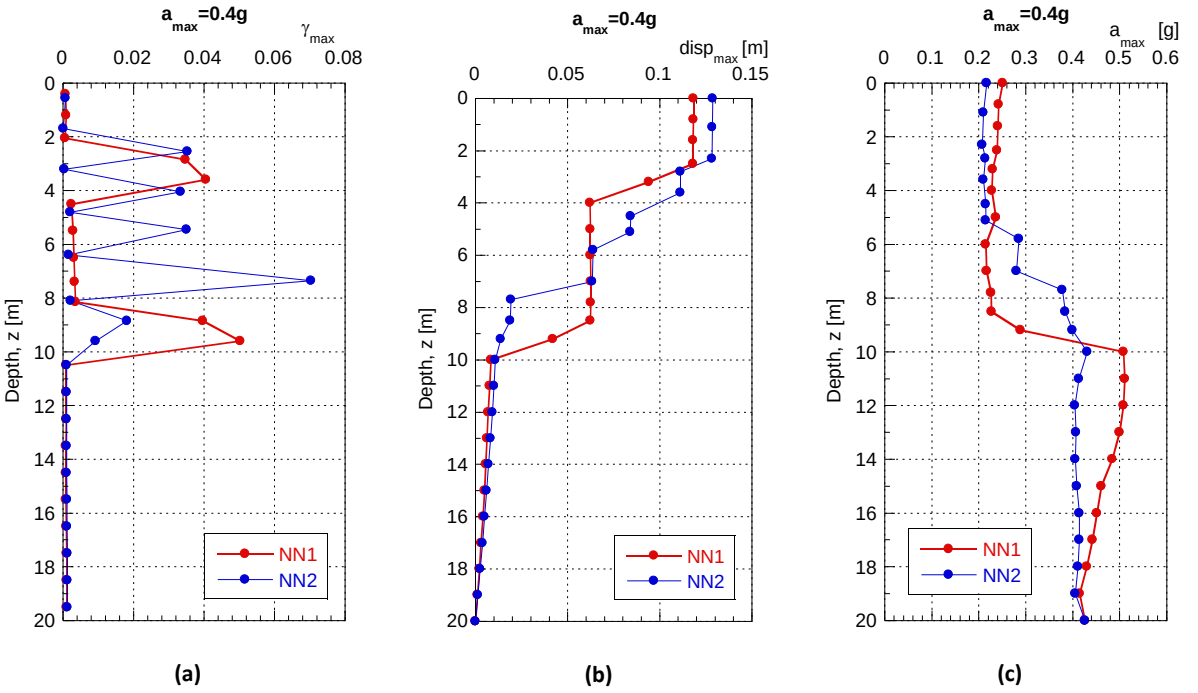

Figure 6.24: Distribution of ground response parameters throughout the depth of both NN profiles for highest shaking intensity, a_{max}=0.4g: (a) maximum shear strain; (b) maximum horizontal displacement; (c) maximum horizontal acceleration

6.8 Comparison of the YY and NN analyses

The key difference between the responses of the YY and NN profiles was the location, thickness and vertical continuity of liquefiable layers, and how these factors influenced whether soil layer interaction had an effect on the response of the soil deposit as a whole. The YY profiles consisted of thick, vertically continuous liquefiable layers with nearly constant (YY1) or increasing (YY2) liquefaction resistance (in accord with increasing soil density) from the layer below the ground water table to 10 m depth. The NN profiles were markedly different, they were vertically discontinuous with numerous non-liquefiable layers interlaid with liquefiable layers of low liquefaction resistance

throughout the profile. As a result, liquefaction was induced in different locations and thicknesses in the different YY and NN profiles.

Figure 6.25 shows the pore water pressure ratio for all four profiles with depth under the most intense loading condition (a_{max}=0.4g). This shows the YY profiles developing large excess pore water pressures in the upper few metres of the soil deposit, from below the water table at 1.8 m to a maximum depth of 6.0 m. On the other hand, the NN profiles liquefy at discrete locations throughout the whole upper 10 m of the deposit, with these relatively thin liquefiable layers isolated between non-liquefiable layers. This difference in the spatial distribution of liquefaction resulted in strains, and therefore displacements, being accumulated at different locations within the soil deposit. Despite this, all four profiles experienced similar values of displacement at the surface under I_1 (0.10-0.13 m).

All four profiles contained liquefied material, so significant damping of acceleration amplitudes was induced in all profiles. However, this was more marked for the NN profiles. Accelerations reduced to around 0.22-0.26g at the surface for the NN profiles, whereas accelerations were approximately 0.23-0.30g at the surface for the YY profiles. All four profiles underwent damping of acceleration amplitudes, and as a result the shallow soil layers were shaken with a ground motion significantly modified to what was input at the base.

This difference in the location, thickness and continuity of liquefiable layers within the soil deposit is the key factor in soil layer interaction. The thick sandy deposits, such as the YY profiles, tend to behave as predicted by simplified methods, however when there is interlayering of liquefiable and non-liquefiable layers, such as is the case for the NN profiles, soil layer interaction can change the dynamic response of the soil deposit. Deep soil layers with low liquefaction resistance, such as the layer at 8.5-10 m in the NN1 profile, once liquefied, can alter how the upper layers of the soil deposit respond to the earthquake loading. This deep liquefied layer will damp out high frequency motion so upper layers are being shaken by a ground motion with a reduced high frequency content and a reduced amplitude. This reduction in the input ground motion can be enough to prevent shallower liquefiable layers from liquefying. This is not observed in the uniform sandy deposits as the soil is continuous so water flow occurs between layers. This can have the detrimental effect of increasing liquefaction susceptibility in shallow layers. Such analyses, in which higher permeability was used in sandy zones, were performed at a preliminary level but are not presented in the thesis. These analyses confirmed significant seepage action, flow induced liquefaction and associated damage for the YY-type profiles, but this aspect is beyond the scope of the present study.

This effect of soil layer interaction was not observed under the I_1 loading, as the shaking intensity was high enough that all liquefiable layers in the NN profiles liquefied. However, this was observed at lower shaking intensities in NN2 (see Figure 6.21). In Section 6.10, the effect of slightly increasing the liquefaction resistance in the shallow liquefiable layers in NN1, and how this small change can cause soil layer interaction to have a significant effect on the response of the deposit, will be investigated.

There are at least three significant aspects of cross-interaction between layers, only one of which has been investigated in this study. One is related to the modification of ground response due to liquefaction developing in certain part(s) of the deposit (dynamic-response interaction), another is the interaction through groundwater flow and dissipation of excess pore water pressures, which is particularly prominent after the intensive shaking has reduced (ground water flow interaction), and finally, the effects of the above two together with the distribution of liquefied and non-liquefied layers, including their location relative to the ground surface, which would significantly influence the surface manifestation (or lack of it) of liquefaction. This study largely focused on illustrating some features of the first aspect of cross-interaction effects (dynamic-response interaction), though the results also provide some indications of the likely effects associated with ground water flow and liquefaction manifestation, albeit through a somewhat subjective interpretation. Hence, further studies in this regard are highly recommended.

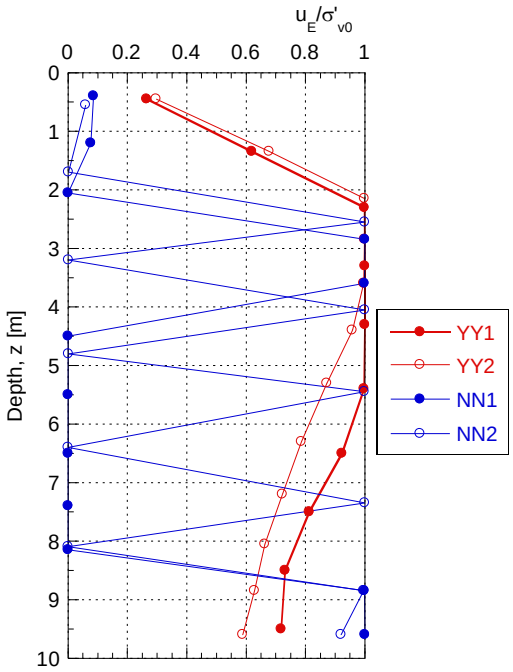

Figure 6.25: Pore water pressure ratio with depth for all YY and NN sites for ground motion with a_{max}=0.4g

6.9 Comparison of results from ESA and simplified method of analysis

The factor of safety (FS), maximum strain and settlement were estimated for all four profiles and three acceleration levels using the simplified liquefaction triggering analysis of Boulanger and Idriss (2014). These results were then compared to those obtained from the 1-D soil column ESA to see when the simplified method was accurate in predicting the response of these soil profiles. A key difficulty in the simplified analysis was in determining appropriate PGA values to produce a seismic demand (*CSR*) equivalent to that of ESA, particularly as the simplified method refers to a seismic demand without effects of liquefaction. To address this issue, a range of PGA values were used for each intensity level in the simplified analyses, these were: PGA = 0.18g – 0.22g and PGA = 0.27g – 0.33g for I_2 and I_3 levels respectively (or $\pm$10% of the base input acceleration, a_{max}=0.2g and a_{max}=0.3g respectively), and PGA = 0.32g – 0.36g for I_1 (or -10% and -20% of the base input acceleration, a_{max}=0.4g). This difference for I_1 was due to the larger nonlinear effects, so reduction in the response accelerations were anticipated for the base acceleration of 0.4 g. The simplified method was found to overestimate the response of the soil deposit in all analyses so only the lower bound values of PGA are presented herein as a less conservative estimate of the soil response.

Figure 6.26(a) shows a comparison of the pore water pressure ratio from the simplified method and from the 1-D soil column ESA for the YY1 profile under I_1. The pore water pressure ratio from the simplified method was estimated from the computed factor of safety assuming a value of r_u = 1.0 for FS < 1.0, and using an approximation for the median value for sand from the chart in Figure 6.27 to estimate pore water pressures associated with FS values greater than 1.0. From Figure 6.26(a) it is evident that the simplified method overestimates the extent of liquefaction in the soil deposit predicting liquefaction from 1.8-8.5 m as opposed to from 1.8-6.0 m as was observed from the ESA.

Figure 6.26(b) illustrates the maximum shear strain from both the simplified method (using Boulanger and Idriss, 2008) and the ESA for the same profile. From this plot, it is evident that the simplified method has predicted excessively large shear strains. Settlements were computed for both analyses using the simplified procedure for estimating settlements based on the shear strains computed for each method in Figure 6.26(b) and following the method of Ishihara and Yoshimine (1992), these are shown in Figure 6.26(c). These settlement estimates show the effect of the overestimation of the response in the simplified method, as this method predicts liquefaction over a greater depth, greater settlement values than those from the ESA are predicted (0.26 m as opposed to 0.07 m). However, it is important to note that the ESA does not account for the damaging effects of water flow and sand ejecta on the surface, effects which may be significant for the YY profiles.

Despite the differences in the predicted response, the simplified method still gives the same prediction as the ESA – that liquefaction will occur and that it will manifest at the surface.

The pore water pressure ratios for the NN2 profile under I_3, calculated with both the simplified method and the 1-D soil column model are presented in Figure 6.28(a). This plot illustrates the inability of the simplified method to predict the effects of soil layer interaction. The simplified method predicts liquefaction in the first liquefiable layer at 2.3-2.8 m, however in the ESA this did not occur. The plots of shear strain and settlement in Figure 6.28(b) and (c) respectively illustrate the consequences of this over-prediction. Shear strains are predicted to the same extent in all liquefiable layers by the simplified method, this leads to an over-estimation of settlement at the ground surface, 0.12 m as opposed to 0.02 m. In the 1-D soil column model, damping of the ground motion as it passed through deeper, liquefied layers prevented the liquefaction of the shallow sandy layer. The simplified method makes the assumption the all soil layers behave independently of each other, and therefore cannot account for this effect. The result is an over-prediction of liquefaction triggering by the simplified method and, as this layer is near the surface, an over-prediction of surface manifestation and the associated effects. Comparison plots between results from the ESA and simplified analyses can be found in Appendix P, for all soil profiles and shaking intensities.

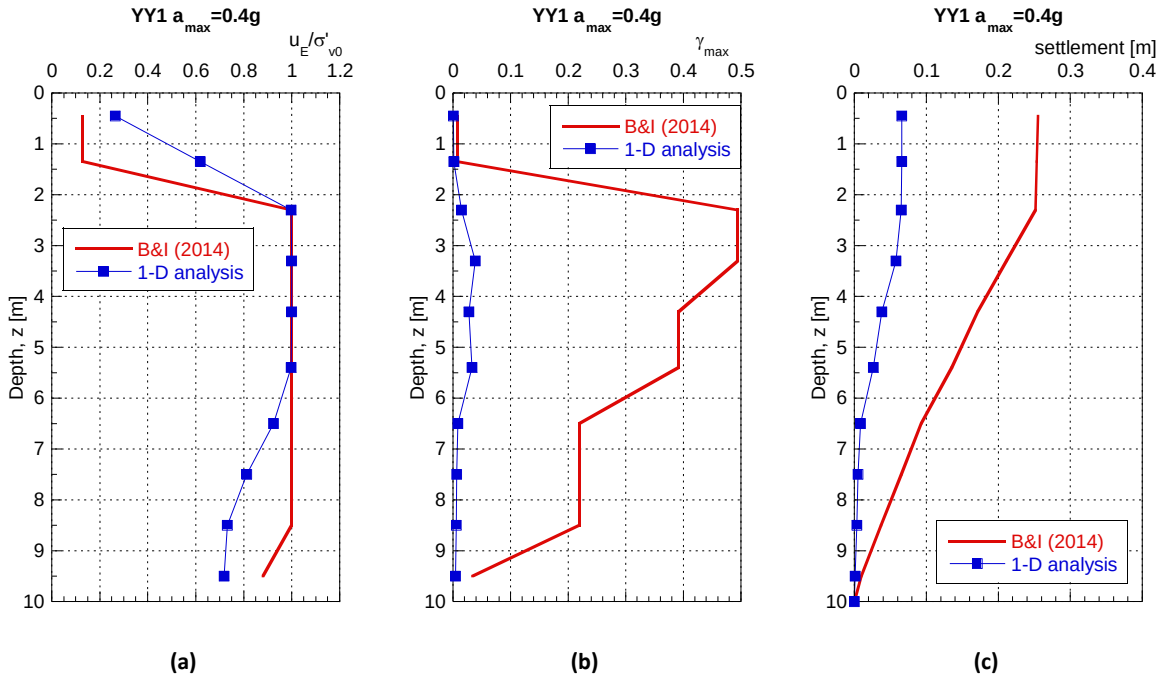

Figure 6.26: Comparison plots for soil response predicted by the simplified method and the 1-D soil column model for YY1, a_{max}=0.4g: (a) maximum pore water pressure ratios; (b) maximum shear strains; (c) vertical settlement

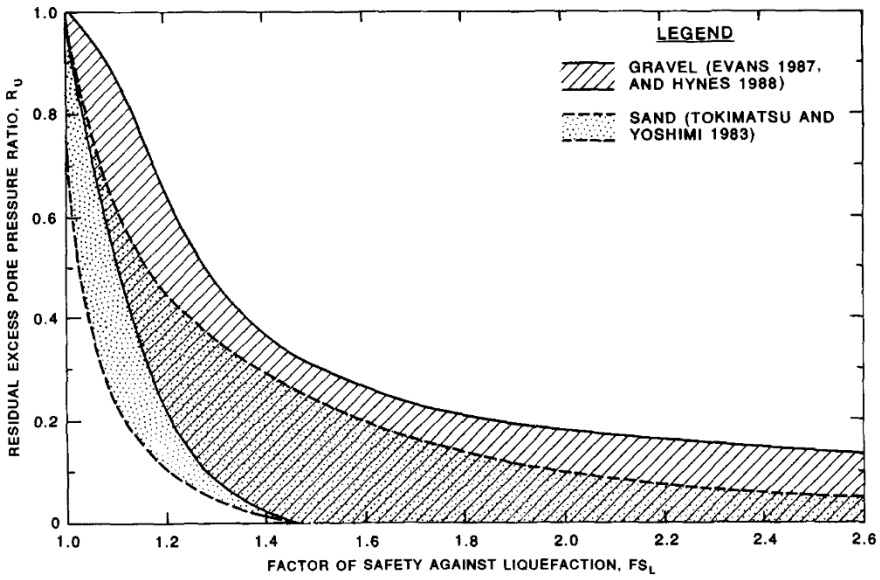

Figure 6.27: Relationship between FS and pore water pressure ratio (R_U) from Marcuson et al. (1990)

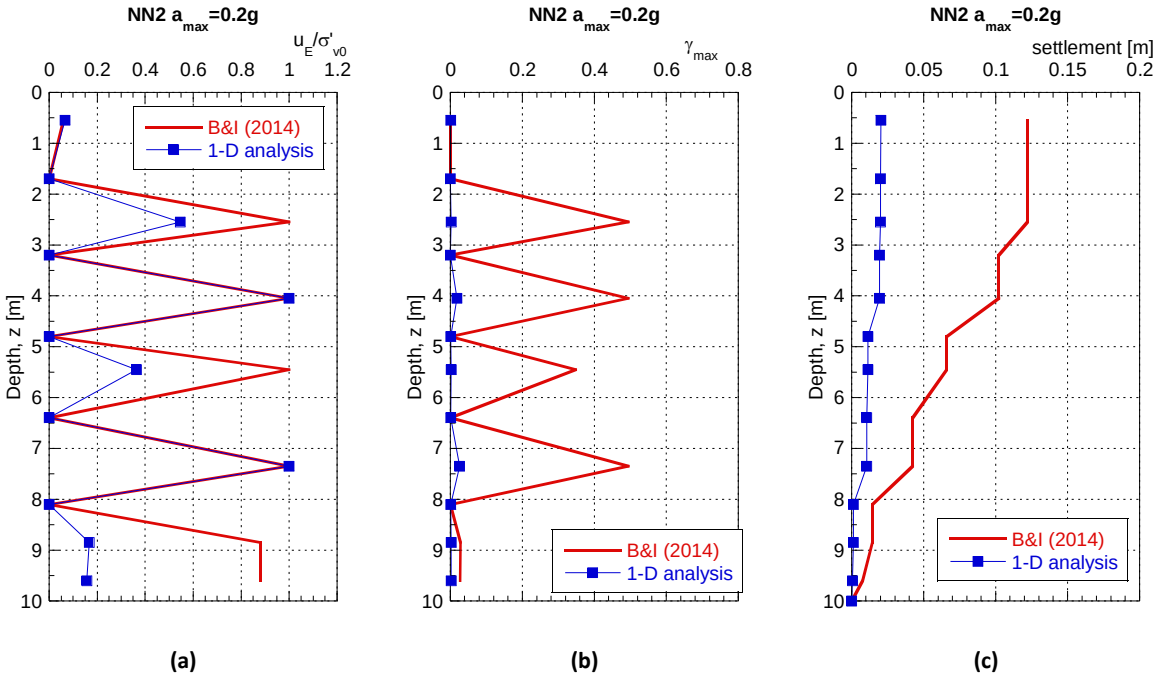

Figure 6.28: Comparison plots for soil response predicted by the simplified method and the 1-D soil column model for NN2, a_{max}=0.2g: (a) maximum pore water pressure ratios; (b) maximum shear strains; (c) vertical settlement

6.10 Sensitivity of the ground response at shallow depths

One of the observations from liquefaction case histories is that a crust layer at the ground surface may reduce or even eliminate liquefaction manifestation in deposits that otherwise are expected to liquefy by the simplified procedure. To scrutinise this aspect of the problem, a further investigation into the effect of increasing the liquefaction resistance of the shallowest liquefiable soil layer (2.5-4.0 m) in the NN1 profile was carried out using the highest intensity shaking (I_1; a_{max} = 0.4g). The liquefaction resistance curve (LRC) for the shallowest layer (q_{c1Ncs}=80) was increased from 1.1-1.4 times its original value. The new higher liquefaction resistances were incorporated into the soil column model by changing the void ratio used to model this layer in the element test simulations (this was to simulate an increase in the resistance through a slight increase in the density of the soil). The results of such incremental analyses were then recorded in terms of the pore water pressures and strains in the deposit.

Figure 6.29(a) illustrates how the pore water pressure ratio changes with increase in *CRR* in the shallowest liquefiable layer of the NN1 profile. This plot indicates that the liquefaction resistance (or *CRR*) in this layer needs to increase by about 30% (relative to the original CRR estimate based on q_{c1Ncs}=80) to prevent liquefaction from occurring in this layer. Figure 6.29(b) illustrates the change in the maximum single amplitude shear strain in the shallow liquefiable layers with percent increase in *CRR*, obtained from the same set of incremental analyses. Single amplitude strains greater than 3% represent a point at which significant damage, associated with full liquefaction, has been induced in the layer. Therefore, the increase in *CRR* to restrict the strains to less than 2% in the shallow liquefiable layer was identified to depict a threshold *CRR* for which damaging effects of liquefaction would be reduced. From the results shown in Figure 6.29(b), this was estimated to be achieved if *CRR* was 1.25 times the original *CRR* value. The sharp change in the shape of this curve after an increase in *CRR* of 1.35 corresponds to a more significant reduction in the excess pore pressures in the shallow layer. In summary, the incremental analyses suggest that liquefaction in the shallow layer would be prevented if *CRR* increased 25% (based on the strain criteria) to 30% (based on the excess pore water pressure criteria).

Figure 6.30 illustrates the pore water pressure ratios for the liquefiable layers throughout the NN1 deposit with a 1.35 increase in CRR in the layers at 2.5-4.0 m depth. This shows that liquefaction develops in the deep liquefiable layer at 8.5-10 m but is prevented from developing in the shallow layer where liquefaction resistance has been increased. When compared to the original response of this deposit to the same level of shaking (Figure 6.19(a)) it is evident that the increase in liquefaction resistance has caused soil layer interaction effects to have a significant impact on the development

of liquefaction in the deposit, as well as its manifestation at the ground surface. The ground motion that is shaking this shallow layer has been significantly damped due to passing through the deeper liquefied layer (see response spectra in Figure 6.31). The increase in liquefaction resistance in the upper layer means that this damped acceleration is no longer sufficient to liquefy this layer, and hence liquefaction is adverted at shallow depths.

The Boulanger and Idriss (2014) simplified method was also used to assess the response of the NN1 profile with a 1.35 increase in CRR in the layer 2.5-4.0 m. Figure 6.33 illustrates the pore water pressure ratio for the upper 10 m of the deposit calculated via both methods. This shows that the simplified method still estimates liquefaction triggering in the upper layer. The simplified method uses the assumption that soil layers behave independently of each other, which is inadequate when there is soil stratification such as in the NN profiles. As a result, the simplified method fails to account for the effect of soil layer interaction on the dynamic response of various layers in the deposit, and therefore overestimates the response of the whole soil deposit.

There are several potential reasons for an increased liquefaction resistance in the shallow liquefiable layers for the NN profiles. Firstly, partial saturation of the soil layers located immediately below the water table can increase their liquefaction resistance. For example, site 38178 at Paeroa Reserve in Riccarton was not fully saturated until a depth of 4.0 m as illustrated in Figure 6.34. V_p is seen to have values well below 1000 m/s in the top three meters, and does not reach levels associated with full saturation of 1500 m/s (the value for waves passing through water) until 4 m depth. Partial saturation is known to increase the liquefaction resistance of a soil as illustrated by Tsukamoto et al. (2002) in Figure 6.32.

Furthermore, the simplified method provides a conservative estimate of soil strength, and in the case of the Boulanger and Idriss (2014) deterministic triggering method, this is the 15th percentile value of *CRR*. The *CRR* value for q_{c1ncs}=80 is 27% higher for a liquefaction probability of 50% compared to 15% (Boulanger and Idriss, 2014). This percent increase is similar to the thresholds previously calculated and hence it is reasonable to expect that the shallow soil layers may have higher liquefaction resistance than modelled previously. Therefore, as shown in the previous sensitivity study, soil layer interaction may have a significant effect on the response of the NN type soil deposits to earthquake loading. As it is the shallowest soil layers that will be affected, surface manifestation of liquefaction can also be prevented. More importantly, the prevention of liquefaction in the shallowest layer as illustrated above, would result in an 8.5 m thick crust layer of non-liquefying soils which is fully consistent with no liquefaction manifestation on the ground surface as was the actual observation for the NN profiles from the Canterbury Earthquake Sequence.

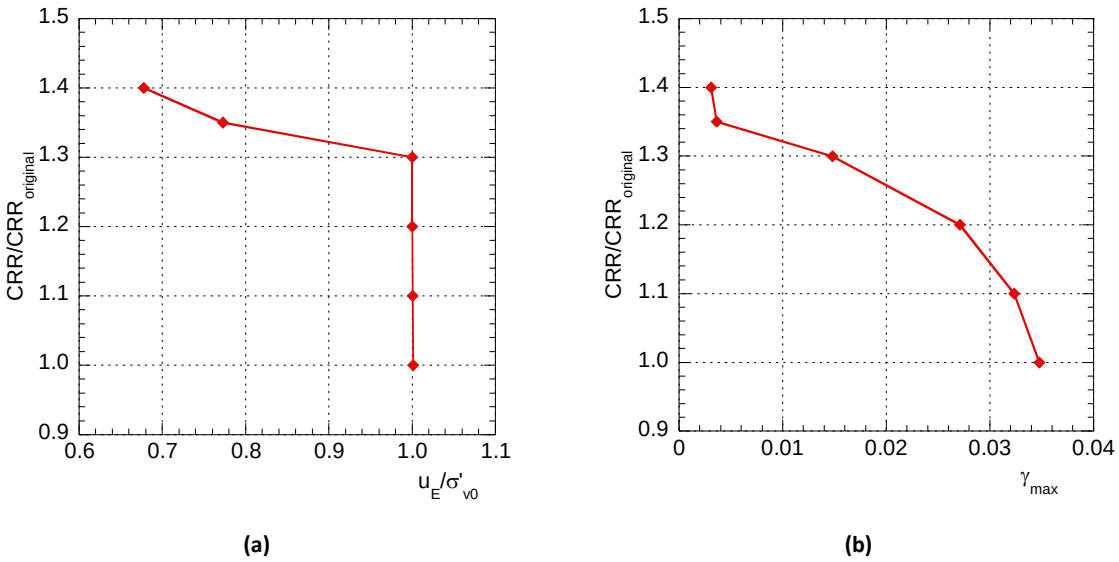

Figure 6.29: Plot of increase in *CRR* required to prevent liquefaction in shallow soil layers of NN1 profile: (a) using pore water pressure ratio; (b) using single amplitude shear strain

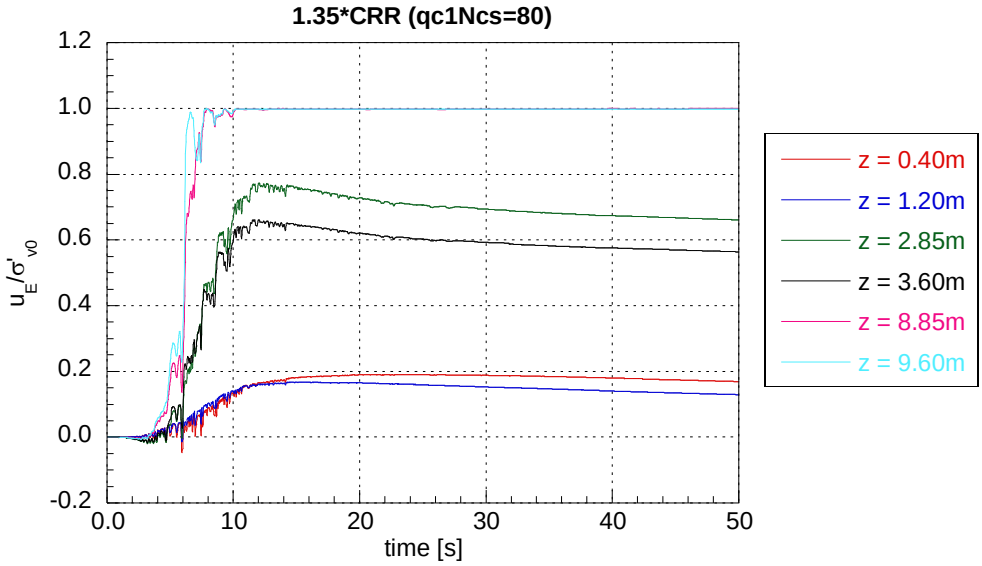

Figure 6.30: Pore water pressure ratios for liquefiable layers in the NN1 profile with a 1.35 increase in liquefaction resistance in the layer 2.5-4.0 m and a_{max}=0.4g

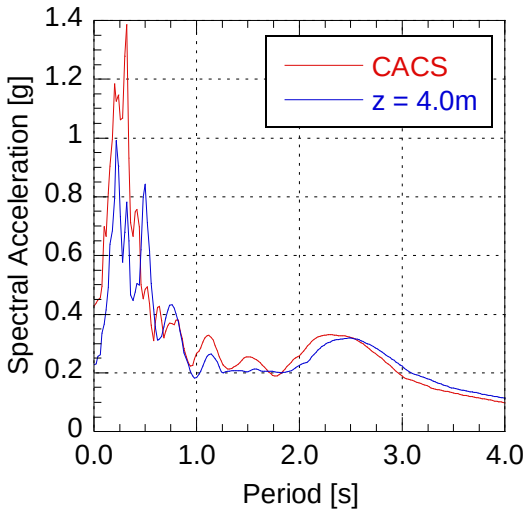

Figure 6.31: Response spectra of acceleration time history at the base of the shallow liquefiable layer for NN1, a_{max}=0.4g

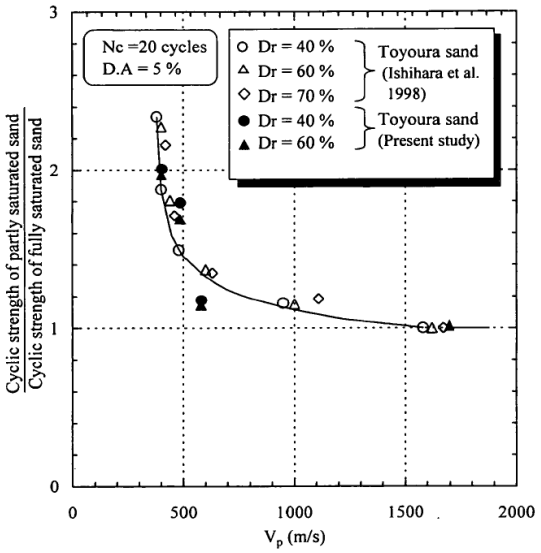

Figure 6.32: Relationship between V_p and increase in *CRR* of sandy soil (Tsukamoto et al., 2002)

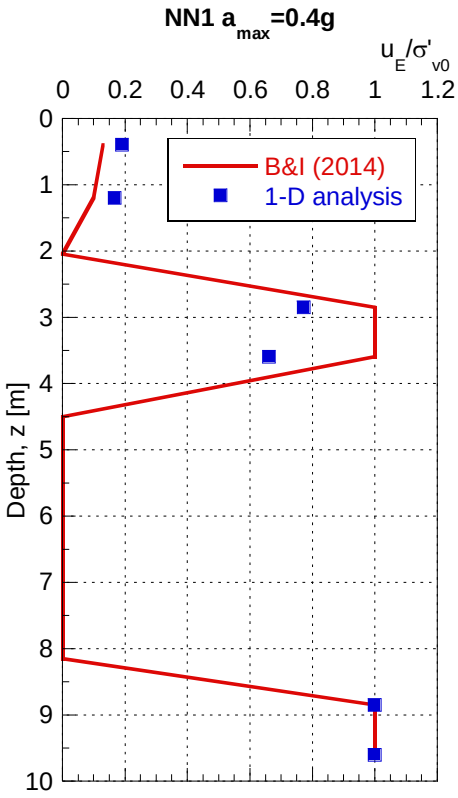

Figure 6.33: Pore water pressure ratio calculated using the simplified method and ESA for NN1, a_{max}=0.4g with a 1.35 increase in CRR in the layer 2.5-4.0 m

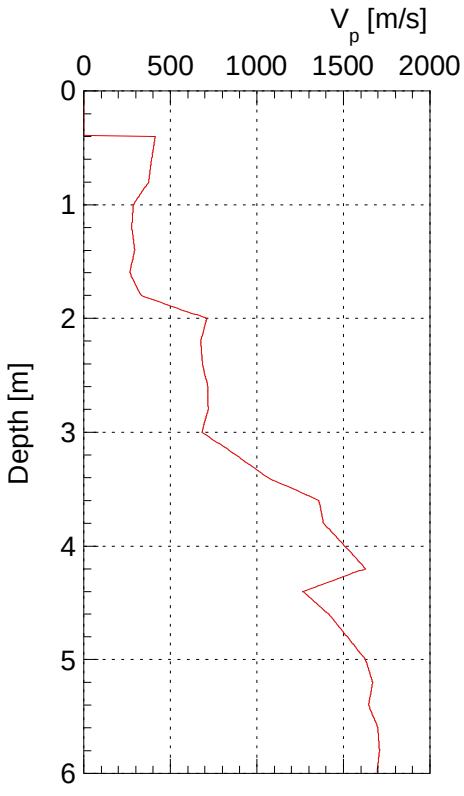

Figure 6.34: V_p data for site 38178 at Paeroa Reserve in Riccarton

7 Summary and Conclusions

In the 2010-2011 Canterbury Earthquake Sequence (CES) there was a significant variation in the performance of different sites throughout Christchurch, from no liquefaction manifestation to severe liquefaction manifestation. Further analysis showed the simplified method of liquefaction evaluation over-predicted moderate to severe liquefaction at some sites where no liquefaction was observed. One of the key differences at many of these sites was the highly stratified nature of the deposits, including interbedded liquefiable and non-liquefiable layers. Hence, the principal aim of this research was to investigate the effect of soil stratification on the development and consequences of liquefaction. Since the simplified method of liquefaction analysis cannot capture the interaction between different layers, nor the system response of a deposit, a rigorous effective stress time history analysis (ESA) was used as the principal tool in this research.

Comprehensive field and laboratory test data from 55 sites in Christchurch was used to develop four representative soil profiles which summarise soil deposit characteristics at sites that liquefied in both the September 2010 and February 2011 CES events (YY1 and YY2 profiles) and sites where there was no liquefaction manifestation in either event (NN1 and NN2 profiles). In this process simplified soil profiles, key layers and soil characteristics were identified for the 55 sites. These profiles were then assessed for common features and representative characteristics through a rigorous geotechnical characterisation and analysis. Since this study aimed to differentiate in terms of liquefaction manifestation, a range of factors were considered such as critical layers and critical zones, their thickness and proximity to the surface, as well as the continuity of liquefiable soils capable of generating significant excess pore pressures (and hence contributing to the liquefaction manifestation). The YY profiles were characterised by thick vertically continuous uniform sandy deposits, whereas the NN profiles were characterised by highly non-uniform deposits (vertically discontinuous in terms of liquefaction potential) with interlayering of liquefiable and non-liquefiable soils. The four representative profiles selected for ESA had the following characteristics in the top 10 m:

- YY1: a thick vertically continuous uniform sandy deposit of low liquefaction resistance, with a critical layer below the water table at 1.8-3.8 m depth. There was a continuous zone of low liquefaction resistance to 6 m depth (q_{c1Ncs} = 80-90) which constituted a critical zone of 1.8-6 m. The soils at 6-10 m had slightly higher liquefaction resistance in accordance with increasing soil density.

- YY2: generally similar to YY1, a thick vertically continuous uniform sandy deposit with a critical layer below the water table at 1.8-2.5 m and critical zone of low liquefaction resistance at 1.8-4 m. The soils below the critical zone had higher liquefaction resistance (i.e. density) than those in the YY1 profile.
- NN1: a non-uniform vertically discontinuous deposit with interlayered liquefiable and non-liquefiable layers. There were two non-liquefiable layers in the top 10 m; one below the water table at 1.6-2.5 m and the other, the key feature of the NN1 deposit, a thick non-liquefiable layer at 4-8.5 m. The liquefiable soils had very low liquefaction resistance similar to those in the critical layers of the YY profiles.
- NN2: generally similar to NN1, a non-uniform vertically discontinuous deposit with highly interlayered liquefiable and non-liquefiable layers. NN2 had five non-liquefiable layers (of thickness ≤ 1.5 m) throughout the top 10 m of the deposit. Again, the liquefiable layers had low liquefaction resistance similar to that of the critical layers in the YY profiles.

A fully-coupled, two-phase medium effective stress analysis (ESA) using a 1-D soil-column finite element model was used to analyse the four profiles. Deconvoluted motions scaled to three intensity levels of 0.2g, 0.3g and 0.4g were used as base input motions in the soil column model to perform a series of 12 time history analyses (three for each of the four profiles).

For the analyses, liquefaction resistance curves (LRCs) for all liquefiable soils in the top 10 m of the deposits were developed by following the simplified triggering procedure of Boulanger and Idriss (2014). Target LRCs were defined based on an estimated representative value of q_{c1Ncs} for each liquefiable layer and on effective overburden stress corrections depending on the location (depth) of the layer within the deposit. In a similar fashion, measured V_s values were used to define the initial shear modulus of non-liquefiable soils, and target G - γ degradation curves were defined to model the nonlinear behaviour of non-liquefiable silty layers or deeper non-liquefiable sandy soils.

An elastic-plastic constitutive model (Stress-Density Model), developed specifically for liquefaction problems, was employed as the constitutive model in the ESA. Model parameters for liquefiable layers were based on Toyoura sand properties, these were then modified to rigorously simulate target liquefaction resistance curves, defined for the characteristic soil layers in the representative profiles. In the model calibration process, the void ratio and a couple of dilatancy parameters were modified to capture the effects of density and to achieve an accurate modelling of the vertical position and slope of the target LRC. The parameters of the model for non-liquefiable soils were determined in a similar fashion using the elastic parameters and the stiffness and strength

parameters of the hyperbolic relationship for plastic deformation to reproduce the target G - γ degradation curve.

All YY analyses were performed allowing drainage and water flow to occur throughout the deposit while the NN analyses were conducted under restricted normal strains, assuming undrained conditions. Following the principal set of 12 effective stress analyses, simplified analyses were performed for the same soil profiles in order to compare the outcomes of the simplified method with those of the ESA. Additional ESAs were performed to investigate and illustrate the important effects of cross-interaction between soil layers on the system response of the deposit and on liquefaction manifestation in particular.

7.1 Key findings and conclusions

(1) System characteristics of a soil deposit including vertical continuity of liquefiable layers, absolute and relative liquefaction resistance of different layers, location and thickness of critical layers and zones, the presence of non-liquefiable layers, and highly stratified vertically discontinuous deposits with interlayered liquefiable and non-liquefiable layers, all have significant effects on the development of liquefaction and its manifestation at the ground surface. Soil layer interaction has a particularly pronounced effect when the soil profile consists of interlayered liquefiable and non-liquefiable layers.

(2) For the YY profiles, liquefaction developed in the critical layers at shallow depths below the water table. In both the YY1 and YY2 analyses, although the lower parts of the deposits below the critical zone did not liquefy under the highest excitation (0.4g), the excess pore water pressures generated at those depths where significant. This implies that, in addition to shaking induced liquefaction and associated deformation, the critical layers were subjected to continuous water flow from the layers below. This produced additional disturbance of fabric and structure and added to the liquefaction effects and consequences in the critical layer and the deposit as a whole. Hence, vertical continuity of liquefiable layers create conditions for a system response that would increase the severity of liquefaction and its manifestation. While the ESA cannot capture details such as liquefaction manifestation on the ground surface, these consequences can be easily inferred from an in-depth analysis of the ESA results.

(3) The key difference for the NN profiles is that the continuity of the deposit and communication of liquefied layers is disrupted by the presence of non-liquefiable layers. Instead, for the NN profiles, system response in the way of soil layer interaction occurs when liquefaction of a deeper layer within the soil profile substantially modifies the seismic demand in the shallow layers. This modification of acceleration amplitudes can reduce the rate of excess pore water

pressure development occurring in shallow soil layers and, in some cases, this can be sufficient to prevent liquefaction (that would otherwise be predicted by the simplified method). Hence, the effects of cross-layer interaction result in dramatically different liquefaction consequences and can prevent liquefaction manifestation at the ground surface.

(4) A sensitivity analysis identified that an increase in the liquefaction resistance of 25% to 30% would prevent liquefaction from occurring in the shallow critical layer of the NN1 profile. This would result in an 8.5 m crust layer of non-liquefying soils which is fully consistent with the observations of no liquefaction manifestation for these sites during the CES. Hence, a relatively small increase in the liquefaction resistance of shallow soil layers can prevent liquefaction from occurring near the surface.

(5) One possible reason for an increase in the liquefaction resistance of these shallow soil layers is the partial saturation of the soil deposit, especially at shallow depths below the water table. This effect has been detected through V_p measurements in the field, particularly at sites where no liquefaction manifested.

(6) The simplified method is relatively consistent with observations in predicating the response of thick continuous sandy deposits. Although the simplified method significantly over-predicts the extent of liquefaction damage for the YY profiles (i.e. over-predicts shear strains and settlement due to volumetric strains alone), both the simplified method and the ESA modelling predicted the same outcome; that liquefaction would occur and manifest on the surface.

(7) The simplified method was unsuccessful in predicting the response of non-uniform soil deposits with interlayered liquefiable and non-liquefiable layers. One of the key assumptions made in the simplified method is that soil layers act independently of each other with no reference to cross-interactions between layers and the system response of the soil deposit as a whole. As a result, the simplified method does not capture the effects of soil layer interaction. Consequently, the simplified method over-predicts liquefaction manifestation for these highly non-uniform soil deposits because it cannot capture the two key mechanisms of soil layer interaction that prevent liquefaction manifestation at the ground surface.

7.2 Recommendations for further research

Future studies should focus on a more in depth analysis, to characterise representative soil profiles in more detail and investigate other aspects of soil layer interaction.

Deconvolution of recorded surface ground motions was used to define the input ground motion for the ESA. This aspect of the analysis could be further investigated through the use of additional ground motions with a wider range of ground motion characteristics.

In this study, four generic simplified profiles were developed as representative of two categories of liquefaction manifestation observed in the CES. Future studies should focus on developing a more detailed and comprehensive characterisation of Christchurch soils. This may be through the consideration of additional representative soil profiles, or from using a more rigorous statistical analysis and a probabilistic framework for performing such classification. More rigorous modelling of the representative soil profiles using laboratory test data for the Christchurch soils should also be attempted. All of the above are already in progress in a separate but related study (Ntritsos, 2016).

This study focussed on only one aspect of soil layer interaction, the modification of the ground motion due to liquefaction occurring in the top 10 m of the deposit. Other key factors such as cross-layer interaction through water flow and dissipation of pore water pressures, and the combination of this and the effect of ground motion modification were not explored in depth. Further research is needed into these additional aspects of soil layer interaction and how they affect liquefaction development in stratified profiles.

References

Beyzaei, C. Z., Bray, J. D., Cubrinovski, M., Riemer, M., Stringer, M. E., Jacka, M., Wentz, F. J. (2015). "Liquefaction resistance of silty soils at the Riccarton Road site, Christchurch, New Zealand". *Proc. 6th Int. Conf. Earthquake Geotech. Eng.,* Christchurch, New Zealand. Paper No. 616.

Boulanger, R. W. and Idriss, I. M. (2014). "CPT and SPT Based Liquefaction Triggering Procedures". Centre for Geotechnical Modelling, Davis, CA

Bowen, H. J. and Cubrinovski, M. (2008). "Effective Stress Analysis of Piles on Liquefiable Soil: A Case Study of a Bridge Foundation". *Bulletin of the New Zealand Society for Earthquake Engineering*, 41(4).

Bradley, B. A. (2013). "A New Zealand-Specific Pseudospectral Acceleration Ground-Motion Prediction Equation for Active Shallow Crustal Earthquakes Based on Foreign Models". *Bulletin of the Seismological Society of America* 103(3) 1801-1822

Bray, J., Cubrinovski, M., Zupan, J., and Taylor, M. (2014) "Liquefaction Effects on Buildings in the Central Business District of Christchurch*". Earthquake Spectra*, 30(1), 85-109

Byrne, P. M., Park, S-S., Beaty, M., Sharp, M., Gonzalez, L., Abdoun, T. (2004). "Numerical modeling of liquefaction and comparison with centrifuge tests". *Can. Geotech. J.,* 41(2), 193-211.

Cubrinovski, M. (1993). "A constitutive model for sandy soils based on a stress-dependent density parameter*"*. PhD Thesis, University of Tokyo.

Cubrinovski, M. (2011). "Sesimic Effective Stress Analysis: Modelling and Application*"*. *Proc. 5th Int. Conf. Earthquake Geotech. Eng.*, Santiago, Chile.

Cubrinovski, M. (2015). "ENEQ620: Advanced Geotechnical Earthqauke Engineering". [Lecture notes]

Cubrinovski, M., Bradley, B., Wotherspoon, L., Green, R., Bray, J., Wood, C., Pender, M., Allen, J., Bradshaw, A., Rix, G., Taylor, M., Robinson, K., Henderson, D., Giorgini, S., Ma, K., Winkley, A., Zupan, J., O'Rourke, T., DePascale, G., Wells, D. (2011). "Geotechnical Aspects of the 22 February 2011 Christchurch earthquake*". Bulletin of the New Zealand society for Earthquake Engineering*, 44(4)

Cubrinovski, M., Bray, J., Taylor, M., Giorgini, S., Bradley, B., Wotherspoon, L., Zupan, J. (2011). "Soil Liquefaction Effects in the Central Business District during the February 2011 Christchurch Earthquake*". Seismological Research Letters*, 82(6), 893-904

Cubrinovksi, M. and Ishihara, K. (1998a). "Modelling of sand behaviour based on the state concept*". Soils and Foundations* 38(3) 115-127.

Cubrinovksi, M. and Ishihara, K. (1998b). "State concept and modified elasto-plasticity for sand modelling". *Soils and Foundations*, 38(4), 213-225.

Cubrinovski, M. and Ishihara, K. (1999). "Empirical correlation between SPT N-value and relative density for sandy soils*". Soils and Foundations*, 39(5), 61-71.

Cubrinovski, M. and Ishihara, K. (2000). "Flow potential of sandy soils with different grain compositions*". Soils and Foundations,* 40(4), 103-119

Cubrinovski, M., Ishihara, K., Tanizawa, F. (1996). "Numerical Simulation of the Kobe Port Island Liquefaction". *Proc. 11th World Conf. Earthquake Eng*.

Darendeli, M. BG. (2001). "Development of a New Family of Normalized Modulus Reduction and Material Damping Curves". PhD Thesis, University of Texas, Austin

GeoLogismiki. (2006). Cliq (Version 1.7.6.49) [Computer software]. Retrieved from https://geologismiki.gr/products/cliq/

Geonet. (January 2017). M 6.3, Christchurch, 22 February 2011 [Website page]. Retrieved from http://info.geonet.org.nz/display/quake/M+6.3%2C+Christchurch%2C+22+February+2011

Geonet. (January 2017). M 7.1, Darfield (Canterbury), 4 September 2010 [Website page]. Retrieved from http://info.geonet.org.nz/display/quake/M+7.1%2C+Darfield+%28Canterbury%29%2C+4+September+2010

Google Maps. (February 2017). Retrieved from https://www.google.co.nz/maps/@-43.5071447,172.7115055,12.5z?hl=en

Green, R. A., Cubrinovski, M., Cox, B., Wood, C., Wotherspoon, L., Bradley, B., Maurer, B. (2014). "Select liquefaction case histories from the 2010-2011 Canterbury earthquake sequence". *Earthquake Spectra,* 30 (1), 131-153.

Idriss, I. M., and Boulanger, R. W. (2008). "Soil liquefaction during earthquakes". Earthquake Engineering Research Institute, Oakland, CA.

Ishihara, K. and Yoshimine, M. (1992). "Evaluation of settlements in sand deposits following liquefaction during earthquakes". *Soils and Foundations*, 32(1), 178-188

Kramer, S. L. (1996) "Geotechnical Earthquake Engineering". Upper Saddle River, New Jersey: Prentice Hall

Marcuson III, W. F., Hynes, M. E., Franklin, A. G. (1990). "Evaluation and Use of Residual Strength on Seismic Safety Analysis of Embankments". *Earthquake Spectra*, 6(3), 529-572

Markham, C. S. (2015). "Response of Liquefiable Sites in the Central Business District of Christchurch, New Zealand". PhD Thesis, University of California, Berkeley

McGann, C. R., Bradley, B. A., Taylor, M. L., Wotherspoon, L. M., Cubrinovski, M. (2015). "Development of an empirical correlation for predicting shear wave velocity of Christchurch soils from cone penetration test data". *Soil Dynamics and Earthquake Engineering*, 66-75

Murashev, A., Kirkcaldie, D., Keepa, C., Cubrinovski, M., Orense, R. (2014). "The development of design guidance for bridges in New Zealand for liquefaction and lateral spreading effects". New Zealand Transport Agency (NZTA) research report 553.

New Zealand Geotechnical Society (NZGS). (2010). "Geotechnical earthquake engineering practice: Module 1 - Guideline for the identification, assessment and mitigation of liquefaction hazards".

Rathje, E. M., and Kottke, A. (2010). Strata (Version alpha) [Computer software]. Retrieved from https://nees.org/resources/strata

Robertson, P. K., and Wride, C. E. (1998). "Evaluating cyclic liquefaction potential using the cone penetration test." *Canadian Geotechnical Journal*, 35(3), 442–459

Seed, H. B. and Idriss, I. M. (1971). "Simplified Procedure for Evaluating Soil Liquefaction Potential". *Journal of the Soil Mechanics and Foundations*, ASCE, 97, 1249-1273.

Stringer, M., Beyzaei, C., Cubrinovski, M., Bray, J., Riemer, M., Jacka, M., Wentz, F. (2015). "Liquefaction Characteristics of Christchurch Silty Soils: Gainsborough Reserve". *Proc. 6th Int. Conf. Earthquake Geotech. Eng.*, Christchurch, New Zealand. Paper No. 726.

Tonkin & Taylor. (2015). "Crosshole Geophysics Study: Liquefaction Case Histories in Christchurch City February Land Damage with V_sV_p Study Locations" [Earthquake damage map]

Tonkin & Taylor. (2015). Crosshole Geophysics Study: Liquefaction Case Histories in Christchurch City September Land Damage with V_sV_p Study Locations [Earthquake damage map]

Tonkin & Taylor. (2015). Crosshole Geophysics Study: Liquefaction Case Histories in Christchurch City Technical Categories with V_sV_p Study Locations [Earthquake damage map]

Tsukamoto, Y., Ishihara, I., Nakazawa, H., Kamada, K., Huang, Y. (2002). "Resistance of Partly Saturated Sand to Liquefaction with Reference to Longitudinal and Shear Wave Velocities". *Soils and Foundations*, 42(6), 93-104

van Ballegooy, S., Malan, P., Lacrosse, V., Jacka, M. E., Cubrinovski, M., Bray, J. D., O'Rourke, T. D., Crawford, S. A., Cowan, H. (2014). "Assessment of Liquefaction-Induced Land Damage for Residential Christchurch". *Earthquake Spectra*, 30(1), 31-55

Wotherspoon, L. M., Orense, R., Bradley, B. A., Cox, B. R., Wood, C., Green, R. A. (2013). "Geotechnical characterization of Christchurch strong motion stations". *Earthquake Commission Report* (Project No. 12/629) v1

Yee, E., Stewart, J. P., Tokimatsu, K. (2013). "Elastic and Large-Strain Nonlinear Seismic Site Response from Analysis of Vertical Array Recordings". *Journal of Geotechnical and Environmental Engineering* 139(10) 1789-1801

Youd, T. L., Idriss, I. M. (2001). "Liquefaction Resistance of Soils: Summary Report from the 1996 NCEER and 1998 NCEER NSF Workshops on Evaluation of Liquefaction Resistance of Soils" *Journal of Geotechnical and Geoenvironmental Engineering*, 127(4)

Zeghal, M., Elgamal, A-W., Zeng, X., Arulmoli, K. (1999). "Mechanism of Liquefaction Response in Sand–Silt Dynamic Centrifuge Tests". *Soil Dynamics and Earthquake Engineering*, 18(1), 71-85.

Zhang, G., Robertson, P. K., Brachman, R. W. I. (2002). "Estimating liquefaction-induced ground settlements from CPT for level ground". *Can. Geotech. J.*, 39, 1168-1180

Appendix A: Analysis of centrifuge tests

The Boulanger and Idriss (2014) simplified method for evaluating liquefaction triggering was applied to the data in Byrne et al. (2003) as follows.

The model was 24 m thick Nevada sand with the top 16 m dense sand (D_r=75%) the bottom 8 m medium sand (D_r=55%) and the water table at the ground surface as illustrated in Figure A.1. The soil properties are set out in Table A.1. Where the void ratio, e, was calculated from

$$D_r = \frac{e_{max} - e}{e_{max} - e_{min}} \quad \text{A.1}$$

Table A.1: Soil properties for model 3 in Byrne et al. (2003)

	Dense sand	Medium sand	Reference
Dr	75%	55%	Byrne et al. (2003)
e_{max}	0.887	0.887	For Nevada sand in Cubrinovski and Ishihara (2000)
e_{max}-e_{min}	0.376	0.376	For Nevada sand in Cubrinovski and Ishihara (2000)
e	0.605	0.680	Equation A.1

The soil profile was divided into layers based on the location of accelerometers and pore pressure transducers as shown in Figure A.1.

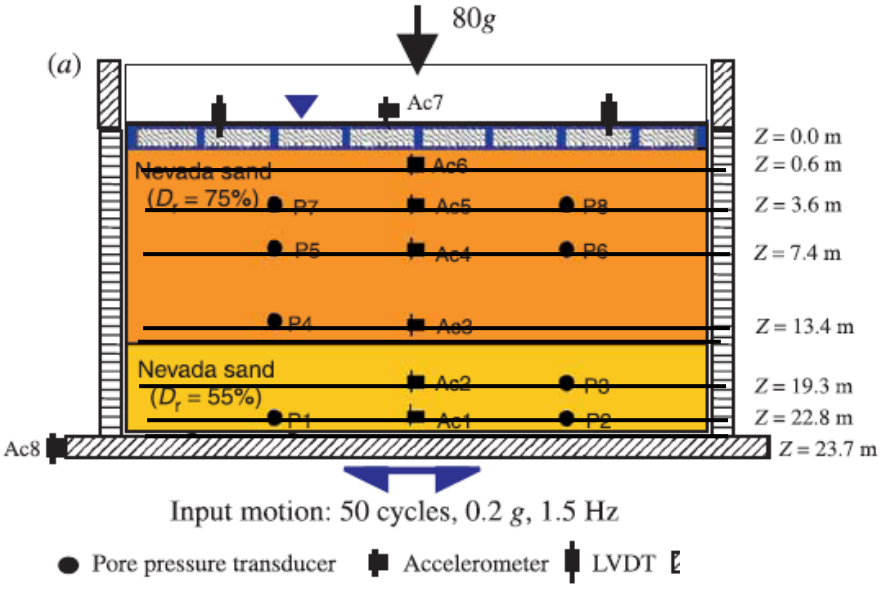

Figure A.1: Soil profile for model 3 (Byrne et al., 2003)

The unit weight of the soil was calculated as per Equation A.2.

$$\gamma_s = \frac{G_s + e}{1 + e} \cdot \gamma_w \quad \text{A.2}$$

Where γ_w is the unit weight of water approximated as 10 kN/m^3 and G_s was taken as 2.65. This gave a saturated unit weight of 20.2 kN/m^3 and 19.8 kN/m^3 for the dense and medium sands respectively. The total and effective confining stresses were calculated assumed an overburden pressure of 140 kPa as applied in the model.

As per the simplified method, the factor of safety against liquefaction triggering was calculated as per Equations A.3-A.8.

$$FS = \frac{CRR}{CSR} \cdot MSF \cdot K_\sigma \quad \text{A.3}$$

The *CSR* for a uniform load is

$$CSR = \frac{a_{max}}{g} \cdot \frac{\sigma_{v0}}{\sigma'_{v0}} \cdot r_d \quad \text{A.4}$$

With r_d

$$r_d = \exp(\alpha + \beta M) \quad \text{A.5}$$

$$\alpha = -1.012 - 1.126 \sin\left[\left(\frac{z}{11.73}\right) + 5.133\right] \quad \text{A.6}$$

$$\beta = 0.106 + 0.118 \sin\left[\left(\frac{z}{11.28}\right) + 5.142\right] \quad \text{A.7}$$

M is the magnitude and *z* the depth below the ground surface.

The *CRR* was estimated as per Equation A.8.

$$CRR = \exp\left[\left(\frac{(N_1)_{60cs}}{14.1}\right) + \left(\frac{(N_1)_{60cs}}{126}\right)^2 - \left(\frac{(N_1)_{60cs}}{23.6}\right)^3 + \left(\frac{(N_1)_{60cs}}{25.4}\right)^4 - 2.8\right] \quad \text{A.8}$$

Where $(N_1)_{60cs}$ is the normalized, clean sand equivalent SPT blow count. SPT *N*-value is corrected for fines using Equations A.9 and A.10.

$$(N_1)_{60cs} = (N_1)_{60} + \Delta(N_1)_{60} \quad \text{A.9}$$

$$\Delta(N_1)_{60} = \exp\left[1.63 + \left(\frac{9.7}{FC + 0.01}\right) - \left(\frac{15.7}{FC + 0.01}\right)^2\right] \quad \text{A.10}$$

And *FC* is the fines content.

The SPT blow count was estimated from the relative density and void ratio range, using the relationship developed by Cubrinovski and Ishihara (1999) (Equation A.11).

$$N_1 = \frac{9}{(e_{max} - e_{min})^{1.7}} \cdot {D_r}^2 \quad \text{A.11}$$

The *MSF* was estimated using Equations A.12 and A.13.

$$MSF = 1 + (MSF_{max} - 1)\left(8.64 \exp\left(-\frac{M}{4}\right) - 1.325\right) \quad \text{A.12}$$

$$MSF_{max} = 1.09 + \left(\frac{(N_1)_{60cs}}{31.5}\right)^2 \leq 2.2 \quad \text{A.13}$$

And the overburden correction factor K_σ was estimated as per Equations A.14 and A.15.

$$K_\sigma = 1 - C_\sigma \ln\left(\frac{\sigma'_v}{p_a}\right) \leq 1.1 \quad \text{A.14}$$

$$C_\sigma = \frac{1}{18.9 - 2.55\sqrt{(N_1)_{60cs}}} \leq 0.3 \quad \text{A.15}$$

Where p_a is the atmospheric pressure.

Using a uniform a_{max} = 0.15 g at the ground surface, a M_w 8.5 earthquake based on the number of load cycles, and assuming a fines content of 8% for Nevada sand (Cubrinovski and Ishihara, 2000), the following results (Table A.2) were obtained.

Table A.2: Spreadsheet calculations for factor of safety against liquefaction triggering using the Boulanger and Idriss (2014) simplified method for model 3 (Byrne et al., 2003)

Layer	z (m)	σ_{v0} (kPa)	σ'_{v0} (kPa)	α	β	r_d	CSR	$(N_1)_{60}$
1	0.0	140	140	0.0159	-0.001	1.01	0.151	26.7
2	0.6	152	146	-0.0090	0.001	1.00	0.157	26.7
3	3.6	213	177	-0.1711	0.020	1.00	0.180	26.7
4	7.4	290	216	-0.4532	0.051	0.98	0.198	26.7
5	13.4	411	277	-1.0032	0.112	0.95	0.211	26.7
6	16.0	463	303	-1.2510	0.138	0.93	0.212	26.7
7	19.3	529	336	-1.5471	0.170	0.90	0.213	14.4
8	22.8	598	370	-1.8147	0.197	0.87	0.211	14.4
9	23.7	616	379	-1.8728	0.203	0.86	0.210	14.4

Layer	$\Delta(N_1)_{60}$	$(N_1)_{60cs}$	CRR	C_σ	K_σ	MSF_{max}	MSF	FS
1	0.368	27.1	0.349	0.178	0.974	1.83	0.757	1.7
2	0.368	27.1	0.349	0.178	0.971	1.83	0.757	1.6
3	0.368	27.1	0.349	0.178	0.956	1.83	0.757	1.4
4	0.368	27.1	0.349	0.178	0.941	1.83	0.757	1.3
5	0.368	27.1	0.349	0.178	0.922	1.83	0.757	1.2
6	0.368	27.1	0.349	0.178	0.914	1.83	0.757	1.1
7	0.368	14.7	0.154	0.110	0.942	1.31	0.910	0.6
8	0.368	14.7	0.154	0.110	0.938	1.31	0.910	0.6
9	0.368	14.7	0.154	0.110	0.937	1.31	0.910	0.6

Appendix B: CACS modulus and damping degradation curves

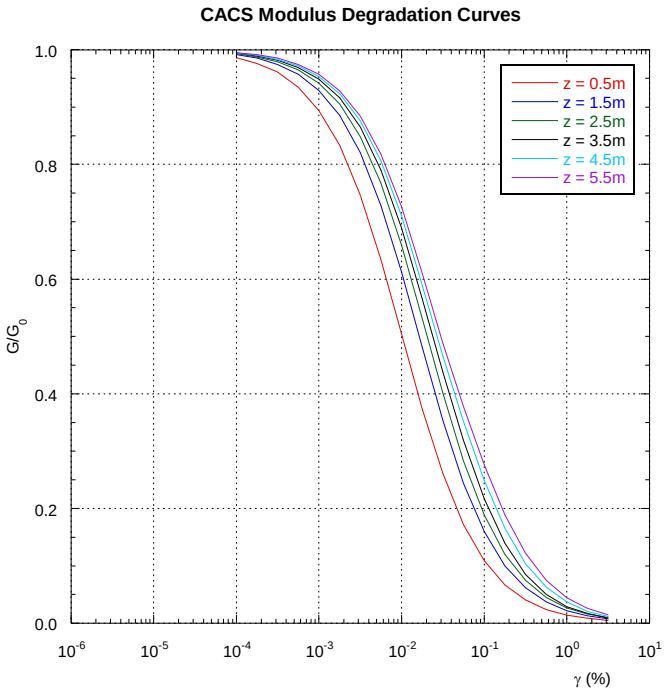

(a)

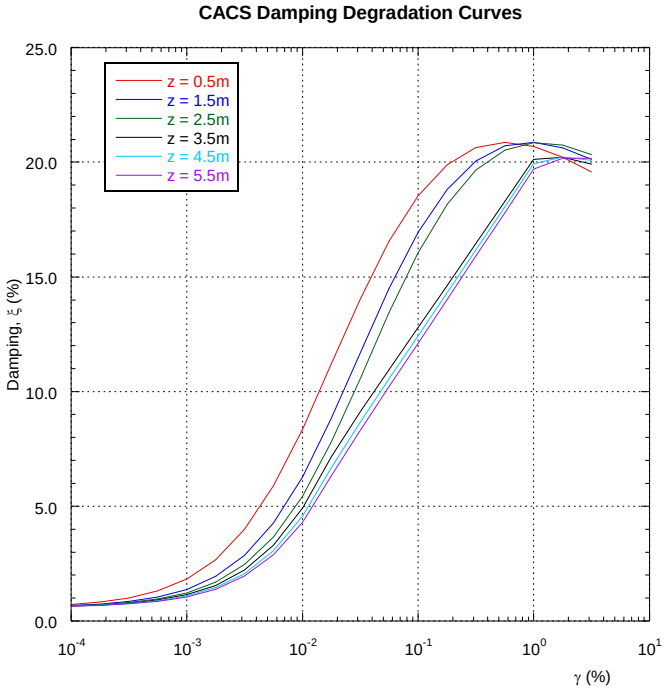

(b)

Figure B.1: Modified degradation curves for CACS: (a) shear modulus degradation curve; (b) damping degradation curve

Appendix C: RHSC modulus and damping degradation curves

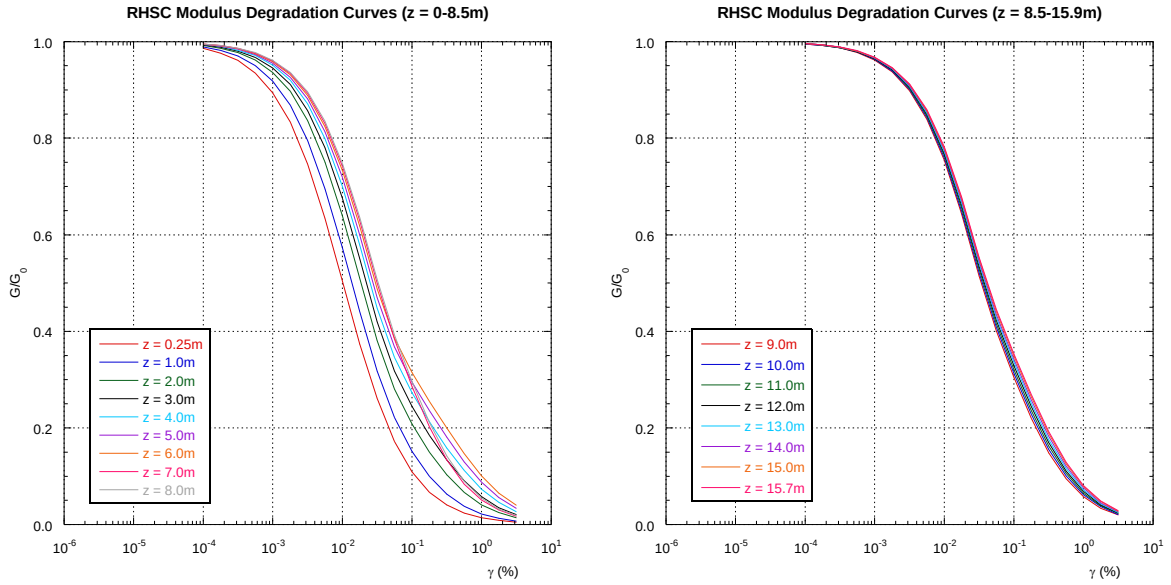

(a) **(b)**

Figure C.1: Modified shear modulus degradation curves for RHSC: (a) z=0-8.5m; (b) z=8.5-15.9m

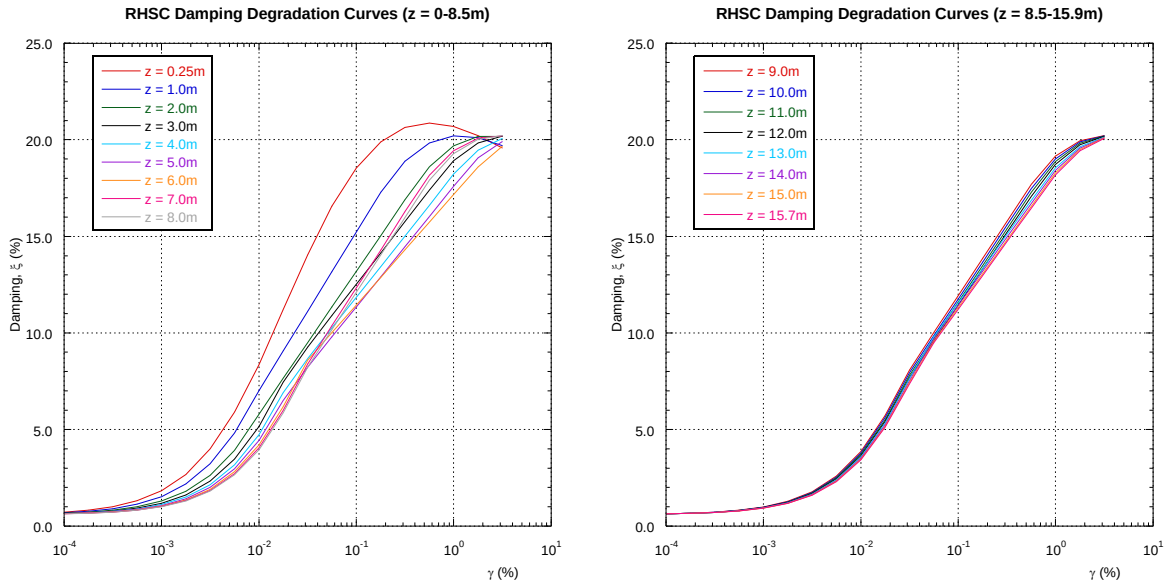

(a) **(b)**

Figure C.2: Modified damping degradation curves for RHSC: (a) z=0-8.5m; (b) z=8.5-15.9m

Appendix D: CHHC modulus and damping degradation curves

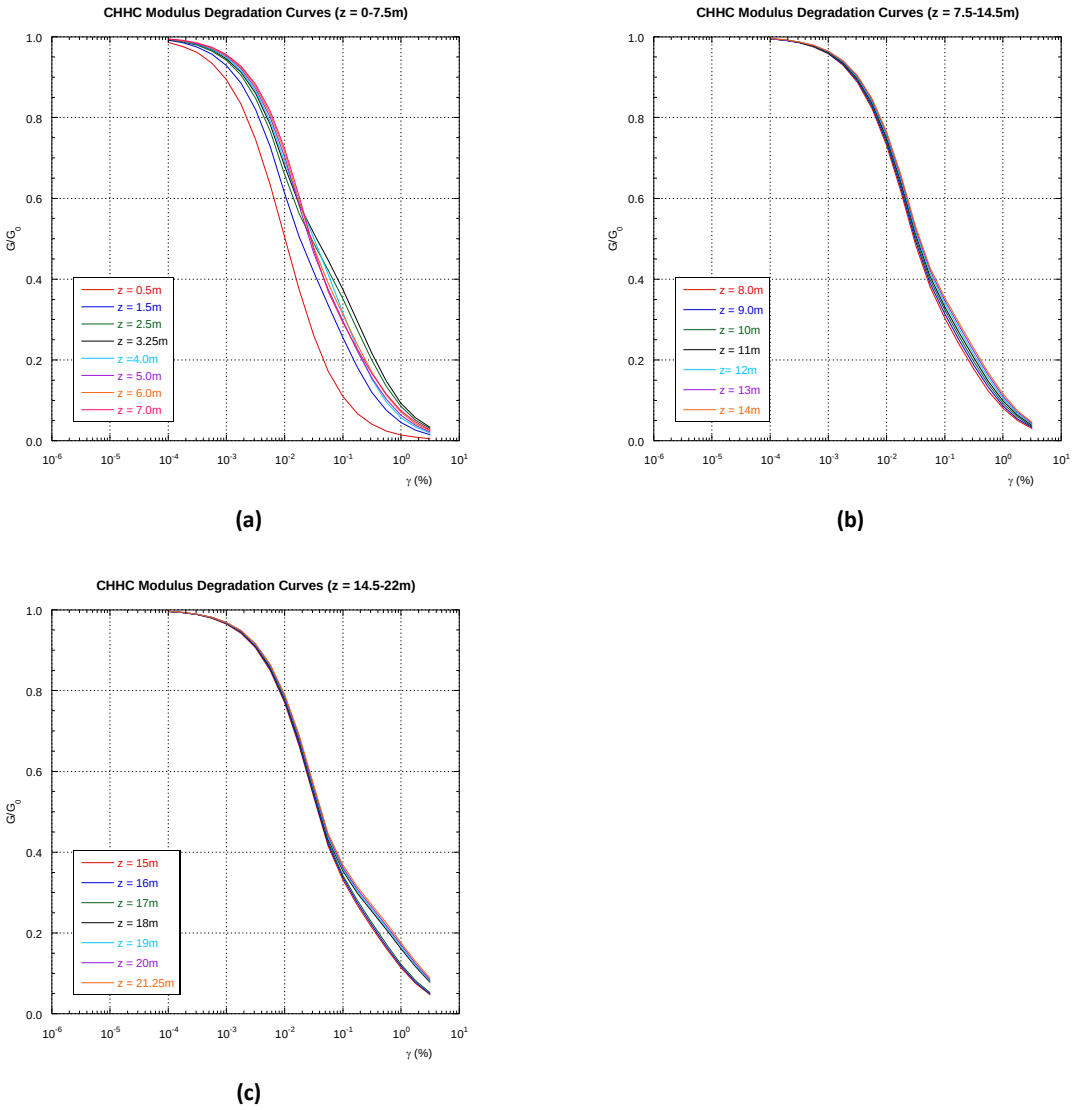

Figure D.1: Modified shear modulus degradation curves for CHHC: (a) z=0-7.5m; (b) z=7.5-14.5m; (c) z=14.5-22m

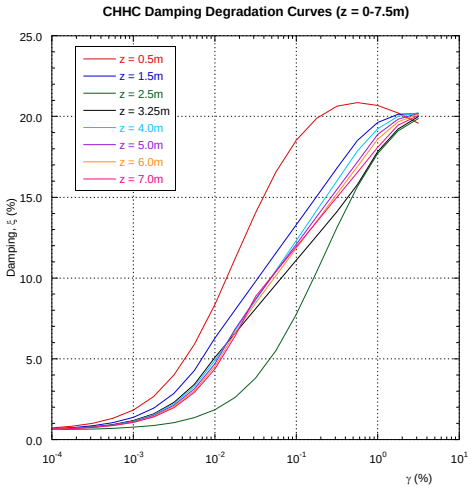

(a)

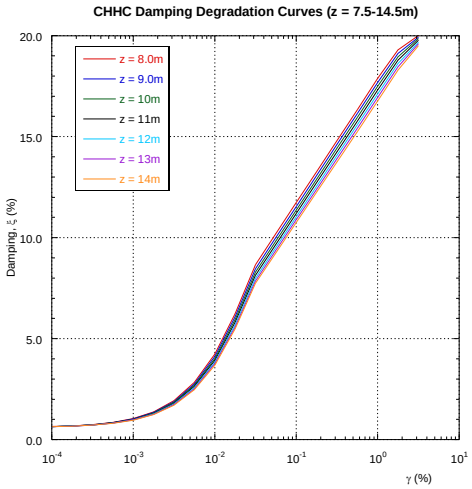

(b)

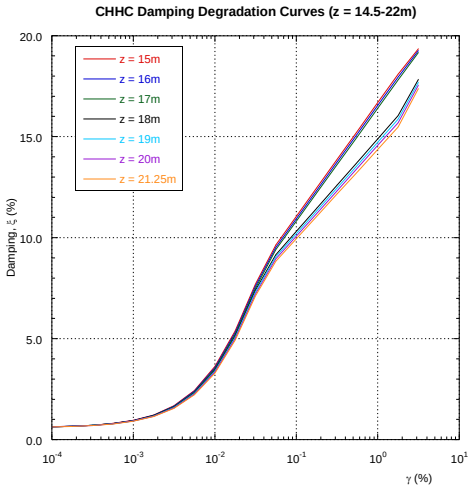

(c)

Figure D.2: Modified damping degradation curves for CHHC: (a) z=0-7.5m; (b) z=7.5-14.5m; (c) z=14.5-22m

Appendix E: Scale factors used in validation of deconvoluted motions

Table E.1: Scale factors for all sites considered in the deconvolution of the 13 June 2011 earthquake

	Motion 13 Jun 2011			
Site		CACS	RHSC	CHHC
	CACS	1	0.73	-
	RHSC	1.36	1	-
	CHHC	3.38	2.45	1

Table E.2: Scale factors for all sites considered in the deconvolution of the 22 February 2011 earthquake

	Motion 22 Feb 2011			
Site		CACS	RHSC	CHHC
	CACS	1	0.63	-
	RHSC	1.60	1	-
	CHHC	2.23	1.70	1

Table E.3: Scale factors for all sites considered in the deconvolution of the 4 September 2010 earthquake

	Motion 4 Sep 2010			
Site		CACS	RHSC	CHHC
	CACS	1	0.97	-
	RHSC	1.03	1	-
	CHHC	0.80	0.77	1

Appendix F: Validation of motions deconvoluted for the 13 June 2011 earthquake

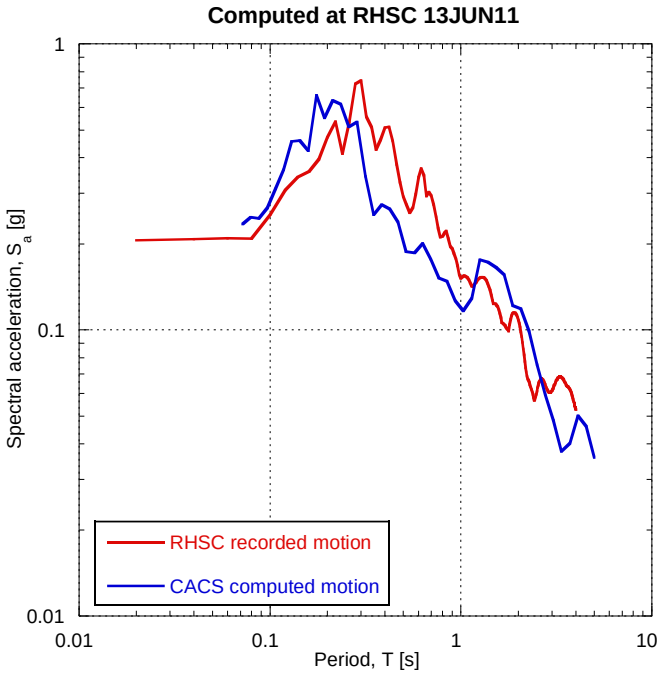

(a)

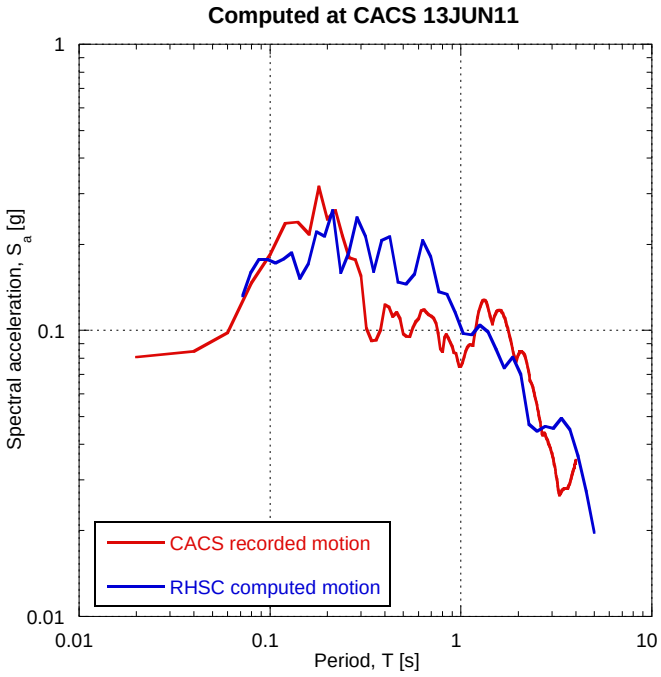

(b)

Figure F.1: Comparison of response spectra between surface motion computed using a deconvoluted motion and the recorded surface ground motion for 13 June 2011 earthquake: (a) CACS deconvoluted motion at RHSC site; (b) RHSC deconvoluted motion at CACS site

Appendix G: Results of critical layer analysis showing for q_{c1Ncs} for a single critical layer per site

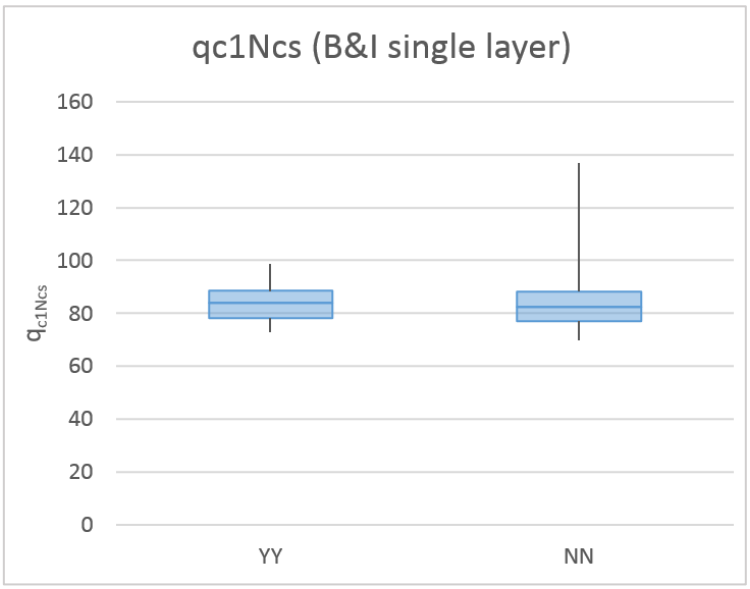

(a)

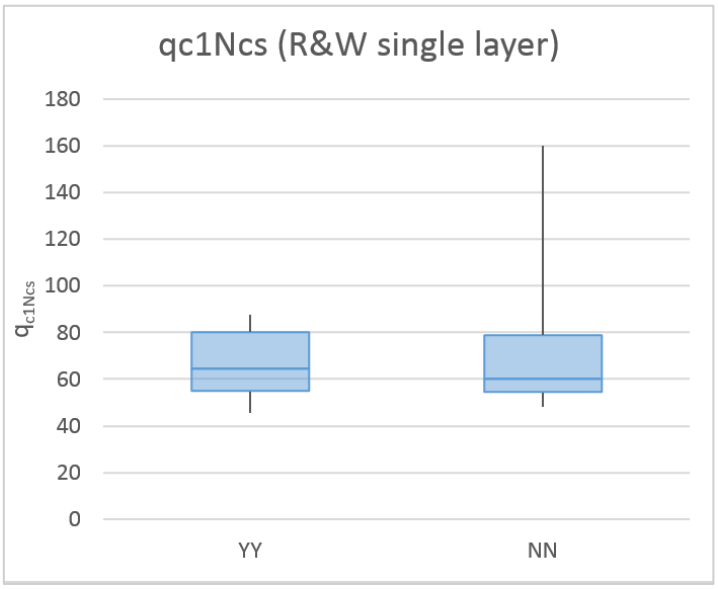

(b)

Figure G.1: Results of critical layer analysis showing comparison of q_{c1Ncs} properties for the YY and NN cases of liquefaction manifestation considering only one critical layer at each site (values at the end of the whiskers represent the minimum and maximum values for each dataset) (a) q_{c1Ncs} from Boulanger and Idriss (2014); (b) q_{c1Ncs} from Robertson and Wride

Appendix H: Target LRCs for YY2, NN1 and NN2 liquefiable layers

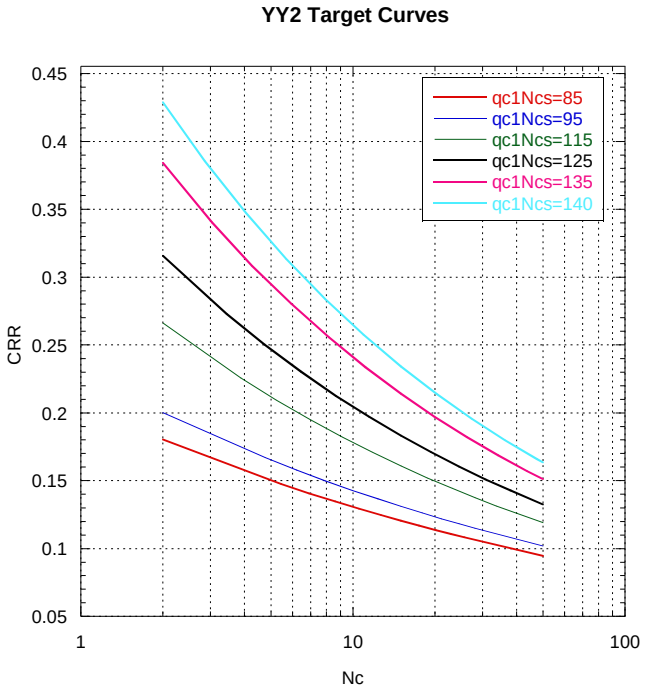

(a)

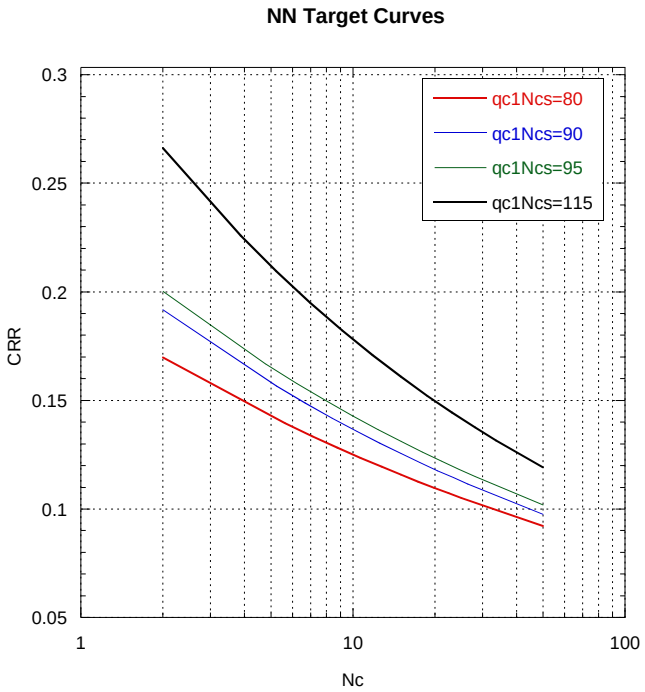

(b)

Figure H.1: Target liquefaction resistance curves for liquefiable soils at 100 kPa: (a) YY1 soils; (b) NN1 and NN2 soils

Appendix I: S-D Modelling of target LRCs for YY2, NN1 and NN2 liquefiable layers

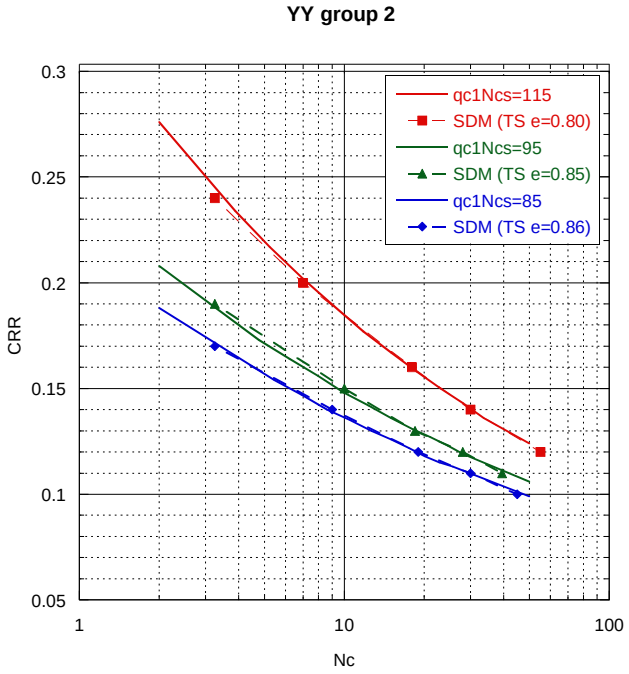

(a)

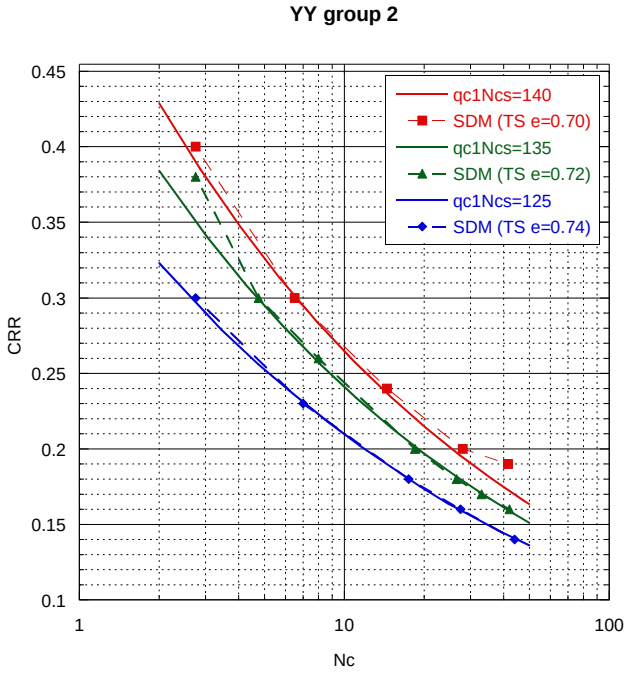

(b)

Figure I.1: S-D Model (SDM) LRCs (symbols and dashed lines) and target LRCs (solid lines) for YY2 soils of different densities: (a) q_{c1Ncs}=85, 95, 115, σ'_{v0}=35.6kPa, 42.0kPa, 48.9kPa (respectively); (b) q_{c1Ncs}=125, 135, 140, σ'_{v0}=65.5kPa, 86.25kPa, 100.9kPa (respectively)

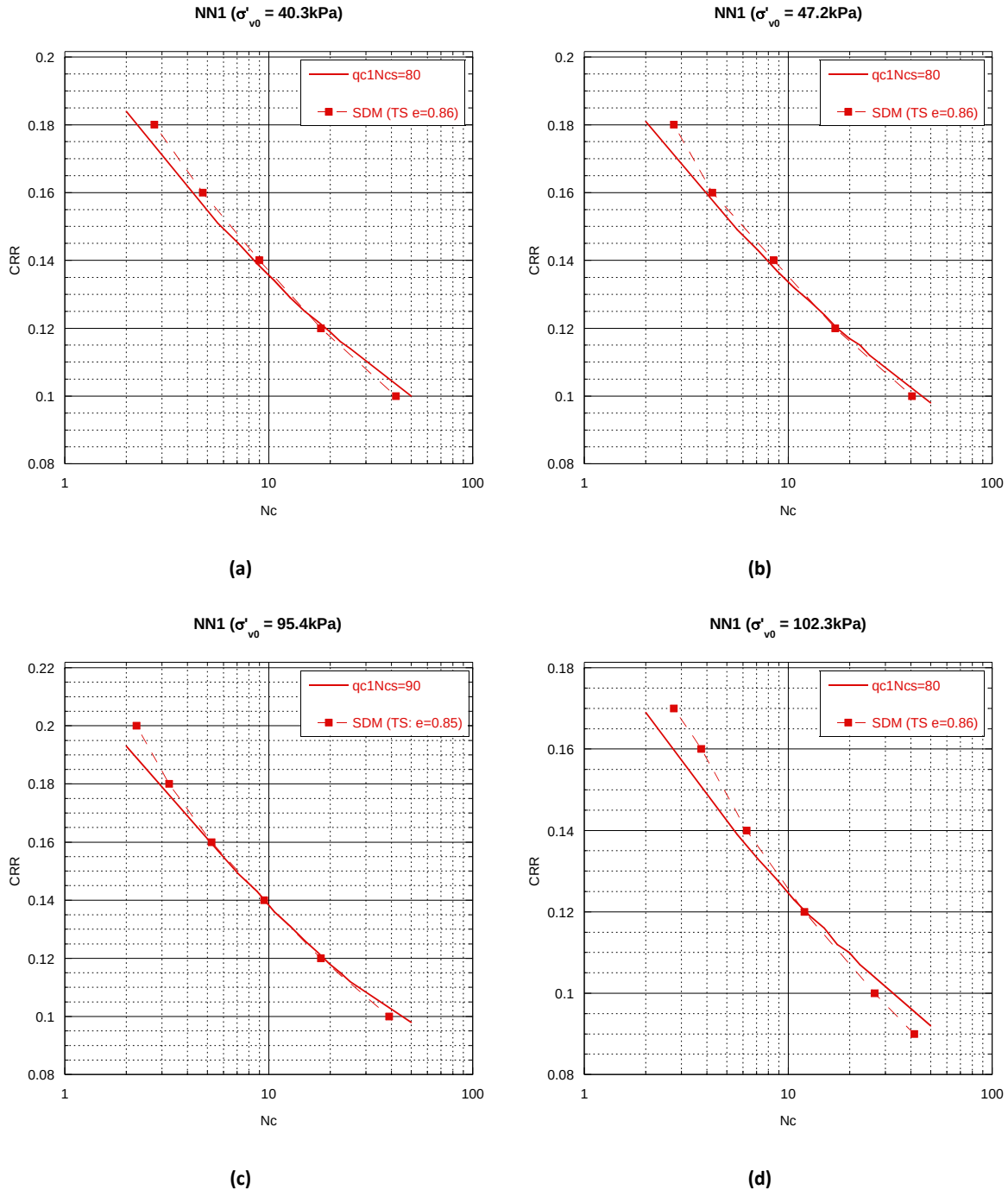

Figure I.2: S-D Model (SDM) LRCs (symbols and dashed lines) and target LRCs (solid lines) for NN1 soils of different densities: (a) q_{c1Ncs}=80, σ'_{v0}=40.3kPa; (b) q_{c1Ncs}=80, σ'_{v0}=47.2kPa; (c) q_{c1Ncs}=90, σ'_{v0}=95.4kPa; (d) q_{c1Ncs}=80, σ'_{v0}=102.3kPa

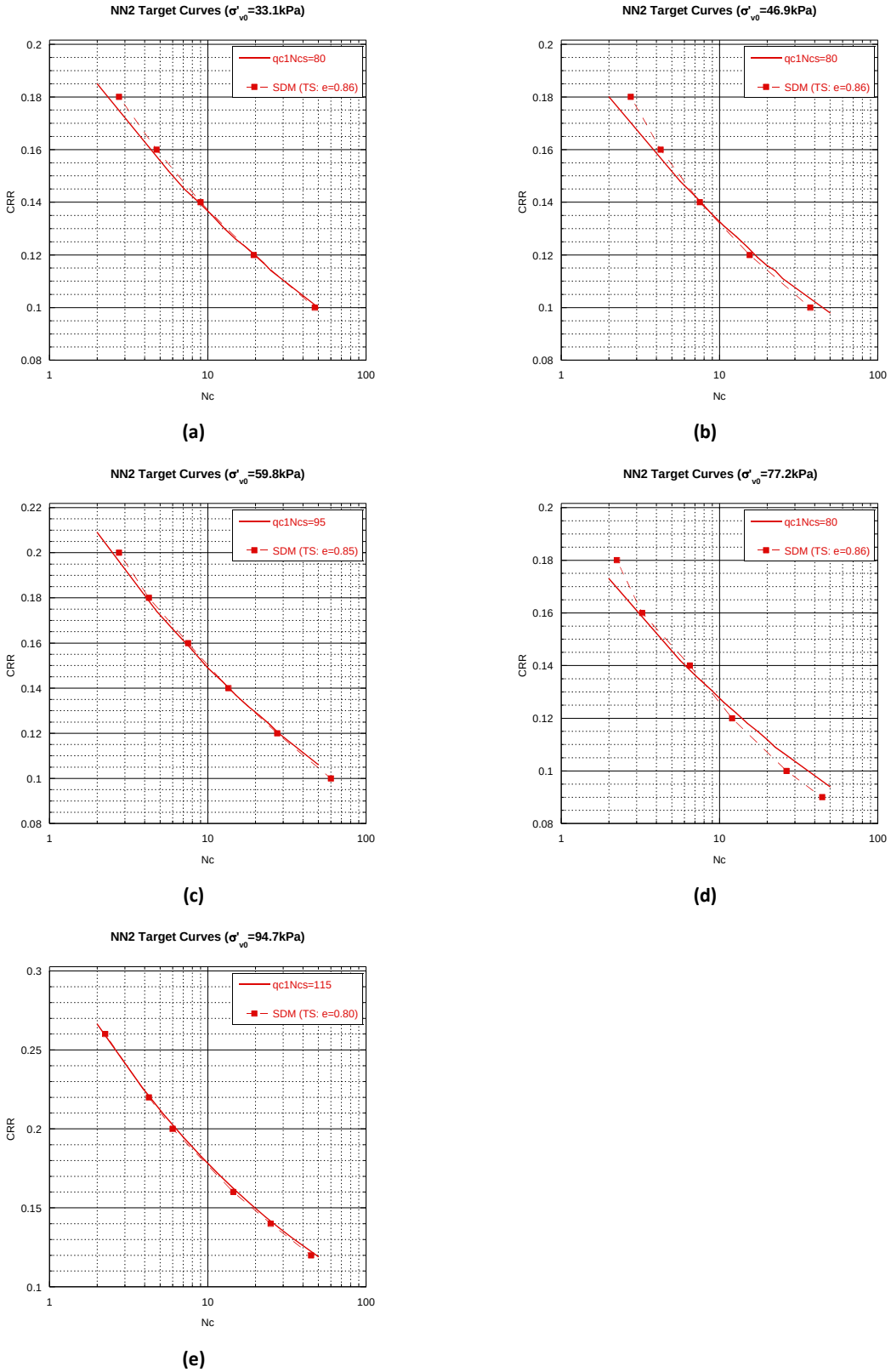

Figure I.3: S-D Model (SDM) LRCs (symbols and dashed lines) and target LRCs (solid lines) for NN2 soils of different densities: (a) q_{c1Ncs}=80, σ'_{v0}=33.1kPa; (b) q_{c1Ncs}=80, σ'_{v0}=46.9kPa; (c) q_{c1Ncs}=95, σ'_{v0}=59.8kPa; (d) q_{c1Ncs}=80, σ'_{v0}=77.2kPa; (d) q_{c1Ncs}=115, σ'_{v0}=94.7kPa

Appendix J: Modelling target degradation curves for the non-liquefiable layers

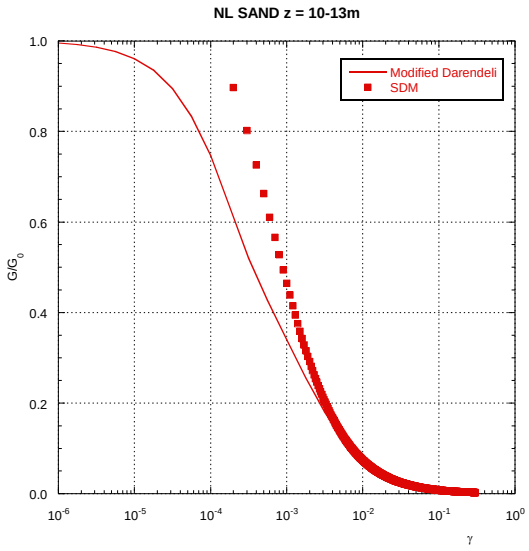

(a)

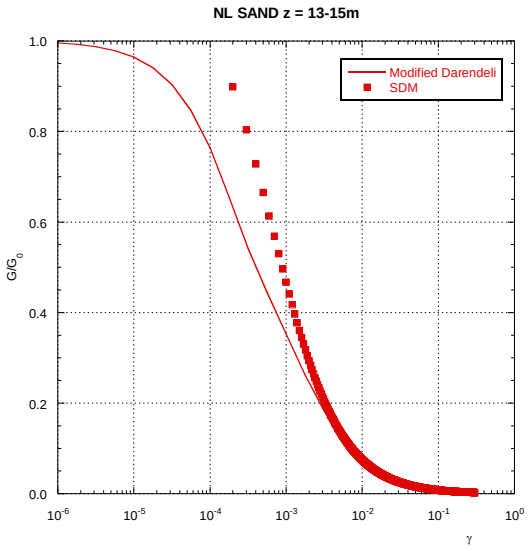

(b)

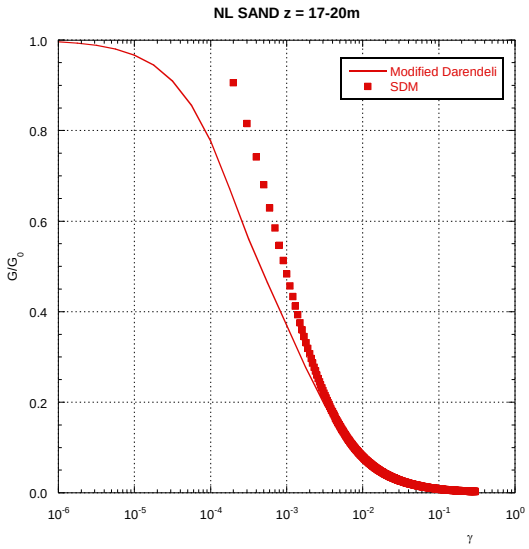

(c)

Figure J.1: Stress density modelling of degradation curves for non-liquefiable sand: (a) at *z*=11.5 m; (b) at *z*=15 m; (c) at z=18.5 m

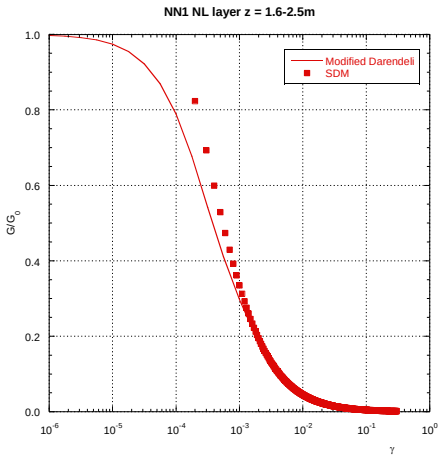

(a)

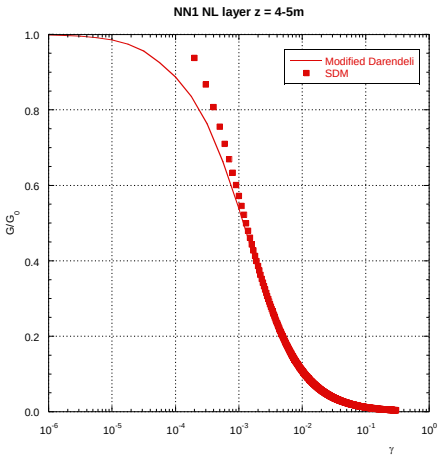

(b)

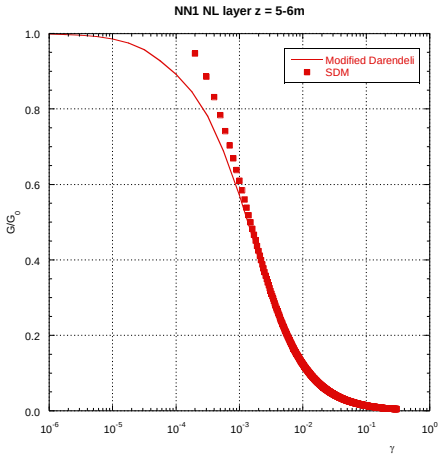

(c)

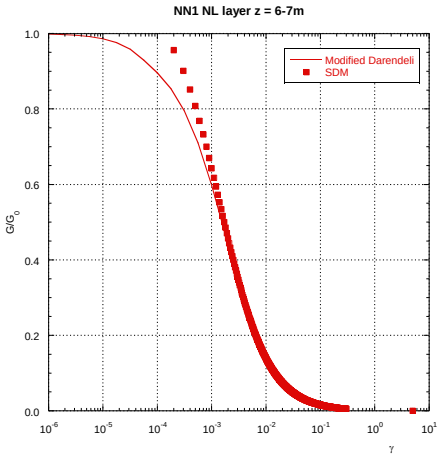

(d)

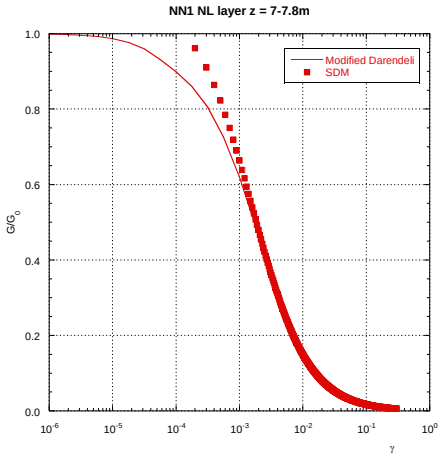

(e)

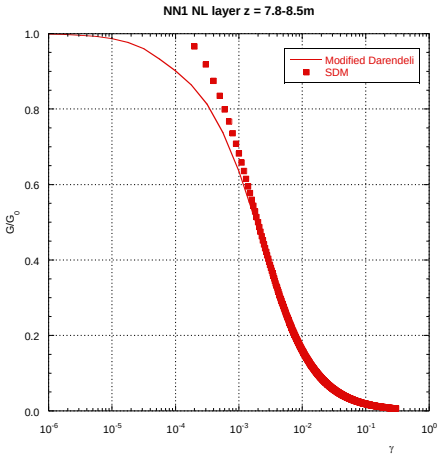

(f)

Figure J.2: Stress density modelling of degradation curves for non-liquefiable silt in the NN1 profile: (a) at *z*=2.05 m; (b) at *z*=4.5 m; (c) at z=5.5 m; (d) at z=6.5 m; (e) at z=7.4 m; (f) at z=8.15 m

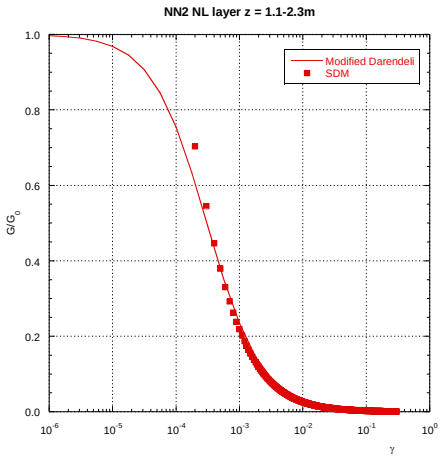

(a)

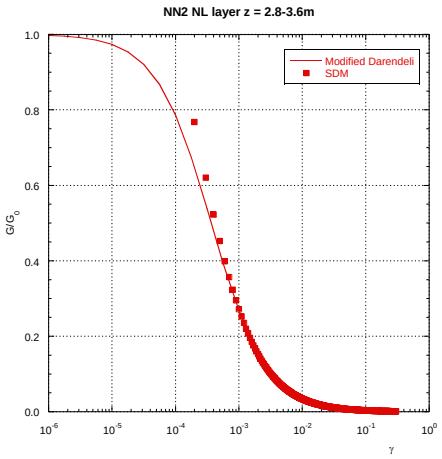

(b)

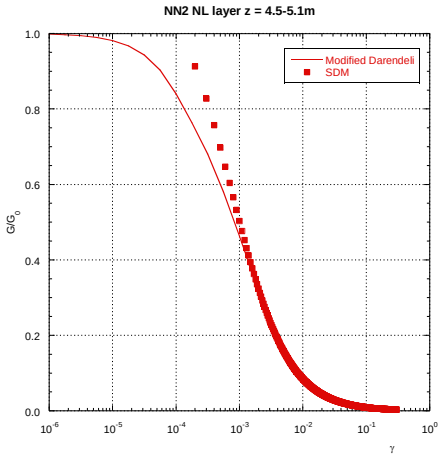

(c)

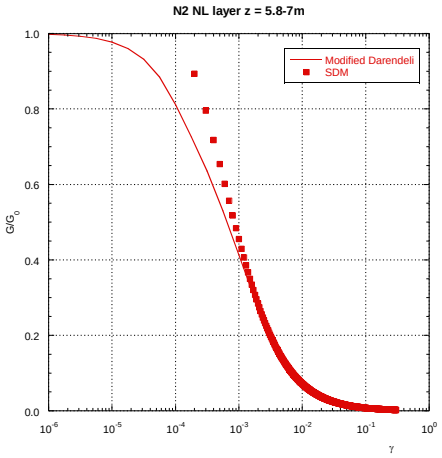

(d)

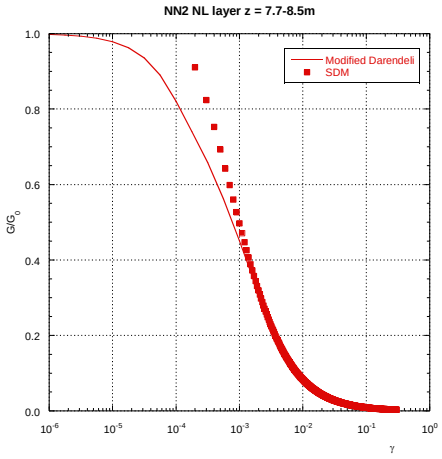

(e)

Figure J.3: Stress density modelling of degradation curves for non-liquefiable silt in the NN2 profile: (a) at *z*=1.7 m; (b) at *z*=3.2 m; (c) at z=4.8 m; (d) at z=6.4 m; (e) at z=8.1 m

Appendix K: Permeability values adopted for each layer in the YY1, YY2, NN1 and NN2 profiles

Table K.1: q_{c1Ncs} and permeability values adopted for use in the ESA for each layer within the YY1 profile

Layer	adopted q_{c1Ncs}	k (m/s)
0-1.8 m	140	$4x10^{-6}$
1.8-3.8 m	80	$4x10^{-6}$
3.8-6 m	90	$1x10^{-4}$
6-9 m	115	$2x10^{-4}$
9-10 m	140	$3x10^{-4}$
10-20 m	(1)	$1x10^{-4}$

(1) Not required for the purposes of ESA modelling

Table K.2: q_{c1Ncs} and permeability values adopted for use in the ESA for each layer within the YY2 profile

Layer	adopted q_{c1Ncs}	k (m/s)
0-1.8 m	140	$4x10^{-6}$
1.8-2.5 m	85	$4x10^{-6}$
2.5-3.2 m	95	$4x10^{-6}$
3.2-4 m	115	$1x10^{-4}$
4-6.8 m	125	$2x10^{-4}$
6.8-8.5 m	135	$3x10^{-4}$
8.5-10 m	140	$3x10^{-4}$
10-20 m	(1)	$1x10^{-4}$

(1) Not required for the purposes of ESA modelling

Table K.3: q_{c1Ncs}, V_s and permeability values adopted for use in the ESA for each layer within the NN1 profile

Layer	V_s (m/s)	adopted q_{c1Ncs}	k (m/s)
0-1.6 m	(1)	140	$4x10^{-6}$
1.6-2.5 m	150	(1)	$1x10^{-7}$
2.5-4.0 m	(1)	80	$1x10^{-4}$
4.0-8.5 m	110	(1)	$1x10^{-7}$
8.5-9.2 m	(1)	90	$1x10^{-4}$
9.2-10 m	(1)	80	$4x10^{-6}$
10-20 m	(1)	(1)	$1x10^{-4}$

(1) Not required for the purposes of ESA modelling

Table K.4: q_{c1Ncs}, V_s and permeability values for use in the ESA for each layer within the NN2 profile

Layer	V_s (m/s)	adopted q_{c1Ncs}	k (m/s)
0-1.1 m	(1)	140	$1x10^{-4}$
1.1-2.3 m	200	(1)	$1x10^{-7}$
2.3-2.8 m	(1)	80	$4x10^{-6}$
2.8-3.6 m	190	(1)	$1x10^{-7}$
3.6-4.5 m	(1)	80	$4x10^{-6}$
4.5-5.1 m	120	(1)	$1x10^{-7}$
5.1-5.8 m	(1)	95	$1x10^{-4}$
5.8-7.0 m	150	(1)	$1x10^{-7}$
7.0-7.7 m	(1)	80	$4x10^{-6}$
7.7-8.5 m	150	(1)	$1x10^{-7}$
8.5-10 m	(1)	115	$1x10^{-4}$
10-20 m	(1)	(1)	$1x10^{-4}$

(1) Not required for the purposes of ESA modelling

Appendix L: Suitability of the CACS 22 Feb 2011 ground motion with scaling factor I_3=1.12 as representative of the 4 Sep 2010 earthquake

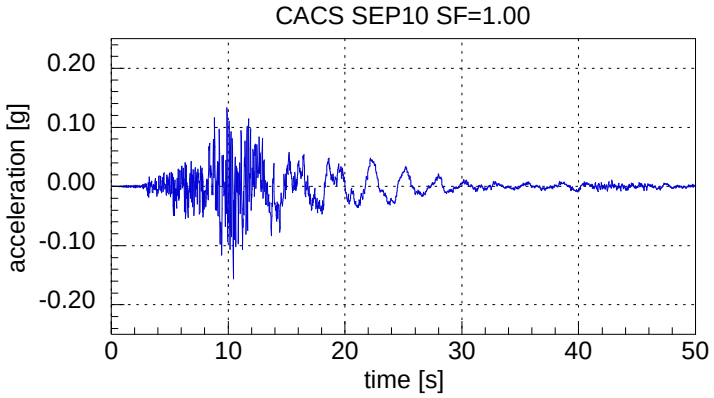

(a)

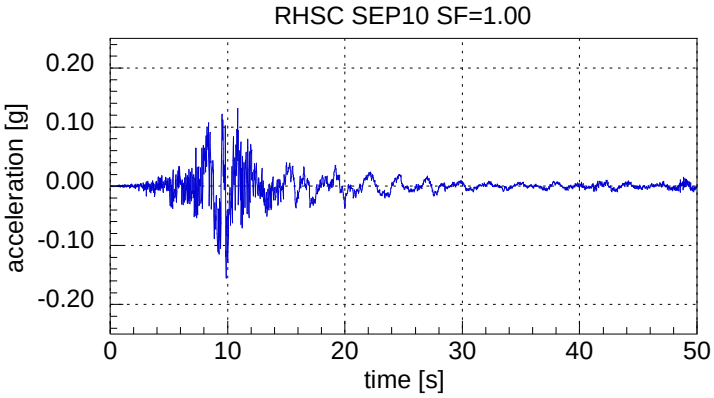

(b)

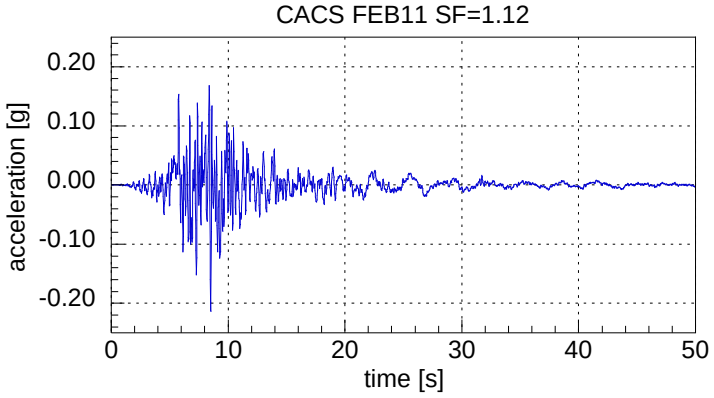

(c)

Figure L.1: Horizontal acceleration time histories throughout depth for YY1: (a) CACS SEP10 motion with scale factor 1.0; b) RHSC SEP10 motion with scale factor 1.0; (c) CACS FEB11 motion with scale factor 1.12

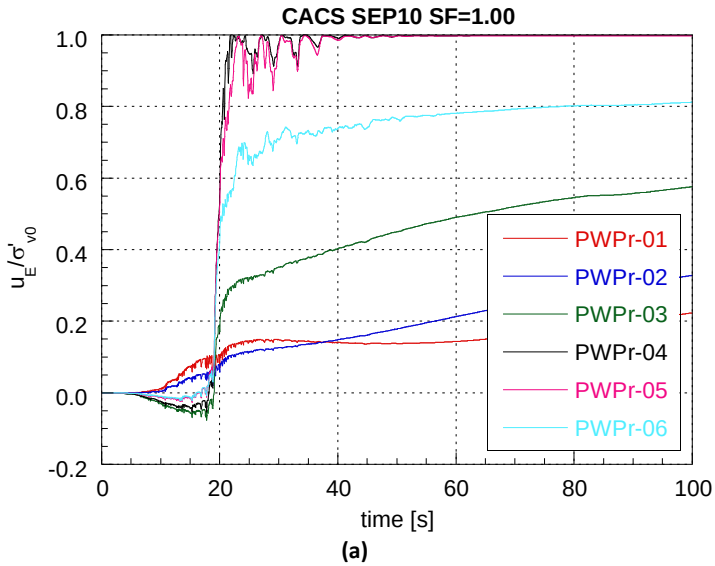

(a)

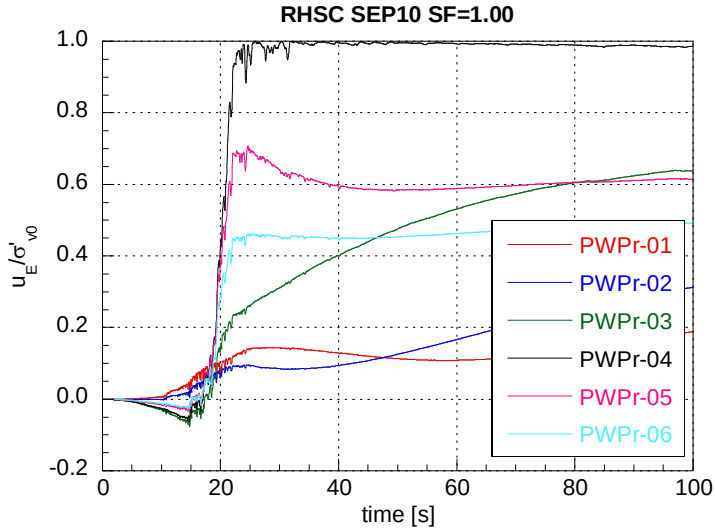

(b)

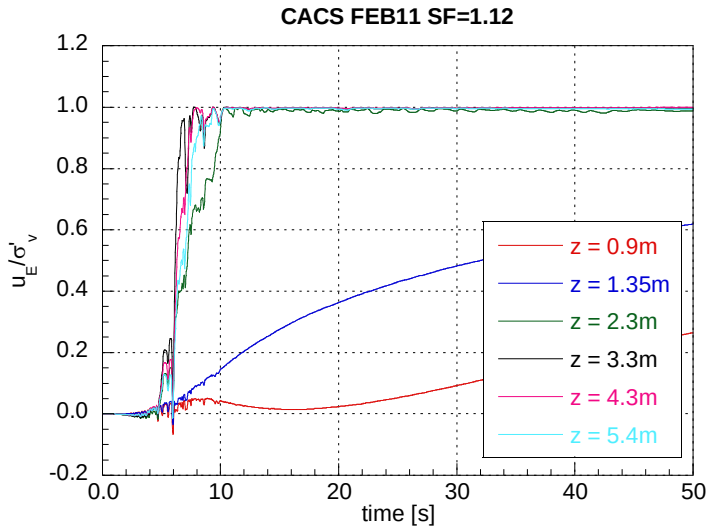

(c)

Figure L.2: Pore water pressure ratio time histories for YY1, z=0-6m: (a) CACS SEP10 motion with scale factor 1.0; (b) RHSC SEP10 motion with scale factor 1.0; (c) CACS FEB11 motion with scale factor 1.12

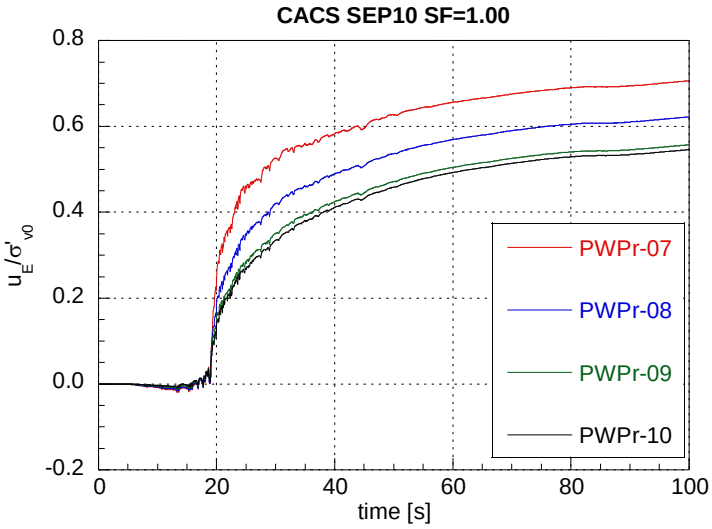

(a)

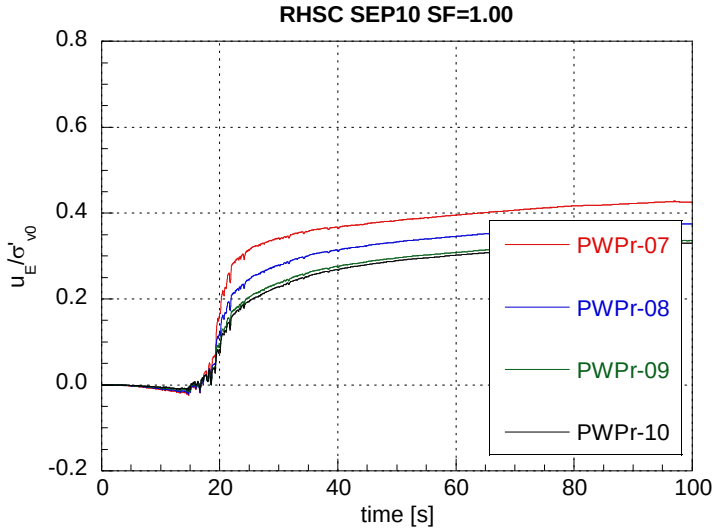

(b)

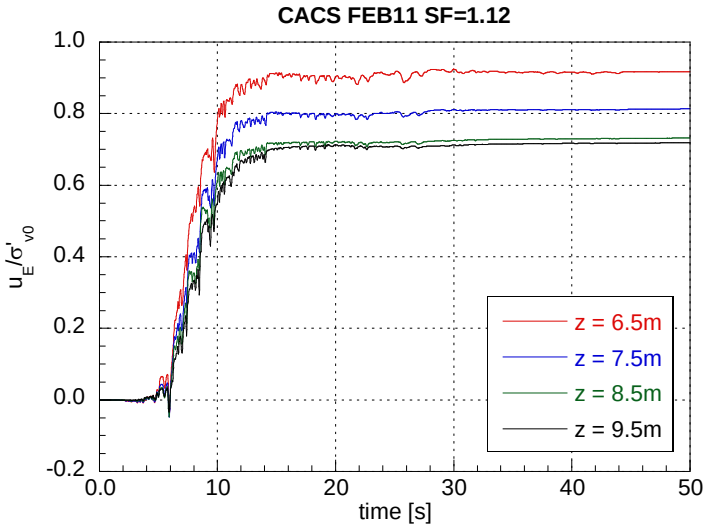

(c)

Figure L.3: Pore water pressure ratio time histories for YY1, z=6-10m: (a) CACS SEP10 motion with scale factor 1.0; (b) RHSC SEP10 motion with scale factor 1.0; (c) CACS FEB11 motion with scale factor 1.12

Appendix M: Stress-strain curves for all layers in YY1 profile with I_1=2.23 (a_{max}=0.4g) input motion

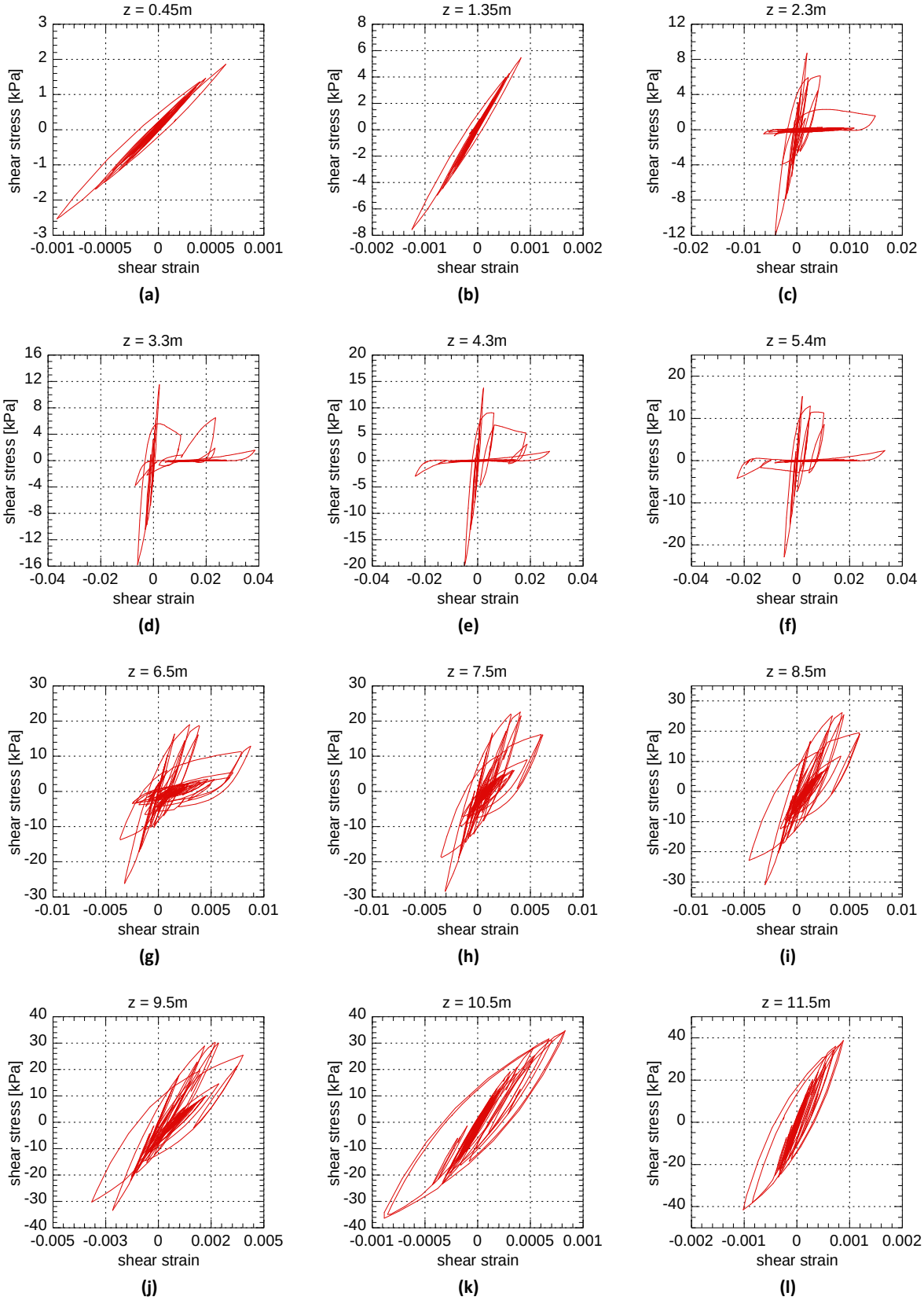

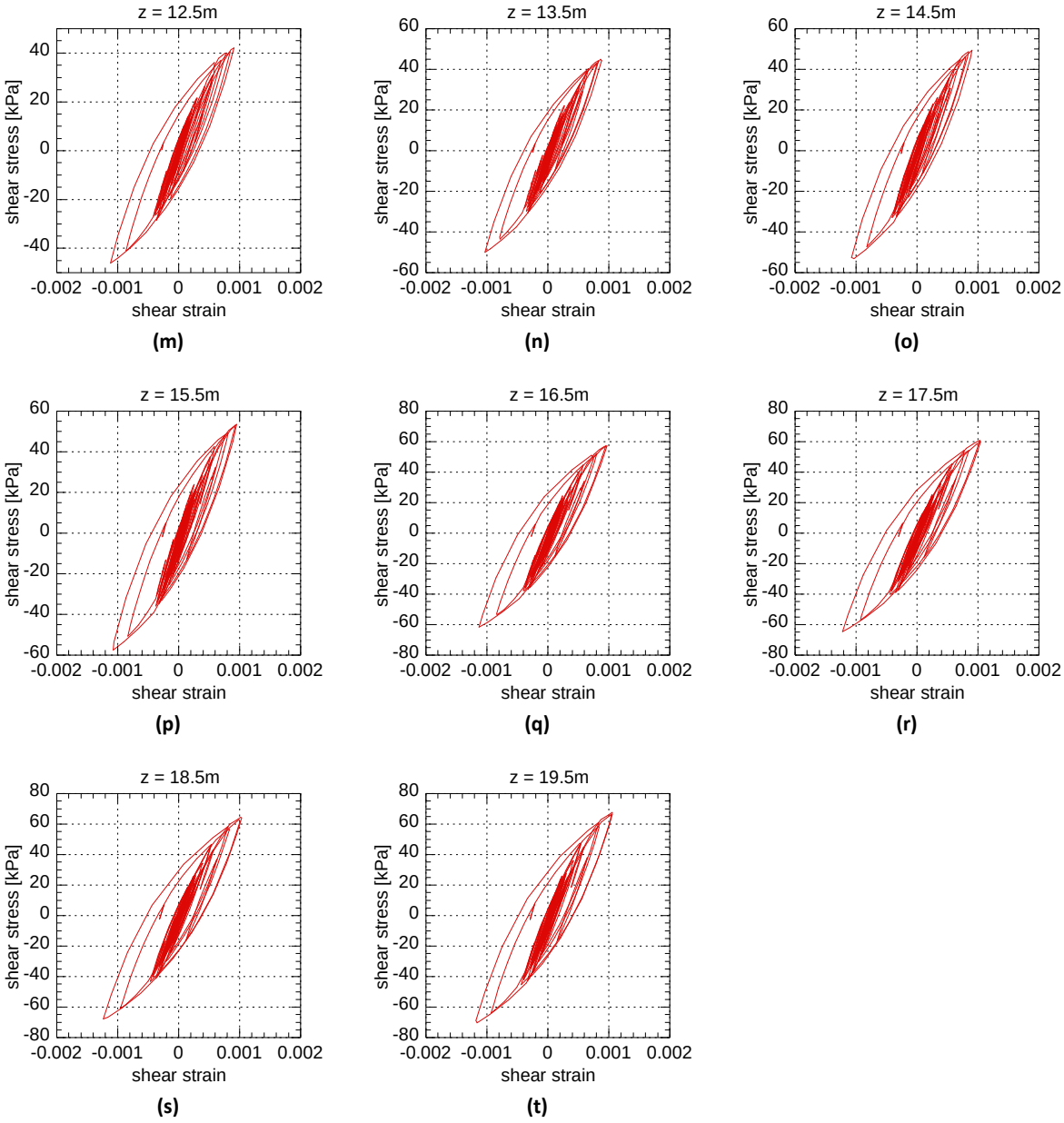

Figure M.1: Stress-strain curves for YY1, a_{max}=0.4g: (a) z=0.45m; (b) z=1.35m; (c) z=2.3m; (d) z=3.3m; (e) z=4.3m; (f) z=5.4m; (g) z=6.5m; (h) z=7.5m; (i) z=8.5m; (j) z=9.5m; (k) z=10.5m; (l) z=11.5m; (m) z=12.5m; (n) z=13.5m; (o) z=14.5m; (p) z=15.5m; (q) z=16.5m; (r) z=17.5m; (s) z=18.5m; (t) z=19.5m;

Appendix N: Comparison of response of YY1 and YY2 profiles for I_2=1.67 (a_{max}=0.3g) and I_3=1.12 (a_{max}=0.2g)

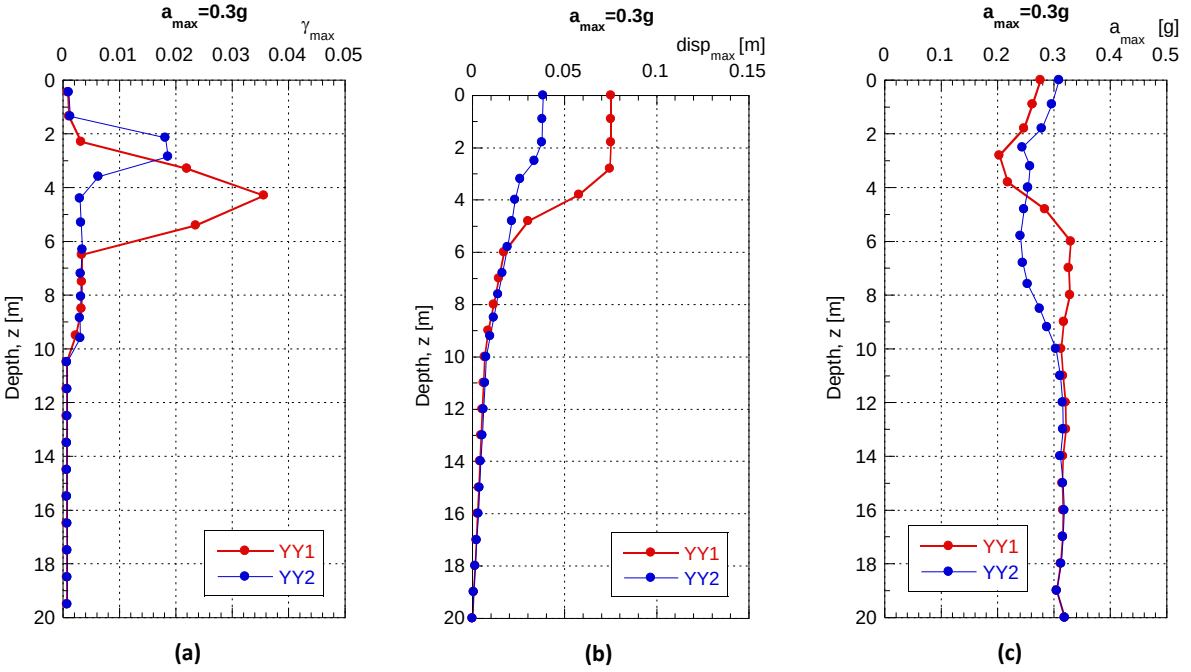

Figure N.1: Distribution of ground response parameters throughout the depth of both YY profiles for intermediate shaking intensity, a_{max}=0.3g: (a) maximum shear strain; (b) maximum horizontal displacement; (c) maximum horizontal acceleration

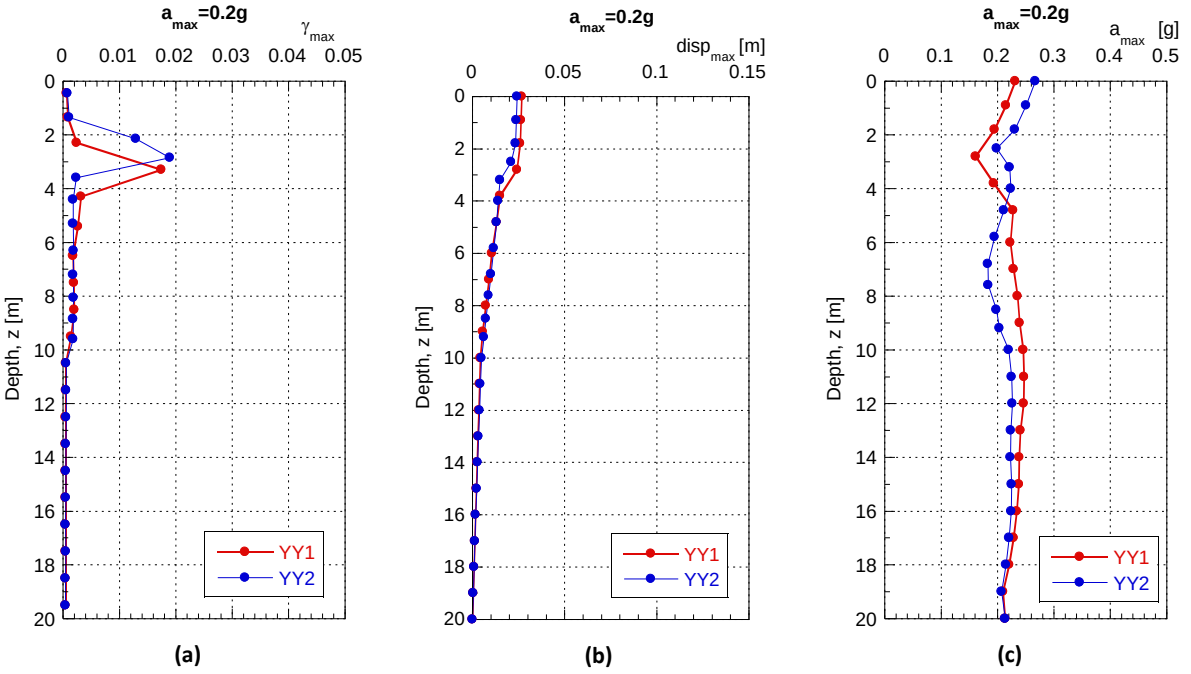

Figure N.2: Distribution of ground response parameters throughout the depth of both YY profiles for lowest shaking intensity, a_{max}=0.2g: (a) maximum shear strain; (b) maximum horizontal displacement; (c) maximum horizontal acceleration

Appendix O: Comparison of the response of the NN1 and NN2 profiles for I_2=1.67 (a_{max}=0.3g) and I_3=1.12 (a_{max}=0.2g)

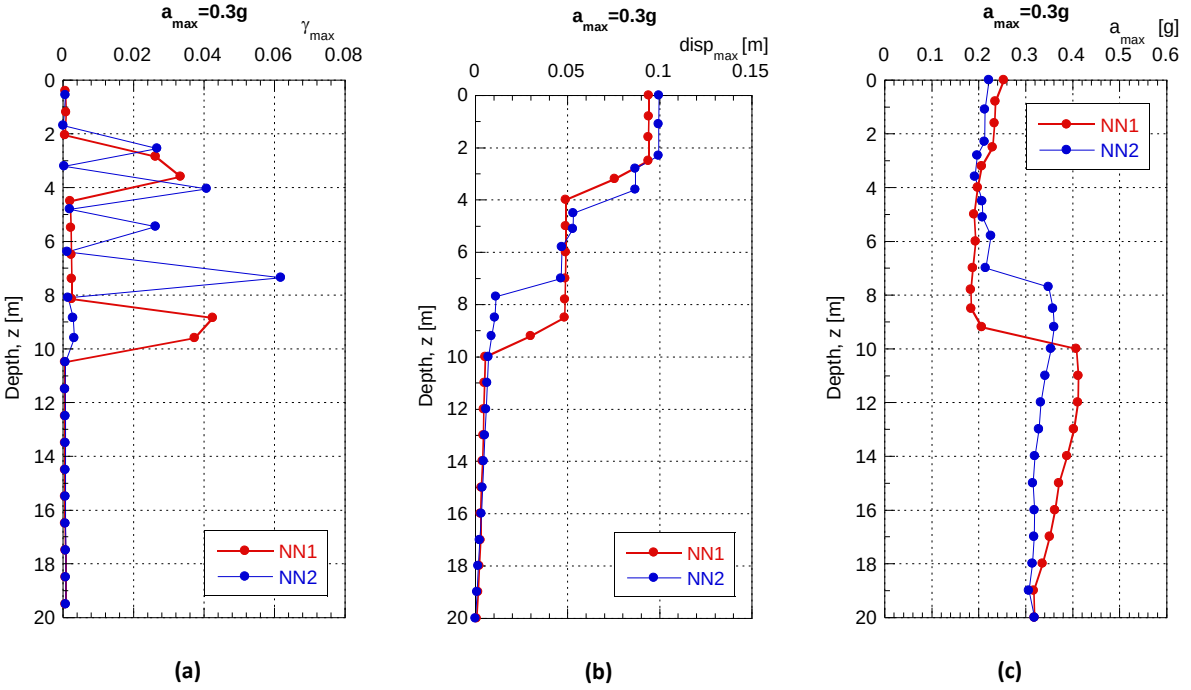

Figure O.1: Distribution of ground response parameters throughout the depth of both NN profiles for intermediate shaking intensity, a_{max}=0.3g: (a) maximum shear strain; (b) maximum horizontal displacement; (c) maximum horizontal acceleration

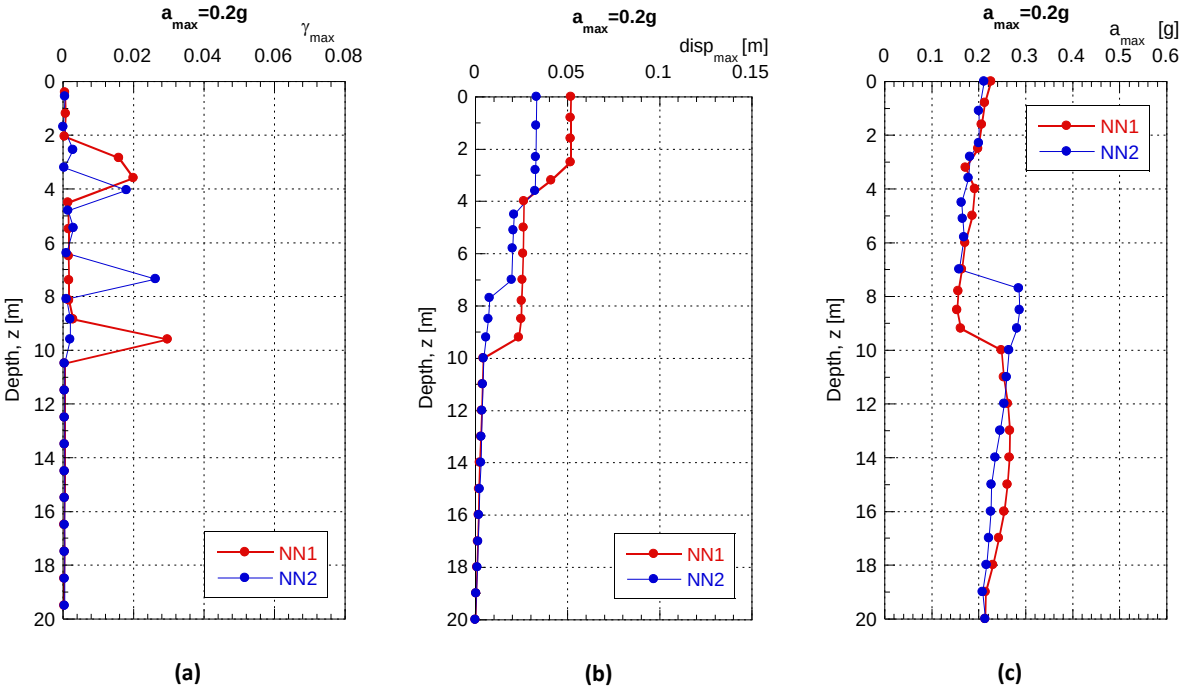

Figure O.2: Distribution of ground response parameters throughout the depth of both NN profiles for lowest shaking intensity, a_{max}=0.2g: (a) maximum shear strain; (b) maximum horizontal displacement; (c) maximum horizontal acceleration

Appendix P: Comparison of results from simplified method and ESA for all soil profiles and all ground motion intensities

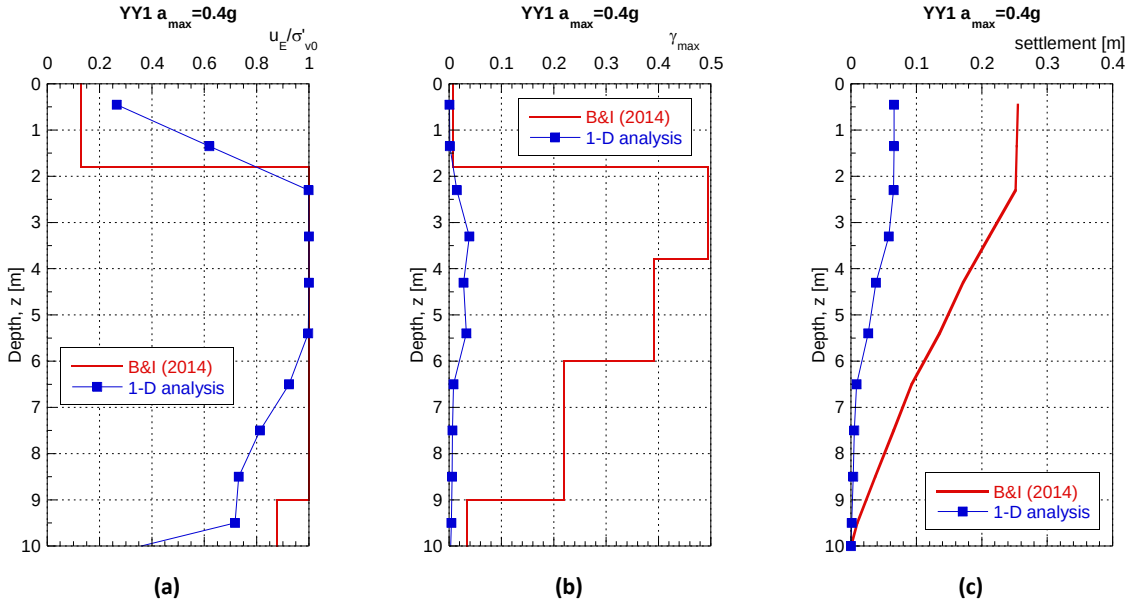

Figure P.1: Comparison plots for soil response predicted by the simplified method and the 1-D soil column model for YY1, a_{max}=0.4g: (a) maximum pore water pressure ratios; (b) maximum shear strains; (c) vertical settlement

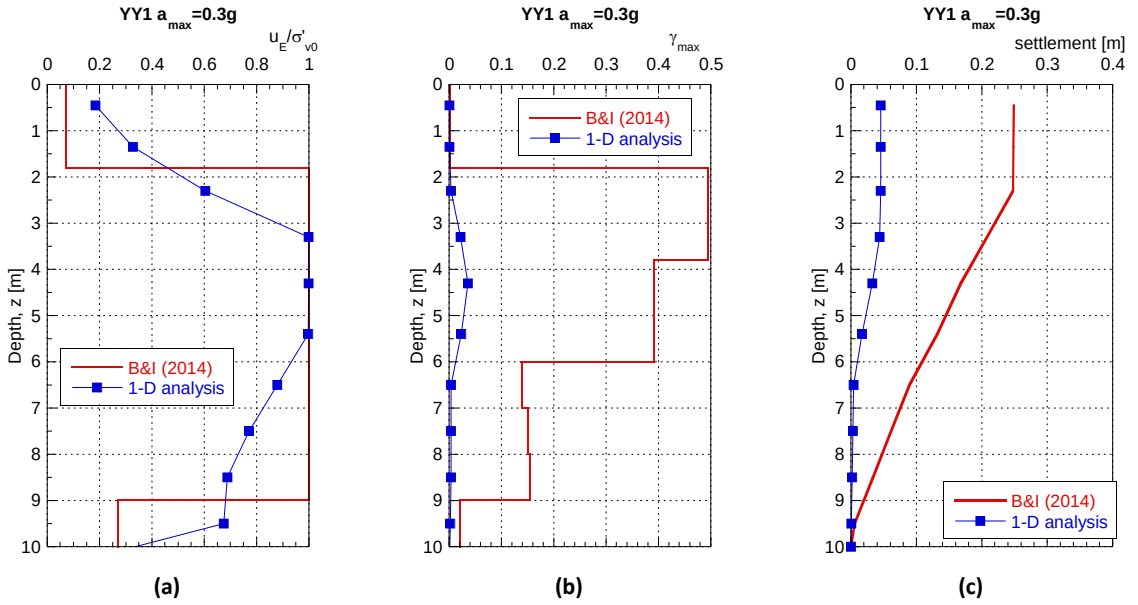

Figure P.2: Comparison plots for soil response predicted by the simplified method and the 1-D soil column model for YY1, a_{max}=0.3g: (a) maximum pore water pressure ratios; (b) maximum shear strains; (c) vertical settlement

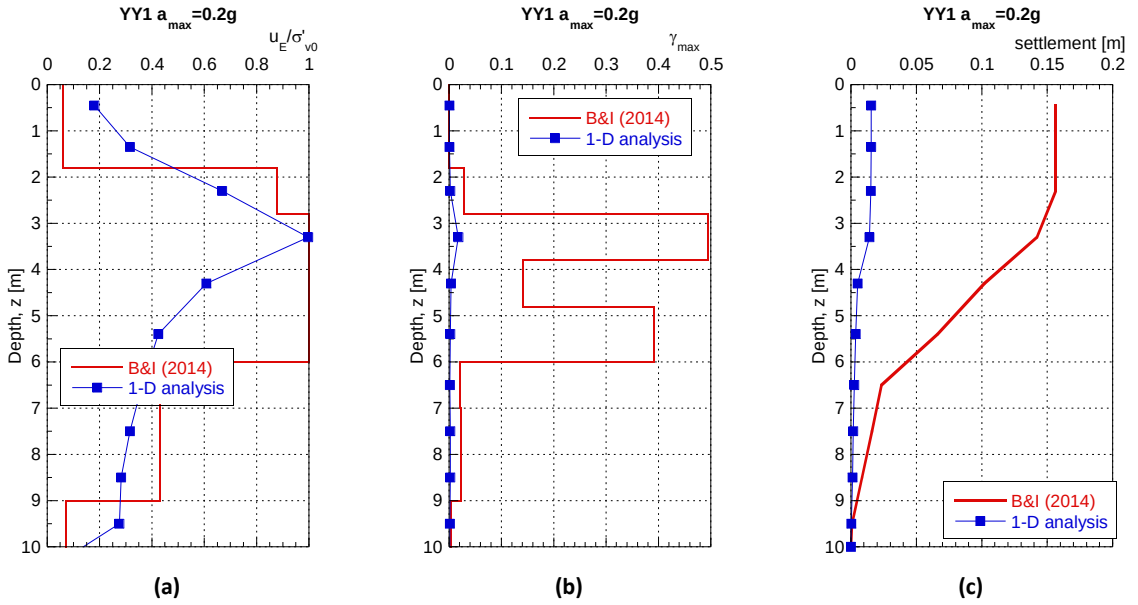

Figure P.3: Comparison plots for soil response predicted by the simplified method and the 1-D soil column model for YY1, a_{max}=0.2g: (a) maximum pore water pressure ratios; (b) maximum shear strains; (c) vertical settlement

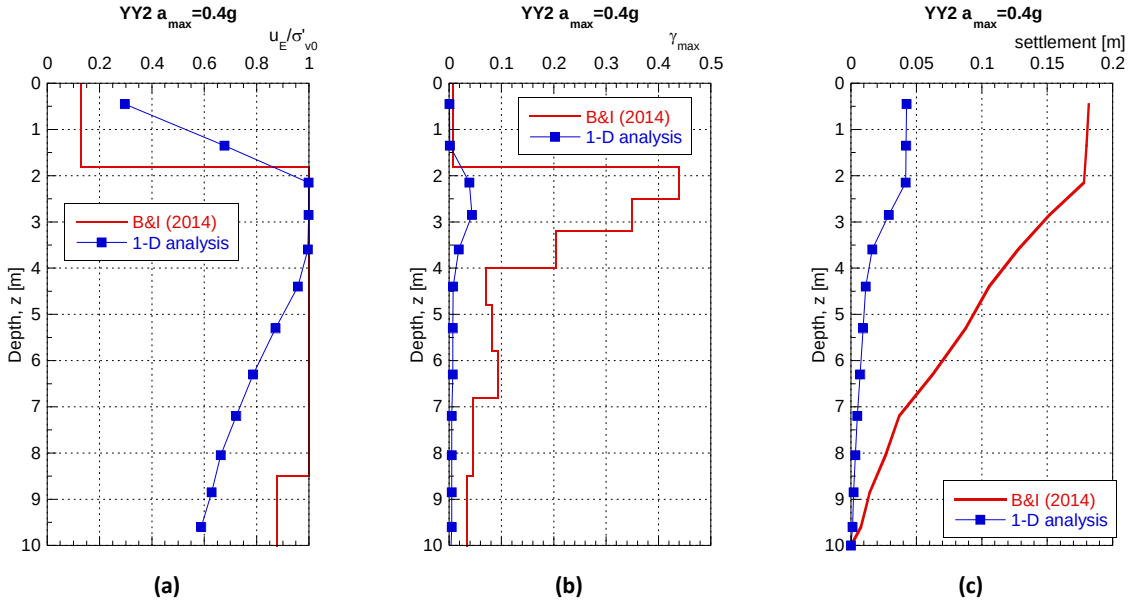

Figure P.4: Comparison plots for soil response predicted by the simplified method and the 1-D soil column model for YY2, a_{max}=0.4g: (a) maximum pore water pressure ratios; (b) maximum shear strains; (c) vertical settlement

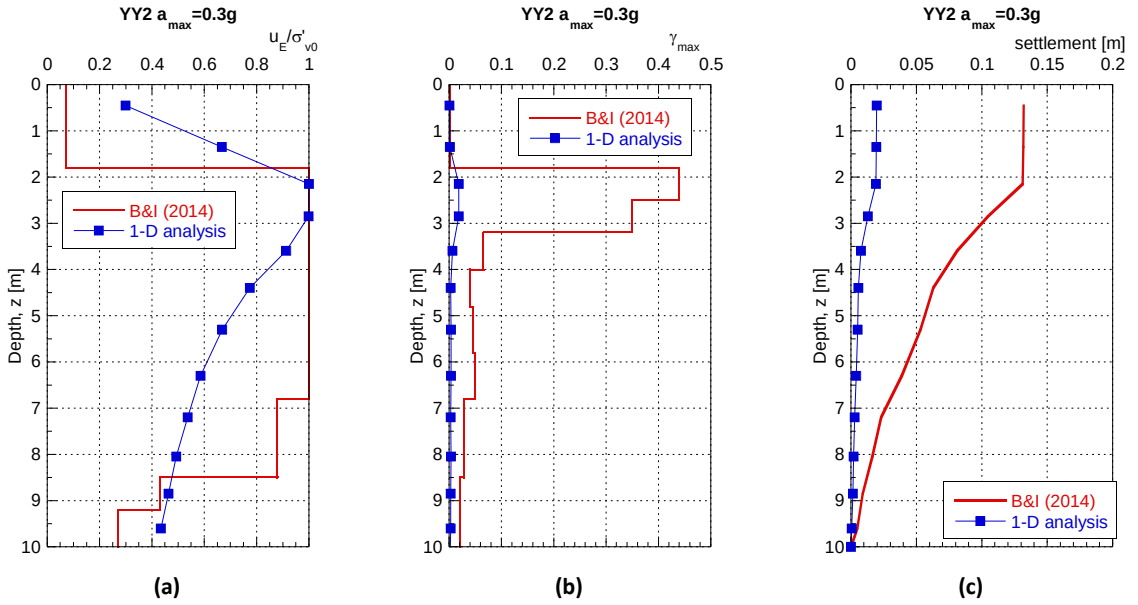

Figure P.5: Comparison plots for soil response predicted by the simplified method and the 1-D soil column model for YY2, a_{max}=0.3g: (a) maximum pore water pressure ratios; (b) maximum shear strains; (c) vertical settlement

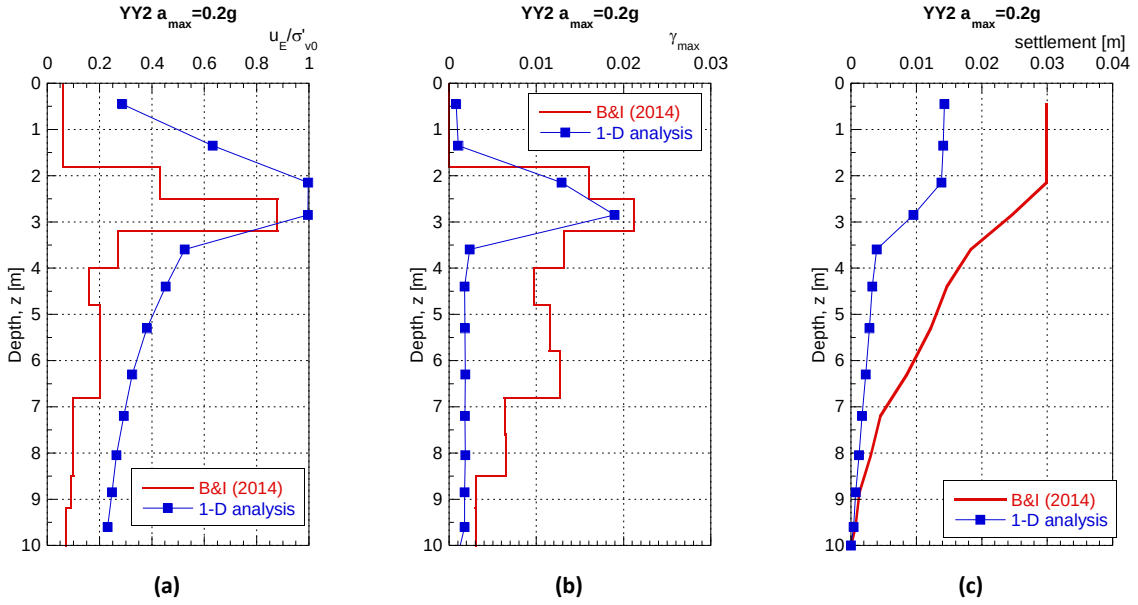

Figure P.6: Comparison plots for soil response predicted by the simplified method and the 1-D soil column model for YY2, a_{max}=0.2g: (a) maximum pore water pressure ratios; (b) maximum shear strains; (c) vertical settlement

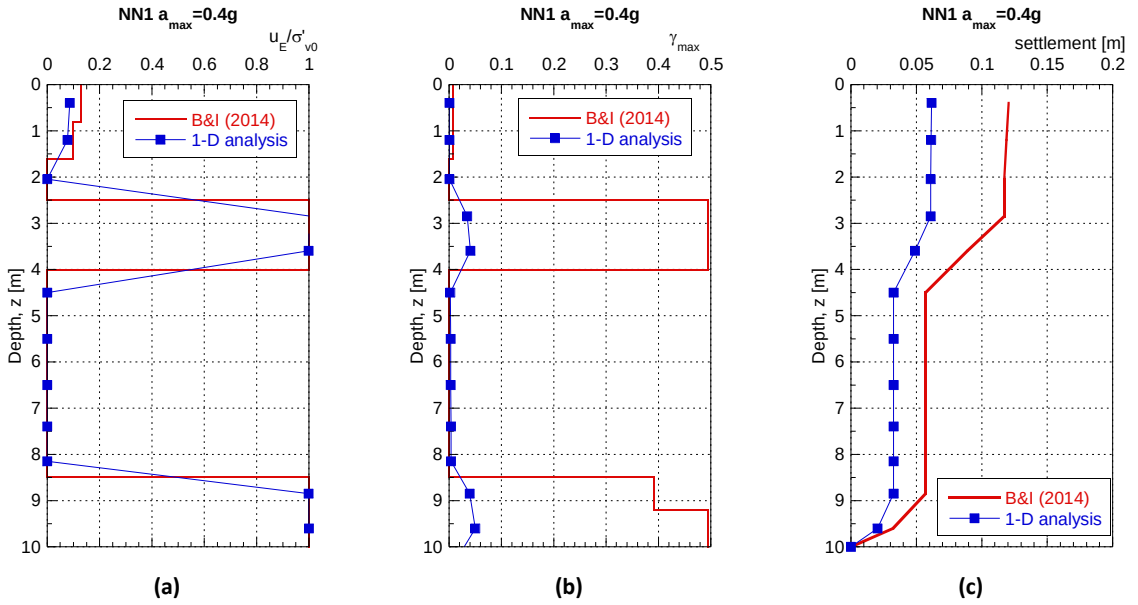

Figure P.7: Comparison plots for soil response predicted by the simplified method and the 1-D soil column model for NN1, a_{max}=0.4g: (a) maximum pore water pressure ratios; (b) maximum shear strains; (c) vertical settlement

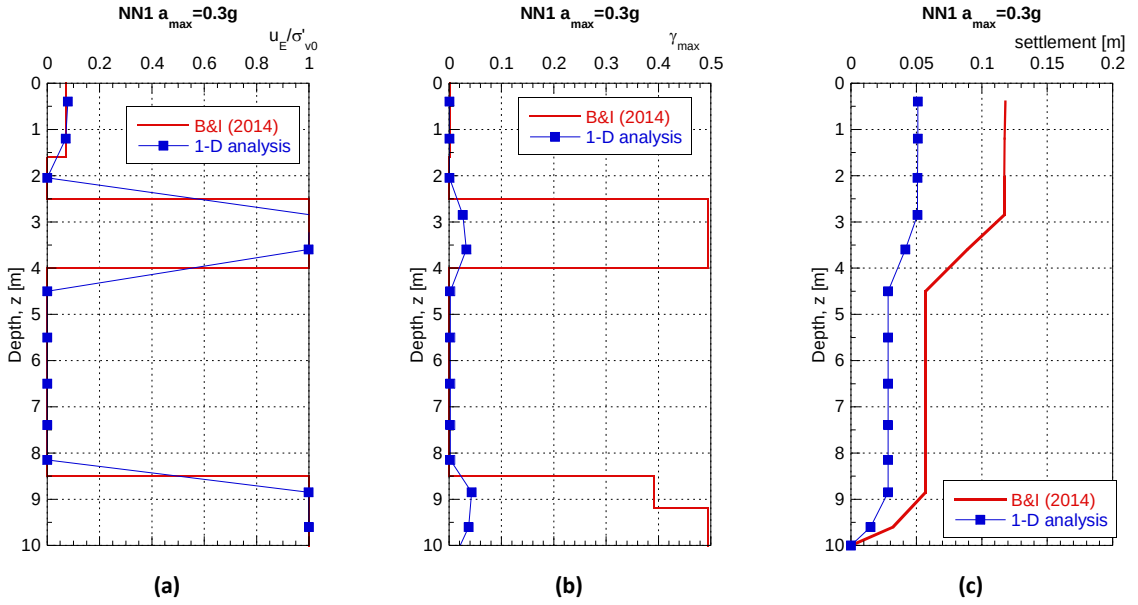

Figure P.8: Comparison plots for soil response predicted by the simplified method and the 1-D soil column model for NN1, a_{max}=0.3g: (a) maximum pore water pressure ratios; (b) maximum shear strains; (c) vertical settlement

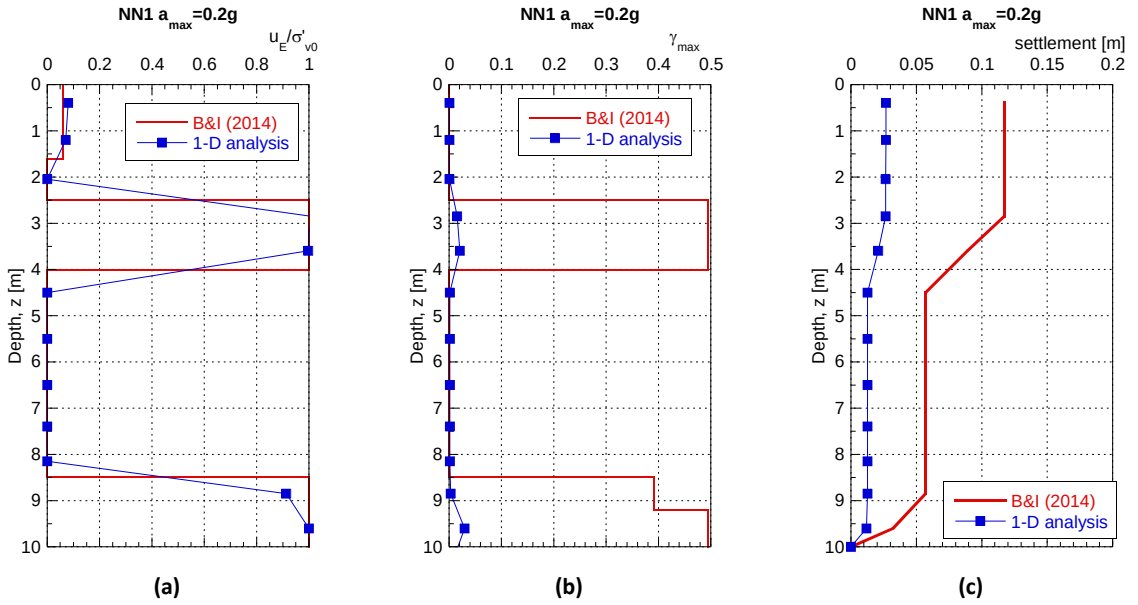

Figure P.9: Comparison plots for soil response predicted by the simplified method and the 1-D soil column model for NN1, a_{max}=0.2g: (a) maximum pore water pressure ratios; (b) maximum shear strains; (c) vertical settlement

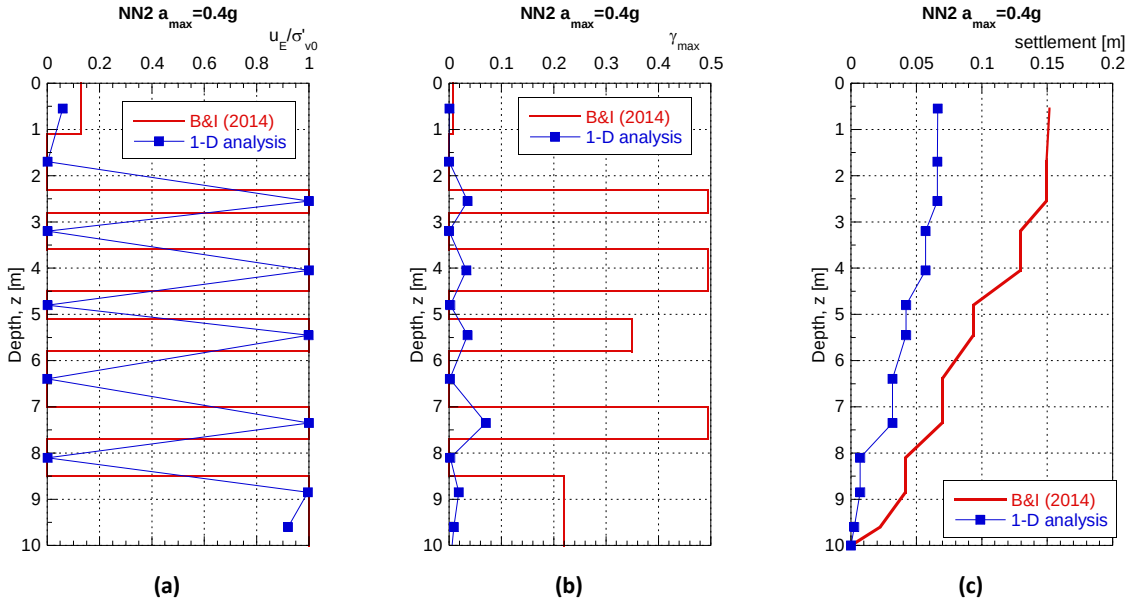

Figure P.10: Comparison plots for soil response predicted by the simplified method and the 1-D soil column model for NN2, a_{max}=0.4g: (a) maximum pore water pressure ratios; (b) maximum shear strains; (c) vertical settlement

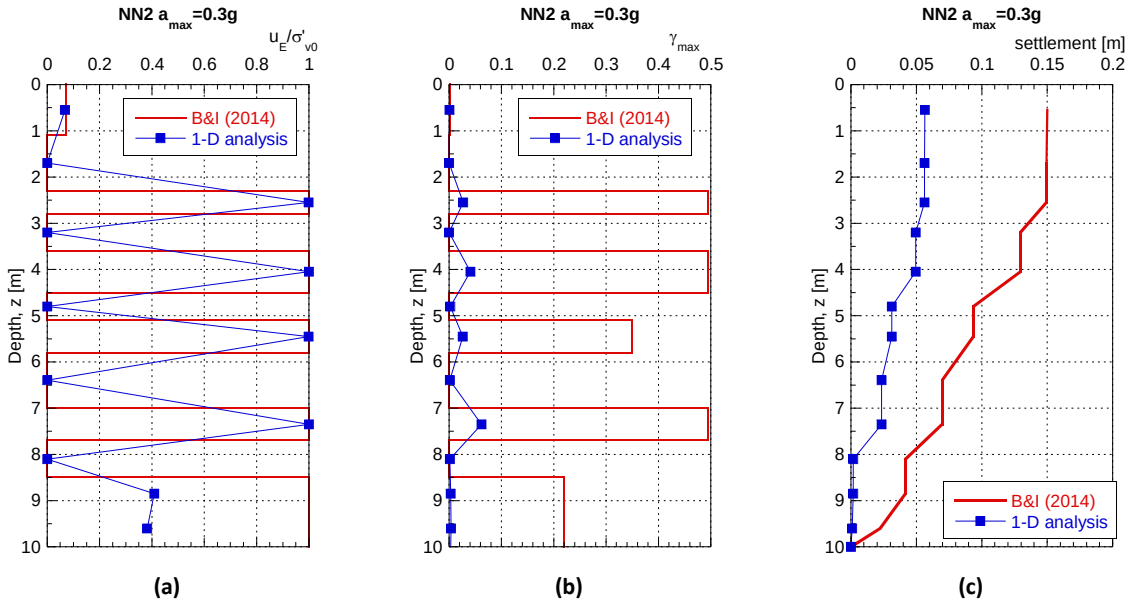

Figure P.11: Comparison plots for soil response predicted by the simplified method and the 1-D soil column model for NN2, a_{max}=0.3g: (a) maximum pore water pressure ratios; (b) maximum shear strains; (c) vertical settlement

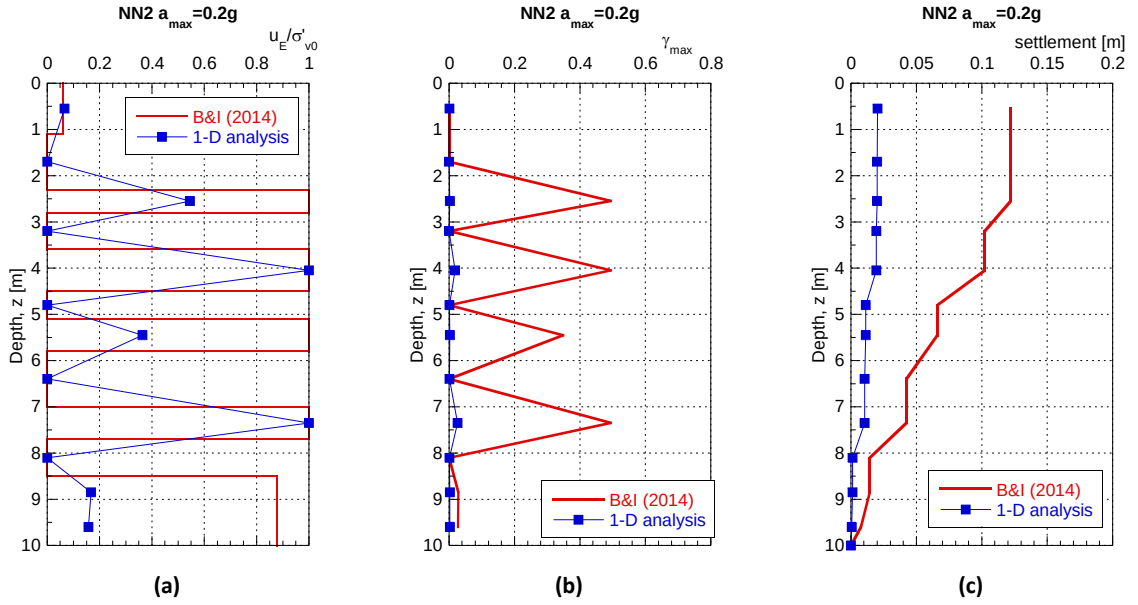

Figure P.12: Comparison plots for soil response predicted by the simplified method and the 1-D soil column model for NN2, a_{max}=0.2g: (a) maximum pore water pressure ratios; (b) maximum shear strains; (c) vertical settlement